PREFACE

I would not have been able to complete this work without the help and guidance from several people. First of all, I want to thank my supervisor, prof. Johan Kr. Tuset, for his support and input during the course of this thesis and Dr. Trond Bergstrom, SINTEF Materials Technology for helping me with matters of both practical and scientific nature.

The work has been sponsored by the Ferroalloy Producers Research Association (FFF) and the Norwegian Research Council. They are both gratefully acknowledged. The FFF control committee has been a forum for fruitful discussions and valuable input. I would especially like to thank Birger Andresen (FeSil) and Karl Forwald (Elkem) for helping me with chemical analysis, as well as showing interest for the work during the period.

I appreciate all help and support from people at my institute, especially Morten Raanes for helping me with the microprobe analysis, as well as everybody else that contributed to the completion of this thesis.

During the program I spent a semester at the University of Wisconsin-Madison, where important experiments were carried out. I would like to thank Dr. Lloyd S. Nelson for his excellent tutoring, as well as helping me getting settled in Madison. I am also grateful to his wife, Lorna, for all support on practical matters. Furthermore, the staff in Department of Nuclear Engineering; Paul Brooks, our skilled technician, Prof. Michael Corradini, his inspiration and fruitful comments related to the work is highly acknowledged.

Trondheim, 25.3.02

Kjetil Hildal

ABSTRACT

Steam explosions are possible during granulation of Si and FeSi75. These explosions are a great hazard, and must be avoided. Norwegian ferroalloy producers have initiated a research program to learn more about such violent melt-water interactions, in a joint effort with NTNU and SINTEF. The focus has primarily been on important parameters that can be controlled industrially, such as water temperature and metal composition. This thesis-work has focused on the effect of small additions of Al and Ca in Si-metal and FeSi75. However, within the same project, experiments on the effect of water temperature have also been carried out.

The work has primarily been of experimental character. Two experimental apparatuses have been used. The first apparatus allows us to rapidly melt a sample of metal in an inert atmosphere to a desired temperature, expose the surface of the melt to an oxidizing agent (i.e. water) and then rapidly cool the sample to room temperature. The oxide that forms at the surface is examined with a microprobe. Thus, information regarding the composition and substance of the oxide layer is available. The second apparatus is suitable for releasing single drops of melt into a water tank, where they can be triggered and explode. A variety of techniques have been used in order to monitor the experiment: regular video, high-speed film, high-speed video, open-shutter imaging and pressure transducer measurements.

Both Si and FeSi75 must be triggered in order to explode. Trigger pressures range from 0.3 MPa (FeSi75) to 2 MPa (Si-metal). We have established at which depths the molten drops can be triggered. Molten drops of FeSi75 can be triggered at depths twice of those of molten drops of Si. The latter can be triggered even if they are partially solidified.

The explosion itself is strong enough to trigger neighbor drops as far away as 400 mm. Thus, we cannot rule out the possibility of large-scale steam explosions during granulation of molten Si or FeSi75, which is in accordance with industrial practice.

By the use of high-speed imaging techniques and pressure measurements, we have been able to describe qualitatively what happens when a molten drop of Si/FeSi75 fragments rapidly in water. As the melt fragments, the rapid heat transfer generates vapor as bubbles, which expand and collapse in a cyclic manner. Large pressure pulses are generated upon collapse of the steam bubble, that is, when water jets impact in the center of the collapsing bubble.

URN:NBN:no-2125

ABSTRACT

The first step in the oxidation of liquid silicon is the formation of gaseous SiO. The fate of this gas now depends on the flow conditions at the surface of the melt. In the case of a molten drop descending in water, most of the gas is flushed away from the surface. Thus, there are only minor traces of oxygen-containing material (i.e. silica) at the surface of the solidified drop.

The addition of small amounts of Al and/or Ca dramatically changes the behavior of the molten drop. A strange effect is the two-fold increase in the fall velocity for molten drops of silicon. A similar effect was detected for molten drops of FeSi75. Alloying elements such as Al and Ca greatly reduce the risk for a steam explosion of molten Si. The significance of these elements is related to the oxidation reactions at the surface of the molten drop of metal. As silicon reacts with water vapor and oxidizes, hydrogen gas is formed. If Al and Ca are present in the melt, these elements will speed up the hydrogen generation considerably. This gas is strongly influencing on the probability for a steam explosion to occur. H_2 stabilizes the vapor film around the drop, that is, much stronger trigger pressures are needed to collapse the film. Even if the trigger pressure is strong enough to collapse the vapor film, violent interactions are almost completely absent. A fragmentation of the melt is observed, but the heat transfer is apparently not rapid enough to generate steam bubbles, i.e. the generation of steam is below the critical limit.

URN:NBN:no-2125

TABLE OF CONTENTS

PREFACE **1**

ABSTRACT **2**

TABLE OF CONTENTS **4**

1. INTRODUCTION **9**

1.1 STEAM EXPLOSIONS – FIELDS OF OCCURRENCE 10
1.2 GRANULATION IN THE METAL INDUSTRY 12
1.2.1 Why granulate Si and FeSi? *13*
1.2.2 Granulation methods *15*

2. FILM BOILING ON A SPHERE **19**

2.1 POOL BOILING 19
2.2 POOL BOILING CRITICAL HEAT FLUX (CHF) 22
2.3 FILM BOILING 23
2.3.1 Film boiling heat transfer from spheres *24*
2.3.2 Physical model for film boiling on a spherical surface *30*
2.3.3 The work of Dhir and Purohit *34*
2.4 MINIMUM FILM BOILING TEMPERATURE AND HEAT FLUX 37
2.4.1 Correlations for minimum temperature and heat flux *37*
2.4.2 Vapor film collapse at minimum film boiling temperature *41*
2.5 EFFECT OF FLOW RATE ON FILM BOILING HEAT TRANSFER 43

3. CHEMISTRY AND EQUILIBRIA OF THE SI-AL-CA-O SYSTEM 45

3.1 SPECIES IN THE SYSTEM 45
3.1.1 Silicon *45*
3.1.2 Ferrosilicon (FeSi75) *46*
3.2 SLAG FORMATION IN THE PRESENCE OF LIQUID SILICON 47
3.2.1 Stability of foreign oxides *47*
3.2.2 Stability of foreign oxides in the presence of silica *50*
3.3 SLAG SYSTEMS AND PROPERTIES 51
3.3.1 Phase relations *51*
3.3.2 Viscosity and density *52*
3.3.3 Distribution equilibria *54*

4. OXIDATION OF LIQUID SILICON - KINETICS **57**

4.1 INTRODUCTION – GAS-DIFFUSION CONTROLLED REACTIONS 57
4.2 WAGNER`S MODEL 57

URN:NBN:no-2125

4.3 TURKDOGAN´S MODEL 60
4.4 COMPARISON OF THEORETICAL MODELS 67
4.5 EXTENSION OF THE WAGNER APPROACH 71

5. STEAM EXPLOSION THEORY 73

5.1 INTRODUCTION 73
5.2 PREMIXING STAGE 74
5.3 THE TRIGGERING STAGE 76
5.3.1 Theoretical models 78
5.3.2 Triggering experiments 80
5.3.3 Effect of pressure 81
5.3.4 The importance of subcooling 81
5.3.5 Methods to prevent triggering 82
5.4 LARGE-SCALE EXPLOSION PROPAGATION AND EXPANSION: MAIN THEORIES 84
5.4.1 Spontaneous nucleation theory 84
5.4.2 Thermal detonation model 87

6. OXIDATION EXPERIMENTS – APPARATUS DESCRIPTION 93

6.1 EXPERIMENTAL APPARATUS 93
6.1.1 Furnace and vital parts 94
6.1.2 Gas analysing equipment 96
6.1.3 Oxidation equipment 97
6.2 PREPARATION OF SAMPLES FOR MICROPROBE ANALYSIS 99
6.3 MICROPROBE 99

7. WATER GRANULATION EXPERIMENTS – APPARATUS DESCRIPTION 101

7.1 GENERAL DESCRIPTION OF THE APPARATUS 101
7.2 FURNACE 103
7.3 WATER CHAMBER 105
7.4 HYDROGEN COLLECTOR 106
7.5 TRIGGERING SYSTEM – IMPACTOR AND SUBMERGED PHOTODETECTOR 108
7.6 PRESSURE TRANSDUCER 110
7.7 OSCILLOSCOPE 111
7.8 IMAGING TECHNIQUES 111
7.8.1 Video imaging 111
7.8.2 Time-exposure photography 112
7.8.3 High-speed video camera 113
7.8.4 High-speed camera 114
7.8.5 Shutter wheel camera 114
7.9 EXPERIMENTAL PROCEDURE 115
7.9.1 Setting up the equipment 115

7.9.2 Performing the experiment *116*
7.9.3. Post-experimental work *116*

8. MISCELLANEOUS 118

8.1 FALL VELOCITY FOR A MOLTEN DROP – THEORY 118
8.2 HEAT/ENERGY BALANCE FOR A SINGLE DROP 119
8.2.1 Heat transfer during fall through gas mixture *120*
8.2.2. Heat transfer during fall through water *121*
8.2.3 Bubble-energy *124*
8.2.4 Summary of heat transfer calculations *126*

9. WATER GRANULATION EXPERIMENTS - RESULTS 127

9.1 COMPOSITION OF THE TEST ALLOYS 127
9.1.1 Rods used in 1998 experiments *127*
9.1.2 Rods used in 1999 experiments *128*
9.1.3 Rods used in 2000 experiments *128*
9.2 RELEASE OF SINGLE DROPS OF MOLTEN FESI75 INTO WATER– AN OVERVIEW 129
9.3 RELEASE OF SINGLE DROPS OF MOLTEN SI INTO WATER – AN OVERVIEW 133
9.4 CHARACTERISTICS AND BEHAVIOR OF THE DROPS 138
9.4.1 Silicon drops – average mass *138*
9.4.2 Average mass – ferrosilicon drops *139*
9.5 MEASUREMENT OF PRESSURE TRANSIENTS FROM THE IMPACTOR 139
9.5.1 Pneumatic impactor *139*
9.5.2 The slug-type impactor *140*
9.6 THRESHOLDS FOR TRIGGERING STEAM EXPLOSIONS 142
9.6.1 Ferrosilicon drops triggered with the pneumatic impactor *144*
9.6.2 Ferrosilicon drops triggered with the slug-type impactor *147*
9.6.3 Silicon drops triggered with the pneumatic impactor *147*
9.6.4 Silicon drops triggered with the slug-type impactor *149*
9.6.5 Threshold depths for triggering molten drops of Si/FeSi75 ..... *151*
9.7 FALL VELOCITIES FOR MOLTEN DROPS OF SI/FESI 153
9.7.1 Fall velocities for molten Si *153*
9.7.2 Fall velocities of molten ferrosilicon *154*
9.8 GENERATION OF HYDROGEN BY MOLTEN DROPS OF SI/FESI 156
9.9 COLLOIDAL MATERIAL 158
9.9.1 X-ray analysis of the colloidal material *160*
9.9.2 Sieve analysis of the colloidal material *162*
9.10 BUBBLE-ENERGY 168
9.10.1 PV-energy output compared to enthalpy of the drop *169*
9.11 PRESSURE TRANSDUCER EXPERIMENTS – CHARACTERIZING THE IMPACTOR 170

9.11.1 Initial investigations of impactor 3 – fine structure of the pressure trace *170*
9.11.2 Interpretation of the pressure-trace based on high-speed video images *173*
9.11.3 Impulses of the triggering transients *177*
9.12 PRESSURE MEASUREMENTS OF THE INTERACTION OF MOLTEN DROPS OF SILICON-ALLOYS WITH WATER 180
9.12.1 High-speed video captures of a steam explosion and the corresponding time-pressure trace *180*
9.12.2 Course of events following triggering of a molten drop of silicon *187*
9.12.3 Time-pressure traces of steam explosions of molten Si/FeSi *190*
9.12.4 Time-pressure traces – impulse characteristics *192*
9.13 AN EXAMPLE VISUALIZING THE EFFECT OF AL/CA ADDITIVES 194
9.14 EFFECT OF WATER-TEMPERATURE 197
9.15 SUMMARY OF DROP-RELEASE EXPERIMENTS 198
9.15.1 Stability of the vapor film: trigger thresholds *198*
9.15.2 Fall velocities *199*
9.15.3 Generation of hydrogen *200*
9.15.4 The formation of colloidal material *200*
9.15.5 PV-energy *200*
9.15.6 Time-pressure traces *201*

10. OXIDATION OF LIQUID SILICON - RESULTS 202

10.1 INTRODUCTION 202
10.2 OXIDATION OF PURE SILICON (ALLOY A) 202
10.2.1 Oxidized samples – general observations *202*
10.2.2 The formation of silica – reaction path *203*
10.2.3 Oxidized samples – effect of melt temperature *204*
10.2.4 Water-granulated samples *207*
10.2.5 FeSi-drops quenched in water *208*
10.3 OXIDATION OF SILICON WITH 0.4 % AL (ALLOY B) 208
10.3.1 Samples oxidized with a small water-jet *208*
10.3.2 Water-granulated samples *211*
10.4 OXIDATION OF SILICON WITH 0.04 % CA (ALLOY C) 213
10.4.1 Silicon oxidized with a small water-jet *213*
10.4.2 Water-granulated samples *216*
10.5 OXIDATION OF SILICON WITH 0.4 % AL AND 0.04 % CA (ALLOY D) .. 218
10.5.1 General observations/effect of melt temperature *218*
10.5.2 Water-granulated samples *222*
10.6 MICROPROBE INVESTIGATIONS OF DEBRIS FROM A STEAM EXPLOSION 224
10.6.1 Debris from a violent explosion *224*
10.6.2 Debris from a coarse fragmentation – alloyed silicon *226*

URN:NBN:no-2125

10.7 SUMMARY 228

11. SUMMARY AND CONCLUSIONS 230

11.1 MOLTEN DROPS OF PURE (FE)SI RELEASED INTO WATER – A QUALITATIVE DESCRIPTION 230

11.1.1 Entrance in water and onset of film boiling 230

11.1.2 Quenching of Si in water – generation of SiO 230

11.1.3 Explosion probability – trigger strength dependence 230

11.1.4 Explosion probability – water depth dependence 231

11.1.5 Steam explosion – fragmentation and generation of pressure waves 232

11.2 THE EFFECT OF ALLOYING THE MELT WITH SMALL AMOUNTS OF AL/CA 232

11.2.1 Fall velocity 232

11.2.2 Increased stability of the vapor film 233

REFERENCES 234

NOMENCLATURE 245

GREEK 245

APPENDIX A – PREPARATION OF TEST RODS 247

APPENDIX B – TIME-PRESSURE TRACES FOR STEAM EXPLOSIONS OF MOLTEN SI OR FESI75 249

APPENDIX C – THERMODYNAMICAL CALCULATIONS USING EES 256

C.1 – HEAT TRANSFER DURING FALL FROM FURNACE TO WATER 256

C.2 – HEAT TRANSFER DURING MELT-WATER CONTACT 258

URN:NBN:no-2125

1. INTRODUCTION

This thesis describes experimental work related to the study of steam explosions occurring during granulation of ferroalloys. The experimental work is part of a larger safety research project sponsored by the Norwegian Ferroalloy Producers Research Association (FFF) and the Norwegian Research Council. The objective is to increase the knowledge of the complicated physical explosions that are still not very well understood. The researchers in the field have as so far not provided a complete model of the steam explosion process, although major progress has been made.

In the granulation of Si and FeSi alloys, the manufacturer pours huge amounts of molten metal into a water pool. By breaking up the metal jet before it enters the water (prefragmentation), one will get small drops of Si/FeSi after they have solidified, typically in the 5-25 mm diameter range. This is favorable for further use of the material, as there is no need for crushing later on, the transportation is simplified and good material properties are obtained due to the quenching. However, this way of cooling the molten material can in certain circumstances be very dangerous. As the molten material descends through the water, the conditions are just about right for a steam explosion to occur. It is characterized by rapid heat transfer from the hot liquid to the cold water, causing an explosive evaporation of the water. This can cause severe damages on plant facilities and are a major hazard for the workers. During the last 40 years, several accidents have been reported in metallurgical industry. These accidents, however, were due to accidental contact between molten metal and water. In the granulation industry, this contact is done deliberately as stated above. Thus, it is urgent to know the system and the influence different parameters have on the likelihood of a steam explosion.

The approach chosen in the present experimental work has been to simulate the industrial process by doing single drop experiments. That means that one also has to considerate scaling when comparing to a real situation where tons of molten metal is dropped into the water pool. The large-scale problem is of course far more complex than the single drop experiment. However, to understand the basics of the steam explosion phenomena, one has to start with the simplest system. The single drop experiments were carried out at available facilities at the University of Wisoconsin-Madison (UWM), USA. Parameters such as system stability, explosion strength, effect of alloying, subcooling, melt temperature and effect of additives to the coolant was examined.

1.1 Steam explosions – fields of occurrence

If a hot liquid (melt) contacts a cooler volatile liquid, the energy transfer rate can in some circumstances be so rapid that an explosion results. Such explosions can present a hazard in any industry where there is a potential for contact between a hot liquid at a temperature well above the saturation temperature of a cold volatile liquid. These kinds of explosions are known by a variety of names (Fletcher *et.al.*, 1997). They are often referred to as *vapor explosions* because of the rapid generation of vapor. In the hydrocarbon transport industry they are known as *Rapid Phase Transitions* (RPTs). In the nuclear industry they are known as *Fuel Coolant Interactions* (FCIs) or *Molten Fuel Coolant Interactions* (MFCIs). In the water reactor context they are known as *Steam Explosions* (SEs), which is probably the oldest name in use. We will in the subsequent chapters use the terms “steam explosions” and “vapor explosions” somewhat arbitrary, but in this context they refer to the same situation.

Steam explosions are a well-known hazard in the metal casting industry (Reid, 1983). They are particularly common in the aluminum industry, where ways of preventing them have been investigated for the last 30 years (Long, 1957). The move to the use of Al-Li alloys in the aircraft industry has increased the severity of the problem as these alloys can explode, chemically augmented, with greater violence (Page *et.al.*, 1987). The increase of recycling of scrap aluminum has shifted the hazard from casting operations to scrap loading in the furnace, where water contained within the scrap poses a significant risk (Epstein, 1992). The same problem can happen during steel production, if wet scrap metal is loaded into the steel furnace. Also, during transfer of hot metal from the steel furnace to a processing plant, such explosions can occur. A tragic accident happened at Appleby-Frodingham in UK as a result of the accidental entry of water in a unit used for transporting the molten steel (Fletcher, 1997).

Steam explosions are of concern in the transportation of liquefied natural gas over water (Reid, 1983, Katz, 1971), where the potential hazard arises if (cold) LPG or LNG contacts (hot) water either because of a spill as a ship is being loaded or as the result of an accident. Although these explosions are not as violent as those observed in the metal industry, they still represent a significant hazard, especially as they can act as a very efficient means of dispersing flammable gases. Observations show that the explosivity of this system is very sensitive to the composition of the LNG, which changes as the more volatile species evaporate.

In the paper industry a molten salt composed mainly of Na_2CO_3, called "smelt", may contact water within a furnace (Reid, 1983), as for example from the accidental failure of a water pipe used for head recovery. The explosions can also occur in dissolver tanks when smelt is poured into water to convert "black liquor" to "green liquor" (Reid, 1983). Again the explosivity of this system depends very strongly on the composition of the smelt. Explosions can also occur when molten glass contacts water (Arakeri *et.al.*, 1978) and are of concern in the vitrification process for highly radioactive waste. These examples show that the high thermal conductivity of metallic melts is not a prerequisite for an explosion.

The steam explosion is also believed to play a role in submarine volcanism (Colgate, 1973), with the explosion of the island of Krakataou as the largest one ever in recent history (Francis, 1983). There is little doubt that melt-water contact played a role in this enormous explosion, however, the mechanisms are still poorly understood.

Steam explosions are studied in the nuclear industry to assess the consequences in the unlikely event that a severe accident occurs. Cronenberg and Bentz (1978) have summarized FCIs that took place in the nuclear energy industry. The first one occurred in 1952 in the Canadian NRX test reactor, and it was induced by the failure of the shutdown rod system, leading to fuel melting followed by the failure of the calendria tubes after a uranium-water interaction. Following this incident, a destructive reactor experiment was performed in the BORAX boiling-water reactor test in 1954. In this test, most of the fuel plates melted during the power excursion, and, after the metal-water contact, the reactor tank was ruptured by a pressure peak that was estimated to be larger than 40 MPa. Later, in 1961, it is thought that the withdrawal of a control rod in the stationary low power reactor 1 (SL1, boiling-water reactor) led to a power excursion that disrupted the fuel elements into the surrounding water, causing a vapor explosion with a peak pressure estimated at 70 MPa. The pressure vessel rose 3 m after the shearing off of the pipings. Finally, in 1962, another destructive experiment was performed in the special power excursion reactor test-Idaho (SPERT) 1D test reactor, leading to a measured pressure of 27 MPa. It must be noted that all of these explosions resulted from the reactivity excursions and that, in all cases, the fuel was metallic (uranium or uranium-aluminum alloy) and the coolant was water. The only commercial nuclear plant ever damaged by a steam explosion was Chernobyl 4, in 1986. In this reactor, again, an uncontrolled power excursion led to the dispersion of fuel into the surrounding water, followed by one or two steam explosions that destroyed the reactor. These explosions dispersed the fuel and generated hydrogen.

Fletcher (1997) points out that it is important to realize that many other events besides the possibility of an energetic steam explosion must be considered in any severe accident analysis. However, this type of explosion has in general received a great deal of attention in the safety analysis of nuclear plants, generating much research in the field.

Such explosions are also found in certain industrial operations, where melt and water are deliberately mixed in order for the melt to be rapidly cooled (Akiyoshi, 1989). This process is used to produce very fine particles, with the very high cooling rates ($> 10^6$ K/s) resulting in amorphous solids. By controlling the cooling rate, the crystallographic structure, and hence the properties of the solid, can be varied. Here the aim is to work in a certain regime, by which we mean melt temperature, water temperature, contact mode, mass scale, etc., such that explosions are avoided. Clearly here it is important to have a good understanding of the regime under which explosions occur and to be able to calculate the explosion loading in the event that something goes wrong.

Examples of such operations described above are found in the granulation process in ferroalloy industry. This particular field will be described in some more detail in the following section.

1.2 Granulation in the metal industry

Granulation of a liquid metal is a solidification method used to produce small pieces of metal. The method has been in use since the late 1970s; thus, it is a fairly new process. The main problem with the granulation process is obviously the possibility of a violent interaction between the water and the liquid metal. Also, the chemical reaction between water and liquid metal produces hydrogen gas, which in combination with air is highly explosive. Thus, there are safety issues that need to be resolved in order to use the process in a ferroalloy plant. However, experience has shown that granulation can be done in a safe and reliable way (Lundstrom and West, 1994) for many alloys, but granulation of silicon and ferrosilicon offer certain problems.

In spite of the possible catastrophic outcome, several plants use the water-granulation to produce products for a market that is expanding. A growing number of silicone producers find that water granulated silicon metal is favorable in their chemical process. Consumers of ferrosilicon are experiencing less environmental problems by switching to water-granulated qualities, which in addition often are raising the yield (Nygaard *et.al.*, 1995). The customers are also looking for smaller pieces of metal to allow automated handling in the plants. However, several producers seem to have a reluctance

to adopt the granulation process as a fully integrated production step in their plants due to the hazards involved.

No casualties are reported due to explosions in granulation plants, but from time to time smaller interactions between metal and water occur. In 1996, a dramatic incident took place at Holla granulation plant, Hemne, Norway. A loud bang early in the morning woke up the locals in the area, a good substitute for the alarm clock. Fortunately, there was only material damage to the plant. The explosion occurred when a crane failed, resulting in a much too high flow rate of metal into the water tank. The following explosion broke the 22-mm thick steel plates that cover the tank.

1.2.1 Why granulate Si and FeSi?

Nygaard (1995) summarizes the advantages of the granulation process for silicon and ferrosilicon products. The ferrosilicon alloy is cast directly in a water tank to the final shape required by the consumer. Thus, casting, crushing and screening are avoided in the manufacturing process, which eliminates the loss of material as dust during crushing. The rapid cooling in water also gives the ferrosilicon granules a finer and stronger surface/structure than normal casting and crushing of ferrosilicon. The strong granule structure also means that less fines/dust are created during transportation to the consumer and by his own handling. A higher yield with granulated ferrosilicon has been reported by many of the consumers of FeSi.

The chemical silicone industry is together with the aluminum industry the largest consumer of silicon in the world, with an annual demand of about 400 000 tons (Camarasa *et.al.*, 2001). As the use of silicones in various products is increasing steadily, so is the demand for silicon metal to the chemical industry.

Granulated material has a preferred microstructure compared to that of cast silicon. The chemical process, in which silicon reacts with methyl chloride in a fluidized bed (Direct Process) to produce methylchlorosilane, can be written as

$$CH_3Cl_{(g)} + Si_{(s)} \rightarrow (CH_3)_xH_ySiCl_{z\,(g)}$$

where $x + y + z = 4$. The preferred product is dimethyldichlorosilisane ($x=2$ and $z=2$). Note that the Direct Process uses a copper catalyst. The productivity of the Direct Process is controlled by the reaction between silicon, intermetallics and the catalytic system on the surface of each single particle. Thus, an even distribution of the intermetallics is favorable for the process, as

well as the nature of these intermetallics. In normal cast silicon, the intermetallics are usually distributed in thick layers between the grains, and their separation may be more than 500 μm. Typical particles in the Direct Process measure only 100-200 μm. When crushing normally cast silicon, the thick layers of intermetallics will therefore be highly unevenly distributed between the particles, a problem for the Direct Process.

If a more rapid cooling is applied (such as quenching in water), the intermetallics are closely distributed in thin layers. Upon crushing of the silicon prior to the Direct Process, the intermetallics will be evenly distributed between the particles, giving a reactive surface that is beneficial for the Direct Process.

The German company Wacker-Chemie uses a quantitative measure for the microstructure, *quantitative structure index number (QF)* to characterize the structure of various metal samples. The QF number is found from microscope, video camera, PC and image analysis program. They assume that a QF between 25 and 35 is optimal for their process. Different casting techniques give different QF-values, as seen in table 1.1 (Pachaly, 1994).

Table 1.1. Wackers structure index number as a function of solidification process (Pachaly, 1994).

SOLIDIFICATION PROCESS	QF (STRUCTURE INDEX)
Very slow cooling of silicon in big lumps gives big crystals	0.1 –1
Mould casting of silicon in different thicknesses	5 – 10
Water granulation of silicon to sizes between 5 and 15 mm	20 – 40
Air-beam granulation of silicon to 2-3 mm	40 – 50
Atomization of silicon in an inert gas to < 1 mm	60 – 65

It is evident from the above that granulated material is highly beneficial for the silicone producers from a process point of view. Whether the silicon producer can supply the material to a competitive price is of course another issue.

We can conclude that granulated material (Si and FeSi) have advantages compared to standard casting processes when it comes to material properties, thus, this is the motivation to use granulation in the ferroalloy-industry.

1.2.2 Granulation methods

Several methods for granulation of liquid metal are available. The main difference between them is in general the way the liquid metal is split up, and the granulation methods can be classified accordingly:

- *breakup by some sort of water movement*
- *breaking up of a metal stream against an impact element above the water surface*

An example of the latter is the Uddeholm technology, see figure 1.1. The metal jet is poured onto a tundish with a casting hole located exactly over an impact element, a round brick with a flat top, above the surface of the water. Upon impact, the metal jet is split up into drops that are spread over the water tank. The brick is moving up and down with the aid of hydraulics to spread the molten drops of metal more evenly over the water surface. The area above the water is filled with an inert gas to prevent contamination of the liquid metal due to gases in the air, as well is lowering the risk for oxygen-hydrogen explosions above the water tank.

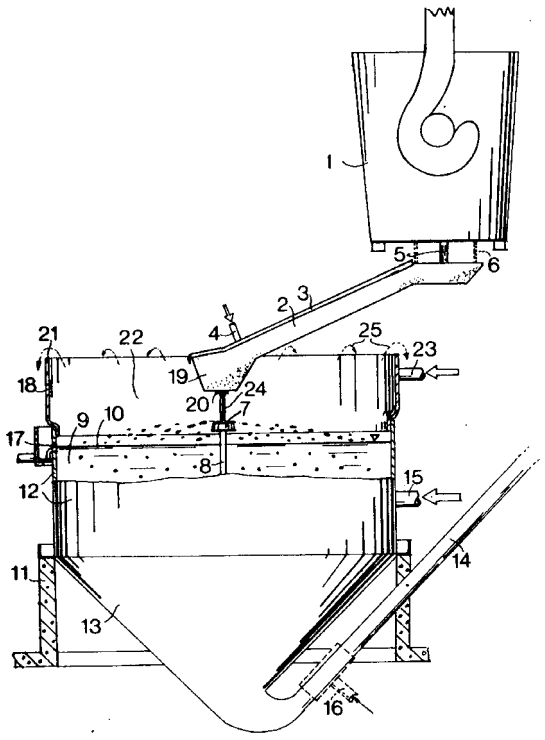

Figure 1.1 – The Uddeholm patent. The liquid metal is poured onto a stone (7) where the stream of metal is divided into droplets. This particular patent was originally developed for the granulation of FeCr and FeMn, however, the method is not limited to such ferroalloys.

Another granulation method, patented by Elkem AS, Norway, falls into the first category. Here the liquid metal jet is poured directly into the water. A flow of water normal to the fall direction ensures breakup of the metal jet. The speed of the water is low, about 0.1 m/s. Several chemical additives to the water are used to modify the surface tension and viscosity of the water. Figure 1.2 shows the process schematically. According to the patent, this method offers better control of the size distribution of the final granules. The amount of small granules (< 5 mm) is reduced, and the average size is increased from 7 mm to 12 mm. Furthermore, the possibility of a steam explosion is reduced due to a better melt distribution in the water and smoother flow conditions.

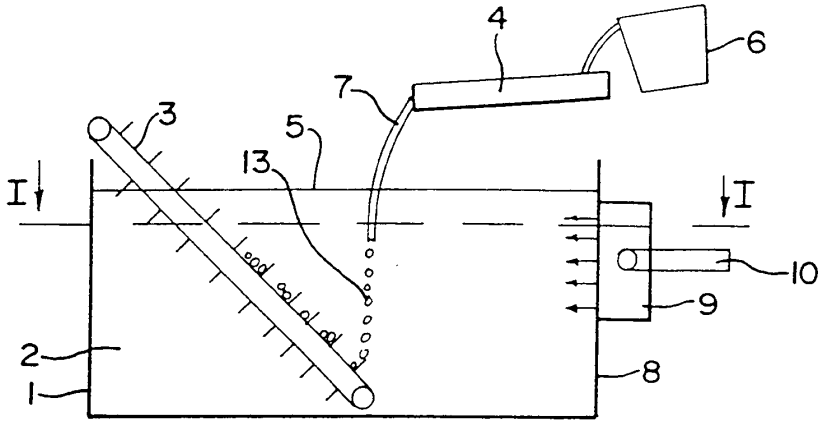

Figure 1.2 – The Elkem method. Water is set into low-speed motion, which again breaks up the liquid metal stream (7) and droplets are formed (13).

Showa Denko (Japan) patented a similar granulation method, but here high-pressure water jets are used to break up the metal jet, as shown in figure 1.3.

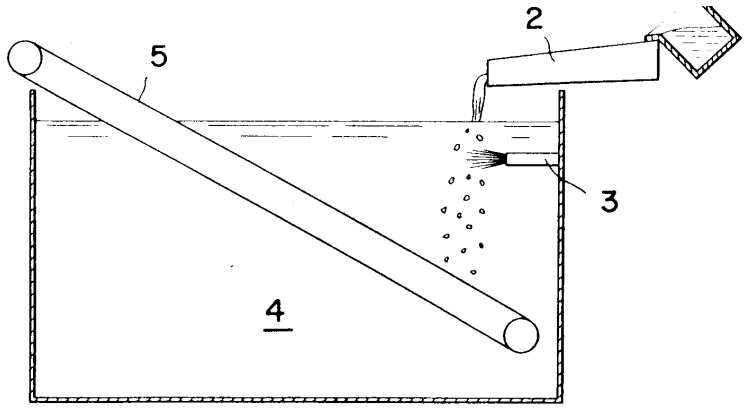

Figure 1.3 – The Showa Denko method. The liquid metal (2) is broken up into droplets by high-pressure water jets (3).

Several other granulation methods exist; some of them quit imaginative. The optimum granulation method should allow high production rates (in terms of tons of metal granulated per minute) but at the same time maintain a proper level of safety. Note that the difference in production rate is large when different metals are compared. Iron can be granulated safely at rates over 3 tons/minute, while silicon can frequently explode at granulation rates less than

1 ton/minute (Lundstrom and West, 1994). Such differences will obviously affect the choice of granulation method.

In any circumstance, the nature of such operational techniques demands that high effort must be taken in order to minimize the possibility of large-scale steam explosions.

2. FILM BOILING ON A SPHERE

The concept of boiling is an important aspect when we seek to analyze a liquid metal-water system. The film boiling mode controls the heat transfer, it also ensures that this heat transfer takes on relatively low values. Thus, the cooling of the melt is relatively slow, allowing the system to be in a metastable mode. The ability for a particular melt-water system to sustain film boiling is extremely important for granulation purposes, as other boiling modes will cause large amounts of water to vaporize so rapidly that a steam explosion may develop.

A lot of work, theoretically and experimentally, has been performed in order to study the boiling characteristics for hot surfaces immersed in various liquids. In this chapter, we will discuss some relevant aspects concerning hot *spheres* submerged in water. Some of these theoretical considerations will be used in a subsequent chapter, where the heat loss and temperature drop is calculated for a single drop of molten silicon, released into water and quenched.

If a surface is in contact with a liquid, with a saturation temperature less than the actual surface temperature, boiling will occur at the liquid-solid surface. This will also apply for two immiscible liquids, as will be the situation for molten metal and water. Based on the relative bulk motion of the body of a liquid to the heating surface, the boiling is divided into two categories: *pool boiling* and *convective boiling.*

2.1 Pool boiling

Pool boiling is the process in which the heating surface (the molten drop of metal) is submerged into a large body of stagnant liquid. Any relative motion of vapor and liquid is related to buoyancy effects. However, for small relative velocities between the hot surface and the water, a pool boiling approximation is justified.

The first extensive study on the effect of very large differences between the temperature of the heating surface and the liquid was done by Nukiyama in 1934. In 1948, Farber and Scorah performed an experiment that gave the complete picture of the heat transfer rate in the pool boiling process as a function of the temperature difference (ΔT) between the hot surface and the liquid. Applying Newton's law of cooling, $q'' = h\Delta T$, the heat transfer

coefficient *h* was used to characterize the pool boiling process over a range of ΔT, as illustrated in figure 2.1.

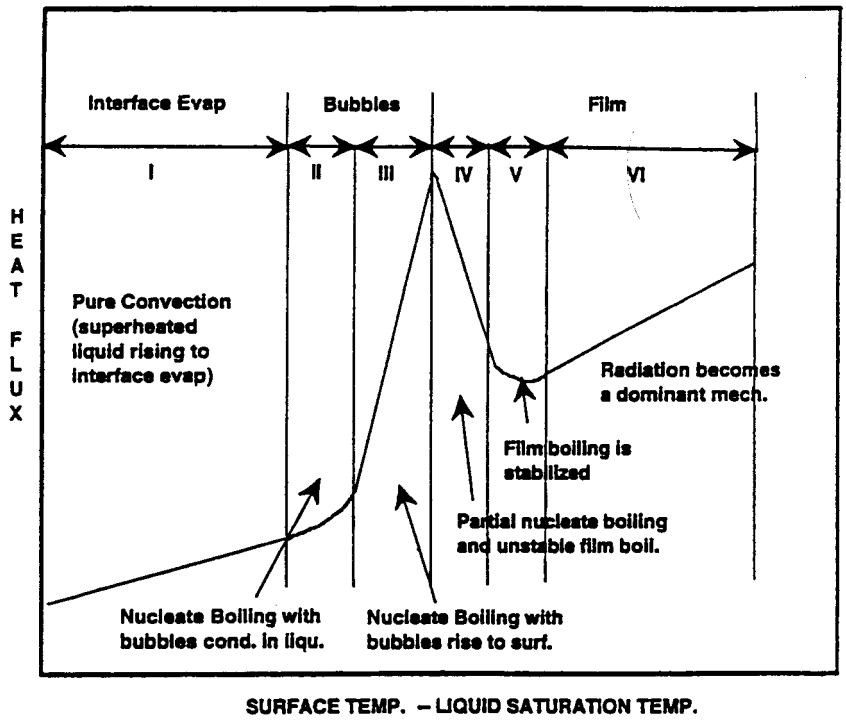

Figure 2.1 – Physical interpretation of the boiling curve (Farber, 1948).

Farber and Scorah conducted their experiments by heating the water at various pressures with a heated cylindrical wire submerged horizontally under the water level. From their experimental observations, they divided the boiling curve into six regions based on the observable patterns of vapor production:

Region I - ΔT is so small that the vapor is produced by the evaporation of the liquid into gas nuclei on the exposed surface of the liquid.
Region II - ΔT is large enough that additional small bubbles are produced along the heating surface, but later these bubbles condense in the region above where the bubble-nucleation takes place due to the lower temperature.
Region III - ΔT is large enough to sustain *nucleate boiling*, with the creation of the bubbles such that they depart and rise through the liquid regardless of the condensation rate. This phenomenon is observed i.e. when we boil water in a kitchen pan.

Region IV – An unstable film of vapor is formed over the heating surface, and oscillates due to the variable presence of the film. The heat transfer rate decreases due to the increased presence of the vapor film.
Region V – The vapor film becomes stable and the heat transfer rate reaches a minimum point.
Region VI – The ΔT is very large, and film boiling is stable such that the radiation through the film becomes significant and thus increases the heat transfer rate with the increasing ΔT.

The physical picture given in figure 2.1 applies for a situation where the temperature of the hot surface is controlled. If the power is the controlled variable, an increase of the power (or heat flux q'' in region III results in a jump in the wire surface temperature to a point in region VI, as shown in figure 2.2. This point of transition is known as the critical heat flux (CHF), and occurs due to hydrodynamic fluid instabilities. This results in the stable vapor film being formed, and the wire surface temperature increases as the heat transfer resistance increases for a fixed input power. If the power is now decreased, the vapor film remains stable in region VI and the ΔT decreases to the minimum point for film boiling within region V. At this point the vapor film becomes unstable and it collapses, with nucleate boiling becoming the mode of energy transfer. Thus, one passes quickly through region IV and III to a lower wire surface temperature. This “hysteresis” behavior is always seen when the power (or heat flux) is the controlled parameter.

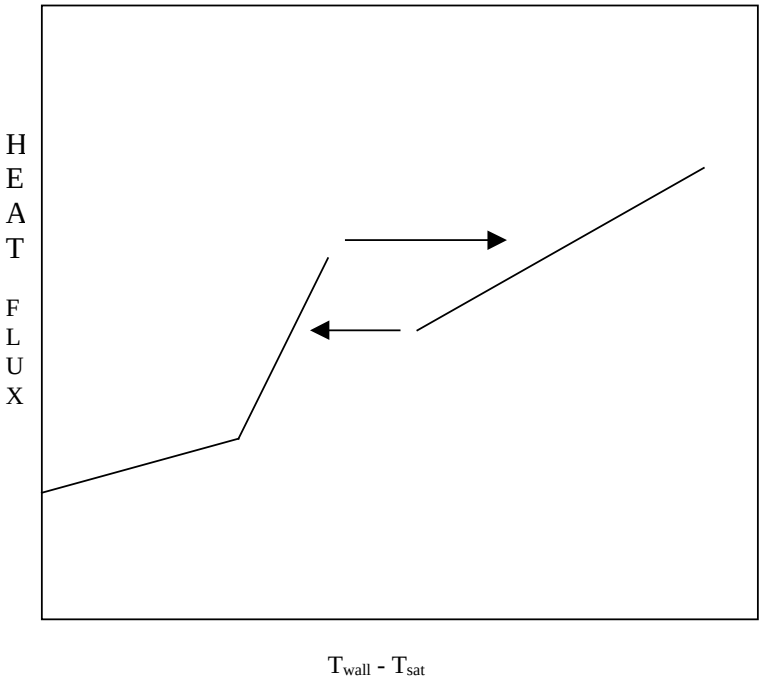

Figure 2.2 – Qualitative picture of pool boiling hysteresis (heat flux controlled boundary condition).

Due to the large temperature differences that exist between a pool of water and a drop of molten silicon (or ferrosilicon), the boiling mode for the water-melt system will be stable film boiling. In section 2.3 we will examine the heat transfer characteristics in more detail, but first we introduce the concept of *critical heat flux*, which was partly indicated by the behavior of the hysteresis curve shown in figure 2.2.

2.2 Pool boiling critical heat flux (CHF)

If we are able to control the input heat flux, an interesting phenomenon occurs as we continuously increase the heat flux. At a certain point, the heater surface temperature will increase dramatically, as shown in figure 2.2. This was originally not well understood. Kutateladze (1951) suggested that the large abrupt temperature increase was caused by a change in the surface geometry of the two phases. Thus, pool boiling CHF may be thought of as the point where nucleate boiling goes through a flow regime transition to film boiling with a continuous vapor film separating the heater and the liquid (Corradini, 1998). In other words, the CHF is the condition where the vapor generation due to nucleate boiling becomes so large that the vapor prevents the liquid from reaching and rewetting the hot surface. An estimate for CHF can be

obtained through a simple force balance on a liquid droplet (Corradini, 1998), which gives a general expression for CHF in pool boiling

$$q''_{CHF} = C_0 \rho_g h_{fg} \left[\frac{g \Delta\rho}{\rho_g^2} \right]^{1/4} \tag{2.1}$$

where C_0 is a constant, found to be in the range 0.12 to 0.18, and $\Delta\rho$ is the density difference between the liquid and the gas. For explanation of the other symbols, see the nomenclature list. Equation (2.1) is valid for the case of a liquid pool at its saturation temperature. If the stagnant pool is kept at a temperature below saturation (subcooled) the vapor bubbles can condense before they get very far from the heater surface. Thus, the heater power can go into directly heating the liquid, thus decreasing the gas flow from the surface. This will again increase the allowable heat flux before CHF occurs. Ivey and Morris (1962) correlated this subcooling effect as a multiplicative correlation to q''_{CHF},

$$q''_{CHF\,sub} \Big/ q''_{CHF\,sat} = \left(1 + 0.1 \left[\frac{\rho_l}{\rho_g} \right]^{3/4} \frac{C_{pl} \Delta T_{sub}}{h_{fg}} \right) \tag{2.2}$$

where ΔT_{sub} is the degree of subcooling in the liquid. Finally, the location of the CHF point on the pool-boiling curve of figure 2.1 is given by the intersection of the nucleate boiling curve and the horizontal CHF-line. Thus, the temperature at which CHF occurs can be found.

2.3 Film boiling

Referring to figure 2.1 again, we now focus on the film-boiling mode. Since this will be the boiling mode for practical purposes (i.e. granulation of a molten metal), we will in the following discuss it in more detail. Film boiling theory has been reviewed earlier, i.e. Kalinin *et.al.* (1975), Sakurai (1990a) and Liu and Theofanous (1995).

Nusselt (1916) developed a model of laminar film condensation on vertical surfaces, suggesting that the condensation is controlled by the heat conduction through the falling film. His pioneering work made the framework for many later researchers, as his model can easily be applied to film boiling under natural convection on vertical plates. Bromley (1950) did exactly this. He analyzed the laminar film boiling heat transfer from a vertical plate and a

horizontal cylinder, with or without radiation, for natural convection, and later (Bromley *et.al.* 1953) for mixed and forced convection. It is fair to say that film boiling heat transfer investigation started with the work of Bromley. Subsequent published models rely on physical ideas similar to those of Bromley for natural and mixed convection, and Witte (1963) for forced convection.

A rigorous formulation of the steady-state problem for natural convection was given by Nishikawa and Ito (1966, 1976). Several numerical solutions of the problem are available, i.e. Dhir and Purohit (1978). An accurate numerical solution is compared with an extensive set of data for cylinders and spheres by Sakurai (1986, 1990a), in fact, the most accurate according to Kolev (1998). This solution is also recommended by Liu and Theofanous after comparison with an extensive experimental database.

Subsequent to Witte's analytical solution for simplified forced-convection steady-state problems in 1963, there have only been numerical solutions provided for this problem in the literature, i.e. Fodemski *et.al.* (1982), Liu and Theofanous (1995).

The effect of radiation and subcooling/superheating on the film conduction heat flux is taken into account in different ways. Some authors superposed the separate effects, recommending some reduction in the radiative component (Sakurai, 1990). Another approach is to take these effects into account by considering them within the formalism describing the local film thickness. The resulting system of differential equations is solved numerically, e.g. Sparrow (1964), Fodemski (1982), Liu and Theofanous (1995). No simple analytical solution is so far reported in the literature.

In the following sections we will concentrate on two often-quoted models that can be used to analyze a molten sphere immersed in a cold liquid.

2.3.1 Film boiling heat transfer from spheres

Even though a number of investigators have studied the concept of film boiling, relatively few have concentrated on film boiling heat transfer from a *sphere*. In this section, we will discuss briefly the development in this field, initiated by the work of Bromley (1950). Liu *et.al.* (1995) concludes that for two-phase flow, no experimental data for sphere film boiling can be located. For single-phase flow, all the meaningful heat transfer data were obtained through short cool-down transients, i.e. by passing a preheated sphere through a liquid tank. This would be good enough for pool boiling or low-speed forced convection film boiling, but not for higher velocities in forced convection film

boiling. Liu also questions the accuracy of the data, due to large heat loss from the support-tube. Also, there is no general correlation that covers all the single-phase flow regimes, but the basic form for each of the single-phase flow regimes has been developed. However, there is some ambiguity regarding the correlation constants C_1, as seen from table 2.1.

Table 2.1. Heat transfer correlations for film boiling from spheres in single-phase flows.

Regime	*Basic correlation*	*Constant*	*References*
Saturated pool	$Nu = C_1 (Ar / Sp')^{1/4}$ (2.3)	0.62* 0.586 0.8** C_1(d)**	T: Bromley (1950) S: Frederking (1963) S: Dhir (1978) T: Breen (1962)
Subcooled pool	$Nu = C_1 (Ar / Sp')^{1/4} M_c^{1/4}$ (2.4a) $\frac{Nu}{1+2/Nu} = C_1 (Ar / Sp')^{1/4} M_c^{1/4}$ (2.4b)	0.696* 0.696 C_1(d´)	S: Michiyoshi (1988) S: Tso (1990) T: Sakurai (1990b)
Saturated forced convection	$Nu = C_1 \mathrm{Re}_l^{1/2} \left(\frac{\mu_l}{\mu_v} \frac{KR^4}{Sp'} \right)^{1/4}$ (2.5)	0.393* 0.553* or 1.1** 0.46* 0.5* 0.554**	S: Kobayasi (1966) S: Epstein (1980) T: Ito (1981) S: Liu (1995) T: Liu (1992)
Subcooled forced convection	$Nu = C_1 \mathrm{Re}_l^{1/2} \mathrm{Pr}_l^{1/2} \left(\frac{\mu_l}{\mu_v} \frac{Sc'}{Sp'} \right)$ (2.6)	0.977* or 2.0** 1.15 1.13	S: Epstein (1980) T: Shigechi (1983) P: Cess (1961)

S = Sphere, T = Cylinder, P = Plate, * theoretical constant, ** experimental constant.

$$Ar = g_0 \frac{(\rho_l - \rho_v) d^3}{\rho_v v_v^2}; \; R = \left(\frac{(\mu\rho)_v}{(\mu\rho)_l} \right)^{1/2}; \; M_c = \frac{E^3 (R \,\mathrm{Pr}_l \, Sp')^{-2}}{1 + E/(Sp' \mathrm{Pr}_l)};$$

$E = (A+CB^{1/2})^{1/3} + (A-CB^{1/2})^{1/3} + (1/3)Sc'$; $A = (1/27)Sc'^3 + (1/3)R^2 Sp' Pr_l Sc' + (RSp' Pr_l)^2/4$; $B = (-4/27)Sc'^2 + (2/3)Sp' Pr_l Sc' - (32/27)Sp' Pr_l R^2 + (1/4)(Sp' Pr_l)^2 + (2/27)Sc'^3/R^2$; $C = (1/2)R^2 Sp' Pr_l$

Correlation (2.4a) does not work well for very small and very large diameter spheres, as pointed out by for instance Breen (1962) and Sakurai (1990b). Sakurai *et.al.* (1990b), based on their systematical experimental data obtained from film boiling on small cylinders, modified their analytical solution (which is the same as Michiyoshi's correlation, equation (2.4a), by introducing a diameter-effect correlation factor C_1 (d') on the right hand side of the equation and a factor $(1+2/Nu)^{-1}$ on the left hand side. Since film boiling on spheres and on cylinders is quite similar, it is reasonable to assume that the Sakurai's

diameter-effect correction factor for cylinders should also apply to the case of spheres. The correction factor $C_1(d')$ is given by

$C_1(d') = 0.5d'^{-1/4}$ for $d' \leq 0.14$
$C_1(d') = 0.86/(1+0.28d')$ for $0.14 < d' \leq 1.25$
$C_1(d') = 2.4d'/(1+3.0d')$ for $1.25 < d' \leq 6.6$
$C_1(d') = 0.47d'^{1/4}$ for $d' > 6.6$

This is applicable for both saturated and subcooled conditions as long as $Fr^{1/2}$ is smaller than 0.2. The correlation factor changes from 0.70 to 0.78 when the sphere diameter is increased from 6 mm to 19 mm, which is very close to the theoretical value of 0.696 obtained by Michiyoshi (1988). As indicated in the beginning of section 2.3, using equation (2.4b) seems to be the best approach when analyzing film boiling from a sphere in subcooled water, as recommended by Kolev (1997) and Liu *et.al.* (1995).

If we turn our attention to the correlation for saturated forced convection (equation (2.5)), we see that in the forced convection film boiling regime the heat transfer characteristics $C_{1,\ sat} = Nu/\ [Re^{1/2}(\mu_l/\mu_v)(R^4K/Sp')^{1/4}]$ is an invariant and equal to 0.5. In figure 2.3 data for saturated film boiling are plotted in terms of equation (2.5). We note that when square root of the Froude number is larger than 2.0, forced convection film-boiling starts. This agrees with what Bromley (1953) found for cylinders.

The effect of small subcoolings (0-2 °C) is shown in figure 2.4. It is obvious that only one or two degrees subcooling can have a significant effect on the film boiling heat transfer, especially in the forced convection regime. Thus, separate correlations are needed in order to predict the heat transfer for saturated/subcooled conditions.

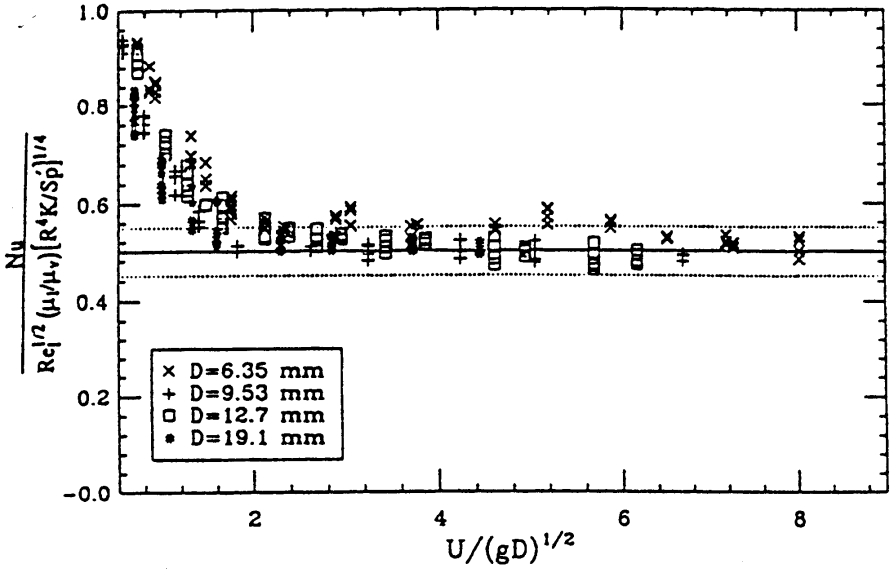

Figure 2.3 – Saturated film boiling data plotted in terms of saturated forced convection correlation, equation (2.5). Taken from Liu *et.al.* (1995).

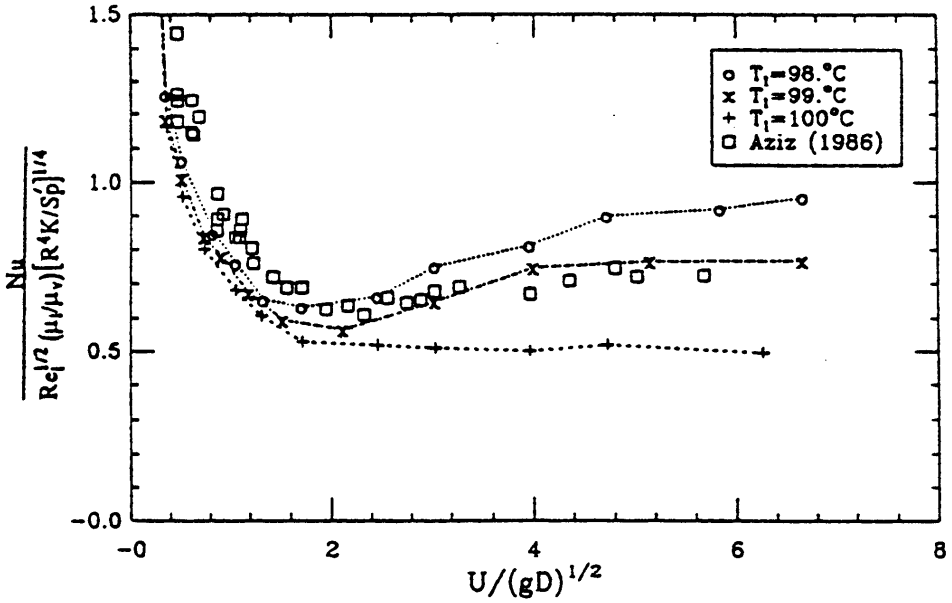

Figure 2.4 – The effect of slight liquid subcooling on the film boiling heat transfer. Taken from Liu *et.al.* (1995).

For highly subcooled forced convection film boiling, a correlation in the form of equation (2.6) is suggested by several workers. Liu *et.al.* (1995) showed from their experimental findings that the coefficient in equation (2.6) varies from 1.3 to 2.0 in the forced convection regime, when they plotted their results in the form of equation (2.6). In addition, they stated that for small subcoolings (e.g. within ~5°C), equation (2.6) is not very suitable. Based on their experimental results, they obtained a correlation that improves the invariance of the correlation constant. Their correlation, which is the sum of the Nusselt number given by equation (2.5) and a modified version of the Nusselt number given by (2.6), i.e.

$$Nu_f = Nu_{sat} + C\,\mathrm{Re}_l^{0.77}\,\mathrm{Pr}_l^{1/2}\left(\frac{\mu_l Sc'}{\mu_v Sp'}\right) \tag{2.7}$$

To explain the empirical exponent of 0.77 instead of 0.5, Liu *et.al.* attributed this to the effect of turbulence. Nu_{sat} indicates saturated conditions. Physically, (2.7) may be interpreted as: the total heat flux equals the heat that is required to sustain the vapor film plus the heat that is convected into the liquid stream.

Liu also suggested a general correlation, i.e. the combination of equation (2.5) and (2.7), valid for both saturated and subcooled forced convection. By trial and error, they found that the Nusselt number could be written in the form

$$Nu = \left[Nu_p^5 + (F(Fr)Nu_f)^5\right]^{1/5} \tag{2.8}$$

where the empirical function

$$F(\mathrm{Fr}) = 1 - 0.2/(1 + \left|\mathrm{Fr}^{0.5} - 1\right|) \tag{2.9}$$

is introduced to correlate the transition data. Thus, Liu showed that all of their experimental data obtained was in a band within ± 15 %. Their error analysis indicated ± 17 % for equation (2.8), thus, it correlated all the data well within the error-limits. If we compare their correlation to that of Epstein (1980) and Dhir (1978), we find that (2.8) predicts much lower (factor of two) heat transfer rates than the other two mentioned for saturated conditions and forced convection. With large subcoolings and high velocity, Liu´s correlation agrees with that of Epstein, and is higher than that of Dhir. In the transition regime ($0.5 < Fr^{1/2} < 2.0$) both Epstein´s and Dhir´s correlation are higher than Liu´s.

2.3.2 Physical model for film boiling on a spherical surface

The theoretical models for film boiling on different geometries are based on the laminar boundary layer theory. For a horizontal cylinder, the physical picture is given in figure 2.5. The same scheme applies for a sphere.

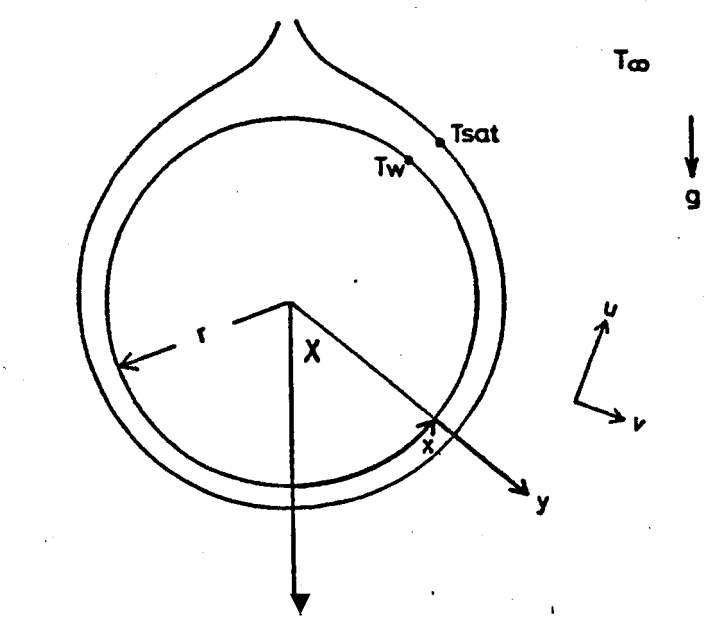

Figure 2.5 – The physical model and coordinates for film boiling on a horizontal cylinder.

The conservation laws for mass, momentum and energy, separately applied to both vapor and liquid layers, are:

$$\frac{\partial}{\partial x}(\rho_v u_v) + \frac{\partial}{\partial y}(\rho_v v_v) = 0 \tag{2.10}$$

$$\rho_v u_v \frac{\partial u_v}{\partial x} + \rho_v v_v \frac{\partial u_v}{\partial y} = g_x(\rho_{l\infty} - \rho_v) + \frac{\partial}{\partial y}\left(\mu_v \frac{\partial u_v}{\partial y}\right) \tag{2.11}$$

$$\rho_v C_{pv}\left(u_v \frac{\partial T_v}{\partial x} + v_v \frac{\partial T_v}{\partial y}\right) = \frac{\partial}{\partial y}\left(k_v \frac{\partial T_v}{\partial y}\right) \tag{2.12}$$

$$\frac{\partial}{\partial x}(\rho_l u_l) + \frac{\partial}{\partial y}(\rho_l v_l) = 0 \tag{2.13}$$

$$\rho_l u_l \frac{\partial u_l}{\partial x} + \rho_l v_l \frac{\partial u_l}{\partial y} = g_x(\rho_{l\infty} - \rho_l) + \frac{\partial}{\partial y}\left(\mu_l \frac{\partial u_l}{\partial y}\right) \tag{2.14}$$

$$\rho_l C_{pl}\left(u_l \frac{\partial T_l}{\partial x} + v_l \frac{\partial T_l}{\partial y}\right) = \frac{\partial}{\partial y}\left(k_l \frac{\partial T_l}{\partial y}\right) \tag{2.15}$$

In equation (2.11) and (2.13), $g_x = g_0 \sin(x/R)$. Boundary conditions are:

$$w_i \equiv \rho_v\left(v_v - u_v \frac{\partial \delta}{\partial x}\right)_i = \rho_l\left(v_l - u_l \frac{\partial \delta}{\partial x}\right)_i \tag{2.16}$$

$$(u_v)_i = (u_l)_i \tag{2.17}$$

$$\left(\mu_v \frac{\partial u_v}{\partial y}\right)_i = \left(\mu_l \frac{\partial u_l}{\partial y}\right)_i \tag{2.18}$$

$$\left(k_v \frac{\partial T_v}{\partial y}\right)_i = \left(k_l \frac{\partial T_l}{\partial y}\right)_i - w_i h_{fg} \tag{2.19}$$

$$(T_v)_i = (T_l)_i = T_{sat} \tag{2.20}$$

$$y = 0; \quad u_v = v_v = 0, \quad T_v = T_w \tag{2.21}$$

$$y \to \infty; \quad u_l \to 0, T_l \to T_\infty \tag{2.22}$$

The earliest work on this field usually neglected radiation, with exception of that of Bromley (1950). He included the radiation effect by adding a simple relation obtained by order-of-magnitude arguments. Sakurai (1990a) derived the solution of the theoretical model with radiation effect by the following way:

Radiation from a horizontal cylinder to the vapor-liquid interface is postulated to be absorbed in a negligibly small thickness of the liquid. The boundary condition given by (2.19) is rewritten in this case to be

$$\left(k_v \frac{\partial T_v}{\partial y}\right)_i + q_{rc} = \left(k_l \frac{\partial T_l}{\partial y}\right)_i - w_i h_{fg} \tag{2.23}$$

It is assumed that the radiation heat flux from the cylinder q_{rc} in equation (2.23) is approximately given by the function of angle X (=x/r) so that the similarity transformation can be applied to the problem,

$$q_{rc}(X) = q_{rp}\gamma(X)/\bar{\gamma} \tag{2.24}$$

$$\gamma(X) = \sin^{1/3}(X)/\phi^{1/3} \tag{2.25}$$

$$\phi(X) = \left(4\int_0^X \sin^{1/3}(X')dX'\right)^{3/4} \tag{2.26}$$

where q_{rp} is the radiation heat flux for parallel plates and $\bar{\gamma}$ is the average value given by

$$q_{rp} = \frac{1}{\pi}\int_0^\pi q_{rc}dX = \frac{\sigma_B}{1/\varepsilon_w + 1/\alpha_{al} - 1}\left(T_w^4 - T_{sat}^4\right) \tag{2.27}$$

$$\bar{\gamma} \equiv \frac{1}{\pi}\int_0^\pi \gamma(X)dX \equiv 0.6122 \tag{2.28}$$

The value of q_{rc} is about 25 % higher than q_{rp} at X=0 and it gradually decreases with the increase in X to about 75 % of that at X=5π/6. The fundamental equations (2.10)-(2.15) are transformed into four ordinary differential equations by using the similarity transformation. The film boiling heat transfer coefficient averaged over the cylinder surface, including radiation contribution can be obtained by solving the differential equations numerically, as done by Sakurai (1990a).

Sakurai compared his numerically obtained solution with experimental results (Siviour and Ede, 1970), see figure 2.6.

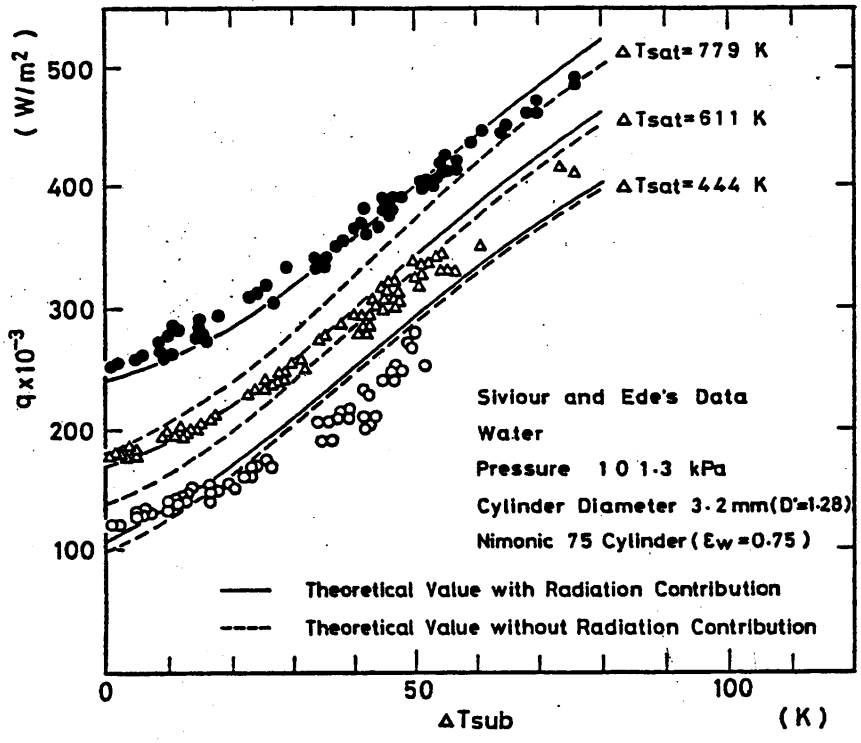

Figure 2.6 – Comparison of the theoretical values including radiation contribution with the Siviour and Ede´s data on 3.2-mm diameter horizontal cylinder (D´=1.28, ε_w=0.75) in water at atmospheric pressure. [Taken from Sakurai, 1990.]

The figure shows experimental data of pool film boiling heat flux on a cylinder in water vs. subcooling with the surface superheat as parameter. These can be compared to the theoretical values including radiation as obtained by Sakurai (1990). These are in good agreement with the data of Siviour and Ede. From figure 2.6, we note that the difference between heat flux with or without the radiation contribution becomes smaller with increased liquid subcooling, keeping the surface superheat constant. Thus, although the radiation heat transfer becomes large at very high surface superheat, it has little effect on the total film boiling heat transfer under high liquid subcooling.

The rigorous solution of the theoretical model can only be obtained numerically. However, approximate analytical solutions can be derived. Sakurai (1990) suggest a correlation of the form

$$\overline{Nu}_v = 0.64 M^{*0.25} \tag{2.29}$$

where $M^* = M_c(Ar/Sp')$, given in table 2.1, except that a modified subcooling parameter Sc^* is used instead of Sc, i.e. $Sc^* = K_a Sc$, where $K_a = 0.93 Pr_l^{0.22}$.

2.3.3 The work of Dhir and Purohit

In 1978, Dhir and Purohit published results from their experimental program, together with a model for subcooled natural convection film-boiling heat transfer. They investigated the quenching of spheres of steel, copper and silver by water in natural and forced flow, both experimentally and theoretically. The physical model and coordinate system they used is the same as the general one described in section 2.3.2.

In this model, it is assumed that a hot sphere is immersed in a pool of *subcooled* liquid. The temperature of the sphere is high enough to sustain film boiling. The sphere is held at a constant temperature and heat is transferred from the sphere by mainly by conduction and radiation through the film. The vapor film is assumed to be very thin, so that the inertia of the film can be neglected and the temperature in the film is assumed to vary linearly. The vapor and liquid boundary layers are assumed to be symmetric about the vertical axis. In addition, the effect of mass transfer at the liquid-vapor interface in thinning the convective boundary layer is assumed to be small.

The energy and momentum equations are solved for the vapor film and the convective boundary layer, with velocity and temperature profiles satisfying the boundary conditions. Thus, Dhir and Purohit calculated that the Nusselt number based on the average heat transfer coefficient could be written

$$\overline{Nu} = \frac{\bar{h} D}{k_v} = \frac{2}{D} \int_0^{\pi D/2} \frac{R(x)}{\delta_v} dx \tag{2.30}$$

The vapor film thickness, δ_v, is found to be a rather complicated function. Equation (2.30) has to be solved numerically. Dhir and Purohit neglected the area above the sphere when integrating equation (2.30). This will cause an error if the water is at saturation temperature, as the vapor dome at the upper stagnation point may occupy 10-15 % of the sphere surface area (Hencricks and Baumeister, 1969), but for subcooled liquids the vapor dome will shrink considerably due to local condensation of vapor. Heat transfer due to radiation was also neglected in arriving at equation (2.30). However, if radiation is

considered, the correction to δ_v is small, but because of additional heat transfer equation (2.30) becomes

$$\overline{Nu} = \frac{2}{D}\int \frac{R(x)}{\delta_v} dx + C_1 \frac{\sigma\left(T_w^4 - T_{sat}^4\right)D}{\Delta T_w k_v} \tag{2.31}$$

where the constant C_1 will generally be less than one, as shown by Bromley *et.al.* (1953).

From their quenching experiments Dhir and Purohit obtained data for both natural and forced convection film boiling of water on a sphere. They also found a correlation for the minimum film collapse temperature and water subcooling,

$$\Delta T_{\min} = 101 + 8\Delta T_{sub} \tag{2.32}$$

where the temperatures are given in ºK. ΔT_{min} is defined as the minimum difference between heat surface temperature and the saturation temperature of the liquid needed to support the vapor film. ΔT_{sub} is the difference between the saturation temperature of the liquid and the pool, or the free stream temperature, T_{sat}-T_∞.

Dhir and Purohit observed that, within the data scatter, the thermophysical properties of the sphere were of no importance as long as the sphere surface was very smooth and relatively clean. However, when the sphere was oxidized or its surface had pits or protrusions, a premature contact of the liquid with the sphere surface was observed to occur.

In their experimental findings, Dhir and Purohit discovered that the predicted heat transfer (Nusselt number obtained from eq. (2.33)) was 25-40 % lower than the measured values, correlated well by

$$\overline{Nu} = \frac{\bar{h}D}{k_v} = \overline{Nu}_0 + \overline{Nu}_{nc}\frac{\mathrm{Pr}_v\, Sc}{\mathrm{Pr}_l\, Sh\mu} + C_1\frac{\mathrm{Pr}_v}{Sh}\frac{\sigma\left(T_w^4 - T_{sat}^4\right)D}{h_{fg}\mu_v} \tag{2.33}$$

where

$$\overline{Nu}_0 = 0.8\left\{\frac{g_0\rho_v(\rho_l - \rho_v)h_{fg}D^3}{\mu_v k_v \Delta T_w}\right\}^{1/4} \tag{2.34}$$

and

$$\overline{Nu}_{nc} = 0.9\left\{\frac{g_0\rho_l^2 - C_{pl}\beta\Delta T_{sub}D^3}{u_l k_l}\right\} \qquad (2.35)$$

Equation (2.33) includes the energy transferred by conduction and radiation across the film. To explain the difference between the theoretically predicted value for the Nusselt number and the experimentally observed value, Dhir and Purohit suggested that small capillary waves at the vapor-liquid interface might cause the interfacial surface area to increase (increasing the heat transfer), and these waves could also result in thinning vapor and liquid boundary layers, with a subsequently increased heat transfer.

The film-boiling heat transfer data obtained for a 25.4-mm stainless steel sphere are plotted in figure 2.7, together with equation (2.33).

The results for forced convection film-boiling heat transfer shows that the Nusselt number increases nearly linearly with the Reynolds number for saturated water. The data are valid for Reynolds numbers varying from 1200 to 19000. The Nusselt number was found considerably higher than Witte's (1968) prediction, but only 30 % lower than Kobayasi's (1965) prediction. However, the assumptions made in these two theoretical models tend to underestimate the heat transfer. The correlation given by Dhir and Purohit for saturated water moving past a 19-mm stainless steel sphere is

$$Nu = Nu_0 + 0.8(\mathrm{Re})^{1/2} \quad \text{for } 1200 < \mathrm{Re} < 29000 \qquad (2.36)$$

For subcooled forced flow, a similar correlation was found. The heat transfer was seen to increase with liquid subcooling and flow velocity. However, for a constant flow Reynolds number, the increment in heat transfer diminishes with increasing subcooling. This is because as the liquid subcooling is increased, the ratio Sc/Sh reaches a constant value equal to 0.125. According to Dhir and Purohit, this indicates that at high Reynolds number the effect of liquid subcooling on heat transfer will be overshadowed by the forced convection effect. The Nusselt number given by (2.37) correlated well with the data obtained by Dhir and Purohit.

$$Nu = Nu_0 + 0.8(\mathrm{Re})^{1/2}\left(1 + \frac{Sc\,\mathrm{Pr}_v}{Sh\,\mathrm{Pr}_l\,\mu}\right) \qquad (2.37)$$

The contribution of the heat transfer by radiation to the total heat transfer is about 10 % at the lowest Reynolds number. The radiation heat-transfer

contribution relatively to the total heat-transfer decreases considerably as the Reynold number increases.

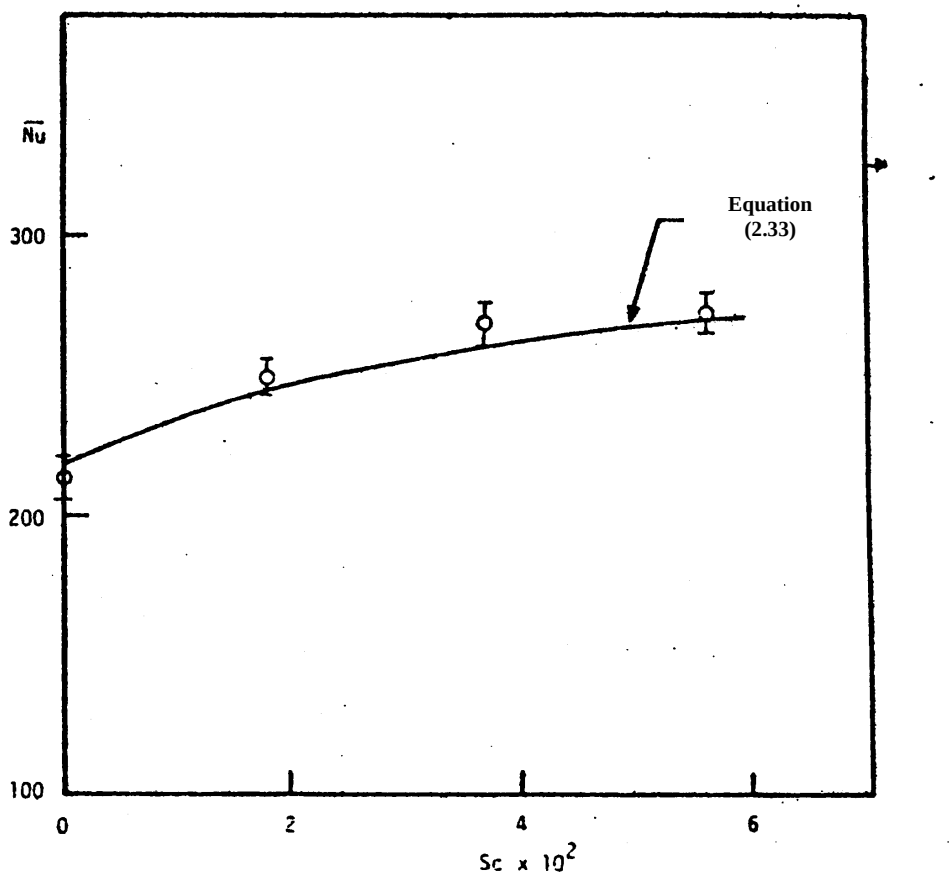

Figure 2.7 – Natural convection film boiling heat transfer for 25.4-mm diameter stainless steel sphere. (Taken from Dhir and Purohit, 1978.)

Dhir and Purohit concluded from their work that the minimum film collapse temperature increases with liquid subcooling but is independent of flow velocity and thermophysical properties of the sphere.

2.4 Minimum film boiling temperature and heat flux

2.4.1 Correlations for minimum temperature and heat flux

To understand a quenching process properly, it is important to have some idea when the minimum film boiling temperature (MFBT) of the surface is

reached. However, there seem to be little experimental data of MFBT on a solid surface in various liquids for a wide range of pressures, thus, no general correlation for MFBT has been reported.

Based on the hydrodynamic Taylor instability of the vapor-liquid interface, Zuber (1959) derived the equation representing the minimum heat flux to sustain film boiling on a horizontal plate. Extending Zuber´s analysis, Berenson (1961) derived the equation for the minimum temperature to sustain film boiling on a horizontal plate, and Lienhard and Wong (1964) derived the equation for the minimum heat flux on a horizontal cylinder. However, experiments by Sakurai *et.al.* (1982, 1984) could not be correlated with the equation of Lienhard and Wong. Figure 2.8 shows this in more detail.

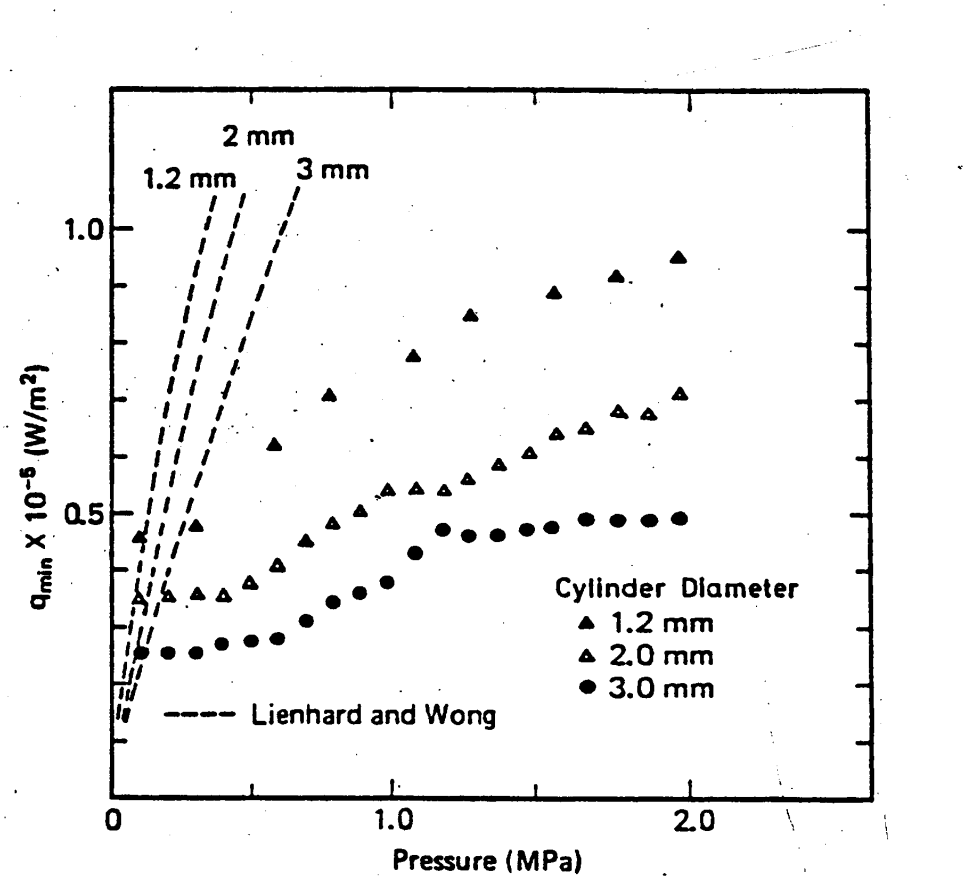

Figure 2.8 – Effect of system pressure on minimum heat flux for saturated film boiling in water, with the cylinder diameter as a parameter.

Clearly the equation of Lienhard and Wong overestimates the effect of system pressure on the minimum heat flux to sustain film boiling in saturated water.

Investigating the effect of the system pressure on the MFBT for a horizontal plate, Yao and Henry (1978) pointed out that the minimum temperature seemed to be determined either by a vapor removal limitation based on the Taylor instability for low system pressures or by the spontaneous nucleation temperature for higher system pressures. They also made clear that MFBT at various pressures were not described by Berenson´s equation except at nearly atmospheric pressures, which can be seen from figure 2.9.

Sakurai *et.al.* (1982, 1984) measured the MFBT, T_{min} and heat flux q_{min}'' with horizontal cylinders of various diameters in water at pressures ranging from 20 kPa to 2 MPa. This is shown in figure 2.9. From the experimental results, they suggested that the MFBT or heat flux for pressures lower than 1 MPa seemed to be determined by the hydrodynamic Taylor instability, while those for the pressures higher than that value were determined by the heterogeneous spontaneous nucleation limit.

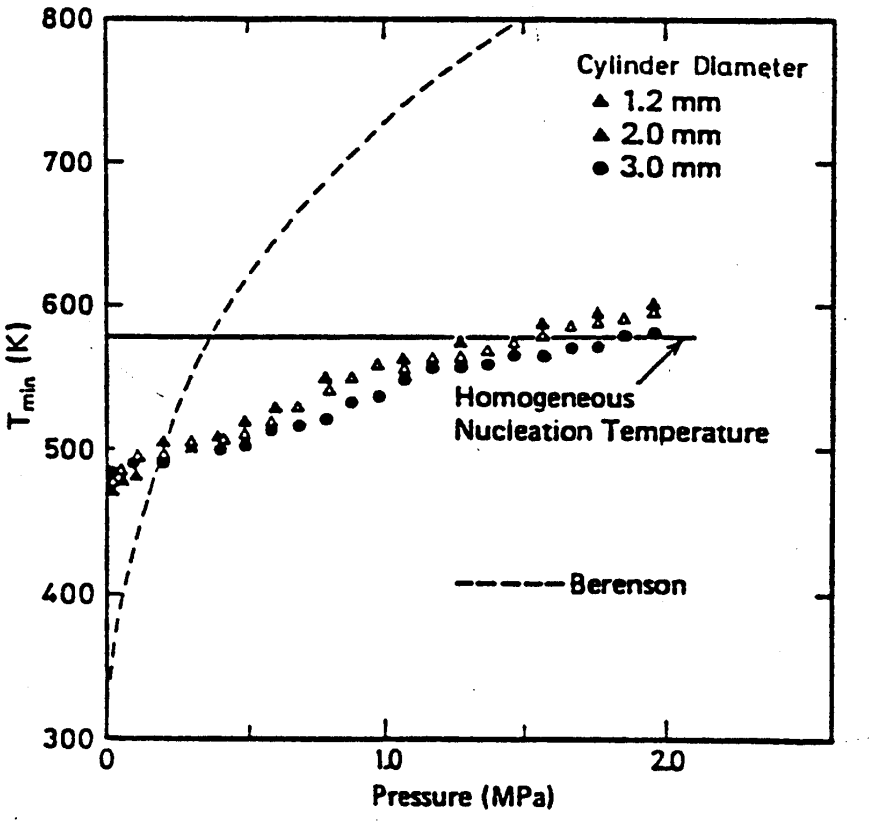

Figure 2.9 – Effect of system pressure on minimum temperature for saturated film boiling in water, with the cylinder diameter as parameter.

The effect of cylinder diameter has little effect on the MFBT. A change in MFBT is only ~ 5 % at constant pressure and different cylinder. For the heat flux, a 50 % difference for different cylinder diameters is observed at a constant pressure. This can be seen from figures 2.8 and 2.9.

Sakurai *et.al.* (1989, 1990) investigated experimentally the effect of system pressure on the MFBT on horizontal cylinders in various liquids under a wide range of pressures and presented a correlation of MFBT on a solid surface with various thermophysical properties in various liquids. They found for the first time that the MFBT agreed with the lower limit of the heterogeneous spontaneous nucleation temperature on the same cylinder in saturated liquid nitrogen at various pressures.

From their experimental results, they obtained a correlation for the cylinder-vapor interface temperature, based on measurements in six different liquids:

$$T_I = 0.92T_{cr}\left(1-0.26\exp\left(\frac{-20(P/P_{cr})}{1+1700/P_{cr}}\right)\right) \qquad (2.38)$$

P_{cr} in the term $1700/P_{cr}$ is in kPa. Furthermore, Yao and Henry (1978) calculated the contact interface temperature T_I at minimum film boiling, based on the solution of transient conduction equation for intimate contact between two infinite slabs:

$$T_I = (T_{\min} + R_\alpha T_{sat})/(1+R_\alpha) \qquad (2.39)$$

The non-dimensional parameter R_a is expressed as $R_a=(k_l\rho_l C_{pl}/k_s\rho_s C_{ps})^{1/2}$. Thus, according to Sakurai, the minimum film boiling temperature on a solid surface with any thermal physical properties in any liquid can be evaluated by equations (2.38) and (2.39). For example, for an oxidized zirconium surface in water, the value of T_I gradually increases with increasing pressure and approaches asymptotically a value around T_H. On the other hand, T_{min} reach T_H at relatively low system pressures and become larger than that at higher system pressures. Then, the value of T_{min} first approaches a certain value near the critical temperature at a system pressure around 3 MPa, and then gradually decreases with increasing system pressure up to 7 MPa due to the increase in the saturation temperature though T_I is nearly constant.

2.4.2 Vapor film collapse at minimum film boiling temperature

The minimum heat flux or surface superheat of the pool film boiling is to be determined by either:

- *Taylor instability vapor removal limitation at the vapor-liquid interface.*
- *The lower temperature limit of the heterogeneous spontaneous nucleation upon contact.*

From the fact that the value of T_I for each liquid almost agrees with the homogeneous spontaneous nucleation temperature at high pressures, it is easily understood that the governing mechanism for the vapor film collapse in the high-pressure region is the heterogeneous spontaneous nucleation limit, which almost equals the homogeneous nucleation temperature. To make clear the governing mechanism of the vapor film collapse in film boiling at lower pressures, the heterogeneous spontaneous nucleation temperature was investigated in liquid nitrogen at various pressures by Sakurai *et.al.* (1989, 1990).

Typical heat transfer process on a horizontal cylinder in saturated liquid nitrogen at atmospheric pressure for slowly increasing heat input is shown in figure 2.10. The natural convection heat transfer from the cylinder obtained for the exponential heat input with the period of 34 s changes suddenly into explosive boiling at a certain surface temperature of the cylinder (point A). The heat transfer coefficients up to the point A agree with the value obtained from natural convection correlation given by McAdams. Owing to the explosive boiling, the surface superheat and the heat flux rapidly changes through the process ABC shown as a dashed line to stable film boiling (point C). The stable film boiling heat transfer curve was obtained by increasing the heat input afterwards up to the point D and then decreasing from the point down to the minimum film boiling point E. This stable film boiling heat transfer curve DE agrees well with the values obtained from the general correlation for pool film boiling heat transfer mentioned before.

After the vapor film collapse at the minimum film boiling point E, the heat flux suddenly increases at first with rapid decrease in the surface superheat, it arrives at a maximum heat flux near the steady critical heat flux, and then decreases to a stable nucleate boiling point F. The developed nucleate boiling curve was obtained by quasi-steadily increasing heat input afterwards up to the point G, where the surface superheat suddenly increases and the nucleate boiling changes to the film boiling owing to hydrodynamic instability near the cylinder surface (Zuber, 1959, Kutateladze, 1959).

It is obvious that the transition mechanisms from fully developed nucleate boiling to film boiling at point G are very much different than those from natural convection to film boiling at point A. The direct transition from natural convection to film boiling was firstly recognized as that caused by the initiation of the heterogeneous spontaneous nucleation, and the surface temperature at that point is the lower limit of the heterogeneous spontaneous nucleation temperature as mentioned later. An important fact to notice is that this heterogeneous spontaneous nucleation temperature at point A is closely in agreement with the minimum film boiling temperature at point E.

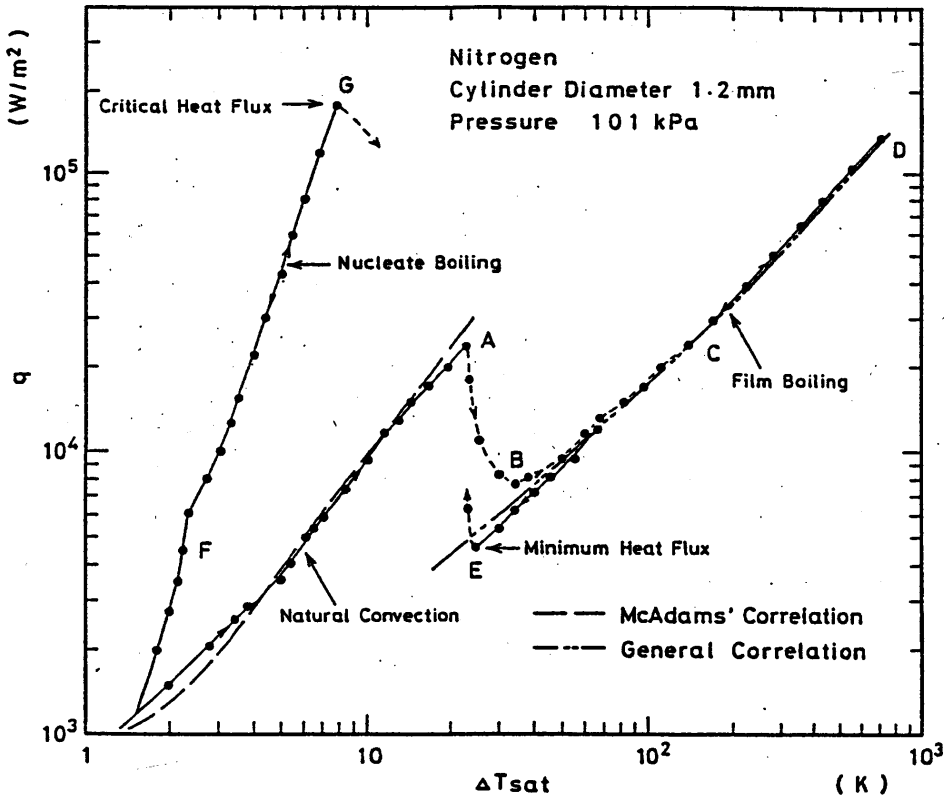

Figure 2.10 – Direct transition process from natural convection to film boiling in liquid nitrogen. (Sakurai, 1990a)

In the same investigation, the heterogeneous spontaneous nucleation temperature THET on a horizontal platinum cylinder (1.2 mm-diameter) was investigated. The heat input was changed exponentially, and three different pressures were applied to the system. The results showed that T_{HET} has lower and upper limits for slow and rapid heat inputs respectively. The difference

between these limits becomes smaller with the increase in pressure, and at a pressure of ~ 5 atm the difference is almost zero.

Based on these findings, and also some experimental results reported by Shioutsi *et.al.* (1989), Sakurai postulated that the vapor film collapse at the minimum film boiling point occurs when the contact interface temperature of the solid surface becomes lower than the lower limit of the heterogeneous spontaneous nucleation temperature beyond which large number of vapor bubbles will be born by the heterogeneous spontaneous nucleation in the cavities on the solid surface. The limits of film boiling heat flux or corresponding surface temperature caused by Taylor instability at the vapor-liquid interface would be larger than those for the lower limit of the heterogeneous spontaneous nucleation respectively, and the Taylor instability is thus not the governing mechanism of vapor film collapse.

2.5 Effect of flow rate on film boiling heat transfer

Bromley *et.al.* (1953) carried out the experiments of saturated film boiling heat transfer on horizontal cylinders with the diameters ranging from 9.8 to 16.2-mm in upward forced flow of various kinds of liquids at atmospheric pressure, and also performed a theoretical analysis of upward flow forced convection film boiling on the outside of a horizontal cylinder to describe their experimental data. They concluded that, under slower flow rates at the values of $U/(gD)^{1/2}$ less than unity, the forced convection film boiling heat transfer coefficients are predicted by the correlation for saturated pool film boiling heat transfer given by Bromley (1950), and that, under higher flow rates at the values of $U/(gD)^{1/2}$ greater than 2, the heat transfer coefficients are predicted by the following equations,

$$\overline{h} = \overline{h}_{CO} + 7h_r / 8 \tag{2.40}$$

$$\overline{h}_{CO} = 2.7\left[Uk_v \rho_v L' / (D\Delta T_{sat})\right]^{1/2} \tag{2.41}$$

In the experiments performed at UWM, the fall velocities for a molten sphere in the water was typically 0.3 m/s, which give a value for $U/(gD)^{1/2} \approx 1$. Therefore, we can approximate the flow conditions to pool film boiling, which indeed simplifies any calculation we wish to perform.

This review-chapter has mainly focused on solid spherical objects in water. We recognize that in the case of *molten* spheres, the physics will be somewhat altered, but to a first approximation, we can use correlations obtained for solid

surfaces at various pressures and in various liquids to predict the behavior of granules of molten ferroalloys in water.

3. CHEMISTRY AND EQUILIBRIA OF THE Si-Al-Ca-O SYSTEM

In this chapter, we will discuss aspects related to the chemistry of the Si-Al-Ca-O system. In order to get an understanding of what is going on during the quenching of a molten drop of metal, we need to know what reactions are possible and most likely to occur. We are limiting the discussion to the temperature range where SiO_2-reduction is important, i.e. from the melting temperature of silicon (or ferrosilicon) up to 1800 °C.

Several of the issues discussed are based on Schei *et.al.* (1998).

3.1 Species in the system

3.1.1 Silicon

Silicon has a melting point of 1412 ± 2 °C (Yaws, 1981), but several other values in the 1400-1420 °C range have been suggested. In liquid state silicon have very similar properties to those of a molten metal. Thus, when referring to silicon as a metal in subsequent chapters, it is understood that it is a liquid phase. Silicon can also exist as a gas in the form of the two species Si and Si_2. However, the partial pressures of these two gases are very low compared to other gases present, thus, for practical applications they can be neglected.

Carbon forms a stable condensed compound with silicon, SiC, which occurs in several hexagonal polytypes called α-SiC and one cubic modification called β-SiC. For practical purposes the difference in stability between α-SiC and β-SiC is negligible. SiC is stable as a solid up to 2830 °C, where it decomposes peritectically (Scace and Slack, 1959). The solubility of carbon in liquid silicon in equilibrium with SiC has been investigated by several workers. The results scatter considerably, between 10 to 200 ppm for 1500 °C (Schei *et.al.*, 1998).

When oxygen is present, two stable compounds can exist, SiO_2 and SiO. SiO_2 appears in the different modifications quartz, tridymite and cristobalite, all of which have high and low-temperature modifications. High temperature cristoballite melts at about 1725 °C, but the heat of melting is low and the resulting melt is highly viscous. Thus, cristoballite is easily undercooled to a glass.

The gas compound SiO is stable at high temperatures, and it is a very important participant in the reactions in the silicon process.

Concerning other elements present in the process, we will limit our discussion to Al and Ca. These elements form stable oxides that will appear in a slag phase together with SiO_2. The equilibrium between the slag and the metal will decide the concentration of these elements in the final product. The slag equilibriums will be discussed in section 3.2.

3.1.2 Ferrosilicon (FeSi75)

This alloy has traditionally been an important product for ferroalloy producers in Norway. We will discuss briefly how the presence of iron influences on the phases in the system. Furthermore, we limit the discussion to silicon containing 75 weight-percent iron.

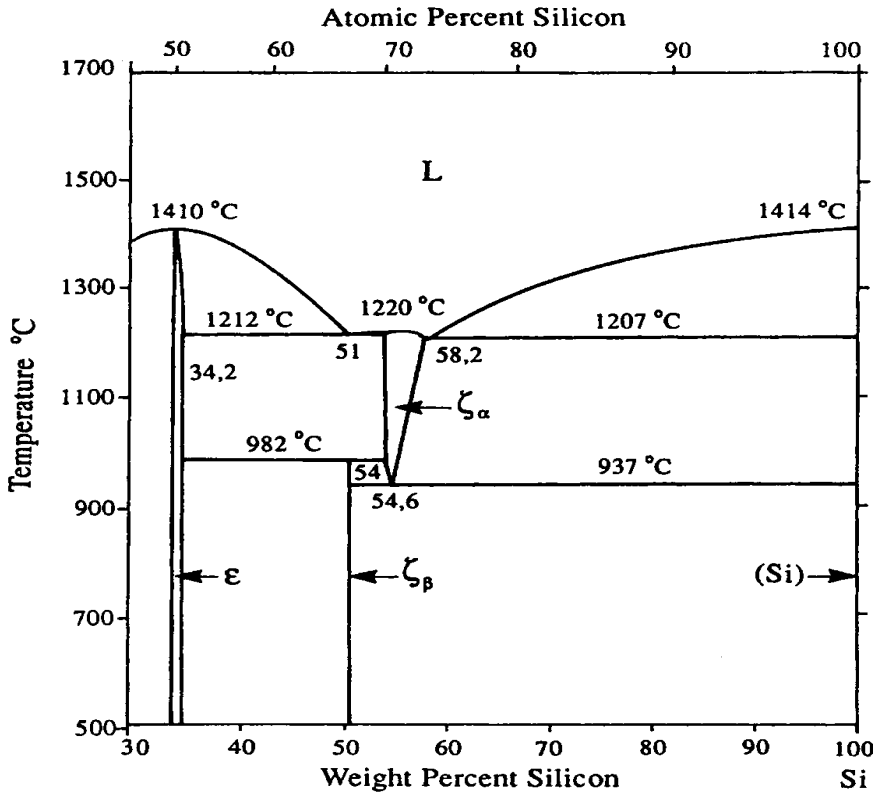

Figure 3.1 – The silicon-rich part of the Si-Fe phase diagram.

A phase diagram for the iron-silicon system is shown in figure 3.1. If we consider molten FeSi75 upon cooling, solid silicon will start to precipitate at

about 1327 °C. The solubility of iron (and any other element) is low in solid silicon, thus, the silicon phase will be very pure. If the cooling rate is low, solidified silicon will be in equilibrium with the increasing iron-rich melt, according to the well-know lever rule. When the eutectic temperature of 1207 °C is reached, the rest of the melt will solidify into a so-called ζ_α-phase and a secondary Si-phase. According to Piton (1968), the ζ_α-phase is primitive tetragonal with one Fe-atom and two Si-atoms per elementary cell. Such a matrix should have been composed of $FeSi_2$. However, the chemical composition of $FeSi_{2.33}$ is explained by the fact at this elevated temperature, approximately one out of six of the Fe-atoms is replaced by vacancies.

Upon further cooling, the ξ_α-phase will precipitate some silicon as the solubility of Si in ζ_α decreases. When a temperature of 955 °C is reached, an eutectoid reaction starts, ζ_α-phase $\rightarrow$ $FeSi_2$ (ζ_β) + Si. Thus, the final matrix will consist of a mixture of $FeSi_2$ and Si.

3.2 Slag formation in the presence of liquid silicon

3.2.1 Stability of foreign oxides

The impurity elements in the final product normally arise from foreign oxides present in the raw materials needed for the process. It is important to predict the behavior of such oxides during the production of silicon. Are they stable, can they form a slag, what will be the final composition of the product? These are questions that are important for the silicon producer. But for a safety analysis of the granulation process, these questions are also vital. Impurity elements in the semi-final product may in theory change the behavior of a molten drop during the granulation process. A liquid slag can form at the surface, altering the physical properties considerable. This section will deal with some of these aspects.

The Ellingham-type of diagram, shown in figure 3.2, shows the standard Gibbs free energies of formation of oxides per mole of oxygen reacted. The diagram visualizes the stability of oxides of selected metals relative to those of silicon and carbon.

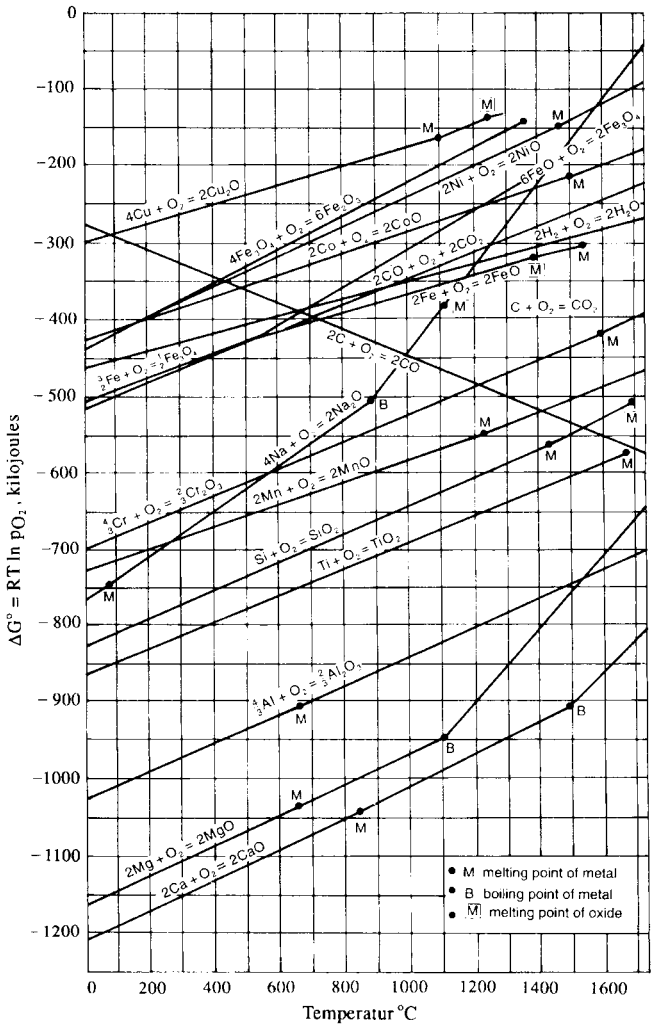

Figure 3.2 – The Ellingham diagram for the oxides of some relevant additional elements in silicon production.

The more negative the Gibbs free energy of formation, the more stable is the oxide. The transition metals like Ni, Co and Fe are all much less stable than SiO_2. This means that oxides of transition metals are likely to be reduced to their pure metal state for a given temperature at partial pressures of oxygen, which is much higher than needed for the reduction of SiO_2 to Si. These oxides also become unstable in the presence of graphite and CO of unit pressure at fairly low temperatures.

Oxides of chromium and manganese should be completely reduced before anything happens to the SiO_2, because of their stability. However, the

temperature needed for the manganese reduction to be completed is at a level where liquid slag formation may take place.

The alkali metal oxides, represented by the compound Na_2O in figure 3.2, are quite stable at room temperature, but their stability decreases rather rapidly with increasing temperature due to the low melting and boiling points of the alkali metals. As shown, if present in the pure state, Na_2O can be reduced to metal vapor by reaction with carbon at ~ 1000 °C. The same happens to the more volatile potassium forming an oxide that is less stable than that of sodium.

The third group of metal oxides to consider are those that require a lower oxygen potential than SiO_2 to react and form metal in its standard state. This group includes the alkaline earth metal oxides and alumina, which happen to be among the most abundant of the impurities entering the furnace charge. Notice that TiO_2, which is the highest and least stable of the titanium oxides, also belongs to this group, as it is more stable than SiO_2 throughout the temperature range of interest. The monoxide, which is the only one of the titanium oxides that coexists with its metal, is not listed in figure 3.2, but it melts at 1750 °C and has a stability similar to that of Al_2O_3 (Chase, 1985).

The high stability of these refractory oxides and the fact that they enter as impurities tied up in silicate minerals with oxide activities less than unity make it likely to assume that they will survive as oxides up to the melting point of silica at around 1700 °C where they become dissolved in a glassy slag. As the temperature increases and liquid silicon starts to form around 1800 °C, their destiny will then be determined by partial distribution equilibria of the following type:

$$\underline{Si} + 2/y\ (Me_xO_y) = 2x/y\ \underline{Me} + (SiO_2) \qquad (3.1)$$

In reaction (3.1), the parentheses refer to components dissolved in a slag phase and the underscored to dissolved elements in the metal phase. The Gibbs free energy change and the standard enthalpy change for reaction (3.1) is positive for all the refractory oxides included in figure 3.2. The equilibrium constant for reaction (3.1) is given by

$$K_R = \exp\left(-\frac{\Delta G_R^0}{RT}\right) \qquad (3.2)$$

The value of K_R for reaction (3.1) is thus much less than unity for elevated temperatures for refractory oxides. The equilibrium constant K_R increases with

temperature for the endothermic reactions with the refractory oxides, making the reduction of these more favorable at high temperatures. For the reactions with the transition metal oxides, as well as some of the alkali metal oxides, the situation is opposite, as reaction (3.1) is exothermic.

3.2.2 Stability of foreign oxides in the presence of silica

Foreign oxides are, in general, insoluble in crystalline silica and are practically insoluble also in molten silica for a majority of the metal oxides. Small additions (beyond ~ 2%) of a divalent metal oxide lead to the formation of a second liquid phase. Alkali metal oxides behave differently, as they seem to be able to give off their oxygen ions completely to the three-dimensional network of Si-O bonds, which dominates the structure of molten silica. By placing themselves in the interstices of the network, a gradual breakdown of the silicate network takes place giving the characteristics of glass melts.

The smaller and more polarizing metal ions, which have a greater attraction for oxygen, form groups that cannot fit into these interstices. These groups must separate from the silica melt with some silica in anionic groups, which are smaller and can arrange themselves along with the metal ions in such a way that their coordination requirements are satisfied. The second liquid phase, a *silicate melt*, forms as a result of this. The SiO_2 activity of this silicate melt must be the same as that for the coexisting molten silica phase, that is, very close to unit activity. When impurities are present, both liquid silica and silicon will act as solvents. If unity activity for these two phases is assumed, it can be shown (Schei *et.al.*, 1998) that the activity of an additional oxide phase can be written as

$$[\%Me] = k_{eff} \frac{\left(a_{Me_xO_y}\right)^{1/x}}{\gamma_{Me}} \tag{3.3}$$

where k_{eff} is the equilibrium constant for reaction (3.1), multiplied with a factor $100M_{Me}/M_{Si}$. Based on relation (3.3), Schei *et.al.* calculated the distribution of some individual elements between silicon and its oxide phase at 1600 °C. They assumed that the liquid silicon contained 0.1% of the impurity metal in solution, and calculated the impurity oxide activity at equilibrium with the silicon melt. Thus, they arrived at the results shown in table 3.1.

Table 3.1. Calculated results from equation (3.3), showing impurity oxide activities in silica at equilibrium with liquid silicon with 0.1% Me at 1600 °C, oxide activities at formation of an oxide phase additional to silica and the minimum of [%Me] needed to form this phase.

Impurity oxide/Me	a_{oxide} *in add. phase* [1)]	a_{oxide} *at [%Me] = 0.1*	*[%Me] at formation of add. phase*
FeO/Fe	0.37	4.8×10^{-9}	[2)]
MnO/Mn	0.12	1.0×10^{-6}	[2)]
Cr_2O_3/Cr	0.12	2.4×10^{-17}	[2)]
TiO_2/Ti	0.6	6.8×10^{-8}	[2)]
TiO/Ti		4.7×10^{-6}	[2)]
Al_2O_3/Al	0.6	0.05	0.35
CaO/Ca	0.0022	0.0092	0.024
MgO/Mg	0.23	1.4	0.17

[1)] Silica saturated silicate melt.
[2)] Values far beyond the validity of equation (3.3).

For the transition metals listed including titanium, the calculated values were of several orders of magnitude small than those for the respective silica-saturated silicate melts. Taking the extremely low concentration of Me_xO_y at silica saturation, the calculations tabulated above imply that these types of metals are distributed quantitatively in the metal phase.

3.3 Slag systems and properties

3.3.1 Phase relations

Based on the data given in section 3.2, it seems fair to conclude (Schei *et.al.*, 1998) that the only impurities present in tapped metal that contribute significantly to slag formation, are calcium and aluminum. In refining the metal, some foreign oxides may deliberately be added in order to improve some specific properties of the slag. However, in this context, we focus on relatively pure alloys. Thus, the only slag-forming elements present are Ca and Al. We will therefore focus on the CaO-Al_2O_3-SiO_2 system, with a phase diagram given in figure 3.3. The diagram illustrates a projection of the liquidus surface where the boundaries between coexisting phases are shown by solid curves and liquidus isotherms by lighter curves. The straight lines represent tielines between coexisting phases at subsolidus.

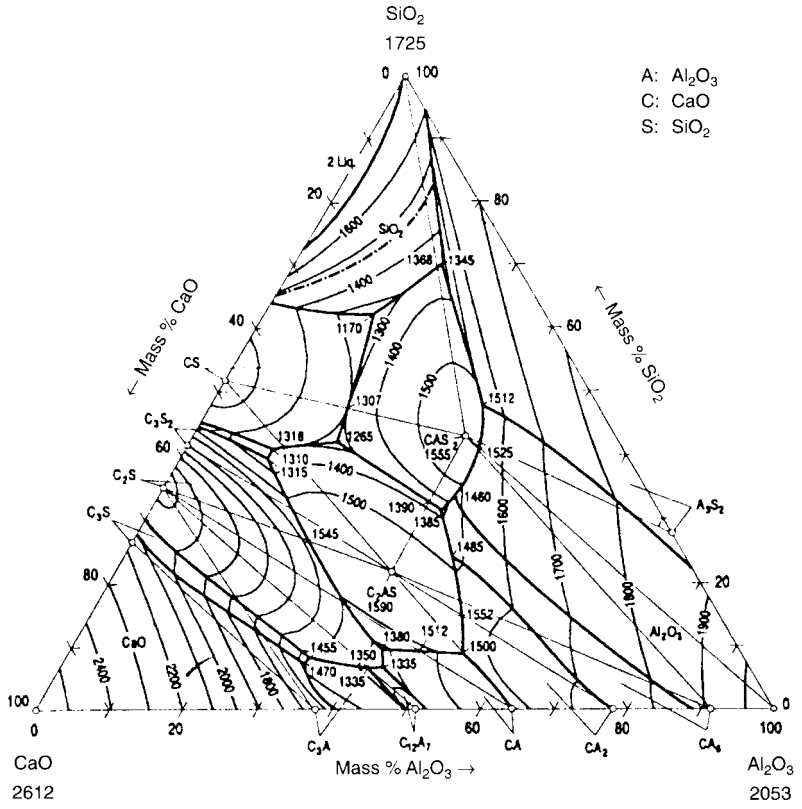

Figure 3.3 – Phase diagram of the CaO-Al_2O_3-SiO_2, taken from Schei *et.al.* (1998).

A homogeneous slag can form over a wide compositional range, even at such low temperatures as the liquidus temperature of silicon. Obviously, when the compositional range is large, the properties of the slag will vary depending on the composition. We will briefly discuss some slag properties with respect to a change in the overall composition.

3.3.2 Viscosity and density

The variation in viscosity within a liquid slag at 1500 °C is shown in figure 3.4. The iso-viscosity contours are running nearly parallel to lines of constant CaO-concentration. When this concentration decreases below 15%, there is a dramatic escalation in the rate of viscosity increase.

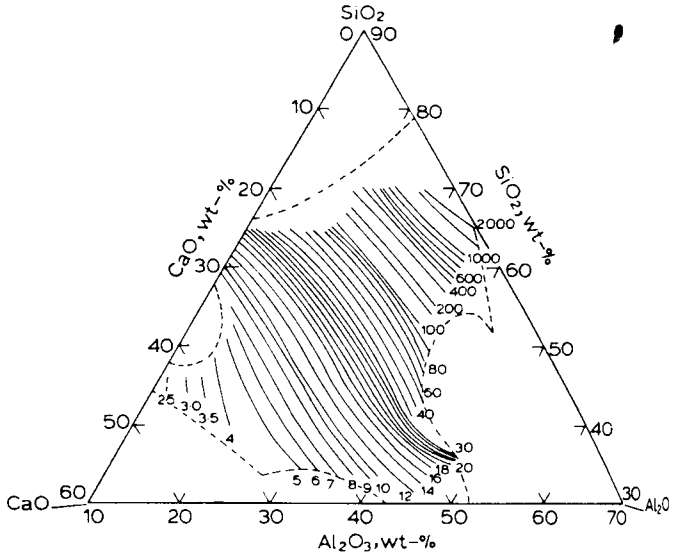

Figure 3.4 – ISO-viscosity [poise] contours of CaO-Al_2O_3-SiO_2 melts at 1500 °C, reproduced from Turkdogan (1983). According to more recent data, values given at contours should be 20% lower (Vdeh, 1995).

The viscosity of pure liquid silicon is recently reported by Rhim *et.al.* (2000):

$$\upsilon(T) = 0.75 - 1.22\times10^{-3}(T - T_m)\ [\text{mPa*s}] \qquad (3.4)$$

In equation (3.4), the melting point of silicon T_m is 1414 °C. Thus, for liquid silicon at 1500 °C, the viscosity is about 0.74 mPa*s or 0.0074 poise, a factor 10 000 less than slags with approximately equal amounts of the three components. Rhim *et.al.* also reports experimental values for density, volume expansion, specific heat capacity, emissivity and surface tension for the temperature range 1350-1850 K.

The density follows a similar dependency on slag composition, see figure 3.5. If we compare with the densities for Si and FeSi75, we find that CaO-Al_2O_3-SiO_2 melts in general will float on liquid FeSi75 (ρ_{FeSi75} = 3.19 g/cm^3 at 1450 °C). On liquid silicon, however, slags with a bulk density ≥ 2.5 g/cm^3 tend to sink (ρ_{Si} = 2.51 g/cm^3 at 1450 °C).

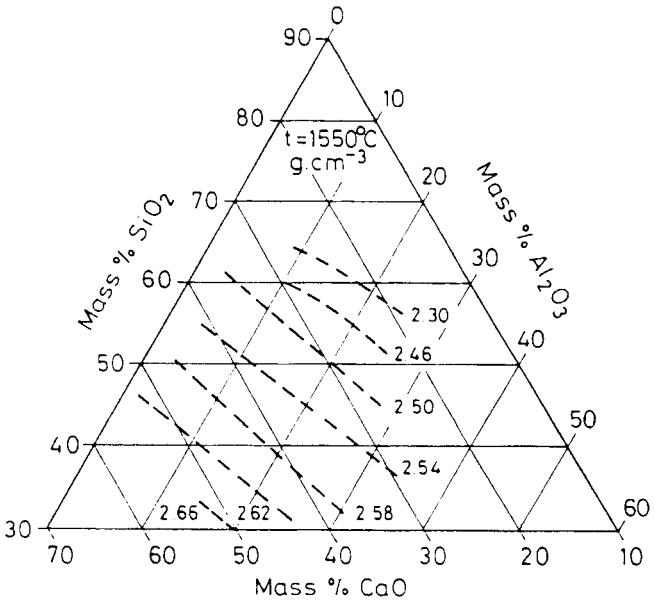

Figure 3.5 – Isodensity curves for the SiO_2-Al_2O_3-CaO system at 1550 °C, taken from Schei *et.al.* (1998).

3.3.3 Distribution equilibria

Hot metal immerged in water will immediately be covered by a vapor film. Thus, the molten metal surface of Si will be exposed to gaseous H_2O at atmospheric pressure. Subsequently, the first chemical reactions that will take place is the reaction between water vapor and liquid silicon (Gibbs free energy of formation taken from Rosenqvist, 1983):

$$Si_{(l)} + H_2O_{(g)} = SiO_{(g)} + H_{2(g)}, \qquad \Delta G^\circ_{1400\ ^\circ C} = -72.5\ kJ/mole \tag{3.5}$$

$$Si_{(l)} + 2H_2O_{(g)} = SiO_{2(s)} + 2H_{2(g)}, \quad \Delta G^\circ_{1400\ ^\circ C} = -300\ kJ/mole \tag{3.6}$$

The former of these reactions is endothermic with $\Delta H_{reaction} = 93.5$, and the latter is highly exothermic with $\Delta H_{reaction} = -706.5$ kJ/mol Si. We also note that the former forms a gaseous product SiO, which mixes with hydrogen and water vapor in the blanketing film. Thus, the properties of the vapor film will change accordingly, depending on the overall composition of the gas mixture.

The impurity elements Al and Ca, which both exist in very small amounts compared to Si, are not likely to react with vapor as is the case for silicon. It will later be shown (chapter 10) that reaction (3.5) dominates during the initial stages of the oxidation process. Eventually, a boundary-layer oxide film of

SiO_2 forms at the surface as the SiO-gas condenses or is being oxidized further (Schei *et.al.*, 1998). The oxygen potential in the metal at the silica-metal interface is then defined by:

$$1/2\ (SiO_2) = 1/2\ \underline{Si} + \underline{O} \tag{3.7}$$

In general, a dissolved metal impurity Me may now react as:

$$x/y\ \underline{Me} + \underline{O} = 1/y\ (Me_xO_y) \tag{3.8}$$

If both reactions are at local equilibrium at the oxide film-metal interface, with the same activity of dissolved oxygen (a_O), reaction (3.7) and (3.8) can be combined. Substituting Me by Al and Ca, we readily obtain

$$\underline{Al} + 3/4\ (SiO_2) = 3/4\ \underline{Si} + 1/2\ (Al_2O_3) \tag{3.9}$$

$$\underline{Ca} + 1/2\ (SiO_2) = 1/2\ \underline{Si} + (CaO) \tag{3.10}$$

The oxidation of a dissolved impurity element is coupled with the oxidation of silicon, since all reactions appear to be under the same rate-limiting step, here assumed to be the rate at which oxygen is supplied at the metal side of the slag-metal interface. If this is true, it is also evident that the oxidation of various dissolved elements is mutually coupled through similar reactions, i.e. as for Al and Ca:

$$2/3\ \underline{Al} + (CaO) = \underline{Ca} + 1/3\ (Al_2O_3) \tag{3.11}$$

However, at low impurity levels, the transport of the impurity elements from the bulk of the metal to the slag-metal interface may very well take over as a rate-controlling step. The recorded bulk distribution will then deviate from the equilibrium values. Equilibrium concentrations for Al and Ca in molten ferrosilicon and silicon are shown in figures 3.6 and 3.7, respectively.

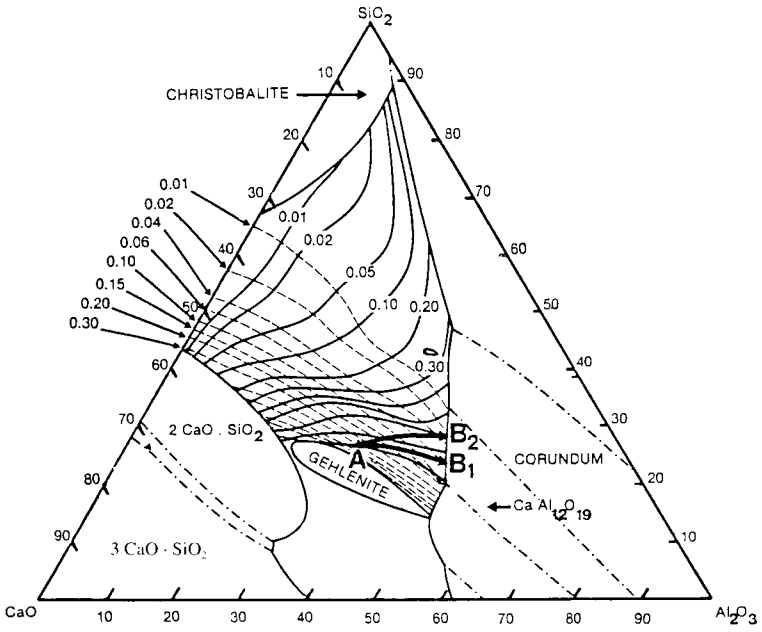

Figure 3.6 – Isoconcentration curves for Al (solid lines) and Ca (broken lines) in FeSi75 at 1550 °C (Tuset, 1985).

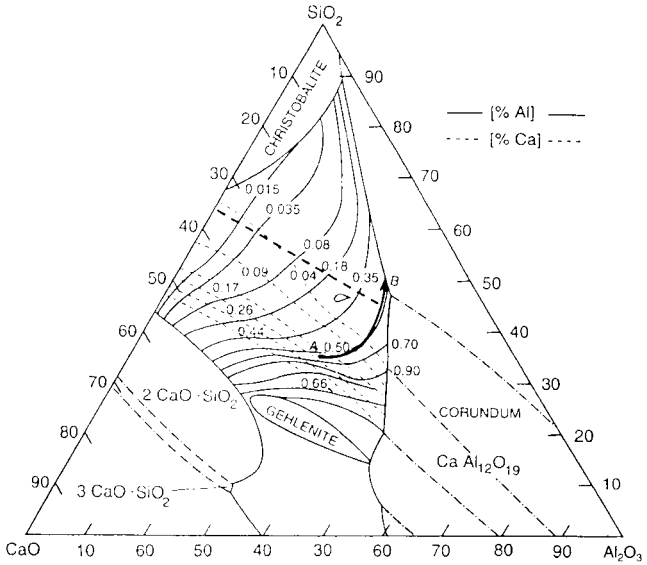

Figure 3.7 – Isoconcentration curves for Al and Ca in silicon at equilibrium with SiO_2-Al_2O_3-CaO slags at 1550 °C (Haaland, 1994).

4. OXIDATION OF LIQUID SILICON - KINETICS

4.1 Introduction – gas-diffusion controlled reactions

In general, the reaction between a metal and air is expressed as $1/2O_2$ + Me = MeO. As the reaction proceeds, nitrogen will flow away from the surface, and the oxygen has to diffuse through a gas layer of increasing concentration of nitrogen. Similar, in the case of a reaction between water (vapor) and metal: H_2O + Me = MeO + H2. Here, the concentration of hydrogen close to the surface will increase as the reaction proceeds. Consequently, the flow of water vapor toward the surface has to diffuse through this layer of H_2.

When a molten metal is exposed to a reactive gas, i.e. oxygen, air or water vapor, the generation of oxide-containing dust is larger than can be expected if only free evaporation of the metal was the transfer mechanism. This phenomenon is known from oxygen-blowing of molten steel, where up to 1 % of the metal is lost as dust or smoke. For the blowing of manganese-alloys, this loss is even larger. The formation of smoke may be caused by:

1) Evaporation of the metal in an atmosphere of inert gas.
2) Evaporation and oxidation of the metal in a mixed atmosphere of inert gas and a reactive gas (i.e. air or water vapor).
3) Loss of metal-droplets in gas-bubbles escaping from the molten metal (bubble-bursting).

In most practical applications, reactive gases will be present in the atmosphere above the molten metal.

4.2 Wagner`s model

In his famous work published in 1958, Wagner discusses some important aspects of the oxidation of silicon at elevated temperatures. At that point, it had been observed that under certain conditions, the rate of attack of metals in aqueous solutions *decreased* when the concentration of an oxidizing agent (oxygen or nitric acid) *increased*. This phenomenon is called *passivity* and can be ascribed to the formation of a thin film of oxide or another metal compound, which slows down the transfer of metal ions from the metal to the surrounding solution. A similar phenomenon occurs when silicon is exposed to oxygen at elevated temperatures.

Consider a silicon sample initially free of oxygen or oxide during heating in an O_2-He atmosphere, where the oxygen content of the gas is gradually increased,

but the total pressure is kept constant. At low oxygen concentrations in the bulk gas, the supply of oxygen to the surface of the sample is low, accordingly the rate of SiO –formation is low, and only little SiO is accumulated at the surface of the sample. If the resulting partial pressure p_{SiO}^{*} at the surface is less than the equilibrium partial pressure $p_{SiO\,(eq)}$ for the reaction

$$\frac{1}{2}\mathrm{Si}(l)+\frac{1}{2}\mathrm{SiO}_2(s)=\mathrm{SiO}(g) \tag{4.1}$$

the silicon surface will remain bare. At higher oxygen concentrations, however, p_{SiO}^{*} will reach $p_{SiO\,(eq)}$ and accordingly a protective layer of SiO_2 may be formed. Consequently, the transition from the active to the passive state is expected to occur if

$$p_{SiO}{}^{*}=p_{SiO(eq)}. \tag{4.2}$$

To calculate the steady-state partial pressure of SiO at a bare silicon surface, Wagner proceeded as follows. He assumed that the reaction between Si and O_2 has a low activation energy. Thus, oxygen molecules hitting a bare silicon surface react readily, and the partial oxygen pressure $p{o_2}^{*}$ at the silicon surface is much lower than the partial pressure $p{o_2}^{\circ}$ in the bulk gas mixture. Hence, the rate of transport of oxygen in gram-atoms per unit area per unit time toward the silicon surface is

$$j_O=j_{SiO}=\frac{2D_{O_2}p_{O_2}^{0}}{\delta_{O_2}RT}=\frac{2h_{O_2}P_{O_2}^{0}}{RT} \tag{4.3}$$

Also, under steady-state conditions, the rate of transport jo_2' of oxygen toward the silicon surface must equal the rate of transport jo_2'' of oxygen away from the surface. Using the proper expressions for jo_2' and jo_2'' and assuming that the ratio of the thicknesses δ_{SiO} and δ_{O_2} may be approximated by

$$\delta_{SiO}\big/\delta_{O_2}=\left(D_{SiO}\big/D_{O_2}\right)^{m} \tag{4.4}$$

where m is a proper fraction whose value depends on whether the boundary layer is laminar or turbulent. In Wagner's original paper, he assumed m = 0.5 as a fair approximation. Thus, he arrived at the following equation, which yields the maximum partial pressure $p{o_2}^{\circ}$(max) in the bulk gas at which a bare silicon surface can be maintained:

$$p_{O_2}^{\circ}(\max) \cong \frac{1}{2}\sqrt{\frac{D_{SiO}}{D_{O_2}}}\, p_{SiO(eq)} \tag{4.5}$$

Thus, if the partial pressure of oxygen exceeds the value given by equation (4.5), SiO_2 will form on the surface of the silicon sample. A steady-state value of the thickness of the SiO_2-layer will be attained when the rate of formation of SiO_2 resulting from the diffusion of ions and electrons across the SiO_2 layer is equal to the rate of consumption due to the reaction

$$SiO_2(s) = SiO(g) + \frac{1}{2}O_2(g) \tag{4.6}$$

with the equilibrium condition

$$p_{SiO} * (p_{O_2} *)^{1/2} = K \tag{4.7}$$

Under these conditions, the rate of oxygen transport in gram-atoms per unit area per unit time is

$$j' = 2D_{O_2}(p_{O_2}^{\circ} - p_{O_2} *)/\delta_{O_2} RT \tag{4.8}$$

where p_{O2}* is the oxygen partial pressure at the surface of the sample. Then, assuming steady-state conditions (no net transport rate of oxygen toward the surface), Wagner arrived at equation (4.9), which determines the oxygen partial pressure at the surface of the SiO_2 layer.

$$2(p_{O_2}^{\circ} - p_{O_2} *) = K(D_{SiO}/D_{O_2})^{1/2}/(p_{O_2} *)^{1/2} \tag{4.9}$$

If one plots the left and the right hand side of equation (4.9) separately in the same diagram, it will be seen that there in general are two possible solutions. Only the higher value of p_{O2}* represent a stable state.

The value of K is very low (1.5×10^{-11}) at 1410 °C (Coughlin, 1954). Thus, the partial pressure of oxygen at the surface of the SiO_2 layer calculated from eq. (4.9), is nearly equal to the bulk partial pressure p_{O2}°. The rate of attack j_{Si} is found to be

$$j_{Si} = \frac{D_{SiO} K}{(p_{O_2}^{\circ})^{1/2} \delta_{SiO} RT} \tag{4.10}$$

Equation (4.10) states that the rate of attack decreases with increasing oxygen pressure in the bulk gas, given that $p_{O_2}^{\circ}$ is greater than $p_{O_2}^{\circ}$(max) as given by eq. (4.5).

If the oxygen partial pressure in the bulk gas is gradually decreased after formation of a SiO_2 layer, the oxide layer will be stable at all partial pressures $p_{O_2}^{\circ}$ which give a real solution of $p_{O_2}^{*}$ as given by equation (4.9). The lowest value, $p_{O_2}^{\circ}$(min), is reached if the two solutions of equation (4.9) become identical. Wagner showed that this minimum value is given by

$$p_{O_2}(\min) = \frac{1}{2}\left(\left(\frac{1}{4}\right)^{2/3} + \left(\frac{1}{2}\right)^{2/3}\right) K^{2/3} \left(D_{SiO} / D_{O_2}\right)^{1/3} \tag{4.11}$$

According to this model, the partial pressure of SiO at the surface will drop several orders of magnitude when the bulk oxygen partial pressure is increased beyond $p_{O_2}^{\circ}$(max) = 6.1×10^{-3} atm. If $p_{O_2}^{\circ} \leq p_{O_2}^{\circ}$(max) the partial pressure of SiO equals the equilibrium partial pressure $p_{SiO(eq)}$ = 1.52×10^{-2} atm over liquid silicon and solid silica. If, however, $p_{O_2}^{\circ} \geq p_{O_2}^{\circ}$(max), the value of p_{SiO}^{*} is determined by $p_{SiO}^{*} \cong K/(p_{O_2}^{\circ})^{1/2}$ and is found to be as low as 2×10^{-10} atm. Accordingly, the rate of attack j_{Si} decreases markedly since j_{Si} for steady-state conditions is proportional to the partial pressure of SiO at the surface.

In his original paper, Wagner does not discuss the fate of the SiO-molecules as they diffuse away from the Si surface through a gaseous boundary layer. In principle, the SiO should react with oxygen in the boundary layer to form SiO_2 when the partial pressure of oxygen reaches a value above which silica is stable. Thus, some of the oxygen should be consumed in advance of the Si surface in a manner similar to that proposed by Turkdogan (see section 4.3), except that now SiO rather than Si would react with O_2 to give SiO_2-fog.

4.3 Turkdogan´s model

This model uses a slightly different approach, as compared to Wagner´s model. Turkdogan consider the effect of a reactive gas on the rate of vaporization of a metal to be a counter flux-transport process. When silicon vaporizes in a stream of argon + oxygen, silicon vapor will diffuse away from the surface, and oxygen will diffuse in toward the surface. At some short

distance from the surface of the metal, silicon vapor and oxygen react and form an oxide, presumably SiO_2. The formation of a silica fume provides a sink for the silicon vapor and oxygen, resulting in the counter flux of these gaseous species. When a steady state of counter flux is established under these boundary conditions in an isothermal system, the concentration profiles for silicon vapor, C_{Si}, and oxygen, C_O, close to the metal surface will be as shown schematically in figure 4.1b. At a particular distance δ, a silica fog is formed and beyond a particular distance Δ, which is the thickness of the aerodynamic boundary layer, the oxygen partial pressure is considered as being maintained constant. The gas flow within the boundary layer is assumed laminar.

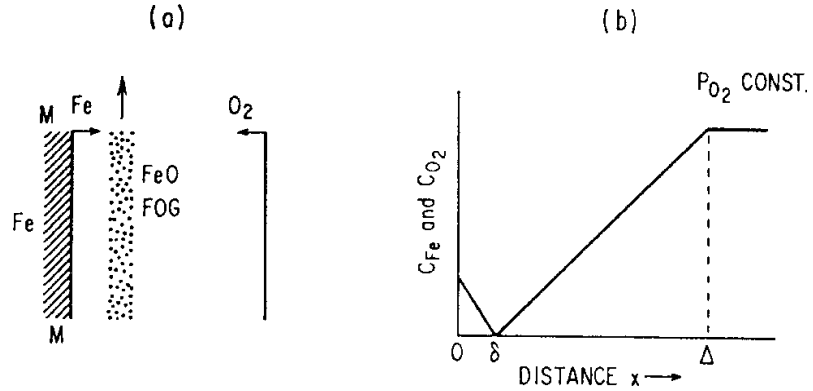

Figure 4.1 – Schematic diagram showing the counter flux of metal vapor (in the original paper, Fe was used as an example) and oxygen in a neutral atmosphere under isothermal conditions, taken from Turkdogan *et.al.*, (1963).

Under the above boundary conditions, the counter flux of silicon vapor and oxygen for a steady state is given by (by Fick´s law):

$$j_{Si} = \frac{D_{Si}}{\delta RT}(p_{Si}^{*} - p_{Si}') \tag{4.12}$$

$$j_{O_2} = -\frac{D_{O_2}}{(\Delta - \delta)RT}(p_{O_2}^{\circ} - p_{O_2}') \tag{4.13}$$

where the notations are the same as those given in section 4.2, and p_{Si}' and p_{O2}' indicate partial pressures at a distance δ from the surface. At this distance, the reaction $Si + O_2 = SiO_2$ is presumed. That requires the counterflux of silicon vapor to be the same as that of oxygen, i.e. $j_{Si} = j_{O2}$. The partial pressures p_{Si}' and p_{O2}' are much lower than the respective values p_{Si}^* at x=0

and $p_{O2}°$ in the bulk gas. Also, the distance δ is much less than Δ. Thus, the following simplification can be made:

$$j_{Si} = -j_{O_2} = \frac{D_{O_2}}{\Delta RT} p_{O_2}{}^{\circ} \tag{4.14}$$

If we identify the average film mass-transfer coefficient h for the transport of oxygen trough the aerodynamic diffusion boundary layer as $h=D_{O2}/\Delta$, equation (4.14) becomes

$$j_{Si} = h \frac{p_{O_2}{}^{\circ}}{RT} \tag{4.15}$$

In the above considerations it has been assumed that the formulation of a layer of a silicon oxide fog at δ does not interfere with the suggested mechanism. Turkdogan assumes that there is sufficient forced or free convection to remove this layer of fog by vertical motion.

According to equation (4.14), for a given temperature and film mass-transfer coefficient, the rate of vaporization of silicon is expected to increase linearly with increasing partial pressure of oxygen in the bulk gas. That means, increasing the oxygen partial pressure decreases the distance δ through which the silicon vapor is transported, see equation (4.12). However, there are two serious restrictions to this mechanism of increasing the rate of evaporation by increasing the bulk oxygen partial pressure:

I) Maximum free evaporation cannot be exceeded
II) For a given metal and temperature, there is a minimum oxygen partial pressure below which the metal oxide fog does not form.

The Langmuir equation gives the maximum rate of evaporation in vacuum,

$$j_{max} = \frac{p_i}{\sqrt{2\pi RTM_i}} \tag{4.16}$$

where p_i and M_i are the vapor pressure of metal (i) and molecular weight of the metal vapor, respectively. When this limiting value of the flux is approached, the form of Fick´s law will not apply. Near this value of the flux, the vapor in contact with the metal surface is no longer saturated and thus the boundary condition assumed is no longer maintained; also δ approaches the mean free path, thus leading to incipient failure of Ficks´s law. Therefore, the plot of j_{Si}

against δ will be as shown by curve FML in figure 4.2a. On further increase of $p_{O2}°$ at Δ, i.e. decrease of δ, the flux of oxygen toward the surface of the metal is greater than the equivalent counter flux of metal vapor, resulting in the oxidation of the metal surface.

By combining equation (4.15) and (4.16), we obtain the critical partial oxygen pressure at vaporization cut-off, i.e. $j_{Si} = j_{max}$:

$$p_{O_2}°(\max) = \frac{p_{Si}°}{h}\sqrt{\frac{RT}{2\pi M_{Si}}} \tag{4.17}$$

This expression for the maximum bulk partial pressure of oxygen, above which an oxide layer will form can be compared to Wagner´s model, equation (4.5).

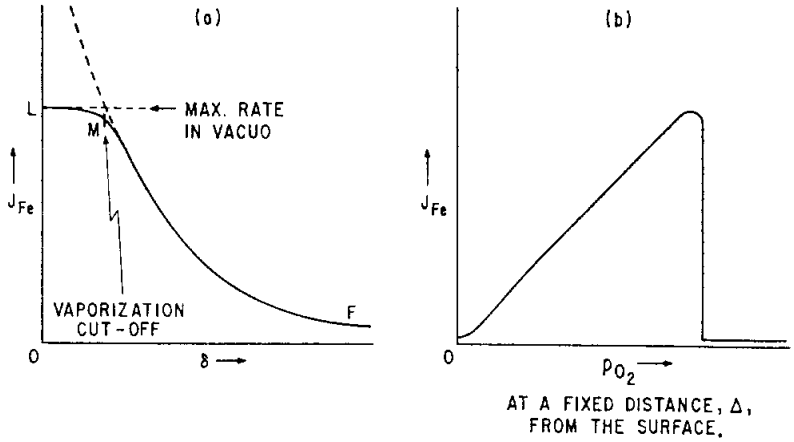

Figure 4.2 – Schematic diagram showing the variation of J_{Si} with δ and P_{O2}.

Depending on the oxygen potential of the oxide (fog) formed at δ, there is a minimum critical oxygen partial pressure below which an oxide fog cannot be formed. Below the critical oxygen partial pressure, the rate of vaporization of the metal in a laminar gas stream is given by the equation

$$j_{\min} = \frac{D}{\Delta}\frac{p_i}{RT} \tag{4.18}$$

where the symbols have the same significance as before. This equation is for the condition that gas flow is laminar over the surface of the metal and at x =

δ, $p_i = 0$. Taking the above two restrictions into account, the relationship between j_{Si} and p_{O_2} expected from equation (4.15) is shown in figure 4.2b.

Turkdogan and his co-workers examined the validity of equation (4.15) and figure 4.2b. In their experiments, the rates of vaporization of liquid copper, nickel, cobalt, iron, manganese, and solid chromium in streams of argon + oxygen were measured in a suitable apparatus. They found that all the experimental data they obtained were in complete agreement with the theory previously described. Figure 4.3 shows graphically their experimental results.

Equation (4.15) can be written in a general form,

$$j_i = \frac{\alpha h}{RT} p_{O_2} \tag{4.19}$$

where α is the number of gram-atoms of metal vapor required to combine with one mole of oxygen at the distance $x = \delta$ very close to the surface of the metal. This relationship is valid for any metal, and we note that j_i is independent of the vapor pressure of the metal and that this rate of vaporization can be predicted by calculating the value of the average film mass-transfer coefficient of oxygen, h, for known boundary conditions. This can be done using an appropriate correlation for the laminar flow of gas over a flat surface, for example that of Eckert and Drake (1959),

$$h = 0.664 \left(\frac{D^4}{\upsilon} \right)^{1/6} \left(\frac{V}{l} \right)^{1/2} \tag{4.20}$$

h = average film mass-transfer coefficient
l = length of the surface in the direction of gas flow
D = interdiffusivity
ν = kinematic viscosity
V = uniform linear velocity of gas away from the interface

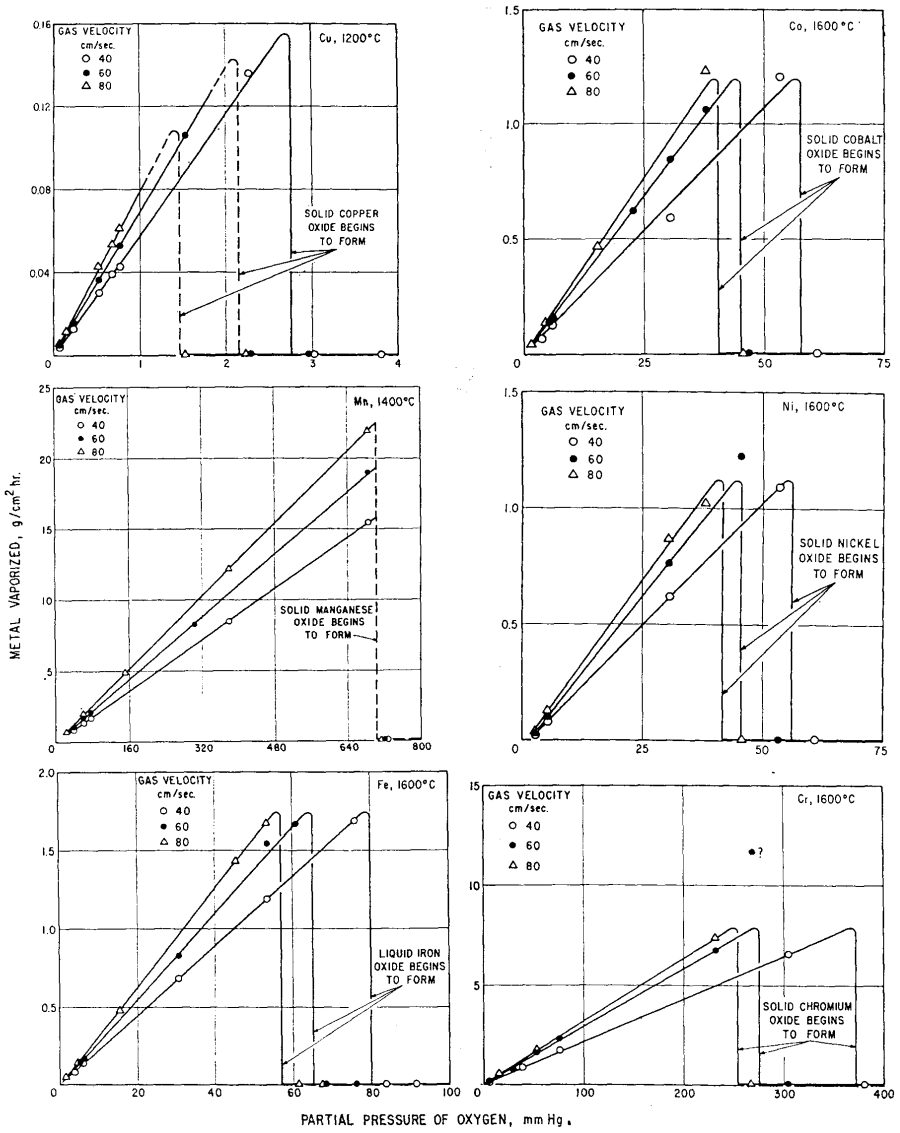

Figure 4.3 – Relationship showing the effects of oxygen partial pressure of Ar + O_2 mixtures and the velocity of gas stream on the rate of vaporization of metals, after Turkdogan et.al. (1963).

The effect of temperature on the rate of vaporization is two-folded. The first effect is as shown in eq. (4.19) and the second effect is that due to increase in the value of *h* with increasing temperature. These effects practically cancel each other out for a given gas velocity and oxygen partial pressure.

By taking the logarithm of each side of eq. (4.19), Turkdogan was able to show (see figure 4.4) that all of their experimental data for the rate of vaporization was located on a straight line, i.e.

$$\log j_i = \log(\alpha p_{O_2}) + \log \frac{h}{RT} \qquad (4.21)$$

In figure 4.4 it is clearly seen that all the data for the various metals, at varying temperatures, fall on the same straight line with unit slope and the theoretical intercept in accord with equation (4.20). Note that only the position of the cut-off is determined by the specific metal and its vapor pressure. The value of α chosen is that of the lowest stable oxide, e.g. $\alpha = 2$ for Ni, Co, Fe and Mn, and $\alpha = 4$ for Cu. Expected vaporization cut-offs for liquid silicon at 1412 and 1600 °C, as predicted from equation (4.16), are also indicated in this figure.

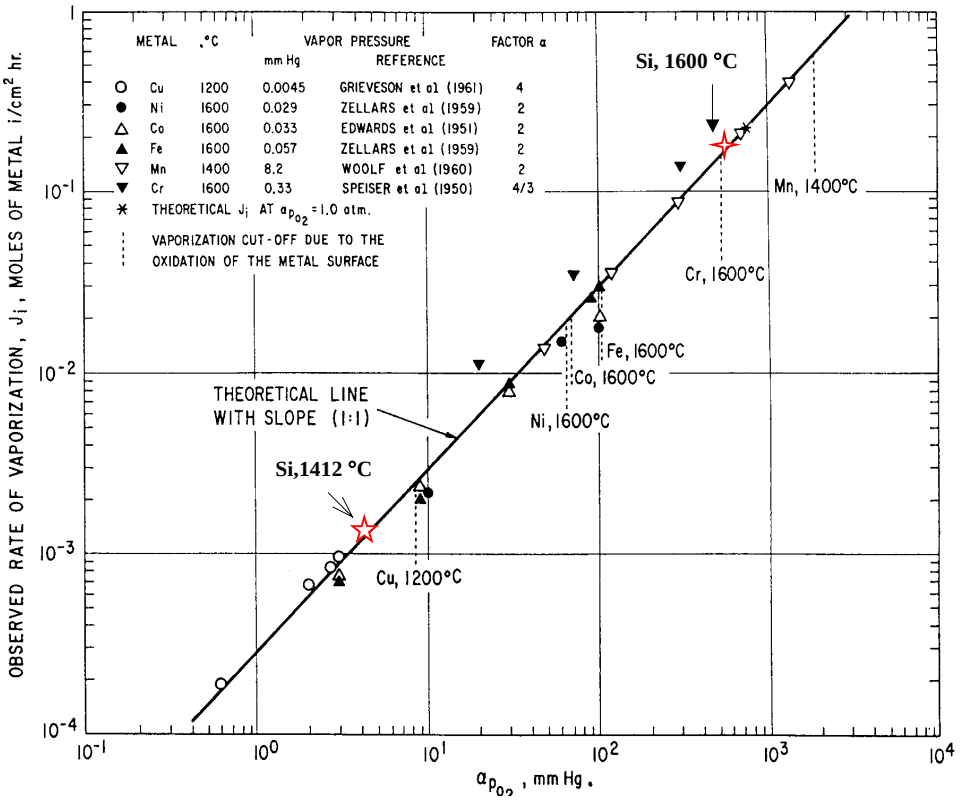

Figure 4.4 – Experimental verification of the theoretical equation (4.21), showing the rate of vaporization j_i as a function of oxygen partial pressure, αp_{O_2}, for gas (Ar+O_2) velocity v = 80 cm/sec.

4.4 Comparison of theoretical models

The Wagner approach of active oxidation has been used to rationalize the experimental observations of Kaiser *et.al.* (1957, 1958) for the active oxidation of liquid silicon. However, as Hinze (1976) points out, the approach of Turkdogan may be valid for certain temperatures and flow characteristics. Indeed, as shown in section 4.3, Turkdogan applied the model successfully to the enhanced vaporization of several metals. The evidence presented by Kaiser suggests that the Wagner model is valid for their experimental temperatures and gas-flow characteristics. Large concentrations of oxygen were found to be dissolved in the Si upon active oxidation; the concentration of dissolved oxygen being proportional to $p_{O_2}^{\circ}$. This could occur only if oxygen had access to the Si surface. In the Turkdogan model the oxidant is consumed in advance of the silicon surface. Therefore, if this model were valid, the Si should remain free of dissolved oxygen.

The basic differences between the model of Wagner and that of Turkdogan can be tabulated as shown in table 4.1.

Table 4.1. Comparison between Wagner`s and Turkdogan`s models for the oxidation of liquid silicon.

Wagner	**Turkdogan**
Assumes that the reaction takes place at the Si surface, according to the reaction: **$Si_{(l)}+O_{2\,(g)} = SiO_{(g)}$**	*Assumes that the reaction takes place within a boundary layer some distance from the surface, according to the reaction:* **$Si_{(g)}+O_{2\,(g)} = SiO_{2\,(s,l)}$**
Both models predict:	
A loss in metal weight due to oxidation	
An increase in weight loss with increasing P_{O2} in ambient gas up to a point where $P_{O_2}^{0}$(interface)=$P_{O_2}^{*}$(equilibrium)	
A maximum value for $P_{O_2}^{(trans)}$ *in the ambient gas when the transition from active to passive oxidation takes place*	
The models predict differently on the following:	
$P_{O_2}^{(trans)} = \frac{1}{2}\sqrt{\frac{D_{SiO}}{D_{O_2}}}P_{SiO(eq)}$	$P_{O_2}^{(trans)} = \frac{P_{Si}^{\circ}}{h_{Si}}\sqrt{\frac{RT}{2\pi M_{Si}}}$
Temperature dependency determined by $\Delta H_{formation}$ of $SiO_{(g)}$	*Temperature dependency determined by $\Delta H_{vaporization}$ of $Si_{(g)}$*

Hinze and Graham (1976) investigated the active oxidation of *solid* silicon in a range of diluted oxygen-argon mixtures at 1400-1650 °K. In particular, they wanted to locate the oxygen partial pressure where a transition from active to passive oxidation occurred.

Their experimental results revealed that the active oxidation of silicon occurred in two stages (I and II). The first stage is associated with a reduction in the sample-weight, in accordance with both models. However, during the second stage, an increase in the weight is observed characterized by a growth of SiO_2-whiskers at the surface. As the partial pressure of oxygen in the ambient gas is increased further, passivity finally takes place. The data obtained indicated that the oxidation reaction is controlled by oxygen diffusion through the gaseous boundary layer in both regimes.

Based on their findings, Hinze and Graham concluded that neither the Wagner model nor the Turkdogan model completely describes the mechanism of Si active oxidation. Although the Wagner model correctly identifies the nature of the gaseous species as SiO at the silicon surface, the existence of stage II active oxidation mode was not suggested. The Wagner model predicts that once the maximum partial oxygen pressure for active oxidation has been reached, the inward flux of oxygen (as O_2) at the Si surface will exceed the outward flux of oxygen (as SiO-gas) and that solid silica will form and grow laterally on the surface. The first part of this prediction was found to be correct, however, lateral growth was not exhibited. Instead, silica whiskers grew perpendicular to the Si surface, and only after a second critical $P_{O_2}^0$ was exceeded did the SiO_2 grow laterally to form a protective layer. Hinze and Graham gave a schematic explanation for the second stage of oxidation (see figure 4.5). When $P_{O_2}^0 < P_{O_2\,(\max)}^0$ (figure 4.5a), stage I active oxidation occurs and the silicon surface remains bare in agreement with the Wagner model. As the bulk partial oxygen pressure is increased, silica will form as the critical pressure (equation 4.5) is exceeded. Initially, the silica will form as tiny islands (figure 4.5b), with most of the surface remaining bare. The tendency for SiO_2 and SiO formation is equal from thermodynamic considerations; SiO-removal from the surface will continue as silica attempts to grow laterally to the surface. The SiO molecules will be exposed to as ever-increasing oxygen pressure as they diffuse away from the surface. Thus, these molecules have a tendency to oxidize forming SiO_2 according to reverse of reaction (4.6), that is,

$$2SiO_{(g)} + O_{2\,(g)} = 2SiO_{2\,(s)} \qquad (4.22)$$

The homogeneous reaction (4.22) is relatively unfavorable because it requires a trimolecular collision of two SiO-molecules and one O_2-molecule in the gas phase. However, the silica islands mentioned previously can serve as nucleation sites for heterogeneous reactions. Since the tip of the island is at a higher P_{O2} than the edges, the availability of oxygen is greatest there. Thus, the islands will grow perpendicular to the silicon surface to form the whiskers observed by Hinze and Graham.

According to the Wagner model, when the partial pressure of oxygen in the bulk gas exceeds a certain value (what Hinze and Graham refer to as $P^0_{O_2\,(\max)\,I}$), the inward flux of oxygen will be greater than the outward flux of SiO and the surface should become covered with a protective layer of silica. This was not found in the investigation by Hinze and Graham. Instead, active oxidation was found to continue independent of time with rates being linearly dependent upon $P^0_{O_2}$. The oxidation rates implied that oxygen transport through the boundary layer is rate-controlling and that oxygen has direct access to the surface. This indicates that the partial pressure of SiO at the surface must increase, or that the thickness of the boundary layer is decreased in order to keep the removal rate of SiO, given by equation (4.23), equal to the incoming flux of oxygen.

$$J_{SiO} = D_{SiO} P^*_{SiO} \Big/ \delta_{SiO} RT \tag{4.23}$$

Once SiO_2 is formed at the surface, P^*_{SiO} is fixed at its equilibrium value P^{eq}_{SiO} given by equation (4.1). Therefore, δ_{SiO} must decrease in order that J_{SiO} be maintained at a level that is sufficiently high to accommodate the inward flux of oxygen. Figure 4.5c shows the manner in which heterogeneous reactions at the tip of the whiskers reduce δ_{SiO}. This mechanism bears some resemblance to the Turkdogan model in that some oxygen is consumed in advance of the silicon surface, thereby increasing the diffusion gradient for the desorbed species. However, in this case the reaction occurs at the tip of the SiO_2 whiskers and enables their growth. By decreasing δ_{SiO}, J_{SiO} becomes increased according to equation (4.23). This allows active oxidation to continue until the oxygen pressure in the bulk gas reaches the cut-off pressure for active oxidation (the experimentally observed $P^0_{O_2\,(\max)II}$). Then, the SiO cannot be removed at a rate sufficiently rapid to avoid formation of a coherent, protective layer of SiO_2, see figure 4.5d.

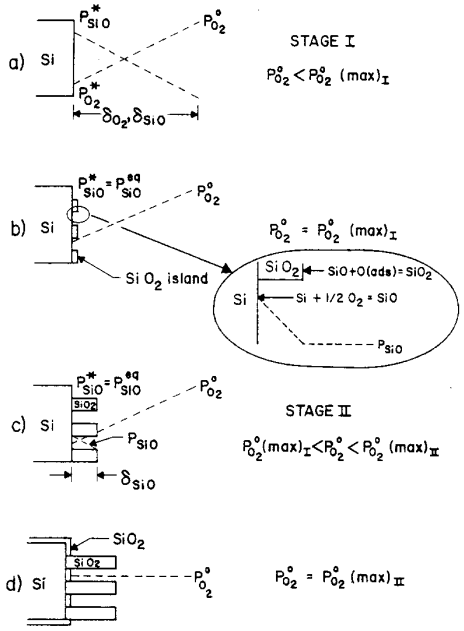

Figure 4.5 – Schematic representation of the mechanism of active oxidation of Si in the viscous gas-flow regime, after Hinze and Graham (1976).

Hinze and Graham also examined the temperature dependency of $P^{0}_{O_2\,(max)I}$ and $P^{0}_{O_2\,(max)II}$ and compared these to the theoretical values as obtained from the models of Wagner and Turkdogan, see figure 4.6. Since these models only predict one $P^{0}_{O_2\,(max)}$, only the lower pressure was calculated. They found that the predictions based on Wagner`s approach were in fair agreement with the experimental results for the transition from active to passive oxidation. The values predicted by Turkdogan were lower than the experimental data, suggesting that Si desorption from the surface during active oxidation is unimportant.

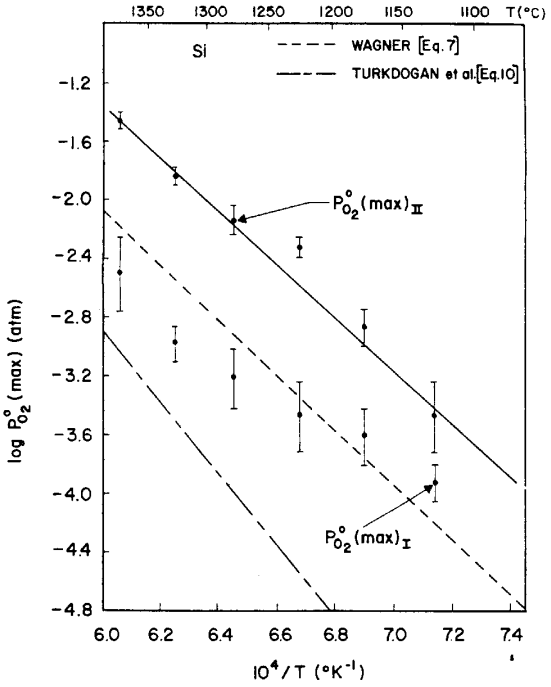

Figure 4.6 – Temperature dependence of $P^{0}_{O_2\,(max)I}$ and $P^{0}_{O_2\,(max)II}$ for silicon active oxidation in the viscous gas-flow regime compared with predictions based on the Wagner model and the Turkdogan *et.al.* model.

4.5 Extension of the Wagner approach

Recently, Ratto *et.al.* (2001) published work where they extended Wagner`s model to include condensation of oxides in the boundary gaseous layer. In this article, an extension of the Wagner theory has been applied for the analysis of oxidation conditions of materials when the gas surrounding the sample is highly reactive. As a limiting hypothesis, instantaneous reactions are assumed and subsequently local equilibrium of all oxidation reactions over the whole gaseous boundary layer. A fundamental result of this work is the derivation of the expression of the curves of the asymptotic behavior of the system. With these curves, it is possible to predict whether the system is under oxidizing or deoxidizing conditions. Two scenarios can occur. The first situation is when the gaseous layer remains homogeneous, i.e. no oxide reaches the saturation point in the layer. The expression for the asymptotic curve is then given by

$$(P^{0}_{O_2,\,\mathrm{eff}}) = P^{0}_{O_2} = P^{\sigma}_{O_2} + \sum_{j} \alpha_j \left|\Psi_{C_j}\right| K_{P_j} P^{s}_{Si} P^{\sigma^{\alpha_j}}_{O_2} = P^{\sigma}_{O_2,\,\mathrm{eff}} \qquad (4.24)$$

where σ indicates metal surface, *j* is an index for the oxides occurring in the system, α_j is a oxygen stoichiometric coefficient in the *j*th oxidation reaction, i.e. $\alpha_j O_2$ + Me = C_j, Ψ_{Cj} is a normalized diffusivity for the *j*th oxide and P is the partial pressure. Equation (4.24) can be seen as the generalized expression of the Wagner theory for any type of reactivity of metal vapors. It holds for both null and instantaneous reactions, as well for any intermediate situation, which is generally the case. On the other hand, when an oxide reaches saturation point inside the layer, the curves representing the asymptotic conditions diverge. In this case, the results obtained by Ratto *et.al.* indicate the region which any other possible asymptotic curve, representing an intermediate situation, can be placed.

This extension still needs experimental data for validation. However, in the limit, the model predicts the same results as the Wagner model. But when condensed oxides are present, the models diverge. Thus, the model may be a useful tool to analyze the kinetics during oxidation of liquid silicon.

5. STEAM EXPLOSION THEORY

5.1 Introduction

The steam explosion is a complex event, nonetheless, it can still be divided into different stages, which can be described in some detail. It is customary to separate the event in four different steps (Board *et.al.*, 1976):

a) The premixing stage (coarse mixing). When the two liquids first come into contact, the coolant starts to vaporize at the fuel-coolant interface, and forms a vapor layer. The heat transfer across this layer is relatively small. The system remains in this non-explosive, metastable state for periods up to a few seconds. During this time the fuel and coolant intermix due to velocity and density differences (e.g. Rayleigh-Taylor and Kelvin-Helmholtz instabilities), and the melt is fragmented into centimeter-scale pieces. Note that this stage is skipped in the granulation process, as the melt is already fragmented prior to water contact. Premixing is a necessary, but not sufficient criteria for a large-scale steam explosion.
b) The triggering stage. If the vapor film collapses in some small region, direct liquid-liquid contact takes place. This dramatically increases the heat transfer, thus vaporizing more coolant. The local pressure rises rapidly, and more fragmentation of the melt occurs.
c) The propagation stage. The local pressure pulse can cause further vapor film collapse, and can under favorable circumstances propagate through the mixture as it will form a shock wave. The effect of this shock wave is both to collapse more vapor film (triggering) and to initiate processes that can cause the melt droplets to fragment. This will again result in a large increase in the heat transfer. For a large-scale steam explosion to occur, this stage is essential to ensure that the energy transfer from the fuel to the coolant is fast enough to sustain the shock wave.
d) The expansion stage. The expanding mixture of vapor and fuel fragments has a potential to induce damage on surrounding structures. Slugs of water or melt driven by the later stages in the explosion event transfer kinetic energy to the structures, and this may cause damage. Also, the propagating shock wave itself can under the right circumstances (e.g. not too quickly relieved) be harmful to the surroundings.

It must be noted that this four-stage description was deduced from experiments in which the hot fuel was poured into the coolant (Berthoud, 2000). There are other contact modes as well, coolant can be poured into fuel, coolant can be injected under pressure into the hot liquid or coolant and fuel can be layered in a stratified mode of contact. Although the details of each of the four stages

may change with the contact mode, each would be present during the explosion (Corradini *et.al.*, 1988).

An important comment to the propagation stage is that in a steam explosion, the timescale for heat transfer is smaller than the timescale for pressure wave propagation. Therefore, the local raise in pressure forms a shock wave, which propagates spatially with a velocity that is greater than the speed of sound in the mixture ahead of the shock front.

5.2 Premixing stage

The concept of mixing is somewhat vague, but qualitatively it can be described as the condition where the fuel and the coolant liquids disperse within one another (Corradini *et.al.*, 1988). Two examples are shown in figure 5.1.

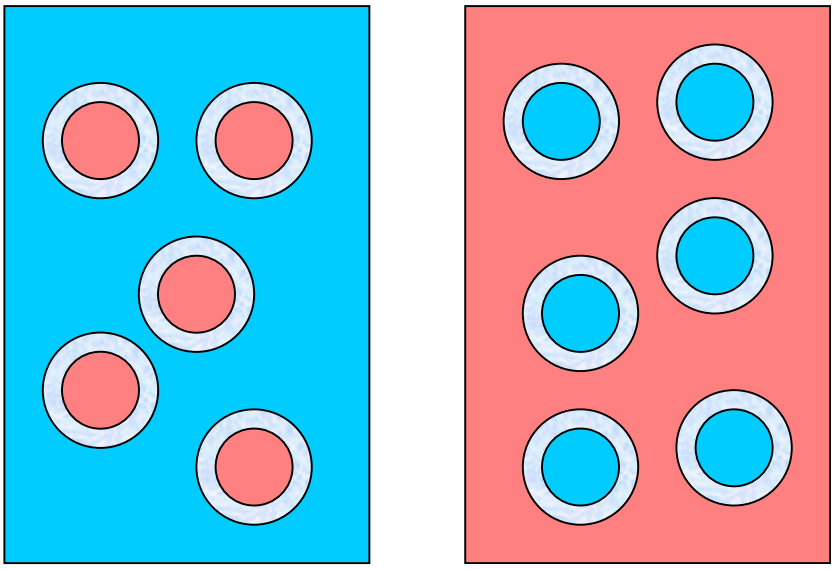

(a) Fuel within coolant liquid *(b) Coolant within fuel liquid*

Figure 5.1 – Two conceptual pictures of fuel-coolant mixing. A vapor film is separating the two different liquids.

The conceptual picture given in figure 5.1 a) applies to most of the different models suggested to describe premixing. During the mixing process the fuel-coolant system is in a non-explosive metastable state, and this allows for the fuel-coolant surface area to increase. Depending on the time the system is allowed to be in this metastable state, the subsequent explosion could become

more efficient. Past research in this field has focused on understanding the transient fluid dynamics and heat transfers between the liquids in the absence of an explosion, and on predicting the physical limits for which mixing can occur. Different reviews deal with this more in detail, i.e. Berthoud (2000), Corradini (1988), and Fletcher (1997). Some of the models will be presented here.

Cho *et.al.* (1976) showed that if tons of melt is to be converted into 100-μm particles, some initial coarse mixing must take place. They considered a situation where fuel is poured into a coolant, and the energy required to fragment and mix a volume V_c of fuel into fragments of size R_c, based on the scheme illustrated in figure 5.2.

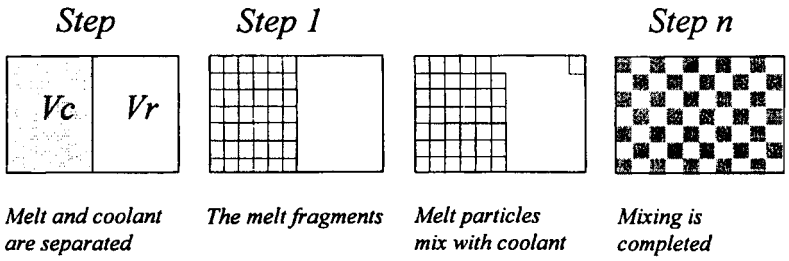

Figure 5.2 – Steps in premixing in the approach of Cho *et.al.* (1976).

They evaluated the energy E_s required to create the surface of the particles, the kinetic energy E_c required to displace the particles and the energy E_f required to overcome the drag during particle displacement. Of these three, the latter is the major contributor to the mixing energy, and the other two may be neglected. E_f is then given by

$$E_f = \frac{3}{8} \cdot C_D \cdot \frac{\rho V_f^2}{t_m^2 R_f} \tag{5.1}$$

where

V_f = initial volume of the fuel mass to be mixed
ρ = average density of the surrounding fuel
t_m = mixing time
C_D = local drag coefficient
R_f = final radius of the fuel after mixing has occurred.

Then Cho and his coworkers showed that it is impossible to get a steam explosion in a single step, that is, by going from step 0 to the final step (R_f = ~ 100 μm) in a time characteristic of an explosion, that is, t_m= ~ 1 ms because

the energy to fragment and mix is larger than the thermal energy of the melt. But if we have a premixing phase in which 1-cm fragments are produced in a 1-s time scale, followed by an explosion phase in which 100-μm fragments are produced in a millisecond scale, the fuel fragmentation energies are far smaller than the thermal one.

The model assumes that the density of the coolant (liquid and vapor) remained constant through the mixing process, and that there was some prior knowledge of initial fuel size and its final size after mixing. The model was the first attempt to quantitatively estimate the energy requirements for mixing, so the assumptions seem reasonable. However, the assumptions were debated. Baines *et.al.* (1980) showed that if the large mass of fuel moves and particles are stripped from it, less energy is required than the progressive mixing process proposed by Cho *et.al.* (1976). Nevertheless, their work clearly indicated that some sort of premixing was needed if a large mass of melt is to be involved in a coherent explosion, as pointed out by Fletcher *et.al.* (1997).

Henry and Fauske (1981) were the first workers to introduce the concept of the water depletion phenomenon. They proposed that for the fuel to exist in a premixed configuration with the coolant, the conceptual picture of figure 5.1 a) must be achieved and sustained. If this situation breaks down, one would revert to a situation where fuel and coolant droplets are in a continuum of vapor as the vapor drives the coolant away from the molten fuel by fluidization. Discrete fuel particles would coalesce into larger particles and reverse the fragmentation-mixing process. Their model was, however, very simplified, and it was criticized based on the fact that mixing is an unsteady, multidimensional process, not steady and one-dimensional. Nevertheless, other workers pursued their idea of fluidization limits.

5.3 The triggering stage

Triggering is the event that initiates the rapid, local heat transfer and pressure rise that is necessary if a propagating wave is to develop. This wave will transfer heat from the melt to the water in a very quick way. The triggering is associated with a local collapse of the protective vapor film around a drop of melt. This is suggested by experimental observations performed by Sallach *et.al.* (1984) and Dufresne (1988). The vapor film collapse may occur for two different reasons.

1) *The melt surface temperature drops below the minimum film boiling temperature.*
2) *Water is forced into contact with the melt.*

If the surface temperature of the melt drops too low, the heat transfer is not high enough to sustain the film boiling. This minimum surface temperature is called the Leidenfrost point. Below this temperature, the boiling will be in the transient region, a very turbulent region were patches of vapor are detached from the surface and water gets in direct contact with the molten material. This mode of vapor film collapse often occurs in situations where low-melting materials (i.e. tin-water) are used. However, this kind of collapse is not very relevant during granulation of Si/FeSi, due to the high temperature of the melt (~1600 °C). A frozen shell will form a long time before the interface temperature reach levels comparable to the Leidenfrost temperature, which effectively would prevent direct liquid-liquid contact upon film collapse.

The film may collapse because of water being forced into contact with the melt. An applied pressure pulse could cause this. This is the usual way of triggering an explosion in experiments, and also the method used in the UWM-experiments. The pressure pulse induces a particle velocity in the coolant, towards the melt, at the liquid-vapor interface. Triggering occurs if this motion is enough to drive the water to the melt, thereby obtaining direct melt-water contact. Also, a bulk flow of water past a drop can cause the film to be convected away from the melt, thus inducing a film collapse. This mechanism is likely to be important in situations where the vapor film is thin. This could be when the water is subcooled or the melt temperature low. Also, entrapment of water under the melt, i.e. against a container wall will cause the water to heat up. If the water is heated to its homogeneous nucleation temperature, it will flash into steam, thereby throwing melt around and force melt-water contact.

One may divide steam explosions into two categories, spontaneous and triggered explosions. Some molten materials explode spontaneously when released into water, i.e. Sn, Pb and Bi, while drops of other melts fall benignly through the water and freeze without fragmentation or other violent interactions, i.e. Fe, Al, Al-Li alloys and FeO_x. Differences between the abilities of various melts to explode spontaneously often occur even though the respective temperatures of both melt and water may lie in the same ranges. When the drops of melt do not explode spontaneously, explosions can be triggered in many cases by introducing pressure disturbances into the water (Nelson *et.al.*, 1999b). Several techniques have been developed for generating pressure transients in water for triggering steam explosions. These include application of mechanical impacts to the walls or bottom of the water chamber (Peppler *et.al.* 1986; Kim *et.al.* 1984; Schins 1986; Epstein *et.al.* 1987), the use of shock tubes (Sharon *et.al.* 1981), underwater electrical discharges (Nelson *et.al.* 1981, 1982, 1983, 1985; Nelson 1995; Arakeri *et.al.* 1978;

Kondo *et.al.* 1976; Anderson *et.al.* 1981; Ciccarelli *et.al.* 1994), chemically enhanced electrical discharges (Nelson *et.al.* 1999c) and the underwater detonation of small amounts of high explosives (Ciccarelli *et.al.* 1994).

It is emphasized that the stability of the vapor film is the key component when examining the trigger requirements. If the system is very stable, a strong trigger is needed. On the other hand, a marginally stable configuration can be triggered quite easily, or maybe just by the system's own fluctuations (spontaneous explosion).

5.3.1 Theoretical models

Most models are based on a one-dimensional geometry, typical as shown in figure 5.3.

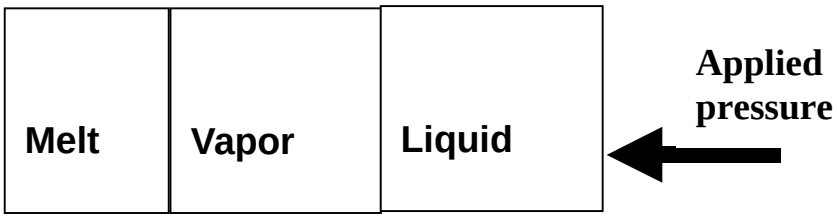

Figure 5.3 – Typical geometry for theoretical trigger models.

It is assumed that a steady-state film boiling is established before the pressure wave arrives at the interface. Conservation equations for mass, momentum and energy are then used to model the development of the system. The models generally differ in complexity of the equation system used and the different processes modeled.

The earliest model appears to be that of Drumheller (1979). He considered the symmetric collapse of film boiling around a sphere. This assumption is questionable, as the pressure pulse needs a finite time to pass the sphere. He also considered the liquid to be incompressible, and used energy considerations to derive an equation similar to Rayleigh`s classical bubble collapse equation. However, no experimental data were provided for comparison with the model.

The model of Inoue *et.al.* (1981) was the first detailed model to be developed that was compared to an experiment (collapse of Freon 113 vapor film). They used a full non-equilibrium model of evaporation and condensation at the liquid-vapor interface, and modeled a Knudsen layer at the melt-vapor

interface. A quadratic temperature dependence of the distance from the vapor-liquid interface was assumed, and the heat equation in the moving melt slug was solved. To determine the motion of the liquid, they used a Newtonian of the slug dynamics. Their results showed the importance of choosing the evaporation-condensation accommodation coefficient correctly. The calculated response of the system, with an applied pressure pulse, was either total collapse of the film or oscillation of the film thickness. Total collapse was judged to have occurred when the film thickness was of the same size as the surface roughness. During the film oscillation, the pressure in the film rose enough to prevent a collapse, pushing the slug away.

Inoue *et.al.* (1982) extended this model to allow for mass flow out of the film. The study showed that pressure pulses with steep fronts (shocks) were more effective at collapsing the vapor film than slow pressure rises. It was also noted that the collapse behavior was very sensitive to changes in ambient pressure.

Corradini (1983) performed a similar analysis. He also examined the effect of different mass transfer assumptions and came to the same conclusions as Inoue (1981). He concluded that the equilibrium model was valid for shock rise times greater than 100 μm.

Knowles (1985) developed a one-dimensional model based on similar assumptions to those of Inoue (1982) and Corradini (1983). His model used a more rigorous treatment of the slug dynamics and heat transfer into the vapor layer. He solved mass and momentum equations in the liquid slug, taking into account the compressibility of the slug, and thereby the detailed behavior of the incident pressure pulse could be modeled. He also solved a finite difference form of the conduction equation in the liquid layer and the melt, rather than assuming given temperature profiles. Equations from kinetic theory were used to simulate evaporation/condensation processes. The kinetic theory equations were modified to allow for the net velocity of the interface, and the pressure and temperature dependence of thermophysical properties was included. He suggested the following criterion for collapse, which was based on observations of simulated triggered collapse of low-pressure films around low temperature surfaces:

$$\tau_p > \frac{\delta \rho c}{p_{trig}} \tag{5.2}$$

where τ_p is the duration of the trigger pulse, δ is the initial vapor thickness, p_{trig} is the trigger pressure, ρ is the slug fluid density and c is the sound speed in

the slug. Equation (5.2) tells us that if the particle velocity of the liquid at the slug-vapor interface multiplied by the duration of the pressure pulse is greater than the thickness of the vapor film, collapse will occur. It applies when film collapse is essentially unresisted. Attempts to apply this model at high pressures were unsuccessful. Knowles attributed this to the development of a metastable phase in the vapor phase during collapse. At higher temperatures, stability was maintained by evaporation from the advancing slug.

In his review, Fletcher (1994) concludes that it is fair to say that even if a number of models have been developed, none of them are validated and they cannot be used with confidence to predict limits on triggerability. Usually, they are difficult to apply in any real situation because of uncertainties in the initial vapor film thickness and the geometry, and the poor knowledge of the trigger characteristics. Model predictions indicate that triggering becomes more difficult at higher pressures and for higher melt temperatures. As the pressure increases, the vapor mass and energy densities increases and the latent heat of vaporization decreases, so that it becomes more difficult to compress the film, more difficult to condense the vapor and easier to evaporate the leading edge of the water slug. This has, however, not been fully quantified for realistic vapor geometries.

5.3.2 Triggering experiments

The earliest experiments on film boiling collapse were mainly studies of a Leidenfrost drop on a heated surface (solid-liquid interface). These were of qualitative character, and are described by Naylor (1985).

As mentioned, Inoue and Bankoff (1981a) did an experimental survey related to a theoretical one (Inoue, 1981b). In their experiments, they examined the triggered collapse of film boiling of Freon 113 or ethanol on an electrically heated nickel tube using a pressure step. The magnitude of the pressure rise varied between 0.1 MPa and 0.5 MPa, and the rise time of the pulse was varied between 80 μs and 344 ms. It was observed vapor film collapse when the pressure step had a magnitude greater than three times the ambient pressure and a rise time less than 150 ms.

Nelson and Duda performed a number of single droplet experiments at the Sandia National Laboratories (SNL). The experiments involved the release of small droplets of various melts, i.e. stainless steel, metallic corium and oxide corium, into water. They triggering behavior of the system was studied for different melt compositions, water temperatures and ambient pressures.

Corradini (1981) analyzed their data, and he came to the following conclusions:

- *Increasing the trigger magnitude can result in an explosion for a case in which an explosion did not occur for a weaker trigger.*
- *Explosions were suppressed at higher water temperatures and high ambient pressures because of the increased vapor film stability.*
- *Certain melt compositions did not lead to explosions, and this could be explained by the presence of noncondensable gases, particularly hydrogen in the case of metallic melts.*

The last point is also very clearly illustrated in the paper by Akiyoshi *et.al.* (1990), who studied the different fragmentation behavior of droplets falling through air or steam. They observed that when the space above the pool of water was filled with steam instead of an air-steam mixture, explosions were more likely to occur. The presence of noncondensable gas in the vapor film made affected the vapor explosion greatly and made the process stochastic.

5.3.3 Effect of pressure

Several experiments have been performed in order to investigate the effect of increased ambient pressure on a steam explosion. Work performed at JRC Ispra (Henry *et.al.*, 1979) with molten salt released into the water, showed that explosive interactions were obtained at an ambient pressure, but no explosions were obtained at elevated pressures (0.5, 1, 2 and 4 MPa). At elevated pressures, different triggers were used (Hohmann, 1982). It was not observed any explosions for ambient pressures above 3 MPa. The results indicate that spontaneous interactions are inhibited by increased pressure, and that a stronger trigger is necessary to initiate an explosion at pressures above 3 MPa. However, this cannot be generalized to other systems, as pointed out by Fletcher (1994).

5.3.4 The importance of subcooling

As mentioned earlier, the vapor film may collapse if the heating surface temperature falls below the Leidenfrost point. It is known that the Leidenfrost temperature depends on several parameters; thermophysical properties of the fuel and coolant, surface roughness, oxide layers, but most important is the degree of subcooling (Bergstrøm, 1994). The quenching of spheres of steel, copper and silver was investigated by Dhir and Purohit (1978) (see also section 2.3.3). They observed that the sphere surface temperature at which the vapor film collapsed increased with subcooling, but was independent of flow

velocity. Due to data scattering, they concluded that the thermophysical properties of the sphere were unimportant, as long as the sphere surface was smooth and relatively clean. However, if the sphere was oxidized or had surface pits or protrusions, a premature contact of the liquid with the sphere surface was seen to occur. Based on their data, they suggested the following correlation:

$$\Delta T_{\min} = 101 + 8\Delta T_{sub} \quad , [°K] \tag{5.3}$$

where ΔT_{min} is the minimum difference between the sphere surface temperature and the saturation temperature of the liquid. It is noted that a smaller degree of subcooling reduces this difference, making the system more stable, i.e. the minimum surface temperature of the sphere to sustain film boiling decreases.

5.3.5 Methods to prevent triggering

Since one started to be aware of the hazards a steam explosion could involve, measures have been take to avoid accidents in industrial applications, sometimes without necessarily understanding why or how they work.

The first work in this field was done by Long (1957), who performed a classic study of aluminum explosions. He poured molten aluminum into a tank of water and observed the following:

- *If the melt was prefragmented prior to the contact with water, it was less likely to explode than if it was released as a coherent mass.*
- *Coating the base of the container with lime or gypsum or allowing it to rust led to explosions in situations where explosions did not occur if the vessel base was made of uncoated degreased steel. Conversely, explosions did not occur if the base of the vessel was coated with grease or oil. The effect of greasing the base is to change the wetability of the surface, decreasing the chance that water can be entrapped under the melt.*

Nelson *et al.* (1988) developed this work further. They examined the effect of a large number of surface finishes and have correlated the explosivity with the wetability of the surface by the coolant. They also postulated that not only does good wetting cause a thin film of water to be entrapped under the melt, but it also promotes superheating of the water since nucleation is suppressed. This assumes that the melt is separated from the water with a vapor film, and this film must then be collapsed in order for superheating to occur.

It has also been found experimentally that increasing the viscosity of the cold liquid can suppress or prevent vapor explosions. The earliest discoveries were done by Flory *et.al.* (1969), who observed that increasing the viscosity of water by about five times using carboxymethlcellulose caused the fragmentation of lead, tin and bismuth to be greatly reduced or totally prevented.

Nelson and Guay (1986) performed several experiments on the effect of increased viscosity of water when drops of molten tin or iron-alumina melt where released into water. They increased the viscosity using glycerol or cellulose gum. Using a 50-kg scale test, they found that molten iron-alumina did not explode when dropped into a cellulose gum solution, whereas similar tests with untreated water had an explosive behavior. They believed the increased viscosity prevents small water-jets to penetrate the melt after a film collapse, consequently preventing rapid fragmentation. It was also noted that the increased viscosity caused more air to be entrained in the vapor film, and as mentioned earlier, this has a stabilizing effect on the film. For the molten tin, they found that tin exploded spontaneously when dropped into water alone. When they increased the viscosity, no spontaneous explosions occurred if the viscosity was over 0.015 Pa*s.

Experiments by Kim *et.al.* (1989) using an iron oxide melt used an external trigger to initiate a steam explosion. They varied the water viscosity between 0.04 and 0.24 Pa*s by adding cellulose gum to the water. Increasing the viscosity reduced the likelihood of an explosion to occur.

Another investigation was done by workers at the Georgia Institute of Technology, where they looked at the effect of surfactants on the spontaneous interaction of tin droplets (at 1073 °K) dropped into water (Kowal *et.al.,* 1993; Skelton *et.al.,* 1995). A variety of surface reactants were used and were found to reduce the peak pressure (to about 65 % of that observed with pure water) of the explosions that occurred. Experiments using dilute solutions of the aqueous polymer polyethylene oxide showed that if the viscosity was increased by 2-13 %, the observed pressures resulting from the interactions actually increased, while if the viscosity was increased further, the occurrence of spontaneous explosions was reduced (Dowling *et.al.*, 1993). When the viscosity was increased by a factor two, no spontaneous explosions occurred. This indicates that there are competing factors that are not understood yet.

The previous cited investigations highlight the sensitivity of the triggering process to the coolant and vessel properties. There is much anecdotal evidence (Becker, 1991) that additives are routinely used in some metal preparations

processes to prevent explosions, but the documentation of these procedures is sparse.

5.4 Large-scale explosion propagation and expansion: Main theories

In order to explain large-scale vapor explosion behavior, two major theoretical hypotheses have been proposed. The first one is formulated by Fauske (1974) and known as the *Spontaneous Nucleation Theory*. It aims to identify explosivity thresholds, and thus contains a set of necessary conditions for a large-scale vapor explosion to occur. The other one is formulated by Board *et.al.* (1975), and it is known as the *Thermal detonation theory*, and focuses on the explosion propagation based originally upon purely hydrodynamic fragmentation behind the shock front. Due to their historical importance, both of these theories will be examined in some detail in the following sections.

5.4.1 Spontaneous nucleation theory

Spontaneous nucleation is a nucleation mechanism by which critical size vapor or cavities are formed as a result of molecular density fluctuations. These take place in a bulk liquid or at any preexisting liquid-vapor or liquid-gas interfaces. In his model, Fauske (1974) proposed a vapor explosion hypothesis as a set of criteria in which spontaneous nucleation was the plausible mechanism for explosive vapor formation given molten fuel and coolant in liquid-liquid contact. To better understand these criteria, let us refresh some fundamental concepts. The contact interface temperature of two semi-infinite masses at initially different temperatures with constant properties is (Carslaw *et.al.*, 1959):

$$T_I = \frac{T_H (k/a_t)_H + T_C (k/a_t)_C}{(k/a_t)_H + (k/a_t)_C} \tag{5.4}$$

where: T = temperature
k = thermal conductivity
a_t = thermal diffusivity
H = hot liquid fuel
C = cold liquid coolant

The next concept to remember, is the nucleation of vapor bubbles inside a bulk liquid. When a liquid is heated above its saturation temperature for the given ambient pressure, it can be said to exist in a metastable state. The liquid is

stable to small thermodynamic fluctuations, but if a sufficiently large perturbation occurs, it will partially vaporize. In order to form a vapor cavity in a bulk liquid, work must be done to overcome surface tension forces, which seek to collapse the bubble, and to expand the bubble against an outer pressure. The vapor nucleus will grow if it is larger than a critical sized nucleus, otherwise it will collapse. The critical size nucleus is such that (Corradini *et.al.*, 1988):

$$P_g - P_c = \frac{2\sigma}{r_{crit}} \tag{5.5}$$

where P_g is the vapor pressure inside the vapor nucleus and P_c the imposed liquid pressure corresponding to a saturation temperature T_{sat}. Thus, the bubble is unstable and collapses for $r < r_{crit}$, or grows for $r > r_{crit}$, given the internal bubble pressure P_g.

The reversible work for nucleation required to form this spherical vapor bubble nucleus in the bulk liquid is given as

$$W = 4\pi r_{crit}^2 \sigma - \frac{4}{3}\pi r_{crit}^3 (P_c - P_g) \tag{5.6}$$

In a state of mechanical equilibrium, this work is expressed as (combining with (3)):

$$W_{eq} = \frac{16\pi\sigma^3}{3(P_g - P_c)^2} \tag{5.7}$$

Finally, the rate of bubble nucleation is given from kinetic theory as

$$J = wNe^{-W_{eq}/k_B T} \tag{5.8}$$

where *N* is a constant approximately equal to the number of molecules per unit volume ($N=10^{22}$ cm^{-3}), w is the collision frequency of the liquid molecules and is a function of temperature with a value nearly constant (10^{10} s^{-1}). The predicted nucleation rate is extremely sensitive to temperature variations. A change in temperature within a couple of degrees changes the bubble formation rate many orders of magnitude. When J exceeds a specific nucleation rate, $J>10^{10}$, the liquid is said to reverse its state. The associated temperature T_{hn} is called *the homogeneous nucleation temperature* or *the superheat limit*. For water, this temperature is approximately 310 °C. The

above superheat limit applies to nucleation in the bulk of the fluid. As a good approximation, the value of T_{hn} is given by (Reid, 1983):

$$T_{hn} = T_{crit}(0.11(p / p_{crit}) + 0.89) \tag{5.9}$$

where the subscript "crit" denotes the value at the critical point.

If the nucleation takes place on an interface between two liquids, the required work to form a bubble can be decreased because of imperfect wetting, i.e. the nucleation temperature is reduced, and is denoted *the spontaneous nucleation temperature* T_{sn}. If complete surface wetting takes place (contact angle = 0°), $T_{hn} = T_{sn}$. The other extreme is no wetting at all (contact angle = 180 °), giving $T_{sn} = T_{sat}$.

Based on the above concepts, Fauske (1974) proposed that for a large-scale steam explosion to occur, the following criteria must be satisfied:

1. *A vapor layer must separate the two fluids from each other, so that film boiling is preventing excessive heat transfer, thus permitting coarse premixing.*
2. *There must be direct liquid-liquid contact due to vapor film collapse to allow rapid heat energy transfer.*
3. *Explosive boiling immediately upon contact, implying that the interfacial temperature must exceed the spontaneous nucleation temperature upon initial contact, causing rapid fragmentation and mixing of both the hot and the cold fluid without time delay.*
4. *Adequate inertial constraint to sustain a shock wave on a time scale required for a large-scale explosion.*

These conditions provided the first conceptual picture of a steam explosion. However, it is not a complete model, and it is difficult to assess the model to practical problems. Henry and Miyazaki (1978) and Henry and Fauske (1979) developed the concept into a mechanistic model. This model is known as *the Droplet Capture model*, and is restricted to a pouring mode of contact and a well-wetted system. This model predicts that explosions are eliminated by elevated pressure (0.9 MPa for water) or a supercritical interfacial contact temperature. The first prediction has some support from experimental work, but criticism has been raised against the model itself. Corradini (1988) discusses these issues in his review, and we will not go into details on the criticism here.

5.4.2 Thermal detonation model

This model was proposed by Board and Hall (1974a, 1975), based on the experimental observations from a tin-water system (Board, 1974b). They proposed an analogy between a chemical detonation and a vapor explosion, and their model has been the framework for most of the ongoing work in the modeling of steam explosions.

The classical picture of a chemical detonation (Yuen and Theofanous, 1999, Angelini *et.al.*, 1994) (steady state, 1D) is a shock wave that passes through a homogeneous mixture of chemical reactants. Due to the adiabatic compression across the shock wave, the temperature increases rapidly, leading to extremely fast chemical reactions. The chemical energy released generates high pressures, thus maintaining steady propagation of the shock wave through the reactants. The chemical reaction is essentially complete in a narrow zone immediately behind the shock front, as measured from experiments.

Using this analogy for a mixture of fuel and coolant, Board *et.al.* (1974a, 1975) proposed that a propagating shock wave causes fragmentation and mixing of the two fluids, leading to transfer of thermal energy from the hot liquid to the cold volatile liquid. This produces high pressures, which drive the shock forward. Across the shock front, a jump in interfacial area and a collapse of the vapor film surrounding the hot liquid leads to a rapid thermal energy transfer. In a narrow zone immediately behind the shock front, the two liquids reach thermal and mechanical equilibrium. The last assumption meant that the detailed complexities of the fragmentation, mixing, and heat transfer processes can be ignored, thus, the thermal detonation model is based on only two states: the initially separated liquids and the final completely mixed equilibrium condition.

Corradini (1988) points out that this model is fundamentally different from Fauske's approach, but the models are not necessarily mutually exclusive, and one may actually complement the other. In particular, the spontaneous nucleation concept is quite useful as part of an explanation of triggering and explosion escalation, while hydrodynamic fuel fragmentation may become dominant once the explosion has escalated to a steady-state explosion front.

In the thermal detonation model, we assume a long tube containing water and vapor film blanketing molten fuel droplets (coarse premixture), see figure 5.4. Then, consider a shock wave propagating through this mixture at a steady velocity. If we take the shock front as the frame of reference, the basic equations for the conservation of mass, momentum and energy for the homogeneous mixture of liquid coolant, vapor coolant and fuel become

$$u_1\rho_1 = u_2\rho_2 \equiv j \tag{5.10}$$

$$P_1 + \rho_1 u_1^2 = P_2 + \rho_2 u_2^2 \tag{5.11}$$

$$h_1 + \frac{1}{2}u_1^2 = h_2 + \frac{1}{2}u_2^2 \tag{5.12}$$

where ρ is the density, u the velocity and h is the enthalpy. 1 denotes the conditions for the initial mixture, 2 denotes the conditions after the shock front has passed. By combining equation (5.11) and (5.12), we obtain (noting that V=1/ρ)

$$\frac{1}{2}(P_1 + P_2)(V_1 + V_2) = h_2 - h_1 \tag{5.13}$$

which provides a thermodynamic relationship between the initial conditions and all possible end-states. Given an equation of state for the reacted material, equation (5.13) gives the locus of all possible end-states on a P-V diagram and is known as the Hugoniot curve or the shock adiabatic curve. Figure 5.5 shows a typical P-V diagram.

For a specific set of initial conditions, there is only one equilibrium final state (point C in figure 5.5) for the material behind the front that ensures that the explosion is both stable and self-sustaining. In this state the velocity of the material leaving the front is just sonic (Mach No. = 1) with respect to the front. This is called the Chapman-Jouguet condition corresponding to tangency of the Rayleigh line and the equilibrium Hugoniot curve. To locate the Rayleigh line, we combine equation (5.10) and (5.11) and obtain:

$$\rho_1 u_1 = j = \sqrt{\frac{(P_2 - P_1)}{(V_1 - V_2)}} \tag{5.14}$$

As j is a constant, a simple linear relationship exists between P_2 and V_2, and all possible end-states must lie on a straight line (the Rayleigh line) through point O, with a slope determined by the mass flux through the front. Also, equation (5.14) shows that the region A-B of the detonation adiabatic is unphysical because it implies an imaginary mass flux.

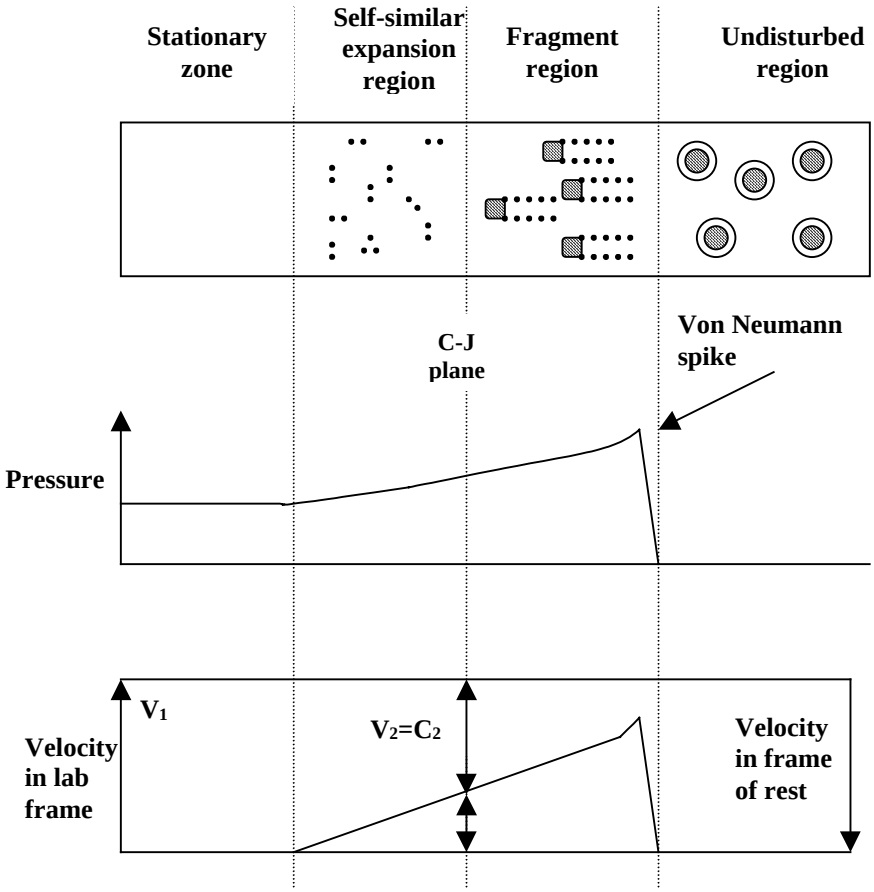

Figure 5.4 – The conceptual picture employed in the Board-Hall model. The figure shows the physical picture on which the model is based (top) and the pressure (middle) and velocity (bottom) fields within the interaction zone.

Board considered that if a strong shock front progresses steadily through the material, then close to the front the relative velocities between the fluids might be sufficient to cause fine fragmentation of the hot material and hence rapid heat transfer. The front leaves behind a mixture in thermal equilibrium at high pressure, and subsequent expansion of this material will drive the front forward.

Returning to figure 5.5, we can now explain the shape of the pressure profile. Initially the pressure rises up to point N on the shock adiabatic as material entering the front is compressed without any “reaction” taking place. The peak pressure point is known as the Von Neumann spike. The pressure then falls, as the reaction takes place, until the pressure reaches point C on the P-V diagram.

At this point the steady state reaction zone is connected to a time-dependent expansion zone. The pressure falls in the expansion zone in a manner determined by the far-field conditions.

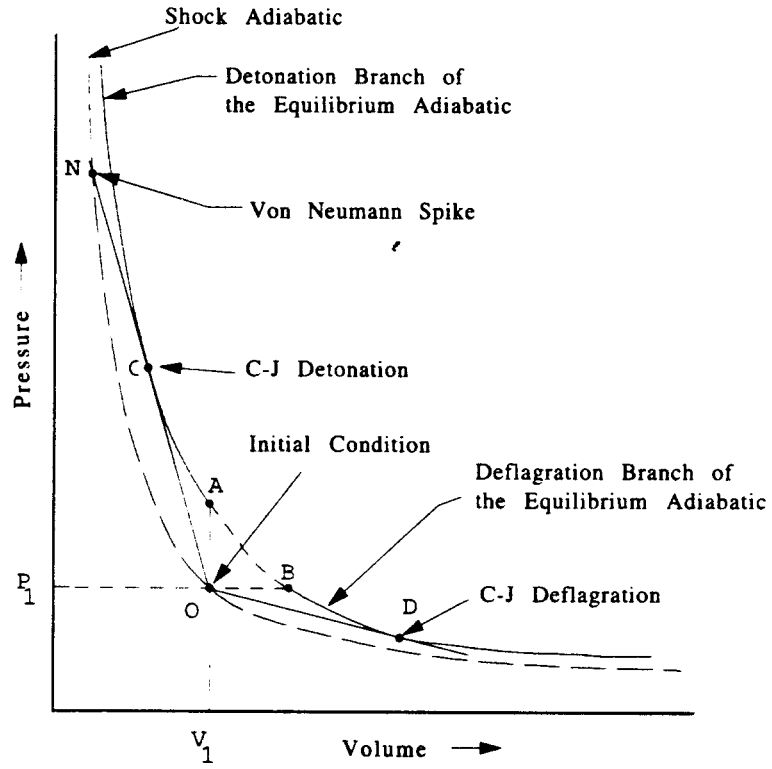

Figure 5.5 – The detonation trajectory in the PV-plane.

Board assumed certain physical mechanisms by which hydrodynamic fragmentation could be produced by (A) the complete collapse of vapor blanketing the fuel and (B) fragmentation due to Kelvin-Helmholtz instabilities and boundary layer stripping which occur because of the differing velocities between the fuel and the coolant materials as the shock wave passes.

Board and Hall used equation (5.10-5.12) to determine the C-J state for the tin-water system. For a mixture consisting of equal volumes of tin at 1000 °C, water, and steam, they showed that the C-J pressure was of the order of 1000 MPa and the propagation velocity was ~300 m/s. They also noted that if there was little or no vapor present initially the pressures would be much higher. Using the fragmentation correlation of Simpkins *et.al.* (1972), they showed that tin droplets with an initial diameter of 10 mm would be fragmented into micron-size particles in a timescale of ~200 μs, giving a "combustion zone"

thickness of ~100 mm. In addition, they predicted that pressures of the order of 1500 MPa could occur in the UO_2-Na system.

The thermal detonation model is only applicable to situations where the energy transfer from the fuel to the coolant is complete. Also, the propagating front must be one-dimensional. The existence of a homogeneous mixture ahead of the front is also an essential part of the model.

This model became very important for future work, as it provided a conceptual picture of the vapor explosion. However, it became evident that it was far from the complete picture. Different critics were issued; both based on experimental observations and theoretical considerations. These critics are discussed in detail in the reviews of Corradini (1988) and Fletcher (1997).

Recently, Yuen *et.al.* (1999) published work which discusses a major problem of the thermal detonation model. They analyzed the tin-water example discussed previously, and applied the model to a complete range of premixture void fractions (defined as the fractional volume of the whole coolant space occupied by vapor) to obtain the C-J pressures shown in figure 5.6. They also included different melt volume fractions: 5, 10, 20 and 50 %. Based on their results, the following trends can be discerned:

- "Lean" premixtures cannot detonate, to supercritical pressures (above the thermodynamic critical value, ~180 bar for water vapor), unless the premixture void fraction is very close to zero. Such low void fractions are not physically possible in premixtures of any significant size.
- "Lean" premixtures can yield weak propagations at the very high end of the void fraction scale.
- "Rich" premixtures can detonate, under most void fractions, but produce only weak propagations (i.e. not highly supercritical) at the very high end of the void fraction scale. However, this (high end) is precisely where rich premixtures of any significant size would find themselves physically, due to heat transfer (film boiling and radiation) during premixing.

In particular, the premixture specification chosen by Board *et.al* (1974b) (the tin-water example), i.e. rich in fuel, is on the one hand necessary to produce a supercritical detonation, but on the other hand it is justifiably open to criticism as physically impossible, shown experimentally by Angelini *et.al.* (1994, 1997) and analytically (Theofanous *et.al.* 1998; Fletcher *et.al.* 1991). The model predicts that explosions cannot propagate unless, in addition to rich premixtures, unreasonably high fragmentation rates are assumed. Nonetheless, the principles of the Board and Hall model have been used in numerous transient multifield models aiming to describe the process. Obviously,

experiments verifying the validity of such numerical models are necessary. In this work, we have concentrated on providing accurate experimental data, which in turn may be applied to a computer simulation.

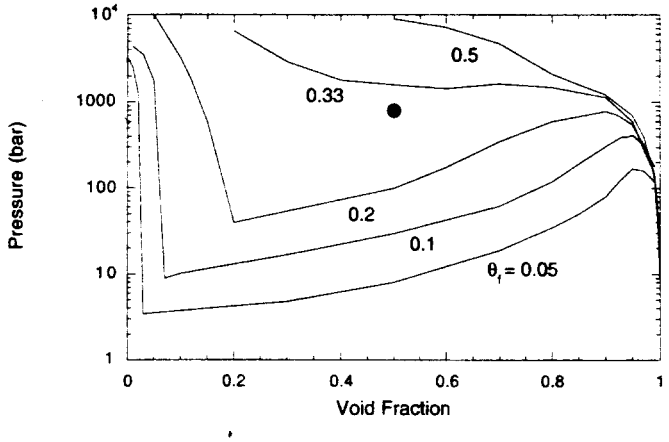

Figure 5.6 – The C-J pressures obtained according to Board and Hall model for 1500 °C tin premixtures in water. The parameter θ_f is the tin volume.

6. OXIDATION EXPERIMENTS – APPARATUS DESCRIPTION

The experimental apparatus has originally been developed as student project works: Bjerknes (1997) and Morsund (1998).

6.1 Experimental apparatus

To oxidize small samples of metal, a simple apparatus has been developed. This apparatus allows us to rapidly heat a sample of metal in an inert atmosphere to the desired oxidation temperature. When the melt has reached the pre-determined temperature, we want to expose the surface of the molten metal to oxygen, either introduced as water or air, followed by a rapid and inert cooling. Figure 6.1 shows a flow sheet of the entire apparatus.

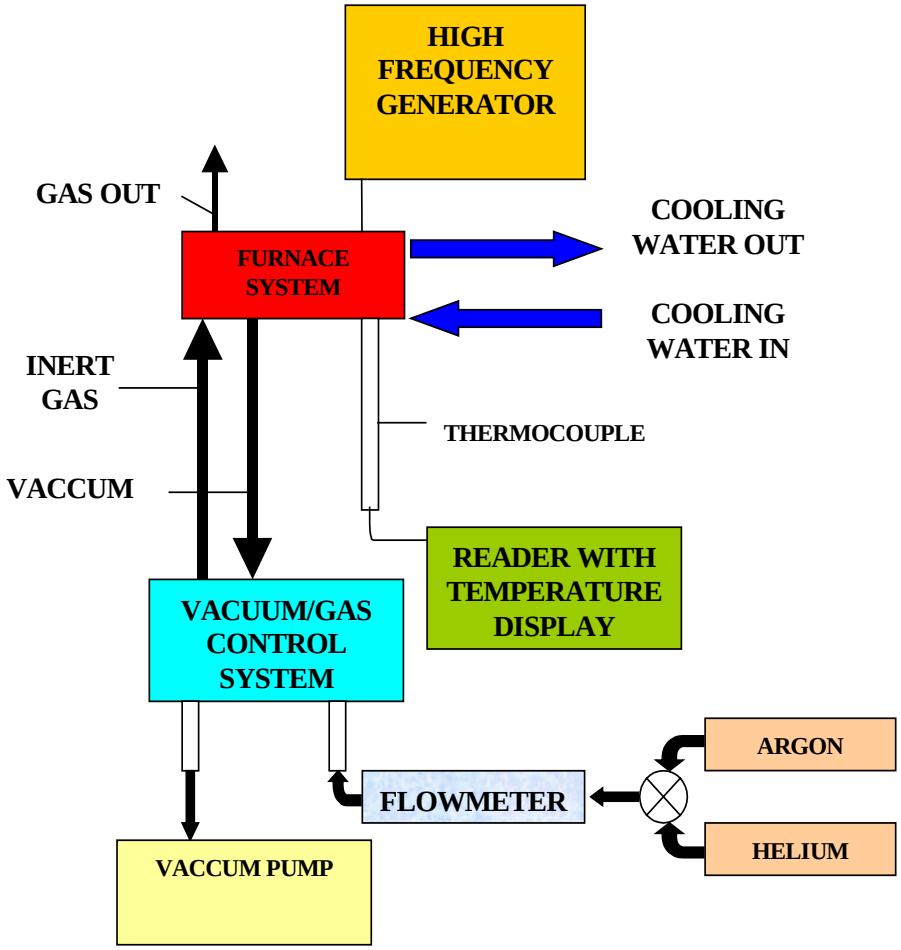

Figure 6.1 – Schematic flow sheet for the experimental apparatus.

URN:NBN:no-2125

As seen from the flow sheet, the residue gas from the furnace is released into air, with no further effort to analyze it. However, early in this work effort was made in order to capture the gas from the furnace and quantify the different species of the gas, as we expected CO, CO_2, H_2O and H_2 to be present along with the inert gas. This gas capturing system will be described in a subsequent paragraph. Unfortunately, the system did not behave as we hoped for, and was later disregarded.

6.1.1 Furnace and vital parts

A schematic cross-section of the furnace is shown in figure 6.2. A graphite susceptor, with the shape of an open cylinder, is located inside a strong, fluctuating magnetic field. Inside the susceptor, we place a small crucible (12 mm high, wall thickness 1.5 mm, and radius 6 mm). These crucibles are made of glassy carbon or alumina. Under the base of the graphite susceptor an S-type thermocouple measures the temperature during the experiment. This thermocouple is calibrated to compensate for the temperature drop between the interior of the crucible and the base of the graphite susceptor. These vital parts are all located inside a transparent silica tube. The tube has double walls, which allow water cooling of the walls, as indicated in figure 6.1. To protect the inside of the silica tube from damaging heat radiation, a screen is placed outside the graphite susceptor. Most of the experiments were performed using a screen of graphite, but a screen of alumina (Pytagoras) was also used.

To create the magnetic field, we use a high frequency generator (Philips PH 1012) connected to a solenoid surrounding the silica tube. The solenoid consists of four loops of water-cooled tubes of Cu, with an outer diameter of 6 mm.

The thermocouple (20 cm long, diameter 3 mm) indicated in figure 6.1 is connected to a reader (Hewlett-Packard 34970A) for a continuous measurement of the temperature inside the furnace. As mentioned earlier, the measured temperature originates from the base of the graphite susceptor, so calibration data is needed to get the correct temperature.

The furnace is connected to a gas/vacuum control system. This is merely a console where we can choose between vacuum or inert gas, either argon or helium. A pressure gauge measures the under-pressure in the furnace during evacuation by the vacuum pump. Typically, pressures down to 0.02-0.04 bar can be reached. After the furnace is evacuated, a switch allows argon gas to flow into the furnace. Then the furnace is evacuated again, and the procedure is repeated four-five times to remove all air from the furnace.

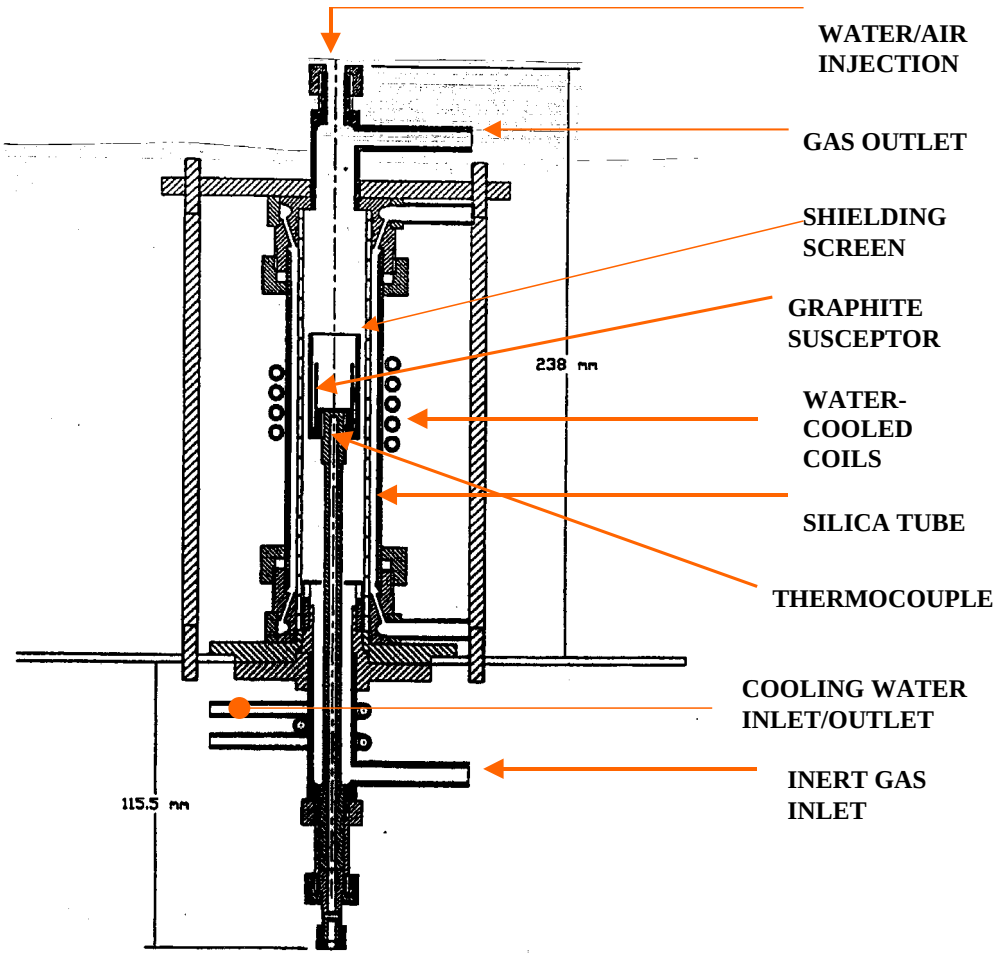

Figure 6.2 – Cross-sectional view of the furnace part of the apparatus.

As indicated in figure 6.2, the oxygen is introduced to the melt through a valve on the top of the furnace system, either as air or water. For the work described in this thesis, water was always used to oxidize the melt.

A video camera (8 mm Canon UC-X30) was used to record the experiments. The camera allows to view the top of the crucible and to observe smoke or light flashes during the experiment.

6.1.2 Gas analysing equipment

The gas analyzing system is connected to the gas outlet of the furnace shown in figure 6.2. The entrance of the analyzing system is heated by a small heating element, which merely is a thin wire wrapped around the glass tube in which the gas flows. The wire is glued to the glass, and a thermocouple (type K) is placed on top. Finally, a layer of insulating material prevents heat losses. A small power supply powers the wire, and temperatures of 100-105 °C can easily be reached. The purpose of this procedure is to avoid any condensation of gas before it has flowed through the analyzing system. The gas analyzing system is shown in figure 6.3.

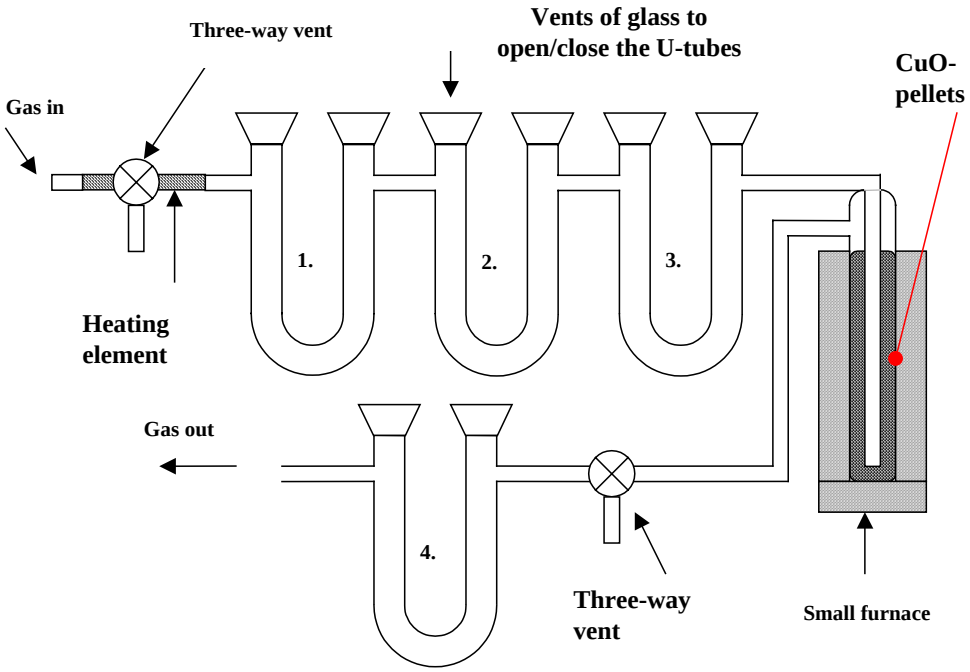

Figure 6.3 – Cross-sectional view of the gas analyzing system.

The gas flows out from the furnace through a glass-tube connection to the inlet of the analyzing system, where it passes through a heated area as explained earlier. Then, the gas flow will pass through four U-shaped glass tubes, which are filled with gas-absorbing material of various kinds. The gas also flows through a glass flask filled with CuO-pellets located inside a small furnace.

The first U-shaped glass tube is filled with a dehydrating agent, $Mg(ClO_4)_2$ (Magnesium perchlorate, anhydrous reagent, GFS Chemicals Inc., Columbus, Ohio, USA). Here we assume that all of the water vapor that did not react with the melt or the crucible will react according to the reaction

URN:NBN:no-2125

$$Mg(ClO_4)_2 + H_2O = MgClO_2 \bullet 6H_2O \quad (6.1)$$

We note that all of the reactions that take place in the U-tubes are solid-gas reactions. After the gas flow has been dehydrated, it flows through the second U-tube where CO gas is converted to CO_2. The tube is filled with Shütze reagent (Alpha Resources, Stevensville, Miami, USA), which is specially designed for this conversion at room temperature without converting H_2 to H_2O. The reagent is yellow, but any reaction that takes place will change the color to red or black, depending on the amount of gas that is converted. The following reaction takes place:

$$CO + I_2O_5 = CO_2 + 2IO_2 \quad (6.2)$$

It is assumed that all of the CO in the gas is converted, and that no unwanted reaction between H_2 and I_2O_5 takes place.

The third U-tube is filled with a mixture of 92% NaOH and 8% vermiculite, and it is assumed that all of the CO_2 present in the gas mixture is absorbed. Then, the gas mixture consists of only inert gas and hydrogen, if the assumptions made are correct. This mixture flow through a glass flask filled with pelletized CuO. This flask is heated by a small furnace, and the temperature on the inside of the furnace is typically 400 °C. It is assumed that the hydrogen reacts with CuO according to the following reaction:

$$H_2 + CuO = H_2O + Cu \quad (6.3)$$

In the last U-tube we assume that the rest of the vapor reacts according to equation 6.1. Thereby, the amount of oxygen captured as vapor in the last U-tube will correspond to the amount of oxygen that has reacted with the melt and the crucible.

The outlet of the analyzing system is connected to a waterjet-pump to compensate for the loss of pressure over the glass tubes.

6.1.3 Oxidation equipment

Water was used as the oxidizing agent in most of the work described in this thesis, but in general air can also be used. The water is introduced to the melt through a syringe and a needle. The needle is made of steel, it is 26 cm long and has an outside diameter of 1.5 mm. On the needle a stopper controls how far down the tip of the needle can go. The position of the stopper can be

adjusted in order to control the distance between the tip of the needle and the melt surface. The syringe can take 1.0 ml of water, typical volumes for these experiments were 0.2 ml.

Figure 6.4 shows the details associated with the upper parts of the apparatus where the water is injected.

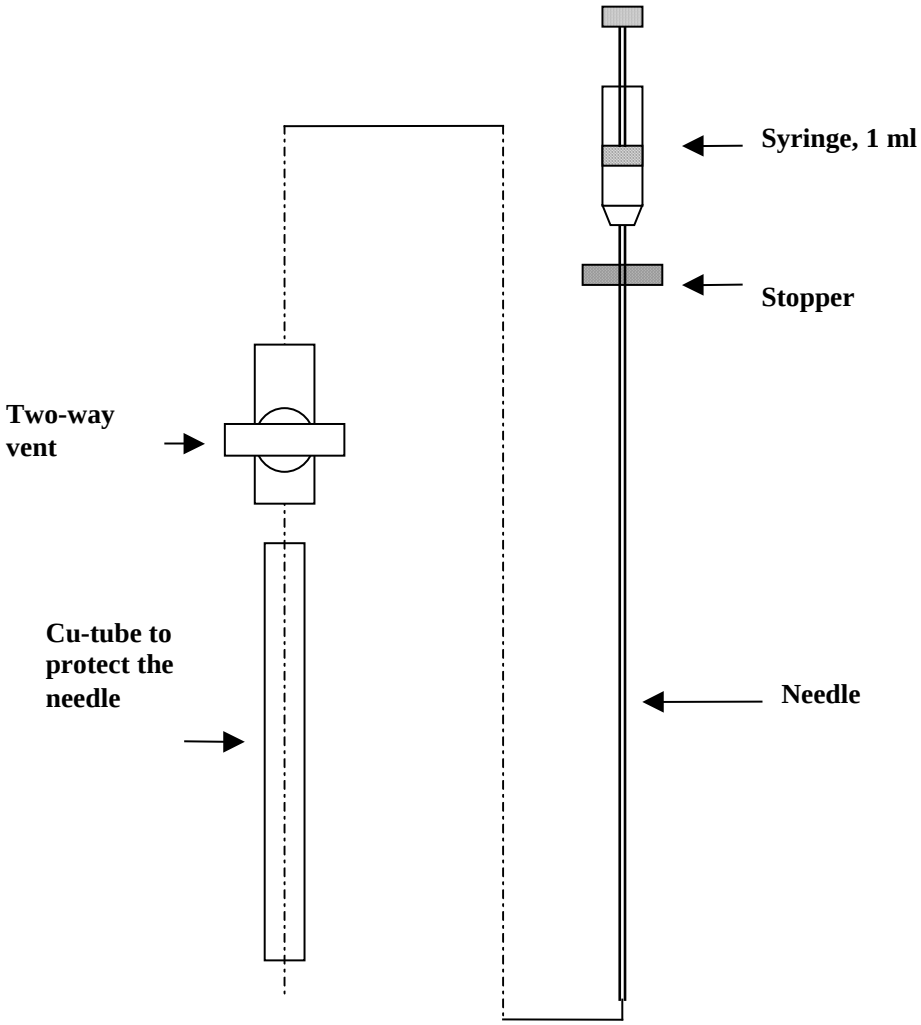

Figure 6.4 – Cross-sectional view of the water oxidation equipment.

During the heating stage of the experiment, the two-way vent shown in figure 6.4 is closed. When the melt has reached the desired temperature, the vent is opened and the needle is inserted through the vent and the protection tube until the stopper on the needle hits the vent. Then, the water is released during a period of 3 seconds. The tube tightens pretty close around the needle, and as

mentioned earlier, the pressure inside the furnace is slightly above atmospheric pressure. In this way, the likelihood of any air coming down the copper-tube is minimal.

6.2 Preparation of samples for microprobe analysis

After the experiment, the small crucibles are removed from the graphite susceptor. Then, the crucibles are filled with a cold casting epoxy resin (EPO-fix). This product is a two-component resin, and it has excellent properties for casting of porous samples. The solidification time is 8 hours, so this epoxy resin is only used inside the crucible. After solidification, the crucible is cast in a cheaper resin, Demotec-20. This is necessary, as we have to cut the crucible in two in order to investigate the oxide layer on top of the now solidified metal sample. Two different steps in the cold mounting process are visualized in figure 6.5.

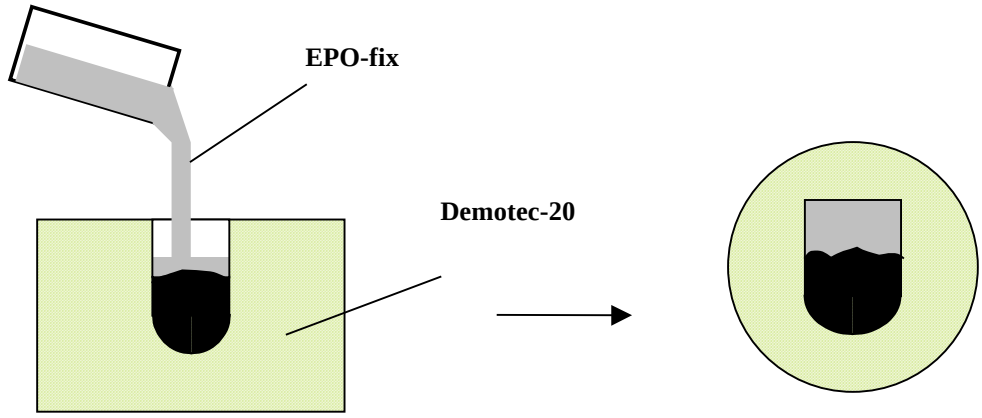

Figure 6.5 – The crucible is filled with EPO-fix, then cast into a cylinder of Demotec-20 (shown to the left). After a cut through the crucible and a final cast, the sample will appear as shown to the right.

Then, the now in-cast crucible is cut with a diamond saw (Struers Accutom), and one final cold mounting is made. After solidification of the epoxy resin, the sample is grinded, polished, cleaned and dried, and finally a thin layer of carbon is put on top of the sample.

6.3 Microprobe

After the samples have been cold mounted and polished, they are examined with an Electron Probe Micro Analyser (EPMA), model JEOL Superprobe JKA-8900M. This microprobe allows us to study the oxide layer that has formed on top of the sample. The microprobe can perform element analysis on

volumes as low as 1 μm^3. Along with the imaging techniques provided by the microprobe, the analysis gives us information about the composition and the structure of the oxide layer. This information is visualized on color micrographs, where each element is mapped according to its intensity as registered by the microprobe WDS-detectors. The intensity distribution can be calculated to give the composition as weight percent, and the corresponding color for each weigh-percent domain is shown next to the picture. It must be noted that this method is more of a qualitative character, as several factors may influence on the intensity distribution, not only the composition itself.

Backscatter images are also available, here the metal (silicon or ferrosilicon) appears white, and the oxide layer is darker. These images provide a visualization of the whole surface, but in order to study the oxide layer in more detail, the element mapping described above is used.

7. WATER GRANULATION EXPERIMENTS – APPARATUS DESCRIPTION

The water granulation experiments have been a joint effort between SINTEF, Trondheim, Norway and the University of Wisconsin-Madison, with funding provided by FFF (the Norwegian Ferroalloy Producers Research Association). The work was initiated in 1996 and the program terminated in 2000.

One of the most important results from this work is the development of an apparatus suited for the release of single drops of molten silicon or ferrosilicon into a tank of water. The apparatus will be described in this chapter, together with an outline of the experimental procedure.

7.1 General description of the apparatus

The apparatus was developed by Nelson *et.al.* (1997), and has been continuously improved since then (Nelson *et.al*, 1998, 1999, 2000). The description given here is based on the latest version.

As already pointed out in the introduction of this chapter, this apparatus allows us to release single drops of molten ferroalloys into water. From the onset of this experimental program, it was believed that the single-drop release was the most promising in order to control the experimental parameters and to simplify the post-experimental analysis. Also, there are other advantages (price, easy to operate, easy maintenance) associated with a simple apparatus. One disadvantage is the challenging aspects of transferring the results from a small lab-scale to large-scale industrial applications.

The apparatus can be divided into three major parts; the framework, the furnace and the water tank. The water tank includes gadgets for inducing explosive melt-water interactions. A triggering device (impactor) is placed in the water tank, and is one of the most vital parts of the system, as it was found to be necessary to provoke explosions. The impactor requires pressurized gas, which accounts for most of the equipment except for the major parts already mentioned. Analyzing equipment is isolated from the apparatus, and it is somewhat limited due to lack of space in the lab. A description of the analyzing equipment will be given in later sections.

A basic sketch of the apparatus is given in figure 7.1.

URN:NBN:no-2125

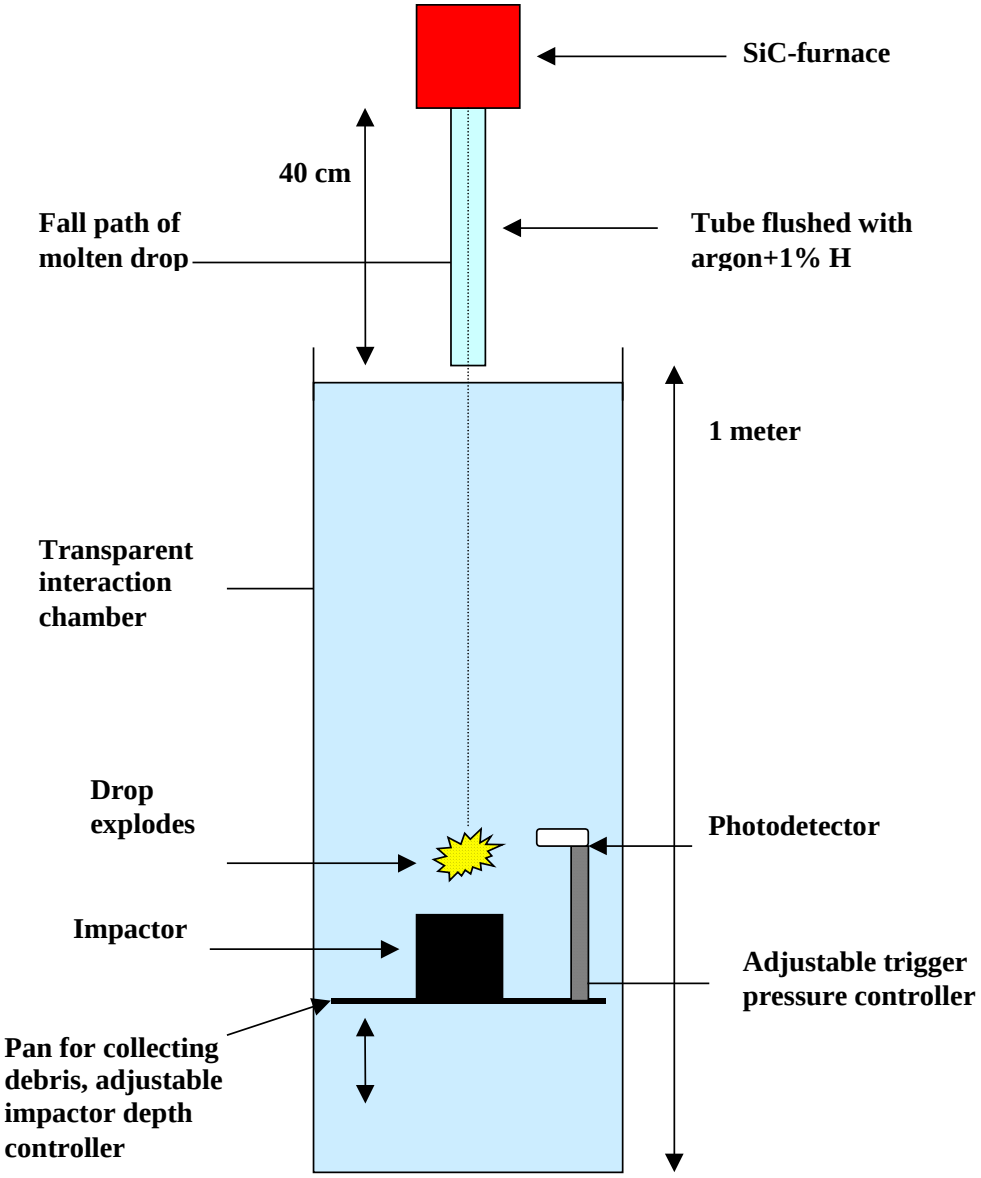

Figure 7.1 – Schematic diagram of the main components of the granulation experimental equipment.

The following sections will deal more explicit with the different parts of the system, along with a description of the analyzing equipment.

7.2 Furnace

The main component of the furnace is a resistively heated helical silicon carbide heating element (I Squared R Element Company, Akron, NY). This element operates in air for a wide range of temperatures, up to 1675 °C, which makes it suitable to produce drops of molten silicon, even more so for the lower melting ferrosilicon. The heating element is powered by 110 volt AC controlled by a 60-ampere variable transformer. A mullite tube is inserted down through the interior of the SiC-element (DIMENSIONS NEEDED!). This tube allows us to melt the specimen in a controllable atmosphere. The tube has an inner diameter of 25 mm, outer diameter of 32 mm and a length of 382 mm.

During the experiment, the tube is flushed from above with a mixture of argon and 1 % hydrogen. This mixture is made from commercial gases (obtained from BOC Gases, Madison, WI), and produced at the facilities of UWM. The use of 1 % hydrogen is motivated from early results (Nelson *et.al.*, 1997), where a black coating was found on the rods that were lowered into the furnace. By using a slightly reducing atmosphere, the occurrence of this coating was eliminated. The gas flow is monitored by a Matheson Type 605 flowmeter.

The SiC heating element is insulated with ALTRA KVS 18/700 insulation, made by Rath Performance Fibers Inc. It is reportedly usable to temperatures as high as 1800 °C. We have also used other types of insulation, but these sometimes caused problems. In a period we had several furnace failures, which we will not deal with here. It is worth noting that most of these failures were related to a too high current through the heating element. To reduce the current we had to improve the insulation of the furnace. Later, no furnace breakdowns have been experienced. To ensure that we are not exceeding the current limits, an ammeter is continuously reading the current through the furnace element.

From figure 7.2, we notice that the silicon rods are mounted in a graphite supporter. This is an improvement compared to earlier experiments, where the rods were supported by a wire of stainless steel, either wounded around the upper end of the rod or passed through a hole drilled horizontally through the upper end of the rod. The wire was attached to a tube of stainless steel that could be lowered into the furnace. This procedure could not be used for rods shorter than about 50 mm, as the wire came too close to the hot zone and failed, with the subsequent fall of the entire rod into the water tank. As a result, rods shorter than 50 mm could not be used. This became a problem, as the rods were usually shorter than the nominally 100-mm due to the brittleness

of the material. Breakage during casting meant that rods were typically in the 50-80 mm range.

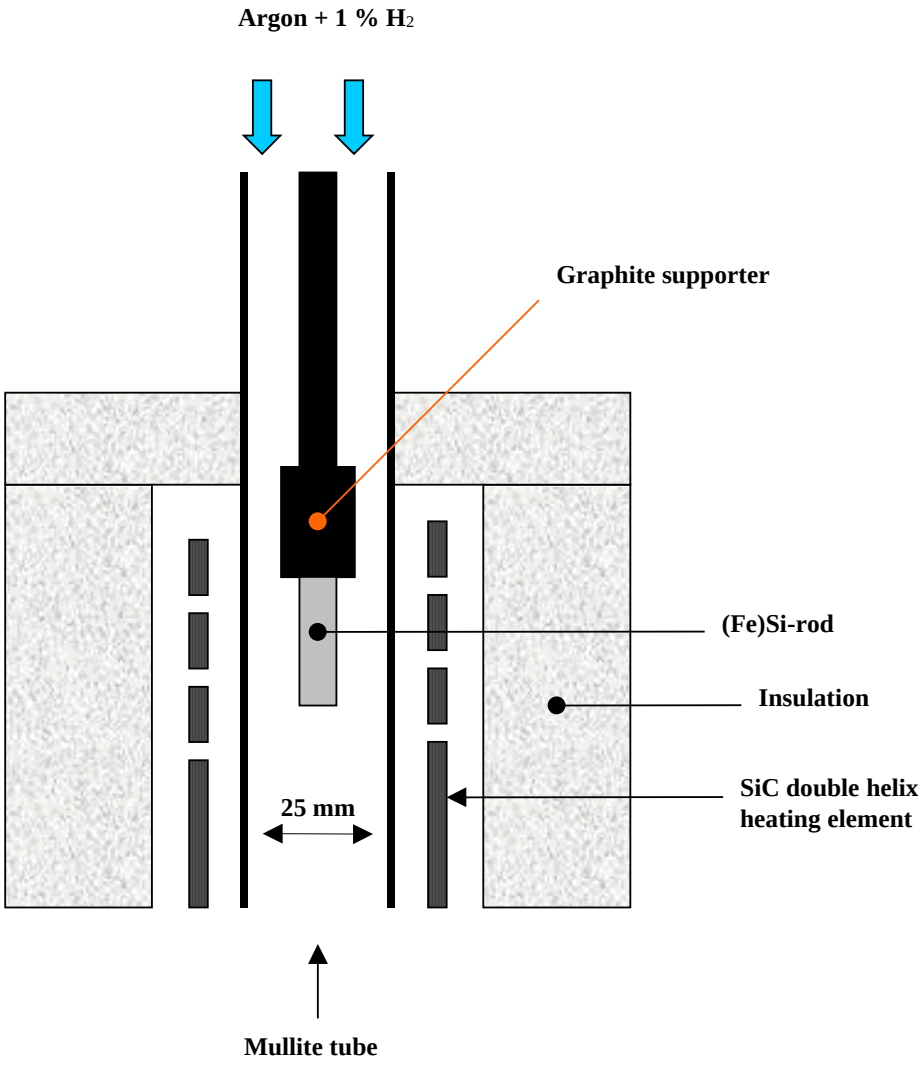

Figure 7.2 – Schematic diagram of the resistively heated tube furnace used to produce drops of molten silicon or ferrosilicon.

As the silicon rods received for the 1999 experiments were mostly shorter than 50 mm, a new procedure for mounting the rods was developed. This was also motivated by the change of material from ferrosilicon to silicon, which meant an increased melting temperature. Instead of using the wire as a support, a 3-mm diameter graphite pin was inserted through a hole drilled at the upper end of each rod. This pin was supported between a pair of holes in the lower end of

a graphite tube, the upper end of which was attached with a second graphite pin to the stainless steel tube normally used to position the rods in the furnace.

Upon heating, the tip of the rod will eventually melt, and a drop of molten (ferro) silicon will fall down the alumina tube into the water chamber. It will be shown that this method gives good reproducibility of the drop sizes. Drops originating from the same rod have almost the same weight, but differences related to minor deviations in composition will probably influence on the size of the drops. This will be shown in later chapters.

The temperature of the furnace is estimated with a disappearing filament optical pyrometer (Pyro Microoptical Pyrometer, serial no. 7189). The pyrometer is aimed at the mullitte tube through a small hole cut in the insulation. The small hole will behave close to a blackbody object, but there is some ambiguity of the measured temperature due to unknown temperature drop through the mullitte tube. No theoretical considerations have been made in order to estimate the temperature drop over the furnace tube, but as the tube is thin (7 mm), we believe the error associated with the pyrometer reading is small. We have also used a thermocouple inserted through another hole in the insulation to obtain a continuously, digital temperature reading. However, since we must make sure the thermocouple does not touch the heating element, it has to be a few centimeters away from the element, consequently even longer away from the tube. Thus, the measured temperature is much lower (~ 100 °C) than as measured with the pyrometer. Since the thermocouple reading must be calibrated against the pyrometer reading, we abandoned this technique.

7.3 Water chamber

The water chamber is constructed from 12.7 mm-thick transparent polycarbonate sheet (Tuffak bisphenol A polycarbonate sheet, Autohaas North America, Philadelphia, PA). This material is transparent, although it has a distinct gray coloration. The inner dimensions of the chamber is 1 m-tall by 30.5 cm square, and holds approximately 90 liters of water during an experiment. The chamber was fabricated by Laird Plastics, Madison, WI.

The water used in these experiments comes from several sources. During the first year of experimental work (1996), three sources at the University of Wisconsin-Madison were used: the Engineering Building (purified but of unknown treatment), the Nuclear Reactor (distilled) and from the tap in the Engineering Research Building (with a definite brown coloration). Later, deionized water from the Lindsay Water Company, Madison, WI was used.

The quality of this water, however, seemed to vary from batch to batch. In 1999, a water deionization system was leased, which supplies water of high quality with a high degree of reliability. This system has been used since. No attempts have been made to determine the effect of water purity on the quenching experiments. Also, the water is not necessarily changed for each new experiment. If the water is visibly contaminated, however, the water tank is emptied and filled with fresh water.

The primary parameter varied in these experiments is the temperature of the water. Four different temperatures have been used; 8, 22 (room temperature), 50 and 90 °C. Ice blocks lowered down into the water chamber was used in order to achieve cold water, and the temperature measured with a 1.3 m-long, 3.2 mm-diameter thermocouple (Type E). When the desired water temperature was above room temperature, immersion heaters were used (Heetomatic 1.1 kW stainless steel bayonet-type pail heaters). To minimize temperature gradients in the chamber, the water was circulated from bottom to top with a Haake constant-temperature water circulation unit. The vertical walls of the chamber were covered with rock wool sheet insulation to reduce heat loss during heating. The insulation was removed shortly before an experiment to allow video and photographic imaging. The experiments concerning different water temperatures were performed by Nelson et.al (1997, 1998). Since 1998, all of the quenching experiments have been done with the water kept at room temperature (17-23 °C).

7.4 Hydrogen collector

In order to estimate the amounts of hydrogen generated by a steam explosion, we used a simple approach – coalescence and gathering of the bubbles in a conical collector at the top of the water chamber and directly measuring their combined volume by displacement of water contained in a graduated cylinder.

The hydrogen bubbles generated by a steam explosion of a single drop of melt are produced in a roughly spherical volume that may have a diameter almost as wide as the water tank. In order to collect the many small bubbles, we placed a conical bubble collector just below the surface of the water at the top of the chamber (see figure 7.1). The base of the conical collector, made of 0.5 mm-thick transparent polycarbonate sheet, is circular and has a diameter of 295 mm, slightly smaller than the 300-mm wide chamber. The upper end of the cone opens upward into a smaller inverted funnel that is attached to a water-filled graduated above. The graduate has a small valve at its upper end with a flexible tube that leads to a water aspirator. The evacuation produced by the aspirator allows us to draw a continuous column of water up through the

funnel into the graduated volume. Once gas bubbles enter the funnel from the cone below, they will pass upward into the graduate and displace an equivalent volume of water. In order to measure various amounts of hydrogen, we prepared interchangeable graduated cylinders with five different volumes – 10, 25, 50, 100 and 250 ml.

The inverted funnel is caused to slide sideways by mounting it on a non-rotating air cylinder (29 mm bore diameter, 76 mm stroke, obtained from the Speedaire Co.). In order to provide a path for the drop to fall into the water unimpeded, the funnel is positioned initially at the right side of the chamber. When the drop falls from the furnace, a photodetector senses its release and starts a time relay. After an appropriate delay to allow the drop to enter the water and fall through the open top of the cone, the relay activates the cylinder with air at a pressure of 0.6 MPa. This activation drives the inverted funnel quickly to cover the outlet of the cone and thus capture all bubbles that rise from the reaction between the melt and the water. A schematic diagram of the hydrogen collection system is shown in figure 7.3.

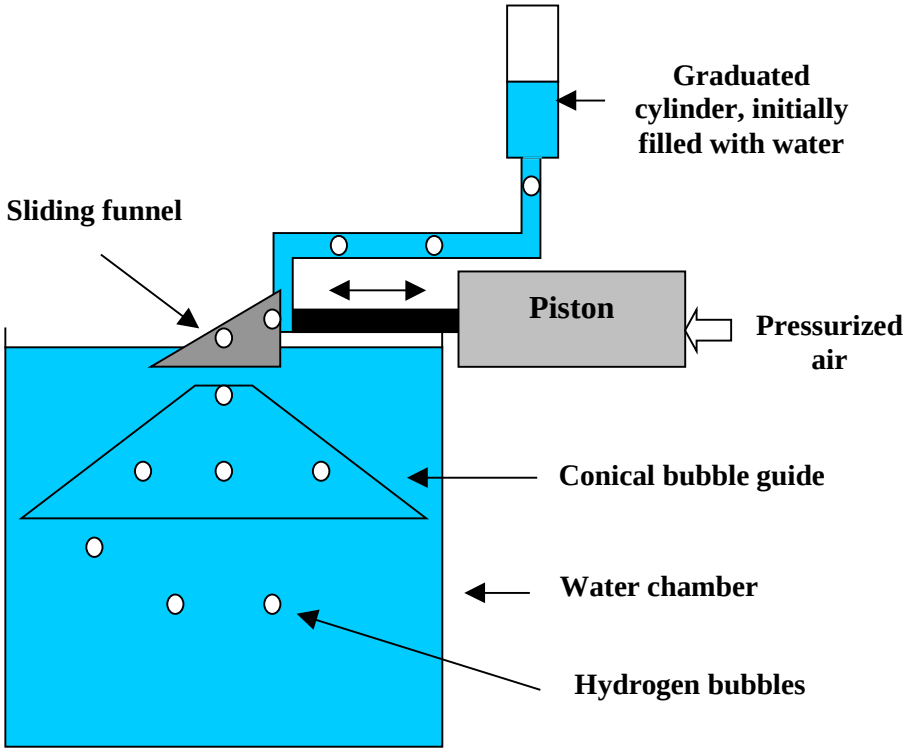

Figure 7.3 – Schematic diagram of the hydrogen collector.

This method for collecting hydrogen gas has two obvious disadvantages. First, the conical bubble guide does not cover the entire cross-sectional flow-area. Thus, bubbles can escape the collector along the walls of the water-chamber, especially in the corners. However, as the explosion usually takes place under the cone, the probability for the bubbles to escape is low. During normal fall paths for the molten drop (straight down) the volume of the bubbles that escape the collector is negligible, as measured from video recordings. In a limited amount of experiments, the molten drop has swerved to one of the sides, thereby increasing the possibility of hydrogen-escape. This can be observed from the video recordings. Thus, we emphasize that it is necessary to check from VCR recordings for each drop release experiment whether bubbles of H_2 escape the hydrogen collector.

The other disadvantage is that we may not achieve an accurate measurement of the amount of hydrogen that is formed upon the silicon-water reaction, as some of the gas can dissolve in the water. If water at 25 °C reaches equilibrium with hydrogen, the solubility of H_2 in water is 19.1-ml H_2/liter water. As the water-chamber takes approximately 90 liters of water, over 1700 ml of H_2 can dissolve in the water, assuming equilibrium is reached. This amount is a factor 100 more than typical values for the collected H_2 during an experiment. However, we performed several test to discover whether hydrogen gas was dissolved in the water. Small amounts of gas (~10 ml) were bubbled through a very small syringe, producing bubbles of approximately 1-mm diameter. The amount of gas collected was always identical to the amount released into the water through the syringe. Of course, even smaller bubbles may dissolve more easily into the surrounding water. We were, however, unable to produce bubbles less than 1-mm diameter.

7.5 Triggering system – impactor and submerged photodetector

In figure 7.1, an essential part of the apparatus is shown. The impactor is located in the water tank, where it rests on the debris catcher pan. This device will at an appropriate time give rise to a strong pressure pulse that is intended to collapse the vapor film surrounding the molten drop, thus trigger a steam explosion. This trigger is needed, as molten drops of silicon or FeSi75 do not explode spontaneously when released into water.

Our impactor exists in three different modifications. In the course of the experimental program, it was found that stronger trigger pulses were necessary to obtain explosions between molten silicon and water, compared to the water-FeSi75 system. However, the impactors used are principally the same. The most striking difference is in the output, i.e. the pressure pulse generated.

A drawing of the impactor is shown in figure 7.4. It operates when a steel slug is driven upward in a rifle-like barrel by gas at high pressure. The slug is 60 grams, with dimensions 15 mm-diameter and 39 mm tall. The pressure transient is generated in the water when the slug strikes the underside of the cover of a welded carbon steel canister. The impactor is fired by electrically open a solenoid valve backed by a ballast volume of 2 liters. The ballast volume is connected with 6-mm polyethylene tubing to a commercial cylinder of gaseous argon at high pressure. The pressure of the driving gas is set by a regulator and a dial-type bourdon gauge, usually to 1.3 MPa. When the solenoid valve opens, the sudden pressurization at the base of the barrel drives the slug upward to strike the surface of the canister. Note that the impactor is completely sealed, so no gas will leak out into the water.

After the impactor has been fired, the slug is driven down into the barrel by applying a back-pressure. This was found to be necessary, as gravity only could not guarantee that the slug fell back to its starting point, probably due to the very tight fit between the slug and the barrel. This procedure was found to significantly increase the reproducibility of the generated pressure transients, as will be further discussed in chapter 9.5.

To fire the impactor at the right time, we use a submerged photodetector. The photodetector senses the passage of the luminous molten drop, and activates a control relay, which in turn switches a time-delay relay. Then, a 110 V AC electrical signal is delivered to the solenoid valve, which opens and lets the pressurized gas through in order to fire the impactor.

The sensor and control relay are the Skan-a-Matic P33001 photodetector switched with the R40100 control, both obtained from Clarostat Controls and Sensors, Richardson, Texas, USA. This photosensor is filtered optically to be most sensitive to light emitted in the near infrared (870-980 nm). Operation of this photodetector in the near infrared is advantageous when photographic and video images are being recorded with reflected light generated by fluorescent tube lamps, as these lamps emit very little radiation in this part of the spectrum. Consequently, there will be minimal interference between the illumination source and the photodetector. This is of practical advantage, as switching on and off these fluorescent lights will not cause the photodetector to activate, thus firing the impactor. It will be activated, however, by incandescent light sources, which emit strongly in the infrared. Such sources include the luminous silicon drops and filament lamps, such as ordinary flashlights.

The output of this photodetector-activated control system is a short 110 V AC pulse fed via a latching relay to switch a time-delay relay (Dayton, Model 6A855), with a range of delays from 50 ms to 999 minutes. We used variable small delays (~300 ms) to fire the impactor with the submerged photodetector. This was done to avoid early firing of the impactor, which means that the molten drop experiences a weak trigger pulse, that is, too weak to induce a violent interaction. However, small modifications of the apparatus eliminated the need for time delay in the photodetector-impactor trigger system. Black coatings were inserted along the walls in the water chamber to minimize light reflections from the walls of the chamber. These reflections caused premature trigger of the impactor, especially for silicon drops. Also, two small plates were mounted on the photodetector, the result being a small horizontal slit in which the sensor was allowed to "see". Consequently, the photodetector is activated only when the molten drop has reached the same horizontal level, as indicated in figure 7.1. We can then control where (depth in water) we want the molten drop to experience a pressure pulse by adjusting the height of the photodetector in the water chamber.

7.6 Pressure transducer

The pressure transducer is used for two purposes. Initially it was only used to investigate the pressure pulses generated by the impactor, but later it has become an integrated part of the apparatus in order to measure the pressure disturbances in the water following a steam explosion. The description of the transducer has been published earlier by Nelson (1999b), and is repeated here.

The transducer is a tourmaline underwater blast transducer, model W138 A01033 CY020AC, obtained from PCB Piezoelectrics, Inc., Depew, New York, USA. This pressure sensor has been designed for various marine applications where it is necessary to measure pressure transients at different depths in water. Its electrical leads are watertight and it is used freely suspended in the water, independent of structures or surfaces that might produce extraneous pressure signals. It uses a tourmaline crystal disc 0.76-mm thick × 3.8-mm o.d. as the pressure sensor. Tourmaline is an isotropic piezoelectric material; that is, its response is independent of the direction from which the pressure transient impacts the crystal.

In this transducer, the tourmaline crystal is enclosed in silicone oil that is encapsulated in a transparent plastic tube. The crystal and signal and ground wires are shielded against electrical noise. These leads are attached to an in-line preamplifier located about 50 mm away, located in the same plastic tube, encapsulated in the oil. The transducer has a 6.2 m-long waterproof coaxial

cable connected at one end, in watertight manner, to the preamplifier and at the other end to a battery-powered signal conditioner, which, in turn, is connected via coaxial cable to a recording oscilloscope.

The transducer has been calibrated by the manufacturer to reliable standards, see Appendix A-1 for certificate details. The sensitivity of the transducer is 683 mV/MPa with strict linearity of 0.89 percent of full scale over the range 0 to 34.9 MPa. Its resonant frequency is 1000 kHz with a rise time of 1.5 μs.

The transducer is attached to an aluminum band shaped as a half-circle, which again is mounted on the fiducial rods. This is visualized in figure 7.4. The position of the transducer related to the center of the impactor is in general the same for all of the experiments.

7.7 Oscilloscope

The signals generated by the pressure transducer are recorded with a Hewlett-Packard Infinium oscilloscope, model 54815A, serial no. US38130105. The bandwidth of the oscilloscope is 500 MHz at a sample rate of 1 Gsa/s with a memory depth of 32 K.

During the experiment, the oscilloscope continuously obtains a reading from the pressure transducer. It can be programmed to start recording when a sudden pressure change occurs, characterized by increase over a pre-determined level. The oscilloscope then takes 32000 readings, typically at a sampling rate of 1GSa/s. This gives us a total recording time of 32 ms, which is sufficient to record the important pressure disturbances following a steam explosion, as will be shown later. The data are saved on a floppy disk and processed on a PC.

7.8 Imaging techniques

Important information is available through different imaging techniques. Standard experiments facilitate the use of a video camera and two 35-mm cameras, but we have also performed experiments with the use of more sophisticated equipment, which allows a better time resolution.

7.8.1 Video imaging

The VHS camcorder (Sylvania Model HQ-VHS) operates at 60 frames per second and produces reasonable time resolution, moderate image quality, color representation and sound. It has been used to determine fall velocities,

triggering distances, the occurrence of the explosions and the duration of luminous and non-luminous phenomena associated with the interactions before and after they are triggered. The video images also provide information about bubble behavior and water motion that accompanies the explosions.

7.8.2 Time-exposure photography

A simple way of obtaining good images is to use open shutter, time-exposure photography in a darkened room. This technique is particularly suitable for drops in the yellow, orange and red wavelengths where photographic emulsions are most sensitive. We used a 35-mm camera, mounted on a tripod, in front of the chamber, and another 35-mm camera viewing the water chamber from the side. In this way, we know the exact location of the melt-water interaction.

To obtain true dimensions of the imaged interactions, we attached a pair of 3 mm-OD $\times$ 177 mm-long stainless steel rods vertically on either side of the impactor. The spacing between these rods, about 135 mm apart horizontally, was measured for each experiment. The spacing between the rods on the photographic images provides a fiducial for calibrating distances that is independent of the degree of enlargement. The shiny, reflective surfaces of the rods make them easily detectable, even on poorly exposed images. These fiducials are also a suitable place to mount the photodetector previously described.

Although the time-exposed photographic images usually have a very high quality, they also have the disadvantage of being time-integrated, giving little information about the dynamic processes involved during the explosions. However, they give excellent information about the size of the explosion, distances in the water and some limited information on change of temperature of the melt, based on the colors as observed from the image. In order to obtain more information concerning the dynamic behavior of the steam explosion, we have used high-speed imaging techniques. In this way, the time resolution is considerably improved. An example of this kind of image is shown in figure 7.4.

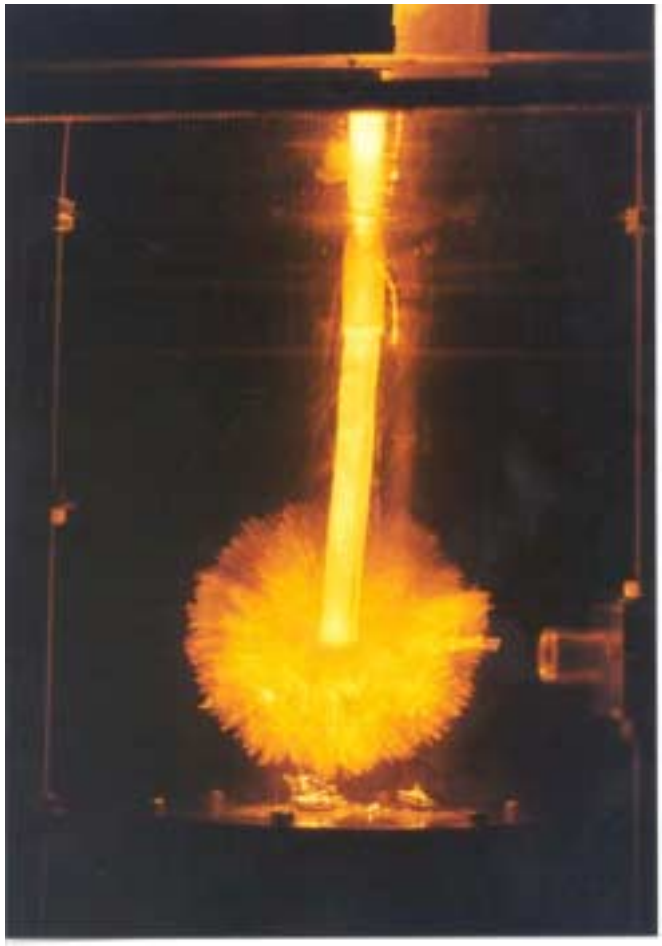

Figure 7.4 – Typical image of a steam explosion obtained using the open shutter technique. The two fiducial rods can be seen on either side of the explosion. The surface of the impactor is visible just below the sphere, with a couple of solidified particles from an earlier drop release. The cylinder-shaped photodetector that triggers the impactor is located to the right of the explosion center. The distance between the fiducial rods is 181 mm.

7.8.3 High-speed video camera

We borrowed a Kodak Ektapro HS Motion Analyzer, Model 4540 from the Engine Research Laboratory, University of Wisconsin. This device can operate with various recording rates, but the memory is limited to 1024 images. We used a recording rate of 4500 frames/second, which gives us a total recording time of 230 ms. This video camera operates in reflected light, provided by two banks of three fluorescent tube lamps, one at either side of the

water chamber. As for the oscilloscope, the video camera records all the time, but we have to set a trigger in to keep the images in the memory. The camera could be triggered in two different ways; we used a relay closure operated by the 110 V AC signal that fires the impactor. In other words, when the luminous drop triggers the impactor, its trigger system closes a circuit, which again triggers the video camera. By trial and error, we found appropriate time delays for the electrical systems to make sure we caught the explosion event both on the oscilloscope and on the video camera.

The Motion Analyzer was connected to a standard video recorder, and the events were recorded on a VHS-cassette. The images obtained allowed us to interpret the pressure-time traces as recorded by the pressure transducer. This will be shown in later chapters.

7.8.4 High-speed camera

In some experiments, a Hycam I high-speed 16-mm camera was used. This work was done before the pressure transducer was used to record pressure-time traces following a steam explosion. The camera can record at rates as high as 10 000 frames/second. It gives high spatial image resolution and good color rendition. The major drawbacks are the time required for processing the film and the relatively high cost of the film. Also, the use of this high-speed camera complicates the experimental procedure. The Hycam camera requires about one second to accelerate to the desire framing rates (typically 1000 frames/second for this work). This is difficult to achieve with spontaneous drop release, however. For these reasons, the Hycam has not been used in the period 1998-2001, which this thesis will focus on.

7.8.5 Shutter wheel camera

The open-shutter imaging technique described in section 7.8.2 yields high quality streak images of the molten drop as it descends through the water, but less information about what is actually happening to the drop at various times during the fall. Therefore, a second 35-mm camera has been used to record time-exposed images of the luminous drops. The camera was allowed to view the experiment through a rotating five-bladed shutter wheel in order to obtain a time resolution of 83.3 ms per chop (12 shops per second) during the fall of the drops. The images produced this way show “dotted” tracks for the main drop as well as for any satellite or other secondary drops produced during the experiment. The camera was placed to view the falling drops from a greater distance than the main camera (section 7.8.2) in order to provide imaging over the entire fall distance of the drops. The images produced with the shutter

wheel, a train of “dots”, complements the frame-by-frame video images in determining the velocities of motion and providing other information about the behavior of the various luminous particles as they fall through the water.

7.9 Experimental procedure

This chapter will explain in detail how each experiment is carried out using the latest modification of the apparatus (including pressure measurements).

7.9.1 Setting up the equipment

As mentioned earlier, the furnace is powered by a 60 A variable transformer. This transformer has a regulator divided into 0-100 % of maximum effect. During the heating stage, we increase the power in steps of 10 % each fifth minute to minimize the heat stress in the SiC heating element. This is carried out until the transformer is at 50 % output, which gives a current of approximately 12 A. As the SiC-element heats up, the resistance decreases, which causes the current to increase. The output from the transformer is therefore reduced in order to keep the current flowing through the heating element steady at 12 A. The specimen rod is kept out of the furnace until the desired temperature is reached. For ferrosilicon this is around 1430 °C, and for silicon 100 degrees more.

After the furnace is switched on, the debris collector pan is inserted into the tank. It is attached with plastic-covered wires in each of the corners to the top of the water chamber. The impactor is then lowered into the water tank and is placed on the pan, and its gas tubes hooked up. Prior to this, the photodetector is positioned at a fixed height above and to the side of the top surface of the impactor (see figure 7.1), as this will decide the strength of the pressure pulse the molten drop experiences. The conical bubble guide is inserted, supported by three wires that just rest on the edge of the water chamber. The moving funnel is mounted at the side of the tank, and the bubble guide is aligned with the expected fall path of the drop to make sure it falls through the hole in the cone (approximately 5-cm diameter). Then the graduated cylinder with the hose connecting it to the funnel is evacuated and filled with water. A valve on top of the graduated cylinder keeps the pressure low in the graduate to prevent the water from flowing back into the water tank. When the molten drop reacts with water, thus producing hydrogen bubbles, these bubbles will eventually end up in the graduate, as explained in section 7.4. We used a 10-ml graduated cylinder for most of the experiments.

The oscilloscope is then connected to the pressure transducer and then the impactor is tested a couple of times. To trigger the impactor, we simply shine a small flashlight on the photo detector. Then we take up three pressure recordings with the oscilloscope by manually triggering the impactor. These three recordings will be compared to the actual experiment with the drop in order to eliminate pressure transients created by the impactor.

The specimen rod is weighed and mounted in the graphite support, and eventually connected to the steel tube that will be lowered into the furnace. The rod is not lowered before we have reached the desired temperature of the furnace, as explained previously.

Imaging equipment is set up; this includes the video camera and two 35-mm cameras. One is placed in front of the water tank, the order is viewing the tank from the side. The open-shutter photographs obtained will give the exact location of the explosion.

7.9.2 Performing the experiment

When the desired temperature of the furnace is reached, the mixture of argon and 1 % hydrogen is allowed to flow through the furnace. The rod is lowered down into the furnace. Depending on the temperature of the furnace, it takes around 5-15 minutes before the tip of the rod melts and releases a drop. At this point the video camera starts recording. The graduated cylinder is checked to make sure the water level is stable. Then, the room lights are turned off and the 35-mm cameras are opened. During the melting procedure, we keep an eye on the temperature in the hot zone, as measured with the pyrometer. Eventually a drop will fall into the water tank, be triggered and explode. Then, the cameras are closed and the room lights turned on. The water level in the graduated cylinder is checked, and an estimate of the amount of collected hydrogen is made. The video camera is turned off, and the experiment is over.

7.9.3. Post-experimental work

The pressure traces obtained on the oscilloscope is saved to a floppy disk, three traces with the impactor only, and the last one showing the impactor and pressure transients created by the interaction between the molten drop and the water, if any. The furnace is allowed to cool down before the argon/hydrogen gas-mixture is turned off and the rod removed from the furnace. During the cooling of the furnace, the impactor is carefully removed from the water chamber, along with any pieces of solidified metal or debris that may still be located on the unit. The debris collector pan is then removed very carefully as

to not lose any debris. When the pan is out of the tank, it is placed on a table to dry along with the impactor overnight. Finally, the rod is weighed to calculate the mass loss (the mass of the drop), and the debris is collected in a small dish and weighed, photographed and stored for later analysis work, i.e. X-ray or microprobe analysis, more of this later.

8. MISCELLANEOUS

8.1 Fall velocity for a molten drop – theory

To obtain a theoretical value for the fall velocity of a molten drop of Si or FeSi75 in water, we have to make a couple of assumptions:

- *the drops fall with a constant velocity (steady-state) when in the water*
- *the effect of entrance is neglected (time-scale is small compared to the total fall time)*

For a molten drop sinking in water at a constant velocity, the drag force must equal the drop weight, i.e.

$$\frac{1}{2}C_D\pi R^2\rho_l v_{drop}^2 = \frac{4}{3}\pi R^3\rho_{sphere}g \tag{8.1}$$

C_D is the drag coefficient (assumed to be constant) and ρ_{sphere} is the density of the molten sphere minus the density of the water to account for buoyancy. For other symbols see the nomenclature list. Obviously, we have also assumed that the drop takes a spherical shape as it descends down in the water.

Equation (8.1) can be rearranged to

$$v_{drop} = \sqrt{\frac{8g\rho_{sphere}R}{3C_D\rho_l}} \tag{8.2}$$

Substituting for R (mass of drop equals density times drop volume) we obtain

$$v_{drop} = \left(\frac{128g^3\rho_{sphere}^2M}{9\pi C_D^3\rho_l^3}\right)^{1/6} \tag{8.3}$$

That is, v_{drop}= constant $\times M^{1/6}$, the velocity only weakly depends on the mass of the drop. The mass is the only parameter that we can measure for each independent experiment. However, the drag coefficient depends on the shape of the particle. A more drop-like shape means that C_D is reduced, which means that the steady-state velocity, according to equation (8.3), increases. Our experimental results reveal interesting information on the fall velocities of

drops with different compositions, indicating that the shape of the granules changes depending on the overall composition.

8.2 Heat/energy balance for a single drop

A simple heat balance was carried out in order to estimate the heat losses during the time-period between release of the drop and triggering, as well as surface energy associated with the breakup of the drop and the heat needed to form steam bubbles as observed in the single-drop experiments.

In the experiments performed at UWM, the drop is released from the furnace at its melting temperature, approximately 1412 °C. Its heat transfer history can be divided into three parts; (a) the fall through the gas atmosphere, (b) the fall through the water and (c) the explosion event. We will in this section estimate the heat transfer for each one of these stages. A number of assumptions are made, these are:

- *The air resistance is neglected through free fall in argon-gas*
- *The molten drop behaves like a black radiant object*
- *The initial drop temperature is equal to the melting temperature of silicon, i.e. 1412 °C.*
- *The calculations are based on a drop mass of 1 gram*

Silicon properties used in the calculations are given in table 8.1.

Table 8.1 – Silicon properties.

Property	***Tabulated value*** [1)]
Enthalpy, 1685 K, liquid Si	ΔH = 86 187 J/mol
Specific heat, 1690 K	C_p = 0.2476 cal/K*gram
Surface tension, 1685 K	$\sigma = 7.25*10^{-7}$ J/cm^2
Latent heat of fusion	h_{fg} = 50.208 J/K*mol
Exothermic energy from the reaction $Si+2H_2O=SiO_2+2H_2$	$\Delta H_{reaction}$ = 150 kJ/mol H_2

1) Thermodynamic properties taken from Brandes (1983) and Handbook of Chemistry and Physics (1983).

The furnace is flushed with argon gas containing 1% hydrogen. When calculating the thermodynamical properties for the gas mixture, however, it is assumed that the mixture behaves like pure argon.

All details (i.e. equation sets, values for thermodynamical properties) regarding the heat transfer calculations can be found in appendix C.

Table 8.2 – Argon properties.

Property	***Value*** *)
Thermal conductivity, 400 K	k_{Ar} = 0.018 W/m*K
Dynamic viscosity, 400 K	μ_{Ar} = 2.29*10^{-5} Pa*s
Density, 400 K, 1 atm	ρ_{Ar} = 1.603 kg/m^3
Specific heat, 400 K, 1 atm	$C_{p,Ar}$ = 521 J/kg*K

*) The values tabulated above were obtained from the internal database in EES.

8.2.1 Heat transfer during fall through gas mixture

During the fall from the furnace to the water, heat is transferred from the melt to the surroundings as convection and radiation heat transfer. The drop is assumed to be spherical, with a diameter equal to the rod specimen diameter (9 mm). As the mass of each drop is well defined (from the weight loss of the sample rod in the furnace), so is the heat content of the drop. The downward argon flow velocity is constant and equal to 0.274 m/s, based on the flowmeter measurements and calibration data from the manufacturer. The temperature profile of the gas nearby the molten drop is not known, but test calculations showed that the gas temperature influence the final result in a very modest manner. In order to obtain a limit for the heat transfer, we used argon properties evaluated at room temperature, i.e. we assumed T_{argon}= 300 °K. An increase in gas temperature from 300 to 700 K only modify the calculations slightly; a 30% reduction in the total heat transfer from molten drop to argon gas was obtained. In any circumstance, the amount of heat is negligible to the total heat of fusion of the silicon drop.

To estimate the heat transfer coefficient, Ranz and Marshall's model for freely falling liquid drops was used. The Nusselt number in their model is correlated by

$$Nu = 2 + 0.6 \times \mathrm{Re}^{1/2}\,\mathrm{Pr}^{1/3} \tag{8.4}$$

where Re is the Reynolds number and Pr the Prandtl number for the flowing argon around the molten sphere. The heat transfer coefficient is given by

$$h = k_{Ar} Nu \Big/ D_{drop} \tag{8.5}$$

It was found that the heat loss due to convection was negligible (see table 8.3). This was not surprising, taken the short fall and the poor heat transfer characteristics of argon into account.

Table 8.3 – Results from the heat transfer calculation, convection in the gas mixture.

Property	***Value***
Heat transfer coefficient	H = 45.5 W/m^2*K
Reynolds number	Re = 1595
Heat loss from molten sphere	$Q_{conv,gas}$ = 3.0 J
Prandtl number	Pr = 0.667
Temperature drop associated with calculated heat loss	2.9 °K

The contribution from radiation heat transfer is expected to be higher, as the temperatures in question are fairly high. It is assumed that the surface temperature is constant and equal to the bulk temperature of the molten silicon. As the Biot-number (Bi) of a molten drop of silicon is much less than 1, this approximation is justified. It turns out that the surface temperature does not change much during the fall in the gas, and the temperature differences are large, so the error involved in the assumption of a constant surface temperature is small.

The radiation heat loss is governed by Stefan-Boltzman`s radiation law:

$$Q_{rad} = A_{drop} t \sigma_{SB} (T_{drop}^4 - T_{gas}^4) \tag{8.6}$$

where *t* denotes the time for the drop to fall through the gas mixture. The results are given in table 8.4.

Table 8.4 – Results from heat transfer calculations, radiation during free fall in gas mixture.

Property	***Value***
Temperature drop associated with radiation heat transfer	$\Delta T_{rad,gas}$ = 32 °K
Heat loss due to radiation	Q_{rad} = 33 J

Since the heat loss is only a small fraction of the latent heat of fusion, the amount of solidification is negligible. To simplify the calculations further, we assume that the heat loss does not cause any solidification of the drop, merely a supercooling of the melt below liquidus temperature.

8.2.2. Heat transfer during fall through water

To obtain a first approximation of the heat transfer during melt-water contact, we used Dhir and Purohit`s correlation for hot spheres submerged in sub-

cooled water, previously described in section 2.3.3. Their correlation for the Nusselt number is

$$Nu = Nu_0 + 0.8\,\mathrm{Re}^{0.5}\left(1 + \frac{S_c\,\mathrm{Pr}_v}{S_h\,\mathrm{Pr}_l\,\mu}\right) \tag{8.7}$$

where Nu_0 is given by

$$Nu_0 = 0.8\left(\frac{g\rho_v(\rho_l - \rho_v)h_{fg}D^3}{\mu_v k_v \Delta T_w}\right)^{1/4} \tag{8.8}$$

This Nusselt number takes into account both convection and radiation heat transfer. We assume that the drop is allowed to descend 400 mm (at steady-state velocity) before the trigger is activated.

Table 8.5 – Some calculated properties for the heat transfer during free fall in water for a molten sphere of silicon.

Property	***Value***
Heat transfer coefficient	h = 483 [W/m^{2}K]
Heat loss	$Q_{conv+rad,water}$ = 223 J
Reynolds number	Re = 2680

This heat loss is about 8% of the latent heat of fusion for Si. Thus, we can expect that some solidification take place before the drop has reached a water depth of 400 mm, preferably at the surface. Indeed, this is observed in the experiments on triggering steam explosions of molten drops of silicon. Pieces of a solid shell could be recovered among the fine debris that is left over in the water after an explosion, indicating that partly solidification had taken place prior to the explosion.

Comparing the heat losses during these different stages, we find as expected that the fall in the water is the far most important one. The contribution from the forced convection in the argon-1% hydrogen atmosphere is negligible. So the heat loss from the release of the drop to the point where it explodes is basically a combination of radiation and forced convection in the water.

Exothermic heat from the oxidation of silicon:

The oxidation of Si to silica is exothermic, and heat will be released as the drop descends in the water. The excess heat for the reaction $Si_{(l)} + 2H_2O_{(l,g)} = SiO_{2(s)} + 2H_{2(g)}$ is around 350 kJ/mole H_2 at 1400 °C (equation 3.6). For an

amount of 5 ml H_2, the heat release is approximately 70 J. In chapter 10 and 11 we show that the oxidation reaction at the vapor-metal interface is more complicated than the above, but the total reaction can at least be approximated by a complete oxidation of silicon to silica.

Energy required fragmenting the drop:
Eventual explosions are associated with a huge increase in the surface area, and therefore some of the energy of the molten drop will be used for the surface expansion work. A simple first-order approximation for the surface energy increase is presented here. We assume that the drop fragments when it is molten, although the experiments indicate that some solidification take place at the surface The surface tension for molten Si is given by (Brandes, 1983):

$$\gamma = \gamma_0 + (T - T_m)\frac{d\gamma}{dT} \tag{8.8}$$

where γ_0=865 mJ/m^2, T_m is the melting point for Si, T the temperature of the melt and $d\gamma/dT$ is equal to –0.13 mN/m*K.

The surface energy is now found by a simple mass balance, according to equation (8.9). The total number of particles with a mean size yet to be decided experimentally, is given by

$$E_{surface} = \gamma A_{tot} = \gamma N A_f = \gamma \frac{V_d}{V_f} A_f = \gamma \frac{d_d^3}{d_f^3} \pi d_f^2 = \pi \gamma \frac{d_d^3}{d_f} \tag{8.9}$$

The subscript f indicates fragments, d the original drop. For simplicity, we take the diameter of the drop to be 9 mm. We could also use the real weight of the drop as measured from the rod loss to calculate the diameter, but it will be shown that the surface energy in any circumstance is very small, thus, this approximation is justified. From a sieve analysis of the fragmented drops (section 9.9.2), average fragment sizes were found to be between 400 and 1000 μm. The lower size corresponds to a larger surface area. Thus, the surface energy is obtained from equation (8.9), using γ = 880 mJ/m^2 (to compensate for some undercooling), d_d = 9*10^{-3} m and d_f = 400*10^{-6} m. The surface energy is then

$$E_{surface} = 5.0\,\text{mJ} \tag{8.10}$$

The initial surface energy of the drop is negligible (a factor 100 lower), thus, the surface energy given in equation (8.10) more or less represents the total

increase in. However, 5 mJ is very little compared to other energies involved. Even if the fragment size were as little as 1 μm, this would merely cause the surface energy to increase 400 times, i.e. to 2 Joules, again a negligible amount.

Note that since the density of liquid and solid silicon is different, (ρ_l=2.51 g/cm^3, ρ_s=2.33 g/cm^3), this will introduce an error by overestimating the molten surface area slightly. However, this error is small compared to the uncertainty in the sieve analysis.

8.2.3 Bubble-energy

When the drop fragments, steam will be generated so fast that a bubble forms. The volume of this bubble can be converted into energy, thus giving an estimate of the energy transferred to the water during a steam explosion. Bubble volumes can be converted into energies using equation (8.11):

$$E(J) = 1013\left[P_{amb}(MPa) \times V(liters)\right] \tag{8.11}$$

where P_{amb} is the ambient pressure against which the bubble grows and V is the volume of the bubble. We assume here that the pressure needed to blow a bubble underwater is not very different from the local barometric pressure plus that of the depth of the water. Because our experiments are performed in relatively shallow water, we neglect the pressure added by less than a meter of water and equate P_{amb} to P_{atm}, the local barometric pressure. That is, for our present purposes, $P_{amb} = P_{atm} = 0.1$ MPa.

Thus, if we can accurately determine the true dimensions of the steam explosion bubbles from our images of the interaction, we will be able to estimate the amount of energy transferred to the water. Ideally, we would like to have perfectly spherical bubbles. However, this is not always the case, and very often some sort of estimate/averaging has to be done. In figure 8.1 (same as figure 7.4), a typical image obtained using the open-shutter technique is shown.

When measuring the diameter of the bubble, we basically draw several circles centered in the middle of the steam bubble, and use the average value of these circles as the final value for the diameter. This method works very well if the steam bubbles are symmetric, but the error is somewhat larger the more asymmetric the bubbles are. This is somewhat compensated by the use of a second camera that view the interaction from the side. Thus, we can view the

explosion in two dimensions, and this gives us fairly good approximations of the bubble size.

Figure 8.1 – A typical image of a steam explosion of a molten drop of silicon. Circles centered in the (estimated) middle of the bubble are drawn, and an approximate value for the bubble diameter is thus obtained.

Also note the double bubble in figure 8.1, which is observed on most of these kind of images. The inner bubble that first forms is brighter, i.e. the melt is hotter, while the secondary bubble is darker, but much larger in volume compared to the first one. In estimating the work the steam bubble does on the surrounding water, the sum of the two bubble volumes is used. That is, we assume that the first bubble collapses completely before the other bubble starts to grow. This is verified experimentally, and will be discussed in a later chapter.

8.2.4 Summary of heat transfer calculations

This section has been intended to give a first-order approximation (order-of-magnitude analysis) of the heats and energies involved during the quenching of a molten drop of silicon in water, with subsequent triggering and steam explosion. The calculated results are shown in table 8.6.

Table 8.6 – Results from the heat transfer calculations for a drop of pure silicon (9-mm diameter) released into water.

Mode	***Value [J]***
Radiation in gas	~ 33
Convection in gas	~ 3
Radiation+convection in water	~ 220
Exothermic heat due to the oxidation of silicon	~ 70
Increase in surface energy due to fragmentation of the melt	< 1
External work (bubble-energy) *)	~ 10-30

*) *See section 9.10*

The enthalpy of a 1-gram drop is approximately 3 kJ. Thus, only about 10% of the available heat energy can be accounted for. The rest is assumed transferred as heat and radiation upon fragmentation of the melt and cooling of the fragments. As the surface area increases with a factor 90 (assuming an average diameter of 100-μm for the fragmented particles, the time needed to transfer the rest of the heat is correspondingly smaller, i.e. the emitted power increases to a value ~15 kW for the fragmented particles. Thus, the drop should in theory quench in ~0.2 s, given that the heat transfer correlations used prior to the triggering are still valid. This is actually in good agreement with direct observations using high-speed video camera (see section 9.12.1), thereby justifying the somewhat simplified calculations previously discussed.

URN:NBN:no-2125

9. WATER GRANULATION EXPERIMENTS - RESULTS

This chapter will summarize the results from the experiments on the release of single drops of molten Si and FeSi75 into water (usually at room temperature), with subsequent triggering and explosive interactions. The experiments were carried out over a three-year period, and some of the results have been published earlier (Nelson *et.al.* 2001, Hildal *et.al.* 2000).

9.1 Composition of the test alloys

One important aspect of this research program has been to link the drop-release experiments to granulation processes in the ferroalloy industry. In so doing, the compositions of the test alloys were usually made as to represent "risky" compositions and "safe" compositions, from an industry point of view. That is, the industry knows from practical operation that as the concentration of impurities (Al and Ca) in the ferroalloys increases, the likelihood of violent interactions between melt and water decreases.

9.1.1 Rods used in 1998 experiments

In 1998, all of the experiments were carried out using FeSi75 as test material. Three different compositions were aimed for, but all of the experiments were performed with non-alloyed rods. The compositions of these rods are given in table 9.1. Unfortunately, no good analysis on other elements exists, but the level of Mn is relatively high, and accounts for most of the contamination. However, other elements but Al and Ca are not believed to be very surface-active compared to the two just mentioned, as described in section 3.2-3.3.

Table 9.1 – Compositions (in weight percent) of non-alloyed test rods for the 1998 experiments.

Element	*1A*	*1C*	*B*	*F1/F2*	*F8*
Si	74.4	74.5	75.0	73.8	73.9
Fe	24.8	24.8	24.4	25.1	24.9
Al	0.06	0.05	<0.01	<0.001	0.002
Ca	0.03	0.03	0.013	0.001	0.007

The material was obtained as rods, with length 50-100 mm and diameter 10 or 16-mm. The rod-making procedure is described in appendix A.

9.1.2 Rods used in 1999 experiments

All of the experiments for the year of 1999 were carried out using rods of silicon with or without additives (Al and/or Ca). Four different alloys were made, pure Si (A), Si with 0.4 % Al (B), Si with 0.04 % Ca (C) and Si with 0.4 % Al and 0.04 % Ca (D). Table 9.2 summarizes the compositions of these four alloys.

Table 9.2 – Composition of Si-alloys used in the 1999 experiments. All numbers are weight percent.

Element	***Alloy A***	***Alloy B***	***Alloy C***	***Alloy D***
Fe	0.016	0.008	0.018	0.019
Ca	0.003	0.003	0.041	0.058
Al	0.035	0.54	0.060	0.50
V	<0.01	<0.01	<0.01	<0.01
Cr	<0.01	<0.01	<0.01	<0.01
Ni	<0.01	<0.01	<0.01	<0.01
Cu	<0.001	<0.001	<0.001	<0.001
Mo	<0.001	<0.001	<0.001	<0.001
Ti	0.005	0.005	0.004	0.005
Mn	<0.01	<0.01	<0.01	<0.01
Mg	0.002	0.002	0.002	0.002
Co	0.001	0.002	0.002	0.002
Zn	0.001	0.001	0.001	0.001
Zr	0.001	0.001	0.001	0.001
Pb	0.001	0.001	0.001	0.001
Sn	<0.001	<0.001	<0.001	<0.001

The element analysis was performed at Lilleby Metall, Trondheim, Norway. The most important alloying elements (Al and Ca) are marked with blue print. We note that the levels of Al were somewhat higher than opted for in alloy B and D; in both cases we aimed for 0.4%. The calcium content of alloy D was also higher than planned for. In later sections/chapters we will usually refer to the different alloys by their nominal composition rather than the actual one as given by table 9.2, unless otherwise stated.

9.1.3 Rods used in 2000 experiments

No new rods were made for the experiments done in 2000. Most of the experiments were carried out using old FeSi75-rods, but also some Si-rods were used, see table 9.1 and 9.2 for element analysis.

9.2 Release of single drops of molten FeSi75 into water– an overview

A number of experiments on the release of single drops of molten ferrosilicon into water have been performed using the apparatus described in an earlier section. For convenience, a summary of the experiments will be given in this section.

Two different rod diameters were used for the ferrosilicon experiments: 10 and 16-mm diameter. Table 9.3 lists all the experiments performed with 11-mm FeSi75. Note that the corresponding drops had a different diameter than the rods, 9 and 11-mm, see section 9.4 for details.

Table 9.3 – Summary of releases of 11-mm drops of non-alloyed molten ferrosilicon into water. All experiments carried out in 1998.

Exp.no	T_{water} *[°C]*	*Alloy*	*Trigger [mm]*	*Impactor [mm]*	*Type of interaction*	*No. of drops*
C-274-1	21.4	1A-1	300	400	Explosion	5
C-276-1	22.3	1A-1	250	350	None	1
C-278-1	22.1	1A-1	150	250	Explosion	2
C-280-1	22.3	1A-1	150	250	Explosion	1
C-282-1	22.5	1A-2	200	300	Explosion	3
C-284-1	23.0	1A-2	250	350	Explosion	3
C-286-1	22.2	1A-2	300	400	Explosion	2
C-288-1	20.9	1A-2	400	500	Explosion	2
C-290-1	21.5	1A-2	500	600	None	2
C-292-1	21.5	1A-3	450	550	None	4
C-294-1	21.5	1A-3	400	500	None	4
C-296-1	21.5	1A-3	200	300	Explosion	2
C-298-1	22.3	1A-4	400	500	Explosion	2
C-300-1	22.6	1A-4	500	600	None	2

The column “trigger” denotes the water level at which the photodetector spots the descending molten drop. In all of the experiments listed in table 9.3, the top-level of the impactor is 100 mm below the trigger depth. In general, this need not be the case. The last column of the table identifies the number of drops that were released in each of the experiment. Usually, the first drop did not explode, so several drops were released until we achieved an explosion. This aspect will be discussed later. For each of the drop releases, we had to reset the impactor and the cameras.

The experiments in 1998 also included several releases of 9-mm drops. A summary is given in table 9.4.

Table 9.4 – Summary of releases of 9-mm drops of non-alloyed molten ferrosilicon into water. Experiments D-1-1 to D-24-1 carried out in 1998, the rest was done in 2000.

Exp.no	T_{water} *[°C]*	*Alloy*	*Trigger [mm]*	*Impactor [mm]*	*Type of interaction*	*No. of drops*
D-1-1	22.5	1C	300	400	None	1
D-3-1	22.1	1C	150	250	None	2
D-4-1	22.1	F8	300	400	None	3
D-5-1	22.2	1C	150	250	None	4
D-7-1	21.3	1C	150	250	None	4
D-8-1	20.8	F1/F2	150	200	None	4
D-11-4	20.6	F1/F2	150	200	Explosion	4
D-12-1	21.1	B	150	200	None	2
D-15-1	20.2	B	150	175	Explosion	5
D-16-1	19.1	B	100	125	None	4
D-18-1	18.7	B	200	225	Explosion	4
D-19-1	19.1	B	300	325	Explosion	4
D-20-1	19.5	B	400	425	Explosion	4
D-21-1	21.0	B	500	525	Explosion	2
D-22-1	20.4	B	700	725	Explosion	2
D-24-1	20.1	B	785	810	Explosion	2
D-163-1	22.0	F1/F2	430	500	Explosion	2
D-168-1	22.8	F1/F2	340	400	Explosion	1
D-170-1	23.6	F1/F2	530	600	Explosion	1
D-173-1	24.3	F1/F2	765	820	Explosion	1
D-175-1	24.4	F1/F2	430	500	Explosion	1
D-178-1	20.7	F1/F2	425	500	Explosion	1
D-180-1	23.0	F1/F2	440	500	Explosion	2
D-182-1	23.3	F1/F2	285	355	Explosion	1
D-184-1	23.4	F1/F2	375	465	Weak	1
D-187-1	23.2	F1/F2	335	435	Explosion	1
D-188-1	22.8	F1/F2	220	270	Explosion	1
D-199-1	24.3	F1/F2	275	355	Explosion	1

Not all of the drops released in the same experiment were triggered. For some reasons, the drops did not always trigger the impactor. Most typically, this was caused by the drop falling behind or to the side of the impactor. Other times, we deliberately let the first drop go, without activating the impactor, as we

suspected the first drop to have a somewhat different composition than the typical composition of the rod. This is only justified by the observations we made during the experiments; the first drop always seemed to behave somewhat differently than the rest of the drops. We suspect this to be due to a high level of impurities in the rods prepared for the 1998 experiments. At a later stage, it was found that our iron source had a high level of Mn. As a result, more slag was formed on the drops upon oxygen contact. This may change the behavior of the drops significantly.

The behavior of the FeSi-drops in water is summarized in table 9.5 (11-mm drops) and table 9.6 (9-mm drops).

Table 9.5 – Behavior of molten ferrosilicon drops (11-mm) when released into water and the corresponding rod losses.

Exp. no	*Rod loss [g]*	*Debris [g]*	*Remarks*
C-274-1	11.50	11.21	#1 exploded, # 2-5 trigg'ed, no explosion
C-276-1	2.27	2.30	#1 triggered, no explosion
C-278-1	4.45	3.91	#1 trigg'ed, coarse fragmentation. #2 trigg'ed, BIG explosion, threw water 2 m.
C-280-1	4.07	3.36	#1 untrigg'ed, #2 trigg'ed, large explosion
C-282-1	6.93	6.51	#1 untrigg'ed, #2 trigg'ed, no explosion, #3 trigg'ed, explosion
C-284-1	6.94	6.64	#1 untrigg'ed, #2 trigg'ed, no explosion, #3 trigg'ed, explosion
C-286-1	4.57	4.19	#1 untrigg'ed, #2 trigg'ed, vigorous explosion
C-288-1	4.43	4.01	#1 untrigg'ed, #2 trigg'ed, explosion
C-290-1	4.34	4.51	#1 untrigg'ed, #2 trigg'ed, no explosion, then rod fell into water tank.
C-292-1	9.23	9.24	#1 untrigg'ed, #2-4 trigg'ed, no explosions
C-294-1	9.26	9.24	#1 untrigg'ed, #2-4 trigg'ed, no explosions
C-296-1	4.74	4.45	#1 untrigg'ed, #2 trigg'ed, moderate explosion
C-298-1	4.70	4.33	#1 untrigg'ed, #2 trigg'ed, moderate explosion
C-300-1	4.42	4.59	#1 untrigg'ed, #2 trigg'ed, no explosion, then rod fell

Table 9.6 – Behavior of molten ferrosilicon drops (9-mm) when released into water and the corresponding rod losses.

Exp. no	*Rod loss [g]*	*Debris [g]*	*Remarks*
D-1-1	2.58	2.68	#1 trigg'ed, no explosion, #2 no trigger, rod fell
D-3-1	No measure	2.64	#1-2 trigg'ed, no explosion, blue globules, rod contaminated
D-4-1	4.29	4.32	#1-3 trigg'ed, no explosions, blue globules
D-5-1	5.37	5.37	#1-4 trigg'ed, no explosions
D-7-1	5.23	5.23	#1-4 trigg'ed, no explosions
D-8-1	4.40	4.66	#1-4 trigg'ed, no explosions
D-11-4	5.74	5.55	#1-3 trigg'ed, no explosions, #4 trigg'ed, good explosion
D-12-1	NM	NM	#1-2 trigged, no explosions, then rod fell
D-15-1	8.67	7.81	#1,3,6 trigg'ed, no explosion, #4-5 trigg'ed, exploded, #2 swerved, no trigger
D-16-1	5.77	5.78	#1-4 trigg'ed, no explosions
D-18-1	18.86	17.98	#1,2,6 trigg'ed, exploded, #4 trigg'ed, coarse fragmentation, #3,5 swerved, no trigger
D-19-1	6.81	6.16	#1,2,4,5 trigg'ed, exploded, #3 sverwed, no trigger, rod fell afterward
D-20-1	17.32	16.28	#1,2,4,5 trigg'ed, exploded, #3 swerved, no trigger, rod fell afterward
D-21-1	5.56	5.08	#2,3 trigg'ed, exploded, #1,4 swerved, no trigger
D-22-1	4.06	3.72	#2,3 trigg'ed, exploded, #1 swerved, trigg'ed but drop was too far from the impactor, no explosion
D-24-1	4.20	3.80	#2,3 trigg'ed, exploded, #1 swerved, trigg'ed but drop was too far from the impactor, no explosion
D-163-1	1.17, 1.18	2.06	#1 not triggered, #2 good explosion
D-168-1	1.19	0.90	#1 trigg'ed, good explosion
D-170-1	1.16	1.07	#1 trigg'ed, moderate explosion
D-173-1	1.17	1.03	#1 trigg'ed, good explosion
D-175-1	1.13	0.99	#1 trigg'ed, good explosion
D-178-1	1.22	1.14	#1 trigg'ed, mild explosion
D-180-1	1.20, 1.12	2.16	#1 swerved to the right, no trigger, #2 exploded strongly
D-182-1	1.48	1.27	#1 trigg'ed, good explosion
D-184-1	1.53	1.55	#1 trigg'ed, but mildly, mild interaction that blew out top of the drop
D-187-1	1.47	1.18	#1 trigg'ed, very strong explosion
D-188-1	1.49	1.33	#1 trigg'ed, strong explosion
D-199-1	1.23	1.05	#1 trigg'ed, good explosion

We experienced several problems during these experiments, as the tables above indicate. First, the rods produced for the 1998 experiments (alloy 1A, 1B and C) were very brittle compared to rods produced earlier (F1/F2 and F8). Thus, handling these rods was difficult, as they broke easily. As a result, the rods were short (~ 50 mm), and as we at that stage were using wires to support the rods in the furnace, the supporting wire came too close to the hot zone, and was facing a possible meltdown with a subsequent fall of the rod into the water chamber. This led to the development of the graphite holder described earlier. The graphite holder eliminated any accidental loss of the test rod into the water; thus, it was a major improvement. Experiments D-163-1 to D-199-1 were carried out using the graphite holder, and as can be seen from tables 9.4 and 9.6, we needed at most two drops in each experiment to obtain an explosion. This strongly improved our ability to measure the rod loss, thus finding the mass of each drop.

9.3 Release of single drops of molten Si into water – an overview

Similar to the previous section, a summary of the experiments on the release of single drops of molten silicon into water will be given. These experiments took place in 1999 and partly in 2000. Only 9-mm drops were used, and the experiments are listed in table 9.7.

Following the experiments listed in table 9.7, we decided to use the slug-type impactor (impactor 3). It can be seen from the table above that it was necessary to bring the molten drops very close to the impactor in order to achieve an explosion. By using the more powerful impactor, we were hoping to initiate the explosion further away from the surface of our trigger source. Applying impactor three, we conducted a number of experiments on the release of molten, non-alloyed silicon into water, and they are listed in table 9.8.

Table 9.7 – Summary of releases of 9-mm drops of non-alloyed molten silicon into water. Explosions were triggered with the pneumatic impactor. (RT = room temperature)

Exp.no	T_{water} *[°C]*	*Alloy*	*Trigger [mm]*	*Impactor [mm]*	*Type of interaction*	*No. of drops*
D-36-2	0 (Ice)	A-3	None	None	None	1
D-38-1	RT	A-4	None	None	None	3
D-40-1-1	18	A-4	380	400	None	1
D-40-1-2	18	A-4	320	400	None	1
D-43-1-1	RT	A-4	150	200	None	1
D-43-1-2	RT	A-4	150	200	Coarse	1
D-45-1-1	RT	A-4	130	200	Coarse	1
D-45-1-2	RT	A-4	120	200	Coarse	1
D-46-1-1	17	A-9,10	140	200	Coarse	1
D-46-1-2	17	A-9,10	120	200	None	1
D-48-1-1	15	A-9,10	175	200	None	1
D-48-1-2	15	A-9,10	190	200	Explosion	1
D-50-1-1	RT	A-9.10	None	810	None	1
D-50-1-2	RT	A-9,10	None	810	None	1
D-52-1-1	RT	A-9,10	350	400	None	1
D-52-1-2	RT	A-9,10	None	400	None	1
D-52-1-3	RT	A-9,10	385	400	None	1
D-53-1-1	RT	A-9,10	185	200	Explosion	1
D-53-1-2	RT	A-9,10	175	200	None	1
D-55-1-1	RT	A-9,10	175	200	None	1
D-55-1-2	RT	A-9,10	175	200	None	1
D-55-1-3	RT	A-9,10	150	200	None	1
D-56-1-1	16.5	A-9,10	160	200	None	1
D-56-1-2	16.5	A-9,10	150	200	None	1
D-56-1-3	16.5	A-9,10	170	200	None	1
D-56-1-4	16.5	A-9,10	190	200	Explosion	1
D-59-1-1	19.5	A-9,10	None	300	None	1
D-59-1-2	19.5	A-9,10	285	300	Explosion	1
D-61-1-1	23	A-9,10	385	400	Explosion	1
D-62-1-1	17	A-9,10	475	500	Coarse	1
D-64-1-1	19.5	A-9,10	475	500	Coarse	1

Table 9.8 – Summary of releases of 9-mm drops of non-alloyed molten silicon into water. Explosions were triggered with the slug-type impactor.

Exp.no	T_{water} *[°C]*	*Alloy*	*Trigger [mm]*	*Impactor [mm]*	*Type of interaction*	*No. of drops*
D-71-1	25	A-8	None	None	None	3
D-74-1	24	A-8	None	None	None	3
D-77-1-1	23	A-8	150	350	None	1
D-77-1-2	23	A-8	300	350	None	1
D-83-1-1	21	A-8	None	350	None	1
D-83-1-2	21	A-8	230	350	None	1
D-86-1	21	A-8	High[1)]	350	None	3
D-90-1-1	22	A-8	320	400	Coarse	1
D-90-1-2	22	A-8	340	400	Explosion	1
D-94-1-1	21.5	A-8	230	400	None	1
D-94-1-2	21.5	A-8	360	400	Explosion	1
D-97-1-1	19.5	A-8	240	400	None	1
D-97-1-2	19.5	A-8	340	400	Explosion	1
D-104-1-1	22	A-8	380[2)]	400	None	1
D-104-1-2	22	A-8	350	400	Explosion	1
D-107-1-1	20.5	A-7	360	400	Explosion	1
D-109-1-1	21	A-7	360	400	Explosion	1
D-111-1-1	21.5	A-7	320	400	None	1
D-114-1-1	21	A-7	365	400	Explosion	1
D-115-1-1	20	A-7	340[2)]	400	None	1
D-120-1-1	19	A-7	360[2)]	400	Coarse	1
D-123-1-1	19.5	A-7	370	400	Explosion	1
D-191-2	24.0	A-5	310	400	None	1
D-194-1	23.3	A-5	335	400	None	1
D-197-1	23.4	A-5	365	400	Coarse	2
D-202-1	24.4	A-5	305	355	Explosion	1
D-205-1	NM	A-5	305	355	Explosion	1
D-207-1	23.8	A-5	310	350	Explosion	1
D-209-1	23.6	A-5	325	360	Explosion	1
D-214-1	21.9	A-5	150	200	Explosion	1
D-223-1	23.2	A-5	260	300	Explosion	1

[1)] No precise measurement of the trigger level, but it was far above the impactor (weak trigger pulse). [2)] Drop fell on the edge of the impactor (weaker trigger pulse compared to falling onto the middle of the impactor).

We also conducted a few experiments on alloyed silicon-drops, see table 9.2 for element analysis. These experiments are listed in table 9.9.

Table 9.9 – Summary of releases of 9-mm diameter molten drops of alloyed silicon into water. Interactions were triggered with impactor 3 (slug-type).

Exp.no	T_{water} *[°C]*	*Alloy*	*Trigger [mm]*	*Impactor [mm]*	*Type of interaction*	*No. of drops*
D-127-1-1	17.5	B	380	400	Coarse	1
D-130-1-1	17	B	360	400	Coarse/Exp	1
D-145-1-1	21	B	330	400	None	1
D-217-1-1	23	B	285	300	Explosion	1
D-147-1-1	17	C	380	400	Coarse	1
D-133-1-1	17.5	C	370	400	Coarse	1
D-135-1-1	17	C	340	400	None	1
D-219-1-1	23.1	C	275	300	Coarse	1
D-137-1-1	17	D	380	400	Coarse	1
D-139-1-1	17	D	360	400	Coarse	1
D-143-1-1	22	D	330	400	None	1
D-221-1-1	21.8	D	275	300	Coarse	1

The results tabulated above are different in respect to ferrosilicon in one important way. Silicon drops need a larger trigger pressure in order to explode. This will be examined in more detail in a later section.

In table 9.10 the behavior of the silicon drops and their corresponding drop mass/rod loss is shown, similar as outlined for the ferrosilicon drops.

URN:NBN:no-2125

Table 9.10 – Behavior of molten silicon drops (9-mm) when released into water and the corresponding rod losses.

Exp. no	*Rod loss [g]*	*Debris [g]*	*Remarks*
D-71-1	3.25	3.31	#1,2,3: no trigger, test of hydrogen collector
D-74-1	2.87	2.94	#1,2,3: no trigger, test of hydrogen collector
D-77-1-1	NM	1.47, 1.45, NM	#1 early trigger, no explosion #2 trigg'ed, but fell behind impactor, no explosion, then furnace overheated and ruined
D-83-1	2.14	2.21	#1,2: early trigger, no explosions
D-86-1	2.28	2.27	#1,2,3: early trigger, no explosions
D-90-1	2.26	2.05	#1 trigg'ed, coarse fragmentation, #2 trigg'ed, good explosion
D-94-1	2.33	1.71	#1 trigg'ed early, coarse fragmentation, #2 trigg'ed, delay on photodetector, good explosion
D-97-1	2.15	2.02	#1 trigg'ed early, nothing, #2 trigg'ed, good explosion
D-104-1	2.51	1.98	#1 trigg'ed, but fell on edge of impactor, no explosion, #2 trigg'ed, good explosion
D-107-1	1.20	0.89	#1 trigg'ed, good explosion
D-109-1	1.07	0.99	#1 trigg'ed, mild explosion
D-111-1	1.13	1.02	#1 trigg'ed, coarse fragmentation
D-114-1	1.04	0.91	#1 trigg'ed, good explosion
D-115-1	0.93	0.97	#1 trigg'ed, drop fell to the left, no explosion
D-120-1	1.25	1.32	#1 trigg'ed, drop fell far to the left, coarse fragmentation
D-123-1	1.55	1.28	#1 trigg'ed, good explosion
D-191-2	1.15	1.15	#1 trigg'ed, no explosion
D-194-1	0.85	0.83	#1 trigg'ed, but drop fell behind impactor, no explosion
D-197-1	2.55	2.55	#1 fell on blinder, not triggered, #2 trigg'ed, coarse fragmentation
D-202-1	1.21	0.86	#1 trigg'ed, strong explosion
D-205-1	1.00	0.88	#1 trigg'ed, mild explosion
D-207-1	1.05	0.86	#1 trigg'ed, good explosion
D-209-1	1.28	0.97	#1 fell on blinder, but trigg'ed and exploded
D-214-1	1.33	1.55	#1 trigg'ed, moderate explosion
D-223-1	1.23	1.01	#1 trigg'ed, strong explosion

9.4 Characteristics and behavior of the drops

The drops are made by the use of the pendant drop technique described earlier. After a drop has formed at the tip of the test rod located inside the furnace, it falls down into the water and quenches. During the quenching process, gas bubbles are released (hydrogen gas, more of this later). Both for Si and FeSi75, *spontaneous explosions never occurred*. This is an important result, nevertheless, quite expected.

9.4.1 Silicon drops – average mass

The silicon average drop mass is calculated based on the rod loss in each experiment divided by the number of drops released in that particular experiment. This gives an average value for one particular experiment, and this value is then compared with the average values for all of the other experiments, and a new average value, based on the entire population of single-experiments average values is then calculated. Ideally, we would like to measure the weight of each drop released. However, in some cases two drops are released; one that fragments and one that explodes vigorously. Thus, there is no way to find a value for the mass of each of the individual drops, and we have to use an average based on the total rod loss. If possible, we have used drop weights based on individual measurements. The same procedure is used for ferrosilicon drops, obviously.

The standard deviation, σ, is defined in equation (9.1), assuming that the values represent the total population.

$$\sigma = \sqrt{\frac{n\overline{x^2} - \left(\overline{x}\right)^2}{n^2}} \tag{9.1}$$

where n is the number of average values, and x is the average value for the drop mass for each of the experiments. Average values for alloyed and non-alloyed drops are given in table 9.11.

Table 9.11 – Average drop-mass for silicon drops.

	Average mass, [g]	***Standard deviation, [g]***
Non-alloyed Si drops	1.10	±0.16 (15 %)
Alloyed Si drops	1.27	±0.11 (9 %)

An average mass of 1.10 gram corresponds to a drop diameter of 9.4 mm. We will for simplicity refer to these drops as 9 mm-diameter drops.

9.4.2 Average mass – ferrosilicon drops

The same procedure as scheduled in the last section was used to estimate the average mass of ferrosilicon drops released into water. These drops were not alloyed with Al or Ca, and the average mass was 1.30 grams, with a standard deviation of 0.14 grams, or just above 10 %. The average masses for small and large ferrosilicon drops are shown in table 9.12.

Table 9.12 – Average mass for ferrosilicon drops.

	Average mass [g]	***Standard deviation [g]***
Smaller drops (10 mm rods)	1.30	0.14
Larger drops (15 mm rods)	2.26	0.08

Using a density of 3.2 g/cm^3, an average mass of 1.30 grams corresponds to a drop diameter of 9.2 mm. Thus, we will also for the case of ferrosilicon refer to these drops as 9-mm drops.

The larger drops, made by melting rods with a diameter of 15 mm, had an average mass of 2.26 grams, with a standard deviation of only 0.08 grams, which corresponds to only 3.5 %, so these larger drops were quite reproducible when it comes to size. The corresponding average diameter was 11.1 mm.

9.5 Measurement of pressure transients from the impactor

The pressure transients generated by the impactor are measured with the tourmaline transducer. During 1998, we used the pneumatic impactor, but for the experiments carried out later, we built a stronger device, a slug-type impactor, which is described in an earlier chapter. The pressure characteristics of both of these impactors will be examined in the following sections.

9.5.1 Pneumatic impactor

This device was used in all of the experiments described in tables 9.3-9.6. To measure the peak pressures from this impactor, we placed the transducer in shallow water, a few millimeters below the water surface, and the surface of the impactor 100 mm beneath the transducer. Also, measurements were performed at deep water, with the transducer at 300 mm and the impactor at 400 mm. These experiments taught us that the output from the pneumatic impactor changes over time, a decrease in the peak pressure of about 17 % was detected over a time interval of two months. Also, the pressure transients were more reproducible when the impactor was positioned further down in the water chamber. Based on the test measurements, the following value was

obtained for the peak pressure from the pneumatic impactor, 100 mm away from the impactor surface:

$$P_{trig} = 0.322 \pm 0.008\ MPa, \pm 2\ \% \tag{9.2}$$

This value gives the trigger pressure in each experiment, provided a measure for the vertical distance between the impactor and the location of the drop upon triggering exists.

9.5.2 The slug-type impactor

It was discovered during the 1999 experiments that drops of molten Si were much more difficult to trigger. Thus, the distance between the impactor and the drop had to be very small in order to achieve an explosion. But the small distance made imaging more difficult, and it was decided to build a stronger and more robust trigger, which was able to give larger pressure peaks. The description of this impactor was given earlier. Here we summarize the output as measured at a water depth of 400 mm, with the pressure transducer centered 100 mm above the impactor.

A test series was conducted after the new impactor was made (hereafter referred to as impactor 3). Compared to the pneumatic impactor, the pressure peak was considerably higher, as shown in figure 9.1. Two sets of measurements with the slug-type impactor are shown as the upper plots in figure 9.1. The earlier set, D-67-1, recorded when only gravity was used to reset the slug, showed considerable variation between the shots, with standard deviations of about ± 10 %. We then discovered that if we vented the driving gas from the gun barrel and applied a backpressure to the impactor's canister after each shot to reset the slug at the bottom of the barrel, the reproducibility between the shots improved significantly. This set is labeled D-69-1. The peak pressure values for the two cases, with or without backpressure, are, respectively:

$$P_{trig} = 1.81 \pm 0.14\ MPa, \pm 10\ \% \tag{9.3}$$

and

$$P_{trig} = 1.77 \pm 0.03\ MPa, \pm 1.5\ \% \tag{9.4}$$

It is evident that using a backpressure makes the output from our triggering source very reliable.

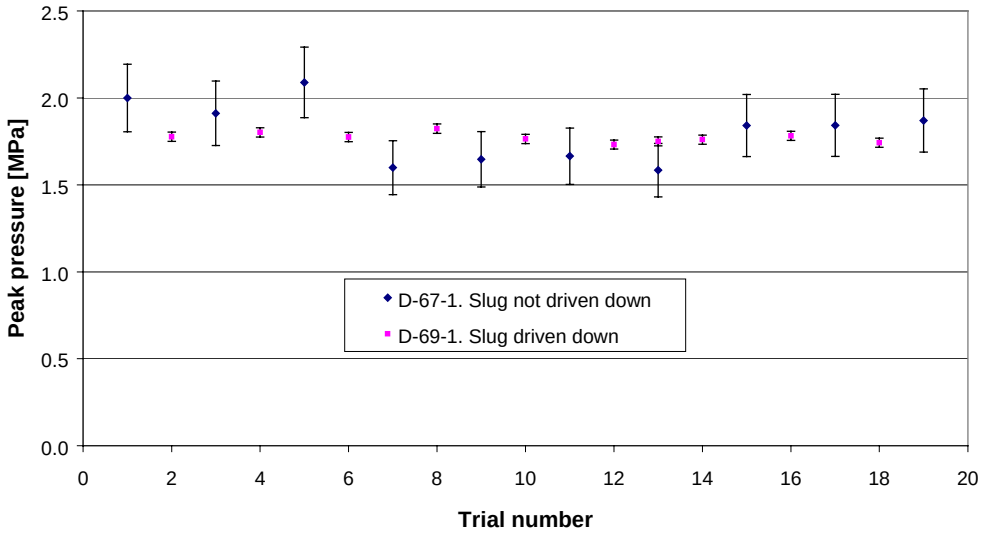

Figure 9.1 - Peak pressures from the slug-driven impactor, with or without applying a backpressure.

Following this test series, some minor modifications were done on impactor three, which slightly changed the output. New tests were carried out, with similar results as those presented in figure 9.1. Backpressures were always applied, also in the following drop release experiments. Thus, the pressure output from the modified version of impactor 3 is measured to be

$$P_{trig} = 1.963 \pm 0.037\ MPa, \pm 1.9\ \% \tag{9.5}$$

This value will be used in the discussion of all experiments performed in 1999 on the release of molten Si-drops. However, it was found that over time, the output of the impactor changed slightly, as did the calibration of the pressure transducer. Therefore, we had do repeat these test series for the 2000 experiments. For these experiments, we have used a value for the peak trigger pressure that is

$$P_{trig} = 1.694 \pm 0.069\ MPa, \pm 4\ \% \tag{9.6}$$

This value was quite consistent during the course (3-months) of the 2000 experimental program.

9.6 Thresholds for triggering steam explosions

One important aspect of this research program was to identify thresholds for triggering steam explosions, both for triggering strengths and depths in the water. The trigger pressure is decided by the vertical distance from the top of the impactor to the photodetector, as previously described. Here we assume that the output from the impactor is constant, with a value given in section 9.3.

In order to calculate the pressure at a given distance, we need an expression for the trigger pressure as a function of the distance. When the slug inside the gun barrel hits the steel plate, an acoustic wave will propagate through the water, similar to a sound wave. We assume that this wave propagates as a spherical wave, as the slug does not strike at the entire steel plate, only at a limited area in the middle. The intensity at a distance r from the source (center of the impactor, or center of an explosion) is given by

$$I = W_{av} / 4\pi r^2 \tag{9.7}$$

where W_{av} is the average power emitted by the source. If we assume no frictional loss of energy to the water, the power must be the same through any spherical surface centered at the source. Thus, intensities at distances r_1 and r_2 are given by

$$I_1 = W_{av} / 4\pi r_1^2 \tag{9.8}$$

and

$$I_2 = W_{av} / 4\pi r_2^2 \tag{9.9}$$

Combining eqs. (9.7) and (9.8), the ratio of intensities on these two spherical surfaces is

$$I_1 / I_2 = r_2^2 / r_1^2 \tag{9.10}$$

It can be shown (Serway, 1992) that the intensity in an acoustic wave travelling in water depends on the pressure amplitude P_m, the density of water ρ_w and the speed of sound in water v_{sw} in the following manner:

$$I = \frac{P_m^{\ 2}}{2\rho v} \tag{9.11}$$

Combining eq. (9.9) and (9.10), we obtain

$$P_{m,1} / P_{m,2} = r_2 / r_1 \tag{9.12}$$

With a given pressure at a known distance from the source, in this case 100 mm from the impactor, we can estimate the trigger pressure a molten drop experiences at any distance from the impactor, given that the drop is reasonably centered over the impactor.

However, if we take energy loss into the consideration, equation (9.12) is not valid. There is no straightforward way to calculate the correct relation in this case. Umetsu *et.al.* (1994) used a correlation proposed by Wakabayasi (1977) with a correlation coefficient obtained by Fujita (1983). Thus, the following expression were used to compensate for the pressure drop as the pressure wave propagates outwards from the center of the explosion:

$$P = P_m R^{0.709} \tag{9.13}$$

where P_m is the pressure measured by the pressure transducer, R is the distance between the center of the explosion and the pressure transducer, and P is the estimated pressure 10 mm from the center of the explosion. Equation (9.13) can also be formulated as

$$P_{m,1} / P_{m,2} = \left(r_2 / r_1 \right)^{0.709} \tag{9.14}$$

which allows for a direct comparison with equation (9.12). Figure 9.2 show calculated peak pressures resulting from various steam explosions using equation (9.12) and (9.14). We will in a later section use equation (9.12) to calculate all explosion impulses relative to a 100-mm separation from the center of the explosion. Depending on the actual location of the explosion, equation (9.12) and (9.14) will predict different values for the pressure as we move away from a 100-mm separation. Thus, in figure 9.2, two extreme cases are shown. In the first case (two lower curves) the peak pressure of the explosions was 0.8 MPa measured 75 mm from the explosion. We observe that equation (9.12) predicts a peak pressure 10% lower than that of equation (9.14). In the second case (two upper curves) the peak pressure of the steam explosion was 1.0 MPa measured 142 mm from the explosion. In this case, equation (9.12) predicts a pressure 11% higher than that of equation (9.14).

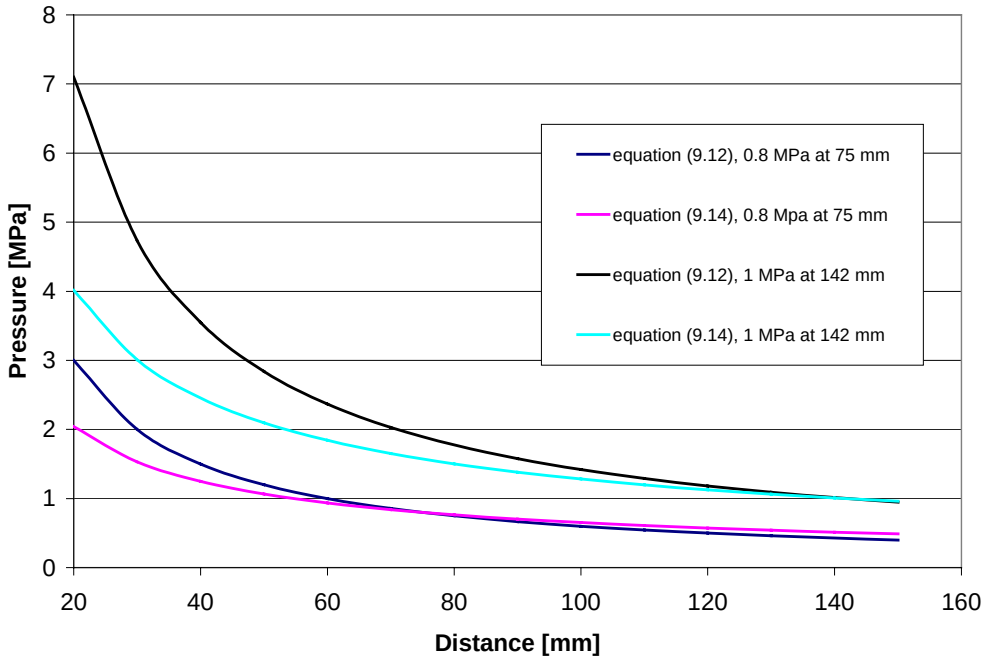

Figure 9.2 – Calculated pressure as a function of the distance to the center of the steam explosion, using measured pressure pulses resulting from steam explosions as input values.

If applied on any other experimentally obtained pressure values, equation (9.12) and (9.14) would give almost identical results for pressures around 100 mm from the explosion center. Thus, we believe it is a fair approximation to apply the more simple equation (9.12) when comparing pressures resulting from different steam explosions.

9.6.1 Ferrosilicon drops triggered with the pneumatic impactor

Using the pneumatic impactor, we were able to trigger steam explosions both for drops originating from the 10 and 16-mm test rods. A summary of the experimental outcome is given in table 9.13.

Table 9.13 - Explosiveness of ferrosilicon drops vs. fall distance in room temperature water. (O = no explosion, X = explosion.) See also table 9.1 for composition of the test rods from which the drops were released.

Triggering depth [mm]	***11-mm drops Alloy 1A***	***9-mm drops Several test rod compositions, see below and table 9.1.***		
	0.3 MPa	0.3 MPa	0.6 MPa	1.3 MPa
50				
100				OOOO
150	OXX	OOOOOO[1)] OOOO[2)]	OOOO[2)] OOOOOX[4)]	OOOOXX
200	OXX			XXX
250	OX			
300	OOOOXX	OO[1)] OOO[3)]		XXXX
350				
400	OOOXX			XXXX
450	OOO			
500	OO			XX
550				
600				
650				
700				XX
785 (Bottom)				XX

[1)] Test rod was alloy 1C, [2)] test rod was alloy F1/F2, [3)] test rod was alloy F8, [4)] test rod was alloy B, see table 9.1 for element analysis. In the last column, alloy B was used for all cases.

It is recognized that table 9.13 by no means offers a complete picture of the triggerability at various depths, nevertheless, some conclusions can be made. First, we note that 11-mm drops of molten ferrosilicon could be triggered to explode 100 mm above the pneumatic impactor. The trigger pressure was approximately 0.3 MPa, as given by equation (9.2). We did not achieve explosions in every case; thus, we were probably close to the threshold trigger pressure. This threshold will in general not be a consistent value, it is more correct to say that the likelihood of an explosion decreases as the trigger pressure goes down. Thus, the first column in table 9.13 reflects the fact that in 50 % of the cases, the drop exploded as a result of being triggered with a pressure pulse of 0.3 MPa. It also seems like that the depth at which the drop was triggered does not play an important role; explosions were triggered from 150 down to 400 mm. At deeper water levels, we did not perform any more

experiments; thus, there is no basis to claim that steam explosions of molten 11-mm ferrosilicon drops cannot occur at water levels below 400 mm.

When we tried to repeat the experiments for 9-mm drops, some interesting results were found. The most important result was that we were not able to trigger steam explosions using a 0.3 MPa pressure transient, for any of the drops released. The triggering was only executed at water levels of 150 and 300 mm, as shown in table 9.13. At such shallow water solidification should not be of any concern. In order to obtain explosions, we decreased the vertical distance between the submerged photodetector and the surface of the pneumatic impactor to 50 mm, thus doubling the trigger pressure as described in the beginning of section 9.4. This time we only triggered at very shallow depths (150 mm). Still, only one out of ten exploded.

We then doubled the trigger pressure again, moving the submerged photodetector down to 25 mm above the surface of the impactor. With a peak pressure of 1.3 MPa, we were able to trigger several explosions, for a total of 19 out of 27. It was possible to trigger explosions at all water depths, except in shallow water (50 and 100 mm). Thus, it seems like that the threshold trigger pressure is somewhere between 0.6 and 1.3 MPa. Without further experiments, it is not possible to narrow down this value. However, based on the fact that the explosions occurred with a high degree of probability when a trigger pulse of 1.3 MPa was applied, the threshold pressure is probably somewhat lower, maybe between 0.7 and 1 MPa.

The effect of the drop diameter to the trigger pressure threshold is worth some comments. Again, referring to table 9.13, we see that 9-mm drops require roughly four times the trigger pressure as their fellow 11-mm drops. This effect is probably due to the greater stability of the boiling film that surrounds smaller drops (Gunnerson, 1979). Thus, a stronger pressure pulse is required with smaller drops to collapse the film and cause the liquid-liquid contact that initiates the explosion. Also, when we look at the compositions of alloys 1A and 1C (table 9.1), these are almost the same. Still, no explosions were detected for the 9-mm drops at 150 mm, using a trigger pressure of 0.3 MPa. For 11-mm drops, explosions were readily obtained. Thus, the lack of explosions for the 9-mm drops cannot be related to composition differences.

When the applied trigger pressure was 0.6 MPa, drops from alloys of similar composition (F1/F2 and F8) compared to alloy B were difficult to trigger at 150 mm. When the trigger pressure was doubled, explosions were more likely to occur, the probability being 0.33 vs. 0.1. But again, we stress that more statistical evidence is needed before we can make more conclusive statements regarding the trigger pressure dependence on the probability of a steam

explosion involving water and this particular alloy composition. Still, it seems fair to say that the drop diameter plays an important role; small drops require larger trigger pressure transients in order to explode.

Regarding threshold depths vs. drop diameter, it is our opinion that we lack results to justify any claims. From table 9.13, one might draw the conclusion that 11-mm drops cease to explode when triggered lower than 400 mm, whereas 9-mm drops can be triggered all the way down to 785 mm, which is the deepest trigger level with the actual apparatus. This effect could be explained by a lower cooling rate for the smaller drops than for the larger ones due to the effect of drop diameter on film boiling heat transfer. Thus, smaller drops would be in a molten state for a longer time, allowing triggering at deeper water. Also, the more pure B-alloy might be able to supercool to lower temperatures than alloy 1A. This will increase the time the drop is still molten, thereby increasing the distance it will sink in water and still be possible to trigger.

9.6.2 Ferrosilicon drops triggered with the slug-type impactor

In 2000, we used both drops of molten Si and FeSi75. The focus was not on triggering thresholds, as we thought they were quite well established through the results of 1998 and 1999, however, such information was still available, and is discussed below.

Since we focused on other parameters than triggering thresholds, we always used quite strong trigger pressures to make sure an explosion was obtained. The trigger pressures were between 1.7 and 3.4 MPa, and in 11 out of 12 experiments the molten drop exploded, which give an explosion probability of 92 %. Strangely enough, the only time the drop did not explode, the conditions were quite similar compared to the strongest explosion in the series. Again, we can only explain this with the stochastic nature of the steam explosion.

9.6.3 Silicon drops triggered with the pneumatic impactor

All of the drop releases experiments in 1999 were carried out using silicon drops. The compositions of the Si-alloys that were used are given previously in table 9.2. We started out using the pneumatic impactor, and triggered the molten drops at different depths in the water. In figure 9.3, the trigger pressure is plotted vs. the trigger depth, with the outcome indicated in the figure. We note that a trigger pressure of 2.1 MPa is necessary to initiate an explosion. This is far more than the ferrosilicon drops required as described in section 9.6.1.

There is only one overlap of non-explosive events and explosions, this happened at a trigger depth of almost 400 mm and a trigger pressure of 2.1 MPa. Further, four cases of coarse fragmentation were observed, but these occurred at a rather small trigger pressure, and thus are not located between explosion and non-explosive events, as might be expected. Thus, they appear somewhat mysterious. The water depth at which they fragmented is very shallow, but it is not quite understood why this would cause the drop to fragment compared to other drops, triggered with the same trigger pressure deeper down in the water chamber.

These experiments initiated the use of a stronger trigger source, as the molten drops had to be triggered very close to the impactor surface. This obscured our images somewhat; also, the error arising from the measured distance from the center of the explosion to the surface of the impactor had a strong influence on the estimated trigger pressure. It was therefore desirable to use a stronger trigger in order to move the explosions away from the impactor, thus getting more precise data for the trigger pulse.

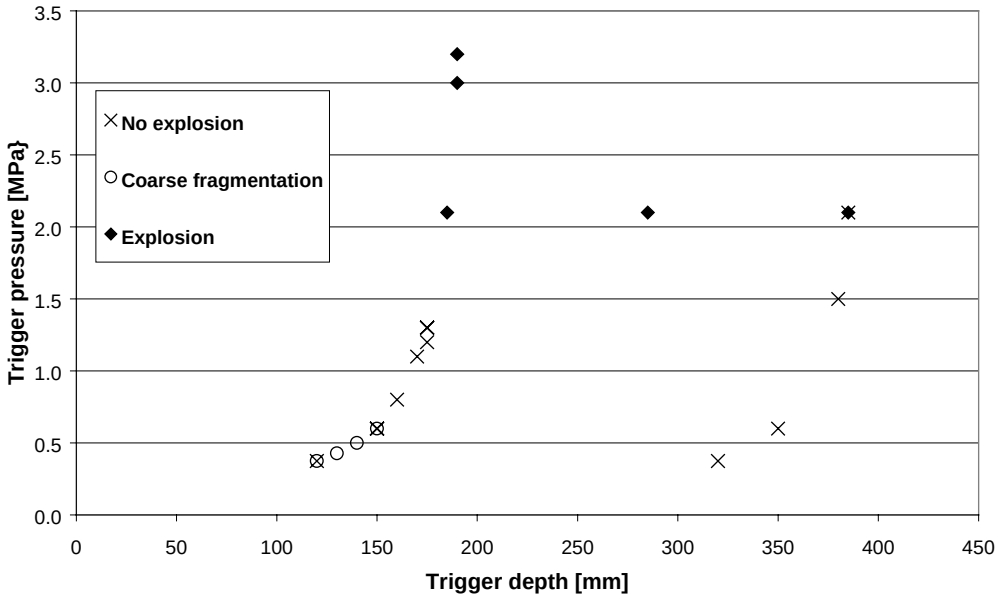

Figure 9.3 – Silicon drops released into water and triggered with the pneumatic impactor, at various depths and trigger pressure, and the resulting melt-water interaction.

Figure 9.3 indicates that we have found a trigger threshold for drops of molten silicon to be around 2.0 MPa. Still, more data is required to narrow down this threshold range or to establish the water depth dependence (cooling time).

9.6.4 Silicon drops triggered with the slug-type impactor

In figure 9.4, the trigger pressure vs. trigger depth is plotted for molten silicon drops released into water and triggered using the more powerful slug-type impactor. Compared to the results shown in figure 9.3, it seems as these drops required *higher* trigger pressures. The data are somewhat sparse around 2.0 MPa, but it is interesting to note that in one case, the trigger pressure was just over 3.2 MPa, still the drop did not explode or fragment. Also, only a coarse fragmentation was obtained with an applied trigger pressure over 4 MPa. These results show clearly that a vapor explosion is a stochastic process, and most questions concerning this phenomenon require answers of a statistical character.

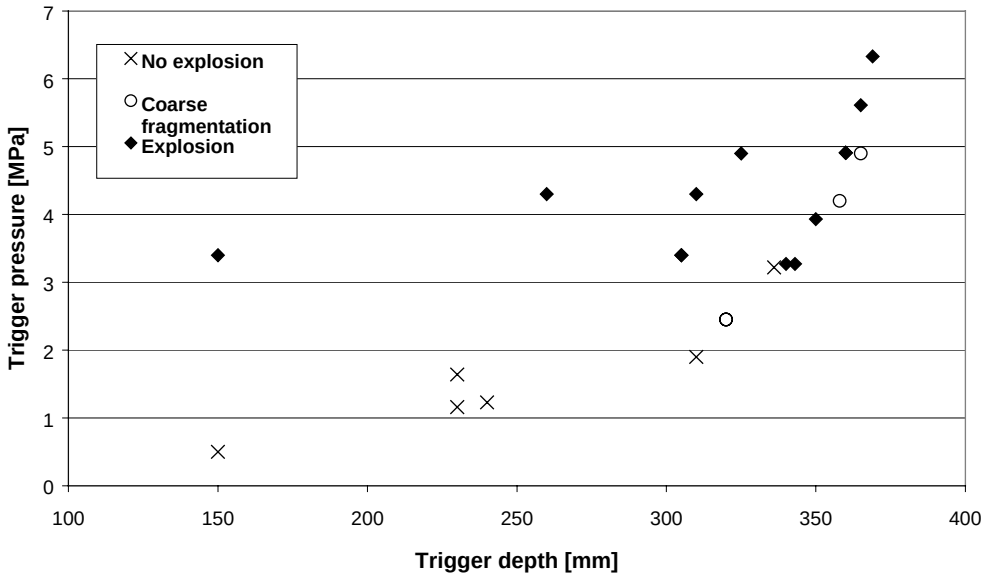

Figure 9.4 - Silicon drops released into water and triggered with the slug-type impactor, at various depths and trigger pressure, and the resulting melt-water interaction.

If we now plot the trigger threshold for both of the impactors used, using the water depth at which the interaction was triggered, we obtain the plot shown in figure 9.5. The following features are emphasized:

- *No explosions occurred when the trigger pressure was less than 2.0 MPa*
- *When the trigger pressure was between 2.0 and 3.3 MPa, the probability for a steam explosion was 78 % (7 out of 9 drops exploded, one fragmented coarsely).*

- *Above a trigger pressure of 3.3 MPa, 4 out of 5 drops exploded. (The only drop that didn`t, fragmented coarsely. However, this drop fell far to the left, and did not hit the impactor. So it is very likely it experienced a lower trigger pressure than the vertical distance from the surface level of the impactor indicated.)*

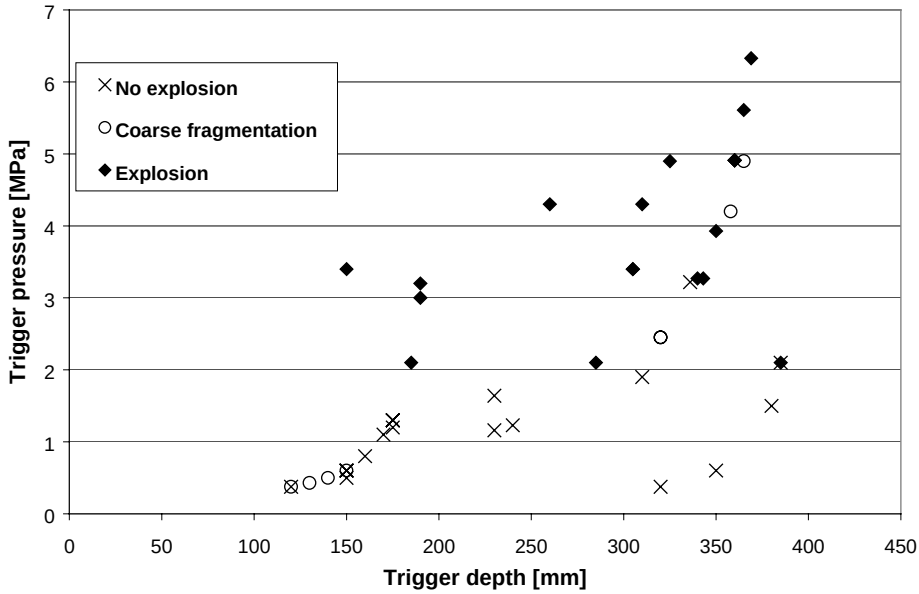

Figure 9.5 – Silicon drops released into water and triggered (using either the pneumatic or the slug-type impactor), triggered at various depths and trigger pressures, and the outcome of the triggering process.

Using alloyed silicon (compositions given in table 9.2), we performed three drop-releases for each of the alloys. We were not able to trigger a steam explosion for any of the alloys, even with very high trigger pressures. The results for alloyed silicon are given in table 9.14. The surface of the impactor was located at 400 mm water depth for each of the experiments, and the interaction thus took place between 300 and 400 mm.

Table 9.14. Trigger thresholds for alloyed silicon drops.

Alloy	*Trigger depth [mm]*	*Trigger pressure [MPa]*	*Type of interaction*
B	333	2.9	None
B	361	5.0	Coarse fragmentation
B	381	10.3	Coarse fragmentation
C	342	3.2	None
C	371	6.8	Coarse fragmentation
C	338	9.3	Coarse fragmentation
D	333	2.9	None
D	359	4.8	Coarse fragmentation
D	378	7.1	Coarse fragmentation

Trigger pressures of the order 3 MPa, which for a non-alloyed drop would have an 80 % chance of triggering an explosion, where not sufficient to trigger alloyed silicon. The drops did not even fragment. However, at elevated trigger pressures (~ 5 MPa or more), the drops did fragment, but explosions were not obtained even for trigger pressures as high as 10 MPa. Thus, we conclude that it is not possible to trigger steam explosions using alloyed silicon-drops, at the trigger pressures investigated. The effect of water depth is not expected to be of importance, even though more shallow water will decrease the ambient pressure slightly. As discussed earlier, the likelihood of a steam explosion falls with increasing ambient pressure.

9.6.5 Threshold depths for triggering molten drops of Si/FeSi75

We have already showed that molten drops of ferrosilicon could be triggered all the way down to the bottom of the tank. An interesting phenomenon was observed, using the shutter wheel camera technique described in an earlier chapter. A molten drop of ferrosilicon was triggered (experiment D-24-1) at water depth of 785 mm, and it exploded. Photographic evidence shows that the drop had started to solidify (figure 9.6).

Figure 9.6 shows that the drop first fell uniformly as a completely molten globule (upper arrows), then started to tumble 1.67 seconds after water entry as a partially solidified “lozenge” (center arrow) before it was triggered and exploded 2.33 seconds after water entry as it crossed the photodetector axis 25 mm above the impactor (lower arrow).

That partially solidified drops can be triggered and participate in a steam explosion has also been observed for other materials. The steam explosion of a partially solidified drop of laser-melted iron oxide has been reported by Nelson and Duda (1985).

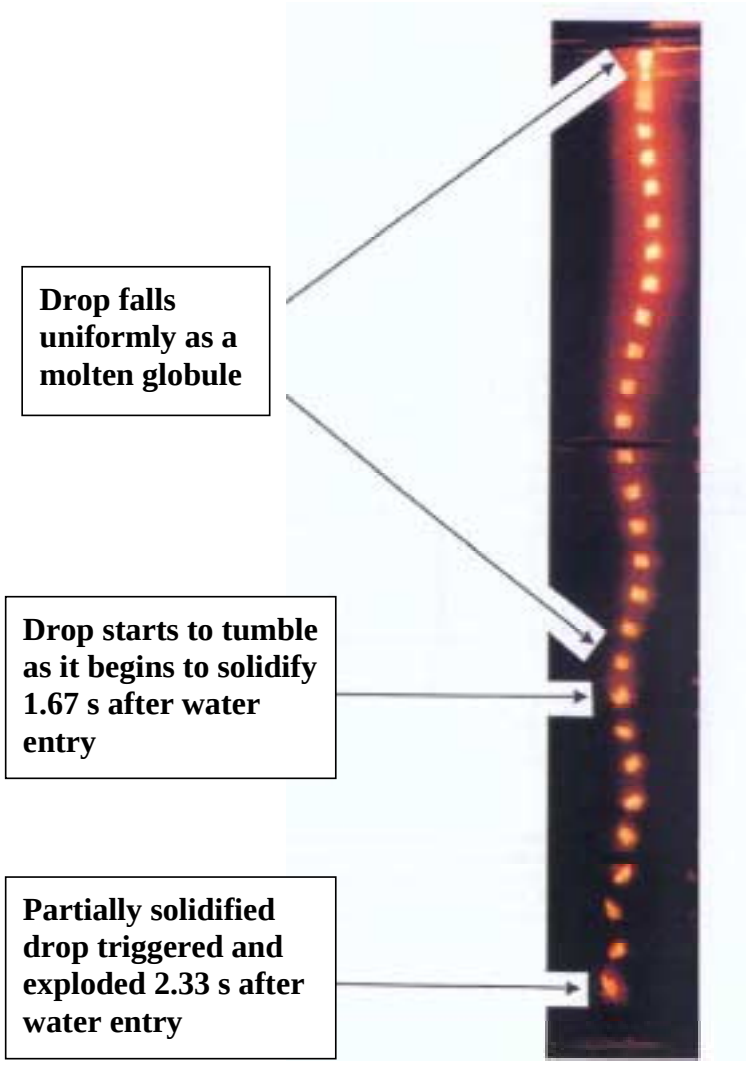

Figure 9.6 – Enlargement of the shutter wheel photography of the 9 mm-diameter drop of alloy B (FeSi75), triggered at 785 mm water depth.

Based on the results given so far, we conclude that we have not found a threshold depth for drops of molten FeSi75, but we note that the drops have started to solidify. This indicates that we are getting close to a threshold depth, or more precise, the cooling time is long enough for a solid shell to form on the surface of the drop.

For silicon drops, we performed only a few experiments at the lowest water depths (see table 9.7 and 9.8). In one experiment, the impactor was placed at the bottom of the water chamber. Two drops were released in this experiment

(D-50-1); one missed the impactor and did not trigger the photodetector, the other fell onto the impactor, and was triggered 0.2 seconds later. Only a fragmentation took place, even though the trigger pressure must have been very high. This indicates that the drop more or less was solidified, but the strong pressure could have caused the globule to fragment physically, and exposed the rest melt (if any) to water. However, the amounts of melt left were probably too small to cause any rapid steam generation.

In another experiment, the impactor was located at 500 mm. Here, the drop was triggered just above (a few millimeter) the surface of the impactor, i.e. a very high trigger pressure, though no good measurement exists. Again, the drop only fragmented coarsely. The same thing happened when we repeated the experiment (D-62-1 and D-64-1). Thus, we more or less disregarded the possibility of initiating steam explosions below a water depth of 400 mm, as the drops had already started to solidify considerable.

9.7 Fall velocities for molten drops of Si/FeSi

As mentioned in the last section, molten drops of FeSi75 can be triggered at a lower water depth compared to Si. Before we can attribute this to an intrinsic property difference between the two alloys, we need to examine in more detail the cooling times involved. By examining the fall velocities, we can find out whether the cooling times for the alloys are of the same order. The fall velocities are easily obtained from our video recordings, just be counting the number of frames it takes for the drop to enter the water and till it passes a specific spot in the tank, i.e. a crossbar used to support the water chamber. Thus, we will be able to find an average velocity.

9.7.1 Fall velocities for molten Si

We found some very interesting results when we investigated the fall behavior of molten Si-drops. It turned out that alloyed drops fell *twice as fast* as their non-alloyed companions did. This is illustrated in figure 9.7, where the fall velocity is plotted vs. the mass of the drops.

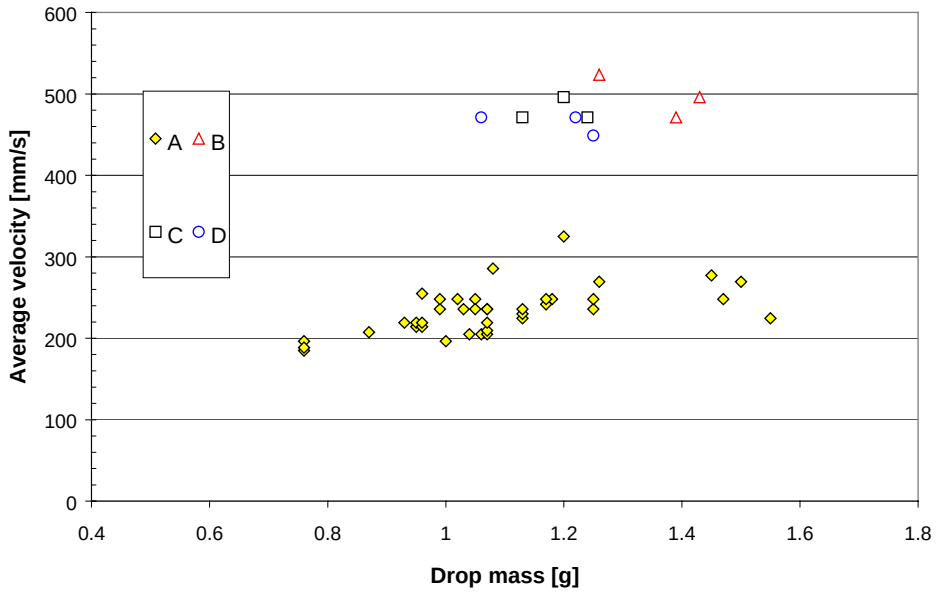

Figure 9.7 – Average fall velocities for molten drops of silicon released into water.

The compositions A, B, C and D are as given in table 9.2. Quite unexpected, the average fall velocity for alloyed drops are 480 mm/s compared to non-alloyed drops, which have an average velocity of 233 mm/s, a factor two difference. Although there is some scattering in the data, the trend is very clear. We see that there is no particular mass dependence, as expected from the discussion in chapter 5.1. If a trend line is added, the mass dependence is $M^{0.4}$, somewhat more than for a spherical drop. This merely confirms that the molten drops do not form perfect spheres.

Also note that as far as the alloyed drops are concerned, they seem to fall with the same rate, regardless of the composition. Drops with only small additives of Al and Ca (alloy C) fall with the same speed as drops from alloy D.

9.7.2 Fall velocities of molten ferrosilicon

Molten drops of FeSi75 did not differ that much in average fall velocity when comparing non-alloyed and alloyed drops as the silicon-drops. Still, the same trend was observed; alloyed drops fell faster than non-alloyed drops. The data are somewhat limited compared to what we have for silicon drops, this is mainly due to experimental procedures. First, we do not have accurate measures for the mass of the drops. In some of the experiments, several drops were released and triggered, thus, we only have an average drop size based on

the number of drops and the rod loss, i.e. the difference in rod-weight before and after the experiment. We have therefore chosen not to include the drop mass in figure 9.8, which shows the fall velocity for alloyed and non-alloyed drops of molten ferrosilicon. One remark on the composition of the alloyed material; this was from a rod used in the 1997 experiments, thus, it is not given in table 9.1. Its composition was 73.8% Si - 25.4% Fe - 0.34% Al - 0.07% Ca.

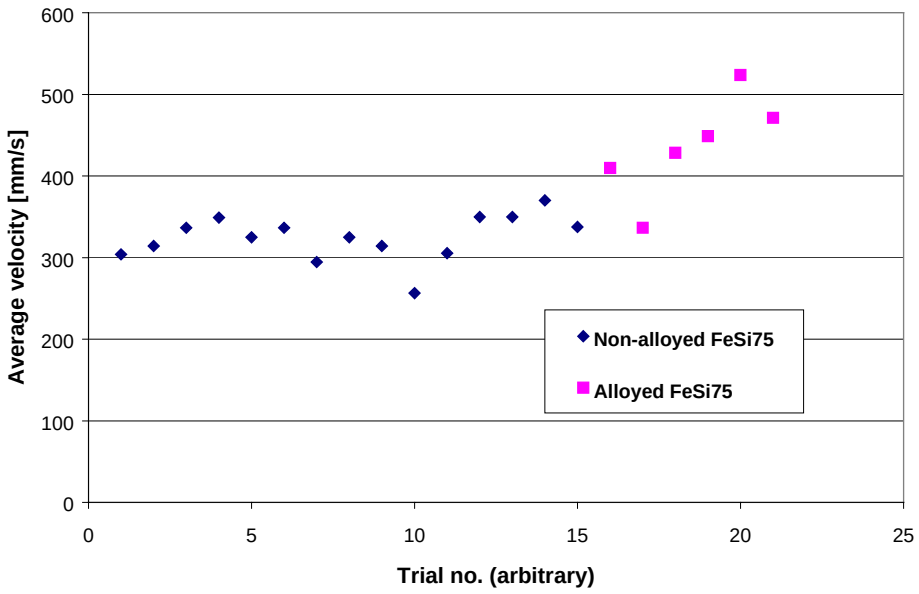

Figure 9.8 – Average fall velocities for molten drops of ferrosilicon (FeSi75) released into water.

The average velocity for non-alloyed drops is 325 mm/s, while for alloyed drops it is 436 mm/s. This difference in fall velocity is smaller than for the case of Si, but still quite remarkable. In figure 9.9, we show registered average fall velocities for both Si and FeSi75 (omitting any mass-dependence, which is quite negligible anyway). Note that the impurity levels in the alloyed drops are not the same, but the results described in section 9.6.2 indicate that the amount of impurities is not that important, as long as it is over a certain level, which still remains undisclosed.

From figure 9.9, we see that fall rates of FeSi are somewhat higher than for drops of Si of the same size. However, when we add Al and Ca to the melt, the fall rates for molten drops of FeSi and Si are quite the same. To explain this peculiar behavior, it is obvious that the impurity levels (Al and Ca) are very important. This will be commented upon in a later section, here we merely list two important factors that may influence strongly on the fall rate of the drop. The first is the drop`s overall increased ability to react with vapor and form

hydrogen. A different gas composition in the vapor layer around the drop may change the fall velocity. Second, the shape of the drop may change due to a change in surface properties.

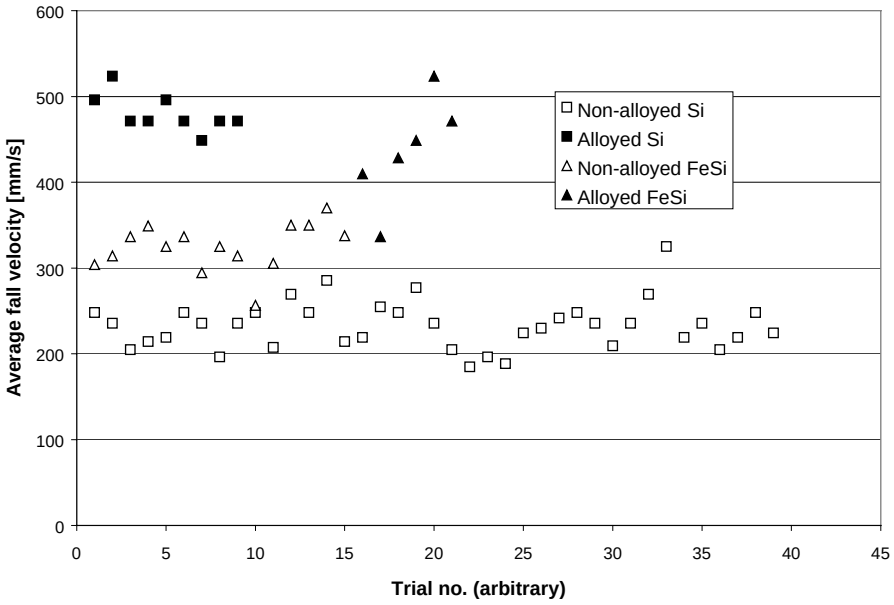

Figure 9.9 – Average fall velocities for both molten drops of Si and FeSi75.

However, we can for now offer only speculations to explain the behavior of drops as observed from figure 9.9. We are at the present time not able to explain the remarkable change in fall velocity with small changes in composition is.

9.8 Generation of hydrogen by molten drops of Si/FeSi

When molten drops of metal are released into water, the melt will react with the vapor film that surrounds the granules. To estimate how much hydrogen that is formed for a particular amount of melt is quite important, both from the standpoints of plant safety and the chemical behavior of the melt.

The video recordings from several experiments showed consistently that bubbles of hydrogen-gas were formed during the fall of the drop in water, both for Si and FeSi. As the drop was descending down in the water, a train of bubbles was released from the molten drop and rose steadily to the surface. Efforts were made to estimate the total volume of these bubbles, based on direct measurements from the video recordings. However, this method is not

very accurate, so the hydrogen-collector was developed (described previously in section 7.4). Thus, we were able to measure the volume of hydrogen generated, regardless of the type of interaction.

When the molten drops were released into water, the sizes and numbers of the hydrogen bubbles depended primarily on the triggering pulses applied to the drops of melt as they fell through the water:

(a) When no pulse or only a low trigger pulse was applied, the drops did not fragment; only a train of bubbles, each several millimeters in diameter, was released as the drop quenched.
(b) When a drop was exposed to a mild trigger pulse, it fragmented coarsely, and larger hydrogen bubbles were formed. Sometimes these coarse fragments burned luminously and rose within bubbles that presumably contained both hydrogen and steam, producing "sea-weed like" photographic images of the sort shown in figure 9.33-34.
(c) When the triggering transient was strong enough to initiate a vigorous explosion, hundreds of tiny bubbles about 1 mm in diameter were generated. These bubbles rose individually and broke trough the surface of the water without coalescing.

Typical results for the generation of hydrogen, depending on the type of interaction is shown in table 9.15.

Table 9.15 – Amounts of hydrogen generated during the interactions of single 9 mm-diameter drops of molten silicon and ferrosilicon. Alloy compositions for silicon are given in table 9.2. (Taken from Nelson et.al, 2001.)

Type of interaction	***Silicon***	***Alloyed silicon***	***Ferrosilicon***
(a) Benign solidification	1 ml	B: ~ 2 ml C: ~ 2 ml D: ~ 2 ml	~ 2 ml
(b) Coarse fragmentation	2-3 ml	B: ~ 6 ml C: ~ 4 ml D: ~ 7 ml	No measure
(c) Vigorous explosions	~ 5 ml	B: ~ 6 ml C, D: No measure	2-4 ml

The amounts of H_2-gas generated in these interactions were never large. As indicated in table 9.15, about 1 ml was generated when a drop of non-alloyed silicon quenched benignly and perhaps 2 or 3 ml when the drop was exposed to a small trigger and fragmented coarsely. Even in the most vigorous

explosions of drops of nonalloyed silicon, the volumes never exceeded about 5 ml (at all room temperatures and a local atmospheric pressure of 0.1 MPa). The obvious reason that hydrogen generation is enhanced in the case of coarse fragmentation or explosions, is the increase of surface area of the melt.

When the silicon was alloyed with small amounts of Al and/or Ca, the amounts of hydrogen generated were somewhat larger. As indicated in table 9.15, about 2 ml was generated when a drop of alloyed silicon quenched benignly and up to 6-7 ml when the drop was exposed to a trigger pulse and fragmented coarsely. And in the one case of a steam explosion with alloyed silicon, the volume of hydrogen generated was only 6 ml.

In order to provide a conservative estimate of the explosion hazards involved, we assume that 6 ml H_2 is generated during a vigorous steam explosion. This volume corresponds to $6/22400 = 2.7\times10^{-4}$ moles of H_2. If we assume that the reaction $Si + H_2O \rightarrow SiO + H_2$ is the main oxidation reaction, the formation of this amount of hydrogen would indicate that 2.7×10^{-4} moles of silicon has been oxidized. Since a 1.1 g drop of $Si = 1.1/28 = 0.039$ moles, the fraction of the drop oxidized is at most about 0.7 %.

Although the amount of hydrogen generated per drop is not large, it must be multiplied by the total number of drops involved at a given time during industrial granulation. Thus every kilogram of molten silicon (roughly thousand 9 mm-diameter drops) that quench in water at room temperature without fragmentation or explosion will generate up to 2 liters of hydrogen. Considering the easy ignition and explosiveness of gaseous hydrogen when mixed with air, this is a hazard that requires appropriate precautions.

9.9 Colloidal material

By weighing the test rods prior to and after an experiment, we are able to find the mass of each drop released, which of course is quite important. If a drop quenches without being exposed to a trigger pulse, the final granule will have the same mass as the measured rod loss, within our error limits (0.01 grams).

In the case of an explosion, the fine debris that forms will eventually sink and land on the collector pan on which the impactor is located. The pan is removed from the tank after the experiment and dried before the debris is collected. During the very first experiments, back in 1997, it came as a surprise that following a steam explosion, we were *not* able to find the same amount of metal that the rod loss indicated. Apparently, the small fragments were

suspended in the water, probably as very tiny particles that did not sink, but merely floated around.

Based on the numbers given in tables 9.5, 9.6 and 9.10, we can calculate the loss of drop mass for each explosion obtained, and we assume that the entire loss is in the water as colloidal material. Some of the numbers are based on an averaged drop mass, i.e. we released up to six drops in some of the experiments, and obtained up to three explosions. Now, since we do not have an exact weight for each of the drops, we are forced to average the rod loss over the total number of released drops. In the case of several explosions during one experiment, we assume that the amount of colloidal material resulting from each of the explosions is the same. In figure 9.10, the amount of colloidal material (or loss of drop mass) for all of the explosions obtained is shown, except for a few experiments where we do not have all the necessary data available.

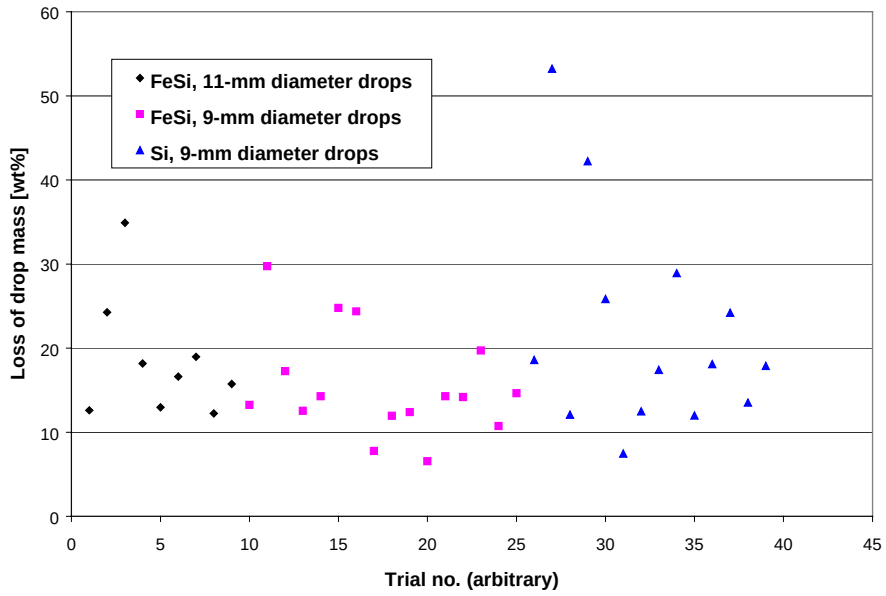

Figure 9.10 – The loss of drop mass for different alloys to the water as colloidal material following a steam explosion.

In the case of ferrosilicon drops, the mass loss is typically between 10 and 20 %. There appears to be no particular effect of drop diameter. For silicon drops, typical mass losses are in the range of 10 to 30 %, but we see that in one case, over 50 % of the drop mass was not recovered from the water. This explosion was very powerful, as experienced in the lab and from the images that were taken. So we expect that the more powerful the explosion is, the more of the initial drop mass is suspended in the water as colloidal material. This will be

discussed in section 9.10, which deals with the energy that is used to form steam bubbles upon fragmentation of the drop.

9.9.1 X-ray analysis of the colloidal material

Efforts have been made in order to capture this material and analyze it. Nelson (1998) observed that the colloidal material appeared on the reflected light video and on photographic images as long lasting turbidity in the water. It could in some cases also be seen visually. This material seemed to have a very fine particle size because it did not settle from the water, even over a span of several days. This material was difficult to separate from the water by filtration, as it tended to clog the filter media. Therefore, Nelson and his group decided to boil down the entire water chamber (around 90 liters) to get to the suspended debris. This was the last effort made that year, and the water chamber thus contained colloidal material from several steam explosions. This material was investigated with X-ray diffraction (Fig. 9.11) at the Department of Materials Science and Engineering at the University of Wisconsin-Madison. The results of these analyses were then compared to X-ray analyses of the starting material (Fig. 9.12), analyzed at Michigan Technological University, Houghton, MI, USA. Debris resulting from a vigorous steam explosion and a coarse fragmentation has also been analyzed, but in all cases the X-ray patterns appeared identical to that of the starting material.

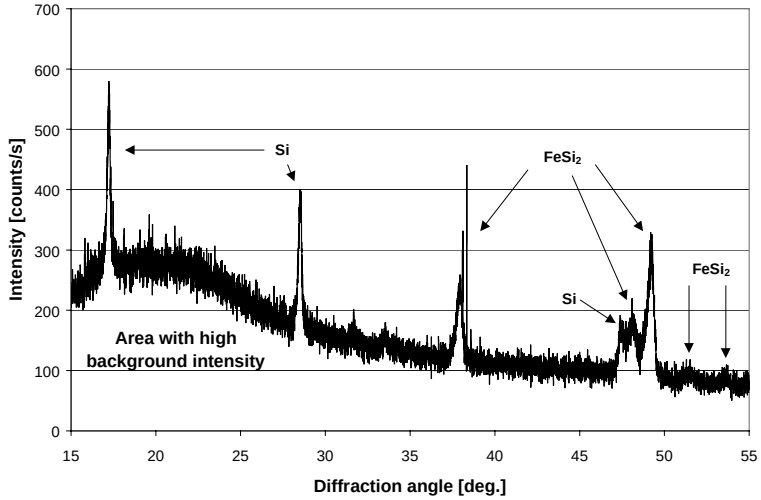

Figure 9.11 – X-ray diffraction pattern from the residue that remained after boiling dry the 93 liters water filling recovered from the chamber in 1997. A number of steam explosions of molten ferrosilicon had occurred in this water, leaving 10 to 20 % of the mass of each drop suspended in the water as colloid.

The crystalline patterns in figure 9.11 were identified with the appropriate software to correspond to Si and $FeSi_2$, the two stable phases for FeSi75. These patterns are identical to those of the starting material (figure 9.12). However, the pattern in figure 9.11 has a significant broad area with high background intensity at low diffraction angles. This "hump" probably results from the presence of non-crystalline material, such as amorphous materials or crystals that have particle sizes too small to produce discrete line patterns. The most likely amorphous material to be produced in a steam explosion of the Si-rich alloy would be SiO_2 formed by gas-phase combustion. Materials with other Fe-Si-O compositions might also have been deposited in an amorphous or fine crystalline state.

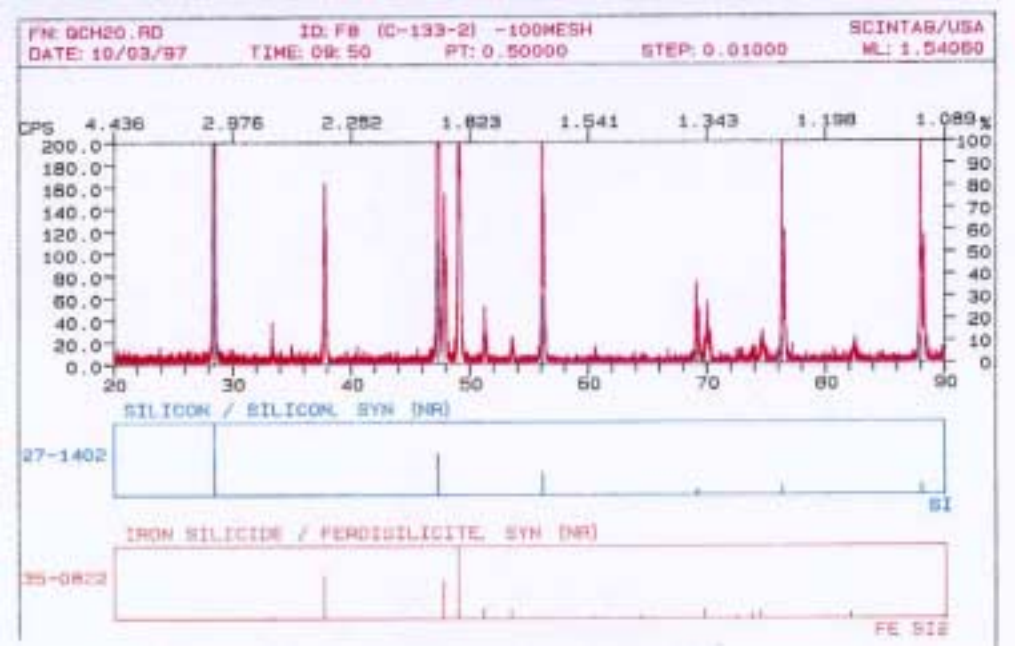

Figure 9.12 – X-ray diffraction pattern of the starting material, FeSi75.

Thus, we believe that some of the fine, colloidal material that stays suspended in the water is very small particles of an amorphous character, resulting from the underwater combustion of the melt. This is consistent with the generation of hydrogen gas that is observed. However, the amount of hydrogen generated is not consistent with an up to 20 % loss of mass for the ferrosilicon drops.

We have not performed X-ray analysis on the colloidal material resulting from steam explosions of molten drops of silicon. Experimental results clearly indicate a gas-phase combustion (chapter 10), which would explain the

formation of small, oxygen-containing particles. But also here, the measured amount of hydrogen is too small to account for gas-phase combustion as the only origin for colloidal material.

The deposition of colloidal products is unusual during steam explosions. It does not seem to form when drops of other melts explode, for example, molten iron oxide (Nelson and Duda, 1982) and aluminum (Nelson, 1995).

9.9.2 Sieve analysis of the colloidal material

Samples of fragmented metal were collected from various types of melt-water interaction events, including both violent explosions and coarse fragmentation. These were analyzed at the Department of Process Metallurgy and Ceramics, SINTEF, Trondheim, Norway. Sieve analyses were conducted on six different samples of silicon metal, and their particle distribution is reproduced in figures 9.13-9.18.

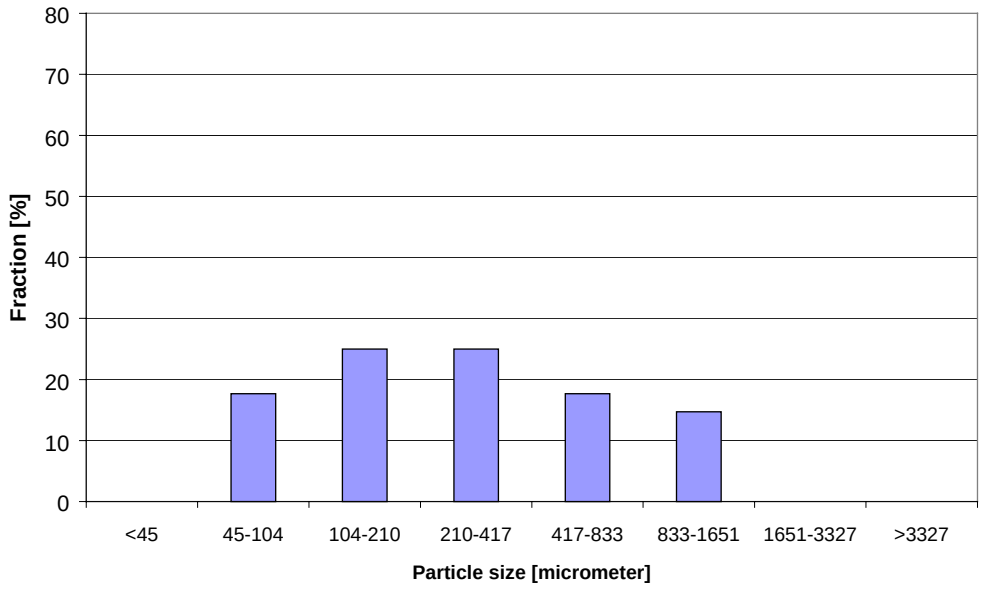

Figure 9.13 – Particle size distribution for an exploded drop of silicon, experiment D-107-1.

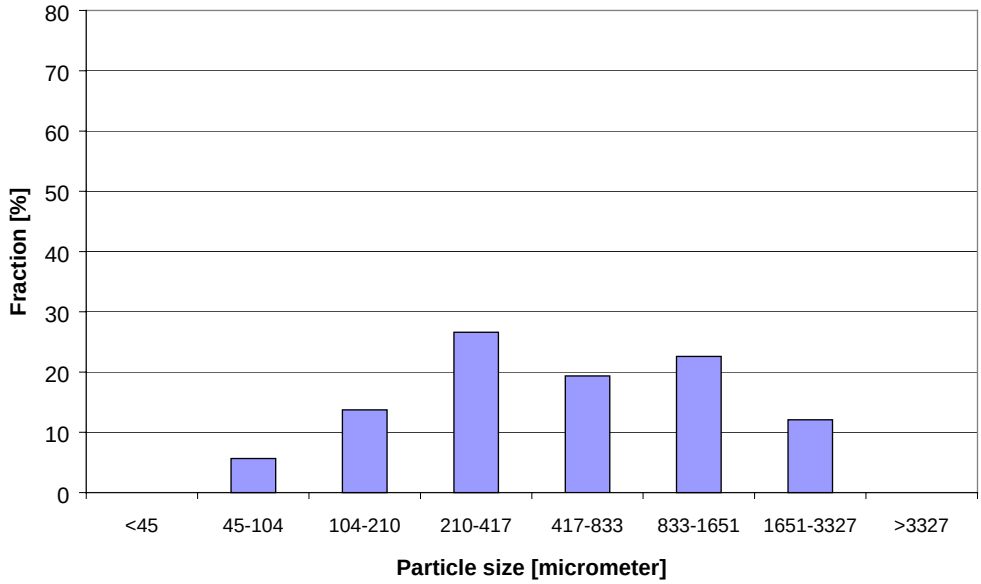

Figure 9.14 – Particle size distribution for an exploded drop of silicon, experiment D-123-1.

Figures 9.13 and 9.14 show the particle size distribution for two steam explosions of pure silicon (alloy A, table 9.2). They appear similar, but we note that the explosion that occurred in experiment D-107-1 seems to have produced finer debris than in experiment D-123-1. Further, the particle size distribution does not contain any particles less than 45 μm-diameter, furthermore, the distribution is somehow "cut off" for the smallest interval, i.e. the amount of material in the 45-104 μm is relatively large, taking into account that the smallest interval (<45 μm) does not contain any particles. Thus, it seems likely that loss of material indeed is related to the fine fragmentation of the melt. Apparently, particles less than ~ 50 μm do not settle in the water. The amount of material not recovered from the water was about the same in each of the experiment (around 0.30 grams), but the drops differed in weight (1.26 vs. 1.55 grams). However, as will be discussed later in this section, there are errors involved in the sieve analysis procedure, which force us to question the validity of the results presented here.

In one case we also achieved a steam explosion with alloyed silicon. The particle size distribution is shown in figure 9.15. It has many of the same features as its "colleagues" (figs. 9.13-14). But the fraction of particles in the 45-104 μm-diameter interval is almost zero. Also, the overall distribution is shifted to the right. This is very consistent with the fact that no loss of mass was detected, i.e. the weight of the debris matched the weight loss of the test

rod. Thus, it seems as the small addition of aluminum prevented particles less than 100 μm to form upon fragmentation.

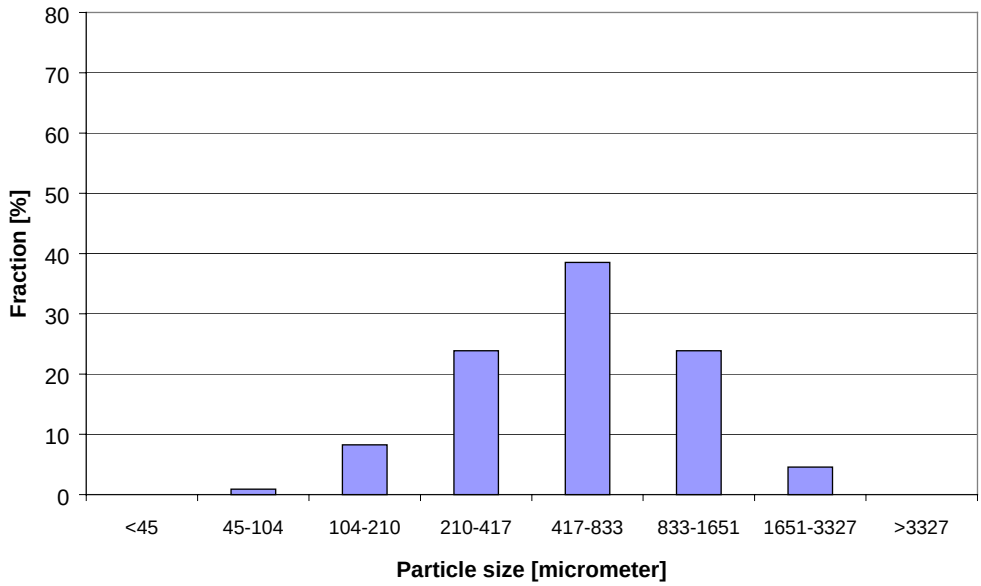

Figure 9.15 – Particle size distribution for a weak steam explosion of an alloyed drop of silicon (alloy B, Si+0.4 % Al, see table 9.2), experiment D-130-1.

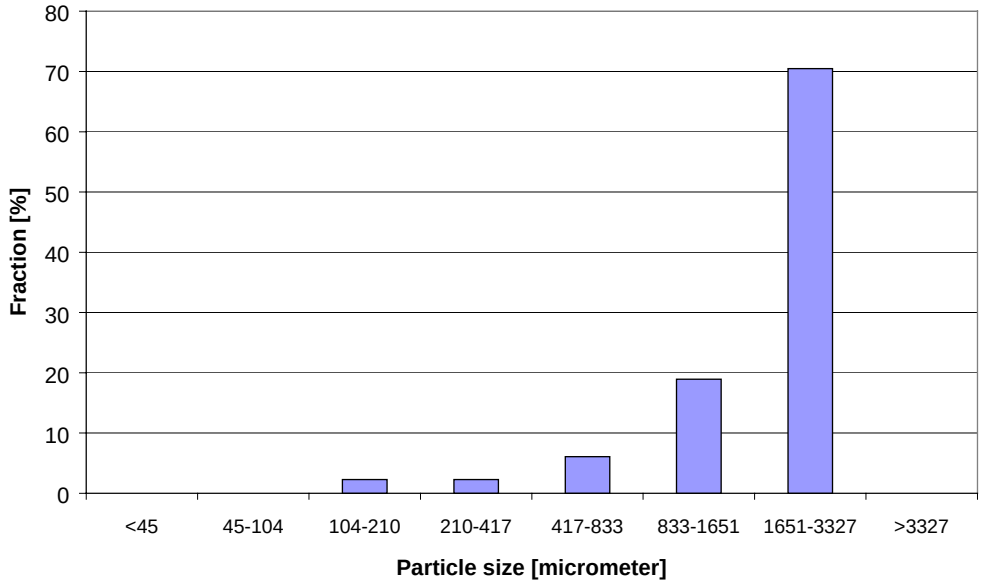

Figure 9.16 – Particle size distribution for a coarsely fragmented drop of pure silicon, experiment D-120-1.

The drops that do not explode (e.g. weak trigger pulse) can in certain circumstances fragment coarsely, without the necessary fragmentation rate to produce large amounts of steam. Particle distributions obtained for such events are shown in figures 9.16-9.17. The fragmentation of the melt has not been as thorough as for the steam explosion events. The particle distribution is shifted towards higher fractions of the larger particles. For the case of pure silicon, the debris consisted of only a few rather large particles. Thus, the distribution shown in figure 9.16 is not very representative for so-called coarse fragmentation events.

Figures 9.17 and 9.18 show particle distributions that are more typical for coarse fragmentation events. The debris is still fine powder, but there is a larger amount of material in the upper interval (~1-mm diameter particles). An interesting effect is observed when figures 9.17 and 9.18 are compared; as the amount of alloying material increases, the melt is not that easily fragmented. The alloy containing both Al and Ca has a higher fraction of particles in the upper interval (above 0.8-mm diameter particles). This is consistent with the observation that alloyed silicon undergoing fragmentation in an explosive manner contains particles that on average are larger than particles resulting from explosive fragmentation of pure silicon.

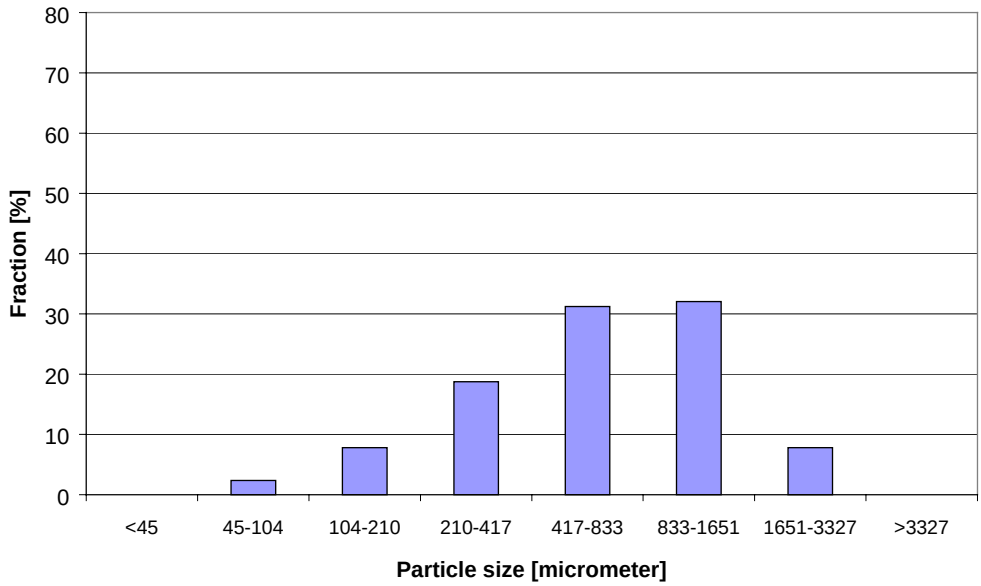

Figure 9.17 – Particle size distribution for a coarsely fragmented drop of alloyed silicon (alloy B, Si+0.4 % Al, see table 9.2), experiment D-127-1.

URN:NBN:no-2125

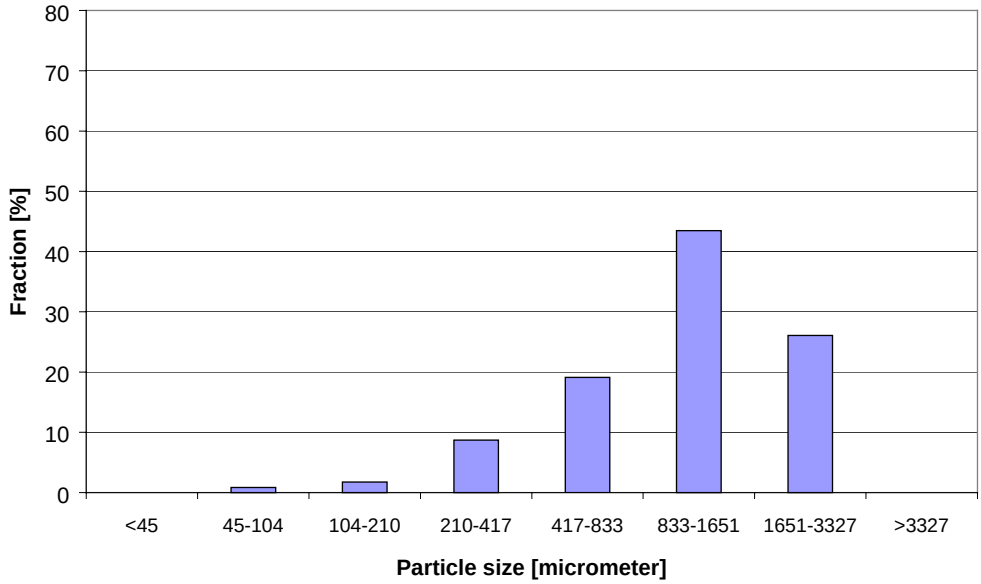

Figure 9.18 – Particle size distribution for a coarsely fragmented drop of alloyed silicon (alloy D, Si + 0.4 % Al + 0.04 % Ca), experiment D-139-1.

Based on the sieve analysis result given in figures 9.13-9.18, we can calculate the average size of the fragments that have been recovered from the water chamber. If we assume that the particle diameters are distributed evenly within each particle size interval, the mean diameter of that particular interval can be taken as a representative value for the diameter of all the particles of the group. Of course, we possess no information about the distribution within each particle size interval; thus, this calculation is more of a qualitative character. However, if our assumptions are correct, the average size of the fragments from one particular sieve analysis is given by equation (9.15):

$$\bar{d} = \frac{\sum_{i=1}^{n} (md)_i}{} \qquad (9.15)$$

The summation is made over the product of the mass fraction m and interval mean diameter d for each of the n intervals. Thus, we obtain the average diameter of the fragments as given in table 9.16.

The average diameter of the debris is an indicator of the explosion efficiency (energy transfer efficiency), as the total energy transfer from the melt is proportional to the water-melt contact area. Debris from typical steam explosions has average particle diameters in the 400-800 μm range. For coarse fragmentation events, the sieve analysis indicated that such events could

generate very fine particles. Indeed, from table 9.16 we observe that the debris appears the same for experiment D-123-1 and D-127-1 (within the accuracy of the sieve analysis), but these two melt-water interactions were quite different as observed in the laboratory.

Table 9.16. Average diameter of recovered debris from various types of melt-water interactions, based on the sieve analysis.

Experiment	*Composition*	*Type of interaction*	*Average diameter [μm]*
D-107-1	Si	Explosion	400
D-120-1	Si	Coarse frag.	2000
D-123-1	Si	Explosion	800
D-127-1	Si + 0.4 % Al	Coarse frag.	850
D-130-1	Si + 0.4 % Al	Explosion	700
D-139-1	Si + 0.4 % Al + 0.04 % Ca	Coarse frag.	1300

The method applied is less reliable for small amounts of material. In our case, the typical weight of debris from a melt-water interaction is around one gram. This is strictly speaking not enough to assure a good result from the sieve analysis, as the laboratory recommended at least 5 grams in order to get a good result. Indeed, in all but one case there was a discrepancy between the amount of debris before and after weighing, as shown in table 9.17.

Table 9.17. Relative loss of material during the sieve analysis.

Experiment	*Weight before [g]*	*Weight after [g]*	*Loss [%]*
D-107-1	0.89	0.68	24
D-120-1	1.32	1.32	0
D-123-1	1.28	1.24	3
D-127-1	1.35	1.28	5
D-130-1	1.26	1.09	13
D-139-1	1.22	1.15	5

Experiment D-107-1 was the most powerful steam explosions of those analyzed. Unfortunately, the loss of debris during the analysis was as high as 24 %. This weakens our conclusion made earlier, as that of particles less than 50 μm stay in the water. It could be that these particles just got stuck somehow during the sieving. However, we cannot rule out the possibility that the laboratory made an error, which is not related to the size of the particles. The other samples were quite good with respect to mass loss during sieving, from 0 to 5 %, with one exception, as can be seen from table 9.17.

9.10 Bubble-energy

In section 5.2.10, we explained how the bubble-energy could be calculated, given that we have a good measure of the diameter of the bubble. This method has been applied to estimate the work the bubble performs against the ambient pressure (bubble-energy). Figure 9.19 shows the results of these calculations, both for Si and FeSi droplets.

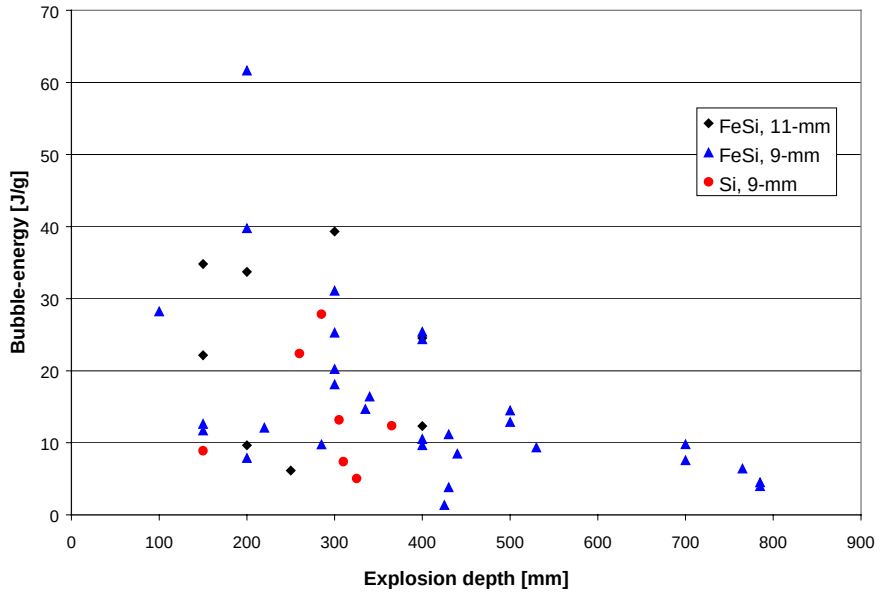

Figure 9.19 – Bubble energy from the explosions of molten drops of Si and FeSi75.

The PV-energies are plotted as a function of the explosion depth as measured from open-shutter photographs like the one shown in figure 5.1. There is considerable data scattering for explosions between 150 and 400 mm. For example, at an explosion depth of 200 mm, we obtained three steam explosions with the molten FeSi75-alloy, with bubble energies of 8, 40 and 60 Joules/gram. The two strongest explosions have an error estimate of approximately 20 %, which would bring the PV-energies quite close in the limits. In these two experiments, the actual trigger pressure was the same. But when we investigate the photograph of the weakest explosion at this depth, we find that the drop triggered 25 mm higher than the other two. The drop triggered 50 mm above the impactor, while the other two drops triggered only 25 mm above the impactor, i.e. these drops experienced a trigger pressure twice as high. This is the main explanation to the substantially lower energy output for the weakest explosion. For explosions at the deepest water levels, the variation in the calculated PV-energy was much smaller.

URN:NBN:no-2125

The error estimates for each experiment is typically between 15 and 20 %, mainly due to difficulties in measuring the proper bubble-diameter for more or less asymmetric bubbles. This applies for all experiments, but some steam explosions inhibited a high degree of symmetry (perfectly spherical bubbles), which reduced the error estimate down to 10 % (for the energy transferred per gram melt).

As indicated in section 8.2.3, the effect of water depth on the ambient pressure is negligible for shallow water (less than a meter). The difference in ambient pressure for 200 mm and 400 mm is only 2 Pa, i.e. 2×10^{-5} atm.

Drops from different rods may differ slightly in composition, even if the overall composition is the same. We can expect quite different behavior with respect to explosivity with only minor changes (i.e. 0.01 % difference) in the levels of Al and Ca in the alloy. We cannot rule out the possibility of macrosegregation in the rods as they cool down after casting.

The bubble-energy can also be coupled to the loss of drop mass as colloidal material (see section 9.9). The general trend is as expected that the energy transfer increases as the amount of colloidal material increases, however, the data scattering here is even larger than when plotting the PV-energy vs. the explosion depth.

9.10.1 PV-energy output compared to enthalpy of the drop

We can now compare the enthalpy of the molten drops of ferrosilicon and silicon with the PV bubble-energies transferred to the water by the steam explosions. As seen from figure 9.19, we have obtained maximum pressure-volume energies that decrease from about 40 J/g to about 8 J/g for the 11 mm-diameter drops and from about 60 J/g to about 2 J/g for 9 mm-diameter FeSi75 drops. The enthalpy of FeSi75 is approximately 2300 J/g at the liquidus temperature (Klevan, 1997). Thus, the bubble energies transferred to the water per gram of melt decreases from about 1.7 % to about 0.3 % for 11 mm-diameter drops and from about 2.6 % to about 0.1 % for the 9 mm-diameter drops. We note that the efficiency of energy transfer increases with *decreasing* drop diameter for the FeSi75-alloy.

The enthalpy of silicon is approximately 83.5 kJ/mol Si when molten at liquidus temperature (Rosenquist, 1983), which corresponds to roughly 3000 J/g. The PV-energies range from about 5 to about 29 J/g for steam explosions of molten drops of silicon, which translates to 0.2 % up to 1.0 % of the total

enthalpy. This is less than for ferrosilicon drops. However, some measurements from video recordings (not shown in figure 9.19) indicated higher PV-energy values than those reported shown above. In three cases, these values were between 50 and 60 J/g, which would indicate that the range of PV-energies is the same for Si and FeSi-drops.

9.11 Pressure transducer experiments – characterizing the impactor

The experiments carried out during the year 2000 were devoted primarily to obtaining and interpreting the pressure-time records during triggered steam explosions of single drops of molten silicon and ferrosilicon. In three of the experiments, we used a high-speed video camera (see section 4.8.3) to obtain images of the explosion process. These images were then compared to the pressure-time recordings, thus improving our understanding of the physical processes that took place.

9.11.1 Initial investigations of impactor 3 – fine structure of the pressure trace

Only the most powerful impactor (the slug-type, impactor 3) was used during these experiments. As the oscilloscope will record both pressure disturbances in the water from the impactor and the steam explosion, we need to analyze the output of the impactor in more detail in order to distinguish trigger pressure waves and explosion pressure waves.

A typical pressure-time record generated by impactor 3 when fired in the water at a depth of 400 mm with the tourmaline transducer 100 mm above is shown in figure 9.20 (experiment D-168-1-4). Note that the trace shows two primary pressurizations, a strong first peak and a smaller peak 2.56 ms later. This time separation is the same (+/- 0.01 ms) for all of the time-pressure recordings we have made, thus, it can be said to be a property of the trigger system.

Initially, we shall characterize these two pressure pulses by their maximum values – the peak pressures – the most easily measured parameter.

As the chamber is quite small, there will be a very complicated pattern of reflected waves in the water following the first, strong pressure peak. We do not intend do analyze all of these, however, we will briefly discuss some of the larger pressure peaks that are reflected waves from internal structures.

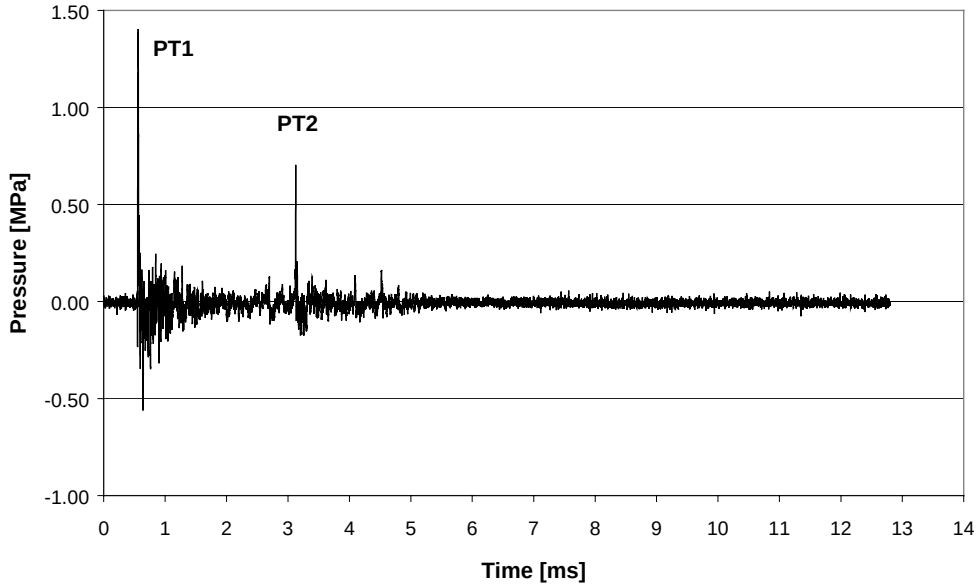

Figure 9.20 – Pressure-time recording obtained from firing impactor 3 alone. The first peak is labeled PT1, and the second one PT2, appearing 2.56 ms later.

As described in section 9.5.2, the peak pressure value was very consistent over a large number of experiments, and had a value of about 1.7 MPa measured 100 mm above the surface of the impactor. We now try to analyze the two pressure peaks in figure 9.20 in more detail. In figure 9.21, the fine structure in the transient PT1 is shown. Three major pressurizations appear, which we denote A, B and C.

In figure 9.21, we see that the separation of peaks A and C is 0.440 ms. We now assume peak C to correspond to the return of a wave reflected from the water surface, a distance of 600 mm (twice that from the transducer to the water surface). Using the speed of sound in water of 1490 m/s, in 0.440 ms the pressure transient will travel 656 mm, which is in relatively good agreement with the 600 mm distance from the transducer to the surface and back. Thus, the assumption seems fair.

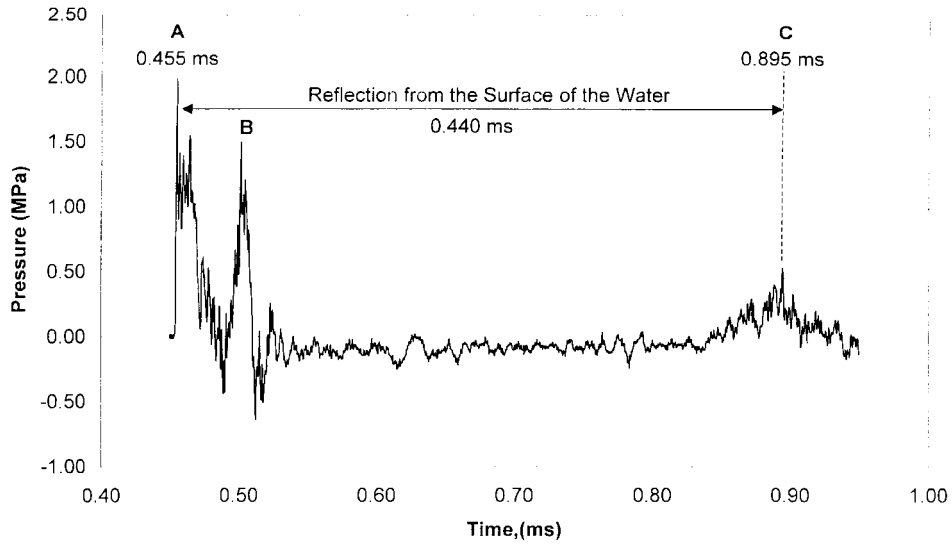

Figure 9.21 – Time-pressure trace, showing the fine structure of PPT1 from figure 9.16.

In order to establish our assumption, we performed another experiment, in which the impactor and transducer were both lowered in the water by 100 mm. Now, the round trip distance from the transducer to the water surface is 800 mm. In the new experiment, the separation between peak A and peak C increased from 0.440 ms to 0.579 ms. This indicates a travel distance of 862 mm, using the same speed of sound as above. Again, this estimate is in good agreement with the known round-trip distance of 800 mm. This confirms our identification of peak C as being produced by the reflection of the initial strong pressure transient from the surface of the water.

The initial pressurization in PT1 is double-peaked, as shown in figure 9.21; these peaks have been labeled A and B. The time separation between these two peaks is 0.047 ms. If we assume that a wave is passed from the surface of the impactor down to the bottom of the steel canister, where it is reflected, this will cause the reflected wave to travel 266 mm longer than the initial pressure wave. Using the speed of sound in steel of 5060 m/s, in 0.047 ms the pressure transient will travel 238 mm, again in good agreement with the known dimensions of the canister.

As shown in figure 9.20, there are two major peaks generated by the impactor when fired alone. The first, PT1, will be shown (next section) to be caused by the impact of the steel slug against the underside of the canister in which it is enclosed plus secondary reflections of acoustic waves from the base plate of the impactor or from the water surface above.

There is a second major peak in figure 9.20, PT2. Initially, we were not able to explain this one with respect to reflections from the walls or other surfaces. However, when we applied the high-speed video camera, the origin of this pressure peak was found, as will be explained in the next section.

9.11.2 Interpretation of the pressure-trace based on high-speed video images

Figure 9.22 shows images obtained in room light with the high-speed video camera system described in section 4.8.3. The camera is set to record at a speed of 4500 frames/sec, i.e. it is 0.22 ms between each frame. Figure 9.15 shows the corresponding time-pressure trace, as obtained with the tourmaline pressure transducer. The times at which each of the images was taken are indicated in the pressure-plot, figure 9.23.

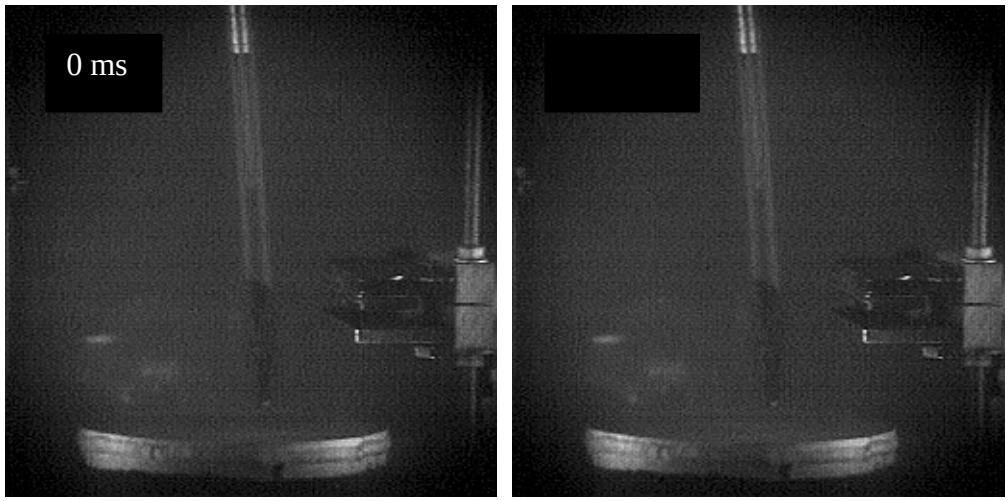

a) Impactor about to trigger.
b) The slug hits the steel plate from below. Parts of the surface turn white, in a disk-like manner.

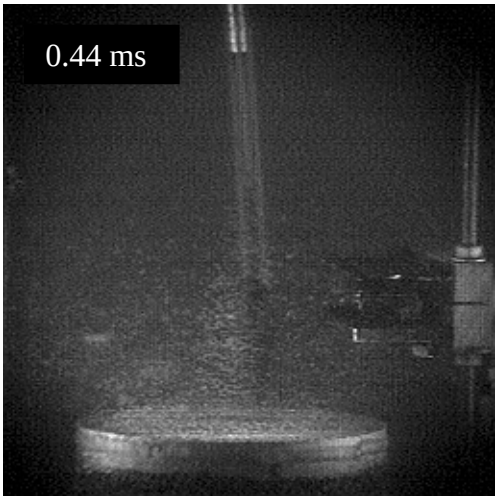

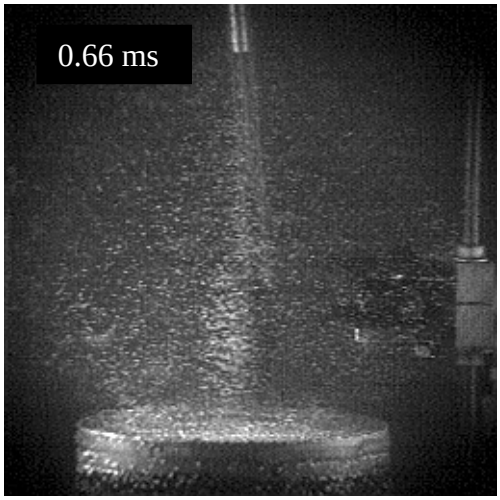

c) A pressure wave has just passed, and behind it tiny cavitation bubbles is forming.

d) The whole volume above the impactor is filled with cavitation bubbles.

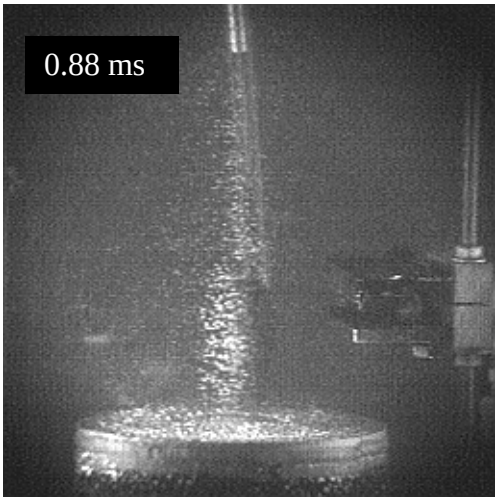

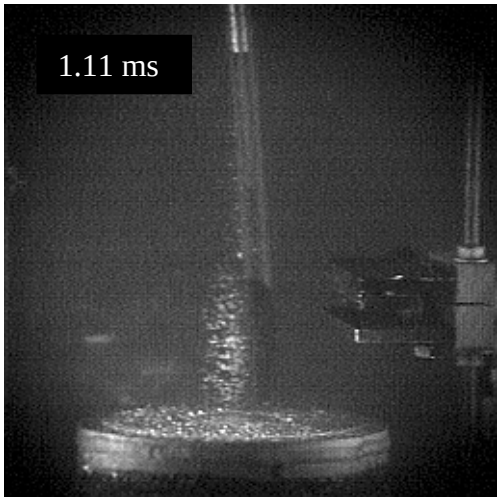

e) The cavitation bubbles are decreasing in number. A white ring forms on the impactor.

f) Even less bubbles. The white ring is moving inward toward the center of the impactor. All images a) – f) are in sequence as obtained with the high-speed video camera.

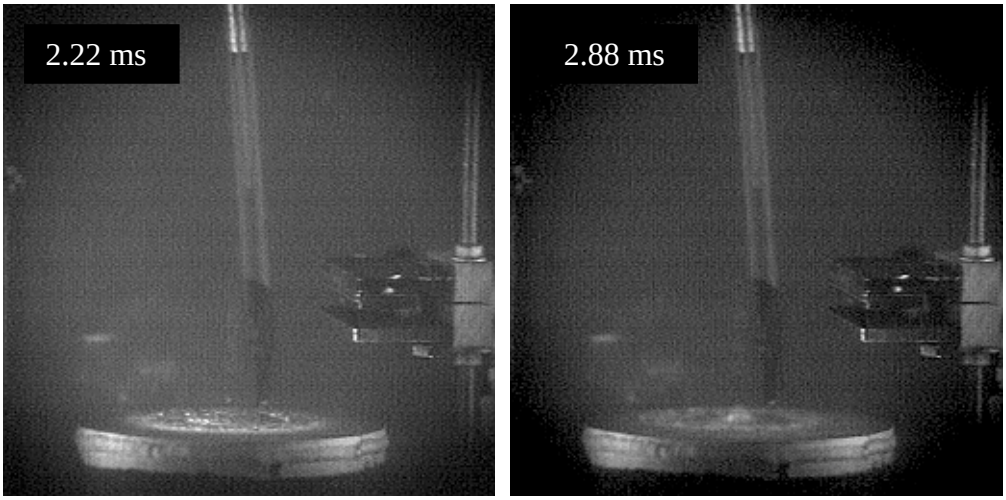

g) The white ring is still moving inwards. No cavitation bubbles left in the water, but some bubbles are resting at the surface of the impactor.
h) A larger bubble starts to grow at the center of the impactor.

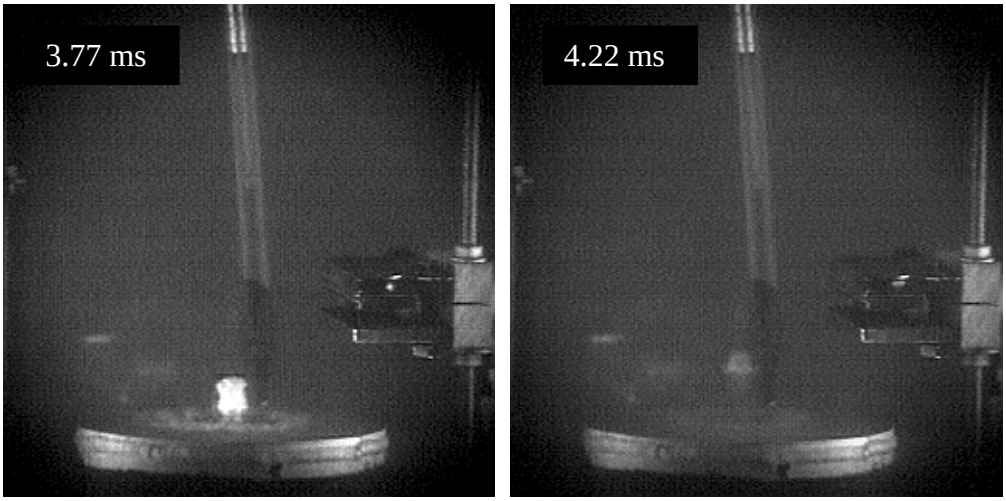

i) A large bubble has been released from the surface of the impactor.
j) The bubble is collapsing, and will disappear completely in a few milliseconds. The surface of the impactor is not vibrating, and the pressure in the water approaches its normal value (atmospheric).

Figure 9.22 – Sequence of images (a-j) showing the firing of the impactor. Time elapsed since the first frame is shown in the upper left corner of each image.

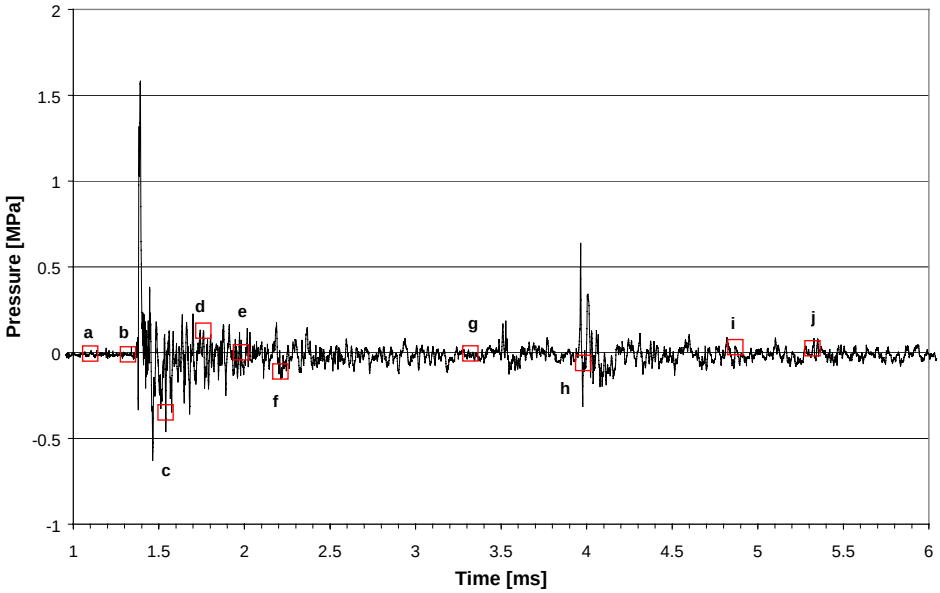

Figure 9.23 – The time-pressure trace for the firing of impactor only. The images shown in figure 9.14 are marked as squares.

Image b) in figure 9.22 shows that the surface of the impactor brightens, and we contribute this to the impact of the slug at the downside of the steel-plate surface. An acoustic wave will start to travel through the water, and this wave (travelling by the speed of sound in water, 1490 m/s) will reach the location of the pressure transducer about 0.08-0.09 ms later, depending on the choice of starting point on the surface of the impactor. As we know the time at which the pressure front reached the transducer (pressure peak value 1.6 MPa at a reference time of 1.39 ms), we know approximately the time image b) was taken, relative to the time scale in figure 9.23. Thus, all subsequent times assume that the pressure wave starts to travel at the time image b) was taken.

The next image, c), show the occurrence of numerous tiny cavitation bubbles, which grows due to reduced pressure behind the front, compared to the ambient pressure. This is a typical feature of the effect of a strong pressure wave moving through water. Behind the front, the pressure will drop below the ambient value, allowing small gas nucleus to grow until they reach equilibrium with the local ambient pressure, i.e. when

$$P_g - P_f = \frac{2\sigma}{r} \tag{9.16}$$

where σ is the interfacial surface tension and r is the bubble radius. When the pressure increases to its normal value, these cavitation bubbles will vanish.

From figure 9.22 c) one may get the impression that the pressure front can be observed directly (the horizontal separation line between water with or without bubbles). However, based on the speed of the wave and the distances involved, we know that the pressure front has already moved out of the area that is viewed by the video camera. This imaginative separation line reflects that in the lower part, the gas nucleus has had sufficient time to grow to a size that can be observed. Above this water level, the bubbles have not yet grown to observable sizes.

In the next image, d), cavitation bubbles are observed throughout the water column, before they start to vanish as the pressure normalizes, image e) and f). Also, in image f) we observe a white ring of bubbles on the impactor that is moving inward, and we attribute this pattern to be that of a small oscillation of the steel plate due to the impact of the slug. Obviously, the steel plate is somewhat elastic, which allows it to swing back below its equilibrium point and up again where it rests after it first have been hit by the slug and pushed upwards.

The ring of bubbles moves inward toward the center, and eventually a relatively large bubble is released from the impactor, see figure 9.22 i). This bubble quickly disappears, i.e. within 1.5 milliseconds. A small pressure peak is observed at the time the ring reaches the center, and we attribute this as the steel plate is moving upwards from a position below the equilibrium position. This motion creates a small pressure wave that travels up through the water. Finally, the impactor comes to rest and no more pressure disturbances can be measured.

To sum up, we have established that the large pressure peak that appears after about 1.4 ms in the time-pressure traces (see figs. 9.20 and 9.23) is caused by the impact of the slug inside the impactor and the steel plate that is on top of the canister. The steel plate oscillates down below its equilibrium level before it moves up again to its initial position. This upward motion creates a small pressure peak after about 4 ms. This small peak is always observed, thus confirming a systematic behavior of the trigger system.

9.11.3 Impulses of the triggering transients

It is important to distinguish the pressure transients created by the mechanical impactor from the pressure transients created by a violent molten metal-water

interaction. The experimental procedure is to record three separate pressure traces, using only the impactor. The impactor can be triggered by shining a flashlight into the photodetector that usually is set off by the bright light of the molten drop. These three recordings are then compared to the recording of the explosion, we will see that pressure peaks resulting from the impactor are easily distinguished from the explosion pressure peaks. We also found that the impactor gives highly reproducible trigger pressure transients. A good measure for this is the impulse associated with each pressure peak. Compared to the peak pressure value, the impulse is less sensible to where the peak occurred (could be between two points). Also, if the peak is very sharp, the error in the measured peak pressure value can be relatively large. The problem of sharp peaks is eliminated using the integral value of the pressure with respect to time. The impulse can be estimated by calculating the integral

$$I = \int_{t_0}^{t_{max}} P dt \tag{9.17}$$

where t_0 denotes the time at which the pressure starts to increase rapidly and t_{max} is the time at which the pressure has decreased to its standard value. The integration is carried out numerically, using the simple formula

$$I = \sum_{i=1}^{i=n} P_{i-1} \Delta t \tag{9.18}$$

where t_n denotes the last time the pressure is larger than the ambient pressure before it takes on a negative value, and Δt is the time interval between each pressure measurement, in most cases 1 μs. By applying equation (9.18) on the recorded time-pressure traces, we obtained the data plotted in figure 9.24. The figure only includes experiments in which an explosion occurred.

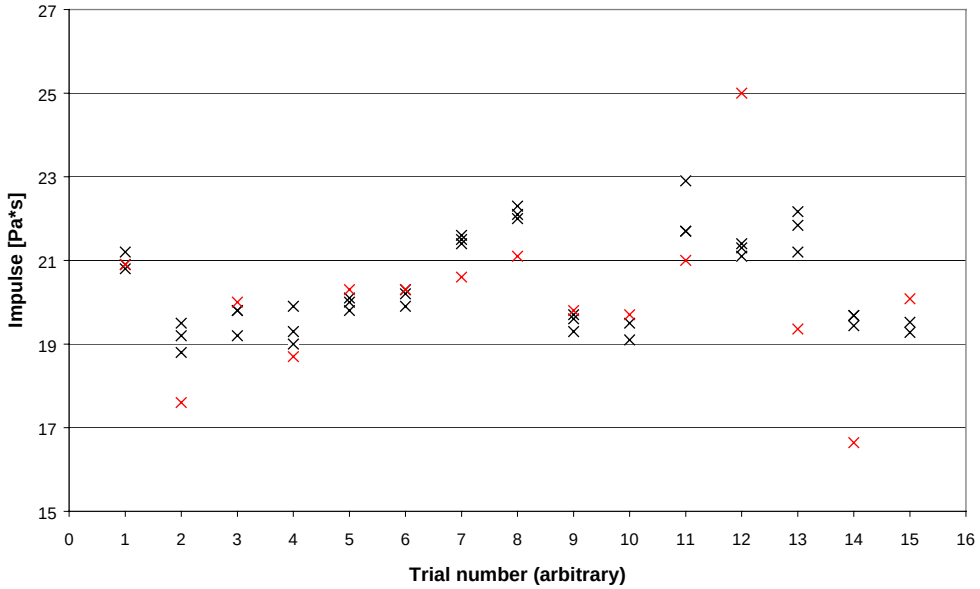

Figure 9.24 – Trigger pulse impulses as obtained from the time-pressure trace for the experiments in which an explosion occurred. The red crosses indicate the actual drop-release experiment, as opposed to the black crosses, for which the impactor was fired alone. Trial number indicates different drop-releases experiments, in chronological order. The distance between the center of the impactor and the pressure transducer was 144 mm, except for trials 12 (129 mm), and 13-15 (113 mm).

As can be seen from figure 9.24, the calculated impulse for the test measurements does not vary much. Furthermore, they are also in good agreement with the measured trigger impulse value in the actual drop-release experiment. The average value is about 20 Pa*sec, with a standard deviation of only 5 %.

The impulse of the second peak (see for example figure 9.20) is found to be very much smaller than the first, large peak, thus, for all practical purposes, it can be neglected. Also, as will be shown later, at this time the eventual melt-water interaction has already started.

9.12 Pressure measurements of the interaction of molten drops of silicon-alloys with water

9.12.1 High-speed video captures of a steam explosion and the corresponding time-pressure trace

In section 9.11.2 we showed video captures of the water tank when the impactor was fired without any molten drops present. In a similar experiment we also released a molten drop of silicon into the water tank, with subsequent triggering and explosion. Time-pressure traces were obtained, as well as high-speed video captures.

Figure 9.25 shows the time-pressure trace that was obtained. Note that in addition to the pattern from the impactor alone (peaks at 1.4 and 4.0 ms), there is a huge pressure peak after about 4.3 ms, which is a consequence of the explosion. Also, some smaller peaks are observed after 15, 16.5 and 22.5 ms.

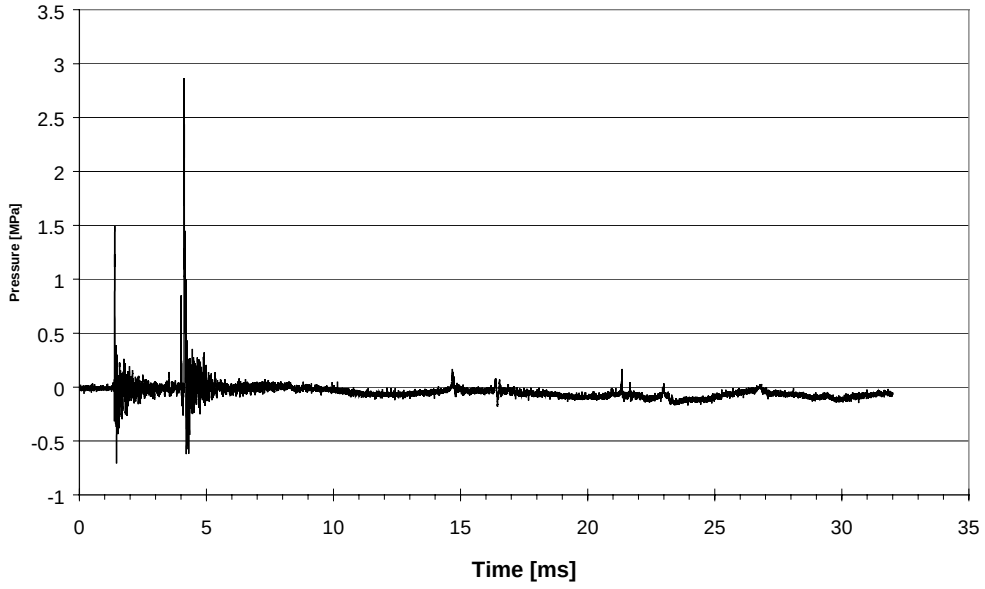

Figure 9.25 – Time-pressure trace for experiment D-202-1-4, in which a strong explosion occurred, using a molten drop of pure silicon.

The time-pressure trace shown in figure 9.25 are broken up into two separate traces to show more details (figure 9.26 a)-b)), and the small squares along the pressure curve indicates that a picture was taken at that particular time.

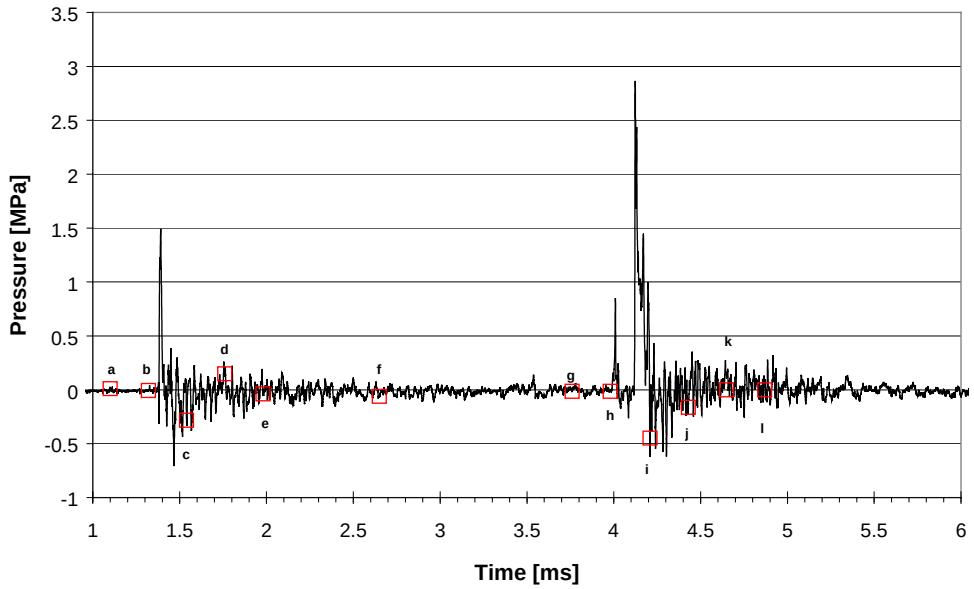

Figure 9.26 a) – The first part of the time-pressure trace shown in figure 9.18.

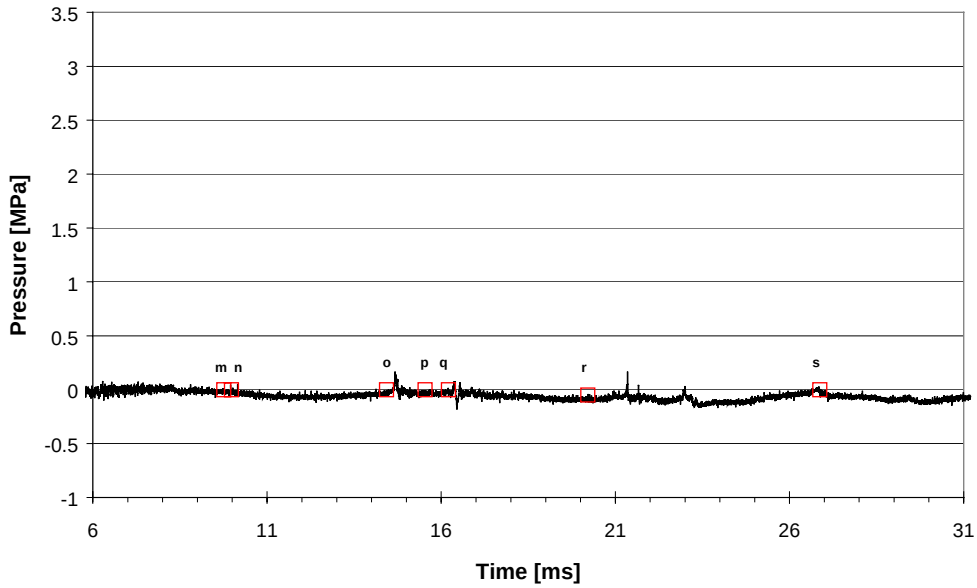

Figure 9.26 b) – The second part of the time-pressure trace shown in figure 9.25.

The indicated frames in figure 9.26 (a-s) was recorded digitally from the high-speed video camera and modified slightly to improve the picture quality. Still,

these images are somewhat overexposed due to the strong light from the molten drop, and the drop appears larger than its actual size. The images obtained with the high-speed video camera are shown in figure 9.27 a)-s).

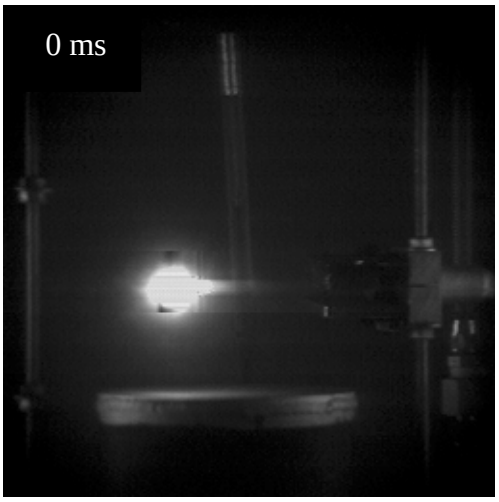

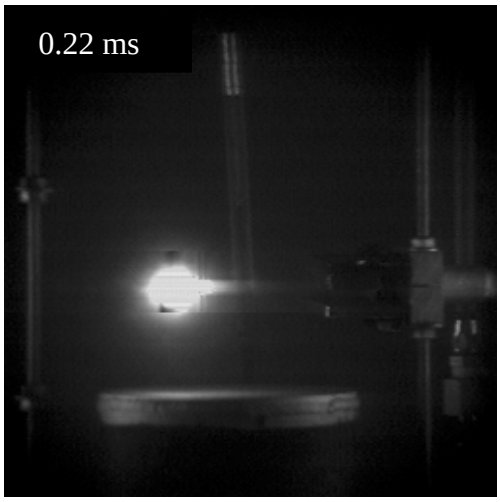

a) Drop is approaching the impactor, no trigger yet.
b) The trigger is activated, small color change can be observed at the top of the impactor.

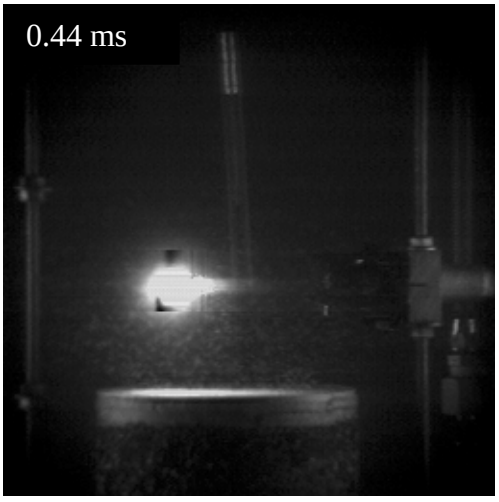

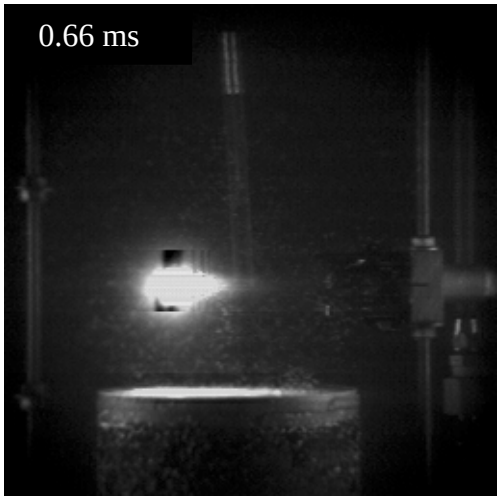

c) Cavitation bubbles below drop indicates that a strong pressure pulse has passed.
d) The drop has started to fragment, melt-vapor mixture expands.

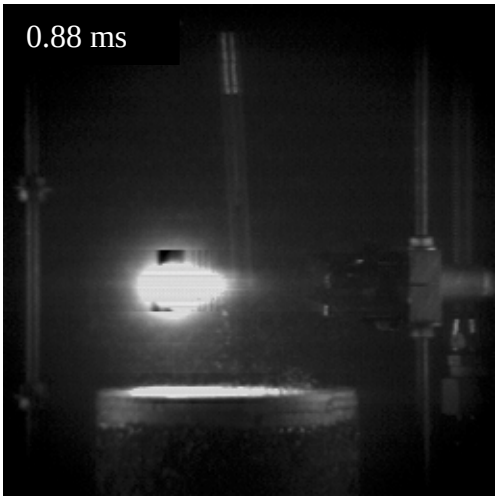

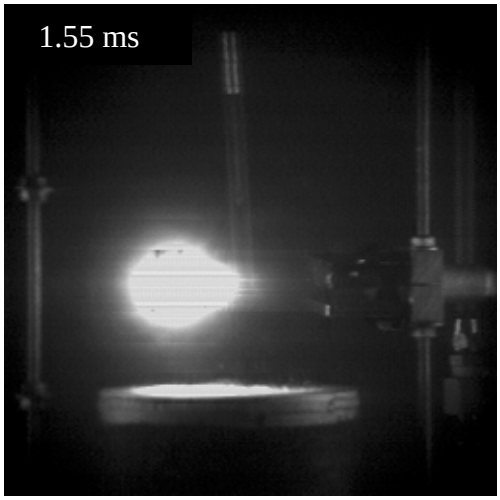

e) Melt-vapor mixture is expanding, still some cavitation bubbles in the water.

f) Still expansion, no more cavitation bubbles can be observed.

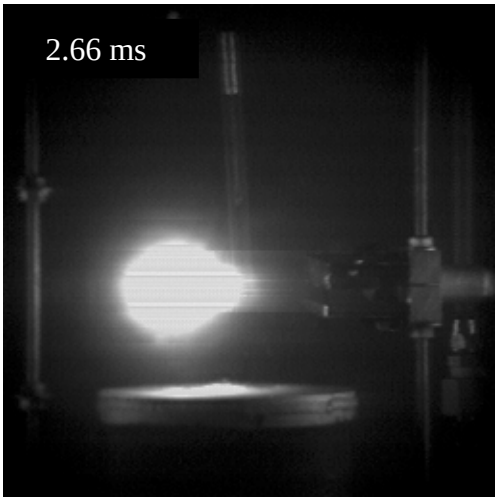

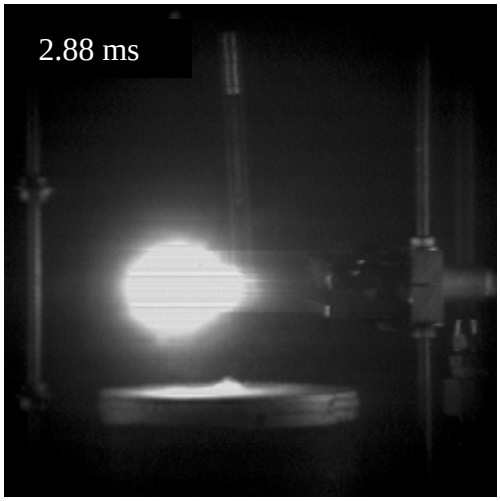

g) The mixture is no longer expanding, and seems to be stable in size.

h) The mixture is now decreasing in size, i.e. the melt-vapor bubble is collapsing.

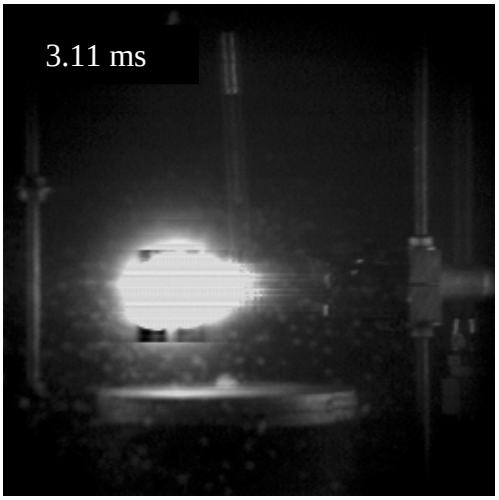

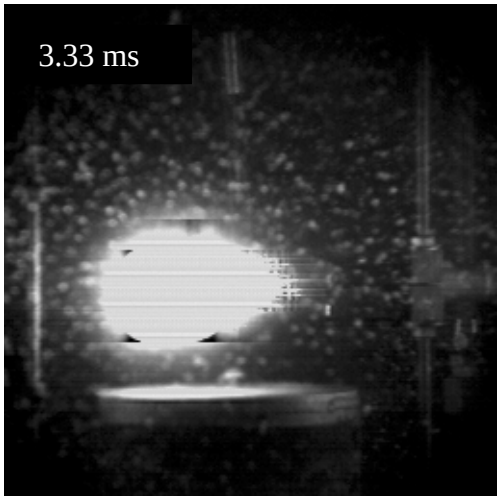

i) Collapsing bubble, cavitation bubbles are forming again, indicating that a pressure transient has passed through the water.

j) Rapid expansion of the melt-vapor mixture. Several cavitation bubbles are seen.

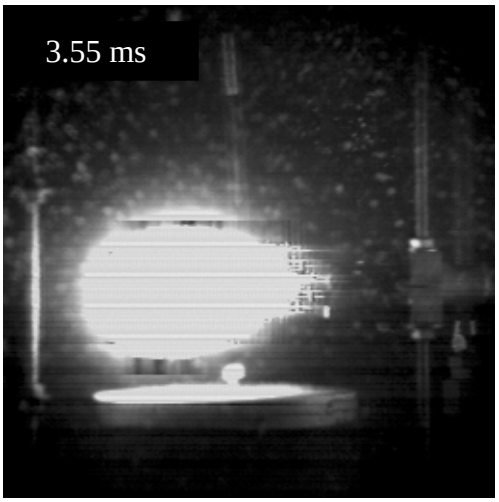

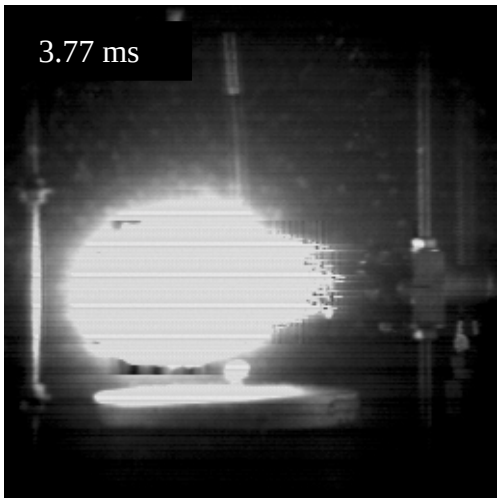

k) Expansion of the melt-vapor bubble.

l) The expansion continues, note that this second bubble is much larger than the first.

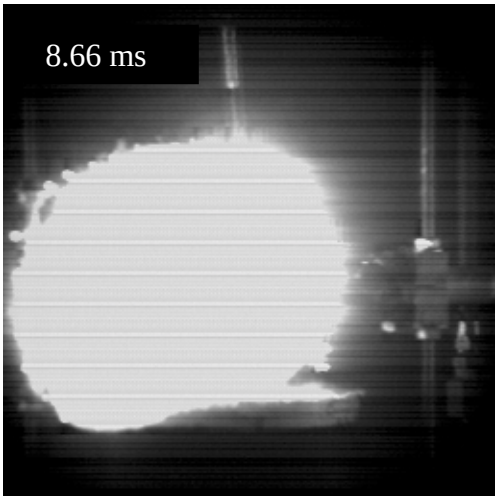

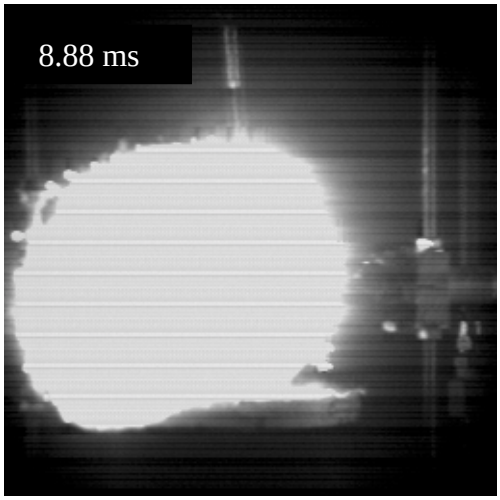

m) The bubble reaches its maximum diameter – the second expansion stage comes to an end.

n) The second collapse is initiated – diameter of the bubble decreases.

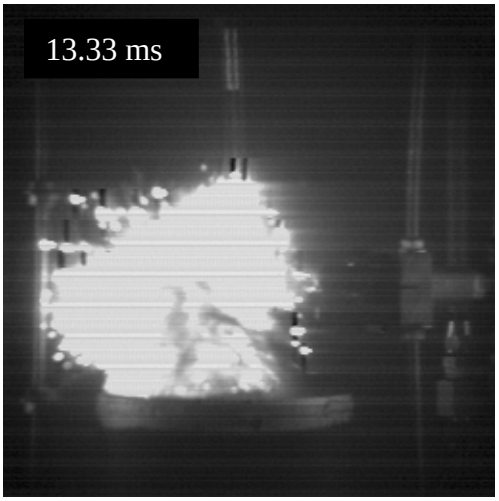

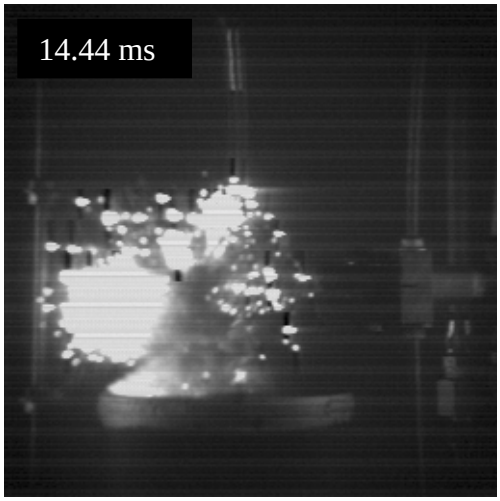

o) The melt-vapor mixture has reached its minimum size.

p) Another expansion cycle starts, but the material is mostly solidified (dark dust), and spreads out close to the surface of the impactor.

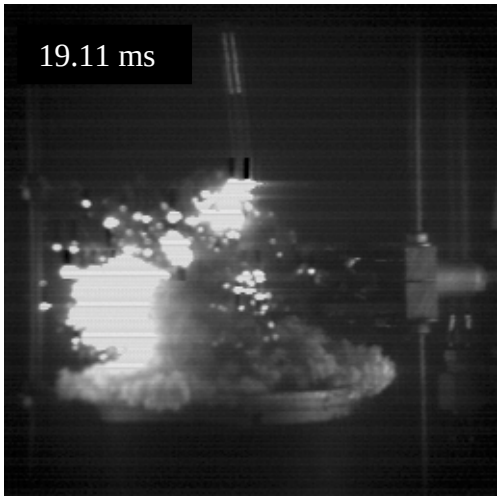

q) The dark cloud is spreading out, but relatively slowly compared to the melt-vapor bubble expansion.

r) Dark material is clearly visible as it spreads out on the surface of the impactor.

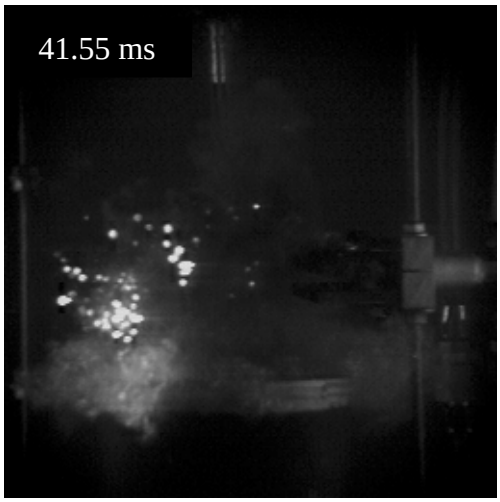

s) The melt is cooling down. Several luminous particles are floating around in the water, apparently burning Si-particles inside a hydrogen bubble.

t) The situation inside the water chamber is quiet, except for these luminous particles that are still visible as long as the video is recording (up to 0.2 seconds).

Figure 9.27 (a-t) – Sequence of images obtained with the high-speed video camera in room light of a molten drop of pure silicon that explodes violently in water.

These images and the corresponding time-pressure trace give us a good qualitative picture of the course of events after the melt has been triggered. An outline follows in the next section.

9.12.2 Course of events following triggering of a molten drop of silicon

Based on the results presented in section 9.12.1, we can now describe the course of events following the triggering of a molten drop of silicon, with respect to pressure changes in the water and their origin. All references to time-pressure traces are the one obtained for experiment D-202-1-4 (figure 9.26), also, all references to images (frames) are with respect to figure 9.27.

After the drop has entered the water, it goes into film-boiling mode. The drop stays in this metastable state until it is triggered, image b). A small change of color of the surface of the impactor can be detected (much easier when viewing the videotape). The pressure transient cannot be observed directly, but in the next frame (c), cavitation bubbles are starting to grow, indicating a low-pressure region (behind the pressure front). As the luminous drop is quite overexposed, we have no way of observing directly the consequence of the impact of the pressure transient on the boiling film. But if we assume that the pressure transient passes the drop at about 0.28 ms (using the time scale indicated on the images shown in figure 9.27), the growth seems to start somewhere between image c) and d), giving a time scale for collapse and growth of the order 0.25 ms.

We again note that our ability to link the time-pressure trace to the high-speed video frames (with respect to time) is based on the assumption that the pressure transient starts to travel exactly at the time image b) was taken. Thus, knowing the distance from the center of the impactor to the position of the pressure transducer and the exact time (sampling rate of pressure 10^6/s) the pressure front reached the transducer, allow us to easily calculate at what time (relative to the time scale of the time-pressure trace) frame b) was obtained.

After the collapse of the vapor film, with a subsequent rapid increase of the heat transfer, vapor forms rapidly and the pressure rises high locally. Thus, a mixture of vapor and melt (vapor bubble) starts to expand. This is first observed in image d). If we take a look at the recorded pressure, nothing really happens after the trigger pressure passed the area. Some oscillations are observed behind the peak. The vapor bubble is growing for about 2 ms, from image d) to image g). If we try to estimate the growth rate of the vapor bubble, we can use direct measurements of the images shown in figure 9.27 as a first approximation. Assuming that the overexposure is the same on all of the images, we measure that the drop grows from a diameter of 6.5-mm (image d)

to 13 mm (image f). Actually, the bubble is still expanding, but we will neglect the latest stage on the growth cycle, as the growth slows down quite a bit. Using a proper scale factor, the bubble grows from 23 mm to 46 mm in 2 ms, that is, the growth rate of the diameter is 11.5 m/s. Considering the initial volume of the melt, this volume increases eight times in 2 ms. The growth rate in the earliest stages of the expansion is even larger, approximately twice as big (about 20 m/s for the growth rate of the bubble diameter). As the difference in pressure between the interior of the bubble and the ambient pressure outside it becomes smaller, the driving force for expansion is reduced, thus the growth rate decreases. Eventually, the expansion terminates and the bubble collapses.

By the time the first bubble collapse, no pressure activity has been measured in the water, except for the trigger pulse. The typical “oscillation-peak” is measured after 4 ms (see figure 9.26a), but we believe that this small peak has no significant effect on the fragmentation of the drop.

The next frame, image i), shows that a number of cavitation bubbles have formed, indicating that a pressure transient has passed. This is in excellent agreement with the time-pressure trace. Referring to figure 9.26a, a very strong pressure pulse was measured just before (about 0.05 ms) image i) was recorded. Based on the photographic evidence, we can conclude that this strong pressure peak is the result of *the collapse of a steam bubble*. As the bubble is collapsing, water flows in from all sides, eventually making impact in the former center of the bubble. Thus, a pressure transient is generated, which is considerably stronger than the trigger pulse used to initiate the first explosion. On the time-pressure trace shown in figure 9.26a, this second pulse is twice the amplitude of the trigger pulse. However, these values have not been calibrated for the difference in distance from the source to the pressure transducer. As we do not have the exact position of the drop at the time of triggering, we have to approximate its position from the video recordings. Still, the correlation factor is only 0.8, i.e. if we reduce all measured pressures resulting from the interaction between the melt and water with 20 %, a direct comparison with the trigger pulse can be made. This is based on the approximation that the distance from the center of explosion to the pressure transducer is 115 mm, while the distance from the center of the impactor to the pressure transducer is 144 mm, i.e. 115/144 = 0.80.

The strong pressure transient disturbs the boiling film covering the now partly fragmented melt, thus, it induces a new and finer fragmentation, with a rapid generation of vapor and subsequent bubble-expansion, see image j). We can also see that the cavitation of the water appears to be almost complete to the observed region, much more than was the case for the trigger pulse. The

following frames show the second growth cycle. The expansion is extremely rapid. We can again approximate the growth rate of the diameter of the bubble. Initially, the (overexposed) diameter is 44 mm, and in 0.66 ms it increases to 82 mm, which is a growth rate of 55 m/s. This is more than twice as fast as compared to the first bubble cycle. The average growth is less; the final diameter of the bubble is 130 mm (5.55 ms later), which translates to an average growth rate of 15 m/s.

From a pressure standpoint of view, nothing happens after the expansion of the second bubble starts. Images k), l), and m) shows the expansion. In image m), the bubble has reached its maximum size, and in the next frame the collapse has started. Thus, the bubble was growing for about 5.5 ms before it collapsed. Strangely, this collapse does not produce a strong pressure transient, as we may have expected based on the earlier results. At the estimated time of impact of water at the center of the former bubble (at about 14.5 ms on the timescale for the pressure recordings), there is only a minor pressure peak. This moment corresponds to image o). As the first bubble-collapse induced a very strong pressure peak, one might expect an even stronger peak following the collapse of the much bigger second bubble.

We will in a later section show that this behavior may not have been typical. During our investigations, we found several cases where at least two strong pressure peaks were measured (strong compared to the trigger transient) in the course of a steam explosion. However, a possible explanation for the absence of a strong pressure transient could be the generation of non-condensable gas, i.e. hydrogen resulting from the oxidation of the melt. If this gas gets trapped inside the collapsing bubble, it may act as a buffer to the incoming water jets and slow them down enough to prevent a hard impact that subsequently sets up a shock wave. This effect will not play a role during the first collapse, as the times involved are probably shorter than typical reaction times for the silicon-oxidation, thus, the partial pressure of hydrogen is low inside the bubble. However, it may be that after some 8-10 ms after the first fragmentation, enough hydrogen gas has been produced to slow down the incoming water jets.

Even though we did not record any pressure transient, the collapse seems to have initiated another growth cycle. Mostly solidified material forms a cloud that spreads out close to the impactor (see images p-r). This bubble is asymmetric, but it behaves very much the same as the two first steam bubbles. A collapse takes place, and based on the video recordings, this collapse should terminate at approximately the same time as a small pressure peak is observed, after about 21.5 ms on the timescale for the time-pressure trace. Furthermore, it appears that this collapse initiates one last expansion, as another cloud of

solidified material sweeps the surface of the impactor. Eventually, there is no more steam production and the conditions normalize. Numerous burning particles are still floating around in the water, presumably inside bubbles of hydrogen/steam. The small solidified fragments cover the impactor and the collector pan, but as much as 30 % of the original material stay suspended in the water (0.35 out of 1.21 gram), a quite typical result when molten silicon fragments in water (see section 9.9).

9.12.3 Time-pressure traces of steam explosions of molten Si/FeSi

During this work, a number of time-pressure traces from the interaction between molten (ferro) silicon and water have been obtained. These can all be found in appendix B.

The time-pressure traces are characterized by periodically sharp peaks following the first peak, which is the trigger pulse applied to set off the explosion. These peaks are a result of steam bubbles collapsing, as showed in section 9.12.1-2. The typical time separation between to consecutive peaks depends strongly on the size of the bubble that causes the last pressure peak. In some cases, the peaks come regularly with 2.5-3 ms separation. But in case of large bubbles, separation times up to 10 ms have been registered. Figure 9.28 and 9.29 show two examples of time-pressure traces. Figure 9.28 contains *five* peaks that we relate to bubble-collapses. These peaks come quite regularly, about 2.5 ms between each peak. None of the peak values are as strong as the trigger peak. In fact, when the photographic evidence is considered, we notice that the molten drop splits up in two parts prior to the triggering. These parts explode separately, thus accounting for the many peaks. As the heat available to vaporize the water is less than usual (smaller drops of melt), the corresponding steam bubbles are also smaller, and their collapse initiates relatively weak pressure peaks. This is another example of the importance of drop size on the strength of a steam explosion.

The second time-pressure trace, figure 9.29, is typical for a strong steam explosion. The first explosion-related peak is of the same order as the trigger pulse. The corresponding steam bubble has a lifetime of about 2.5 ms. The second steam bubble is larger, with a lifetime of about 6 ms. However, the second explosion-related pressure peak is almost negligible, and as discussed in section 9.12.2, the presence of hydrogen gas may have a cushioning effect on the incoming water jets, thus preventing a strong impact of water in the center of the former steam/hydrogen-bubble.

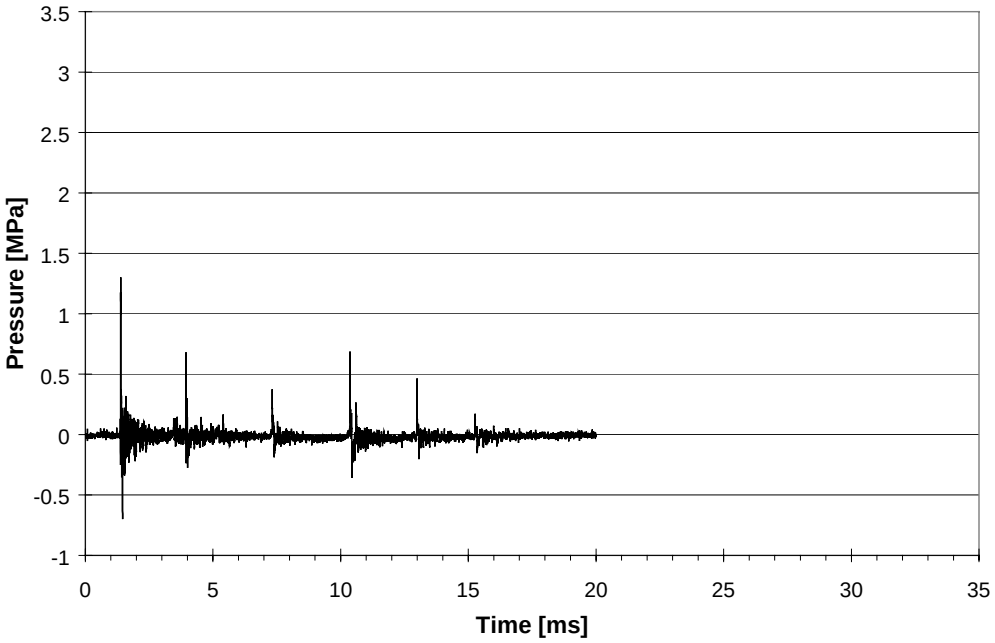

Figure 9.28 – Time-pressure trace for a steam explosion of molten FeSi75. The drop was triggered at a water depth of 425 mm.

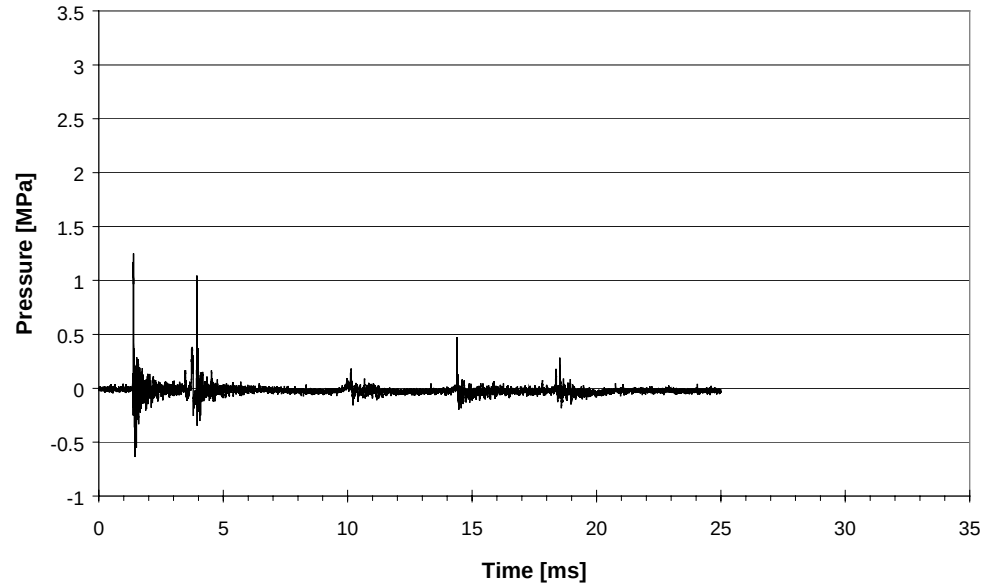

Figure 9.29 – Time-pressure trace for a steam explosion of a molten drop of FeSi75. The drop was triggered at a water depth of 440 mm.

Among the common features of the time-pressure traces is the time elapsed before the first pressure peak is registered, typically between 2.5 and 4 ms after the molten drop has been triggered. No systematic difference with respect to the time between triggering and registration of the first pressure peak between the two main alloys (Si and FeSi75) was detected, which is very reasonable, as the collapse of the vapor film initiates a physical explosion, involving melt of roughly the same temperature. The decisive factor of the duration of the first bubble-growth/collapse cycle is of course the size of the vapor bubble that forms. We are not able to measure the size of this bubble accurately enough to relate the lifetime of the first bubble quantitatively to its maximum diameter.

One of the experiments differed substantially from those described above; the time elapsed from the initiation of the explosion to the registration of the first pressure pulse associated with the explosion was about 7 ms. Furthermore, the pressure peak was very low (see figure A.11, appendix B). The open-shutter photo obtained reveals nothing extraordinary, as the explosion appears identical to several other explosions of the same alloy (pure silicon). We attribute this to the stochastic nature of such an event.

Strong steam explosions have very similar patterns. The first peak is much higher than the subsequent peaks (in many cases these are almost negligible, see for example figure 9.22). Thus, it seems like in these cases, the degree of fragmentation of the drop is very large during the first and second bubble-growth cycle. Thus, most of the heat is transferred in the early stages of the explosion process.

9.12.4 Time-pressure traces – impulse characteristics

Equation (9.17) can be applied to calculate the impulse of each pressure peak resulting from a collapse of the steam-bubble. The number we then obtain is important; it will reveal whether a typical explosion induces a pressure disturbance in the water sufficient to trigger other molten drops nearby. This is a necessary condition for a large-scale explosion to propagate, but not a sufficient one. Merely, it does not imply that a large-scale explosion *will* propagate.

Typical time-pressure traces, along with the high-speed video recordings for explosive events indicate that most of the energy-transfer to the water happens during the first and the second bubble-growth cycle. In general, the first collapse produces the strongest peak pressure (as well as impulse), and following pressure peaks can be neglected in most cases, but exceptions exist. Taking into account that the time factor is of great importance, i.e. it must be

small in order to achieve a large-scale propagation, it seems plausible to only look at the first pressure peak as a possible trigger for other drops.

In figure 9.30, the impulse of the first pressure peak in an explosive event is plotted against the trigger impulse that the molten drop experienced. The trigger impulse is easily calculated as soon as the position of the drop at the time of triggering has been established, using open-shutter photographs taken from the front and the side of the water chamber.

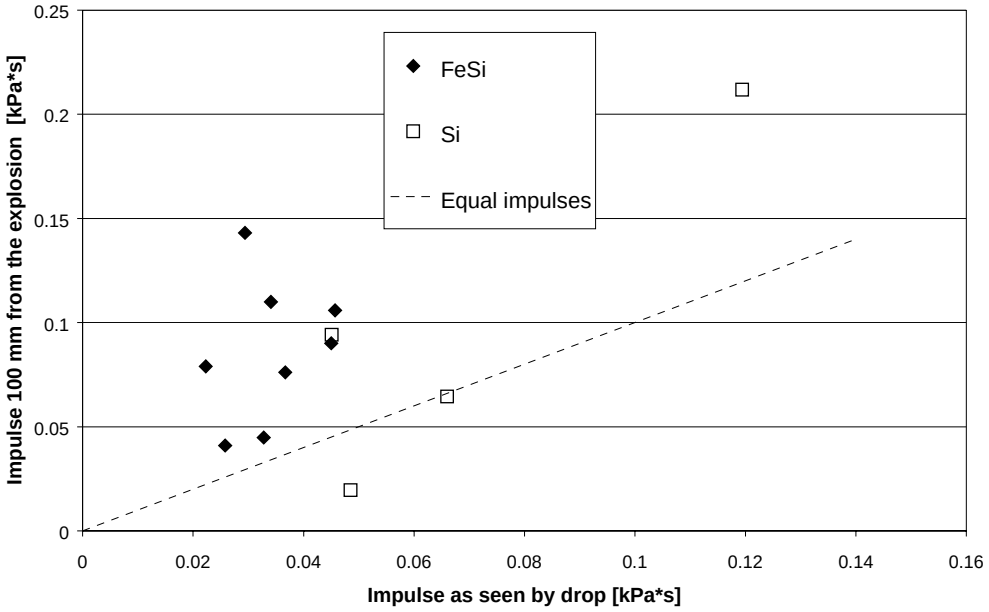

Figure 9.30 – Explosion impulses 100-mm from the drop, plotted against the applied trigger impulse. The dotted line indicates equal values for the two impulses.

In all but one of the explosions, the calculated bubble-collapse impulse was equal or larger than the trigger impulse used to initiate the explosion, i.e. the explosion impulse will be located above the dotted line. The trigger and the explosion impulses usually differed by a factor two, but in one case the explosion impulse was as much as five times larger than the trigger impulse. Thus, some of these explosions are strong enough to trigger a neighbor drop relatively far away. Since the explosion impulses in figure 9.30 are calculated relative to a 100-mm separation between the pressure transducer and the location of the drop at the time of triggering, it is simple to find the distance at which an explosion can trigger an identical neighbor drop. This distance is given by

$$D = \frac{I_{\exp losion}}{I_{trigger}} \times 100 \tag{9.19}$$

where $I_{explosion}$ and $I_{trigger}$ are the values plotted in figure 9.26. Typical values for D based on figure 9.30 are in the 100-400 mm range.

The data scattering in figure 9.30 is considerable, so we cannot establish any relationship between the applied trigger and the corresponding explosion impulses. However, if we perform a regression analysis, the trend line shows a rapid increase of explosion-impulse with increasing trigger impulse, as expected from theoretical considerations. A strong trigger will ensure total collapse of the vapor film, and it may increase the fragmentation rate of the melt. Thus, the heat transfer is enhanced, causing more water to vaporize under high local pressure. Ultimately the collapse of the steam bubble induces a stronger pressure transient compared to that of a weaker trigger transient.

9.13 An example visualizing the effect of Al/Ca additives

Four separate experiments were performed in order to visualize the effect of Al and/or Ca additives to silicon. All experimental parameters were kept constant, except for the compositions (A-D as described in table 9.2). Time-pressure traces were recorded for each experiments, as well as two darkened-room photographs using the open-shutter technique.

The following parameters were used:

- water temperature 22.8-23.2 °C
- impactor surface at 300 mm
- photodetector (trigger level) at 260 mm (intended trigger pressure P_{trig}=4.3 MPa)

Figures 9.31-9.34 show time-pressure traces and open-shutter photographs for each of the four separate experiments. Steam explosions were obtained with the pure silicon alloy and the B-type silicon alloy. Characteristic coarse fragmentation was obtained for the C and D-type alloy. The time-pressure traces for the explosive events are typical; the first bubble-collapse causes the largest pressure peak (roughly 4.5 ms after the drop was triggered). In the case of alloy B, we note that the second bubble is much larger than the first, however, the resulting pressure peak is a double-peak only one-third of the size of the first bubble-collapse related peak. Again, we suggest this is due to the formation of non-condensable hydrogen gas, as discussed in section 9.12.

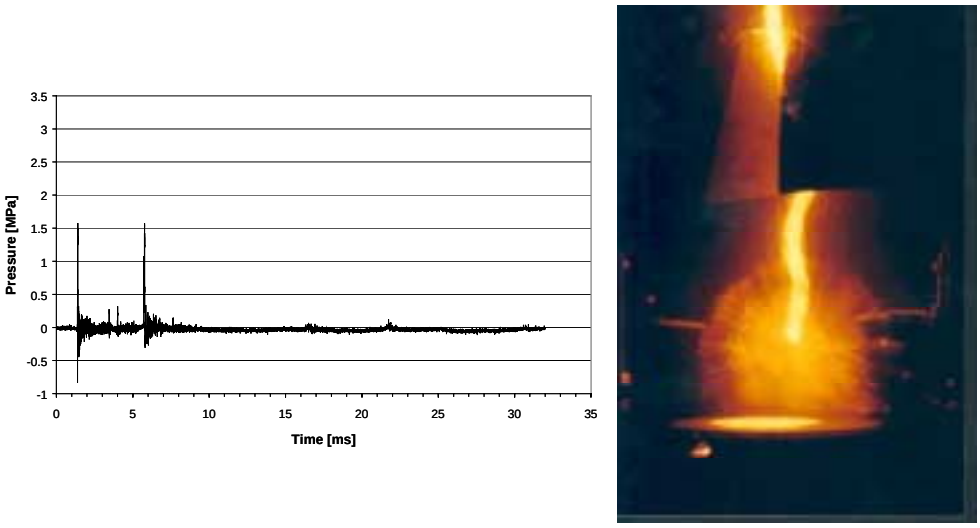

Figure 9.31 – Time-pressure trace and open-shutter photograph for a drop of pure silicon (alloy A). The drop triggered as intended, P_{trig}=4.3 MPa.

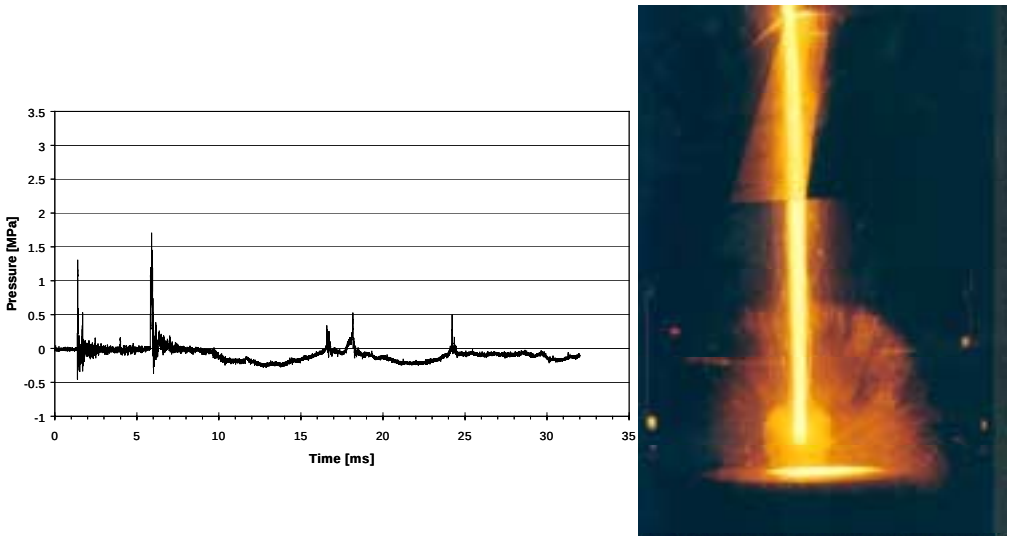

Figure 9.32 – Time-pressure trace and open-shutter photograph for a drop of Si alloyed with Al (alloy B). The drop triggered only 20 mm from the impactor (P_{trig}=8.5 MPa).

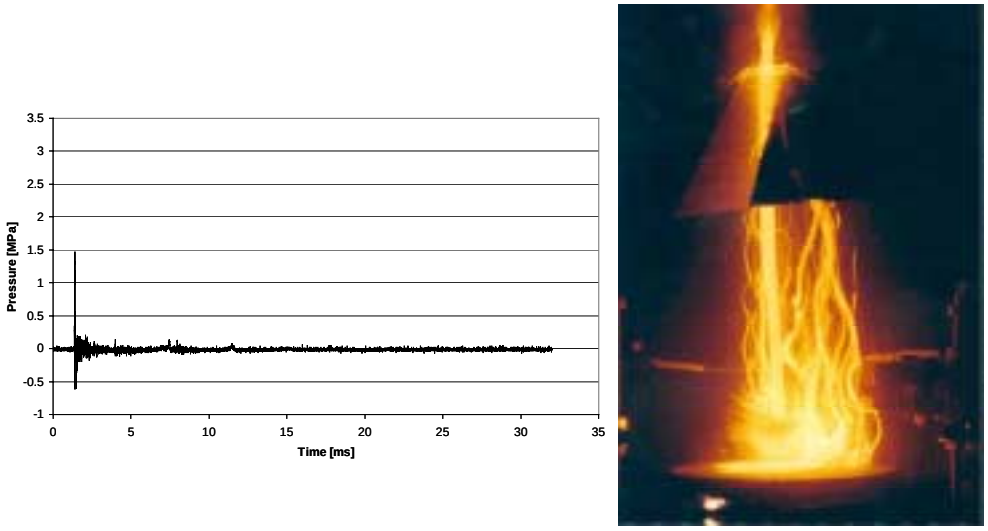

Figure 9.33 – Time-pressure trace and open-shutter photograph of a drop of molten Si alloyed with Ca (alloy C) fragmenting coarsely. The drop triggered later than intended, P_{trig}=6.8 MPa.

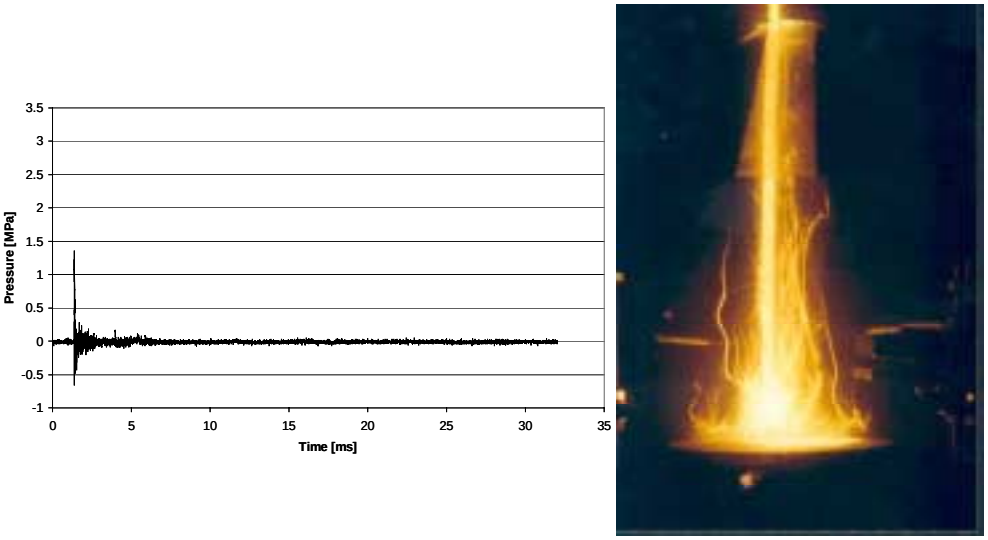

Figure 9.34 – Time-pressure trace and open-shutter photograph of a drop of molten Si alloyed with Al and Ca (alloy D) fragmenting coarsely. The drop triggered than intended, P_{trig}=6.8 MPa (same as for the previous example).

The coarse fragmentation events shown above (figure 9.33 and 9.34) visualize that once the drop has been triggered, an initial fragmentation takes place. However, the existence of Ca in the drop prevents the melt from being fully fragmented. Small luminous particles embedded in gas bubbles rise toward the surface and create visible traces behind. These particles are much larger than the fine debris that can be recovered after a typical steam explosion. Thus, the initial fragmentation appears different when Ca is added to the melt. The melt is not fragmented rapidly and finely enough to achieve the surface area needed to generate steam at a rate that causes steam bubbles to grow. Even if the existence of Ca would cause a liquid slag film to cover the metal, virtually instantly as the melt is broken up subsequent to the triggering event, it is still quite astonishing how such a thin slag film would reduce the melt's ability to fragment into fine debris, as is the case with the pure silicon (as well as the B-alloy once very large trigger pulses are applied). We have in this work not been able to come up with a good explanation for this effect of alloying. However, the outcome of alloying the melt has been in agreement with industrial experience, and we can attribute this effect to the hindering of fine fragmentation of the melt upon the collapse of the vapor film initiated by sudden pressure increases. Alloying with Al causes the same type of effect, but as shown in figure 9.32, such an alloy can still be triggered if the pressure is high enough. Note that in other experiments with the B-type alloy, no explosions were obtained (for the same or higher trigger pressures).

9.14 Effect of water-temperature

For the thesis work, the temperature of the water in the water chamber has not been subject to variation. However, Nelson *et.al.* (1998) released molten drops of ferrosilicon into water at three different temperatures; 8, 20 and 80 °C, using the same apparatus as described in chapter 7. Thus, their observations will be given below for convenience.

Nelson *et.al.* released drops of FeSi75 into water, either pure or with alloying elements (Al/Ca). In the case of alloyed material, no explosions occurred at any water temperature. However, a certain degree of coarse fragmentation occurred for the alloy containing 0.34% Al and 0.07% Ca, similar to those shown in figure 9.33 and 9.34. For the alloy containing 1.4% Al and 0.63% Ca, no fragmentation was observed at all.

Pure ferrosilicon drops could be triggered at any of the three water temperatures. The explosions were most vigorous at 8°C, less vigorous at 20 °C and very mild in hot water. The latter interaction seemed to be a mixture of a coarse fragmentation event (several luminous particles ascending toward the

surface within hydrogen bubbles) and a more typical steam explosion (fragmentation of the melt into very fine debris).

The above observations are consistent with the theoretical aspects as discussed in chapter 3. For instance, Dhir and Purohit`s correlation for the minimum temperature difference between the melt and the saturation temperature of the water (equation 2.32) in order to sustain film boiling is very sensitive to changes in the ambient temperature. If the water temperature is 8 °C, the surface of the melt must be at least ~ 940 °C to stabilize film boiling. However, if the water temperature is increased to 80 °C, a surface temperature of roughly 360 °C would be sufficient to sustain film boiling. Thus, increasing the water temperature has a profound stabilizing effect on the system`s ability to be subject to explosions. Also, the overall heat transfer rates also depend on the pool temperature. Even if the vapor film is collapsed by an external pressure disturbance, the local heat transfer rates may not be sufficient to rapidly vaporize the water. This would explain the strange interactions observed at elevated water temperatures.

9.15 Summary of drop-release experiments

We have previously described the results obtained with the release of single drops of molten silicon/ferrosilicon into water. In this section, we will briefly summarize these results.

9.15.1 Stability of the vapor film: trigger thresholds

The vapor film protecting the melt from rapid heat transfer, is stable in the sense that drops of molten Si and FeSi75 *never* explode spontaneously when released into water (Nelson *et.al.*, 1999, 2000). Actually, quite strong trigger pressures are needed to collapse the vapor film and initiate the explosion. Such trigger pressures have been found quantitatively for the systems in question, along with water depths at which the drop still can be triggered.

Drops of molten ferrosilicon (FeSi75):

Two different drop diameters were used; 9 and 11-mm. For the 11-mm diameter drops, we used a trigger pressure of 0.3 MPa, which initiated explosions in about 50 % of the cases. Thus, the trigger threshold is close to this value, but somewhat smaller. These large drops also contained Al and Ca, see table 9.1 (alloy 1A). However, in this case, the impurities did not seem to have any effect as to prevent steam explosions.

The smaller FeSi75-drops were more resistant against pressure disturbances. We were not able to find an accurate value for the trigger threshold, but based on our findings, it must be close to 0.6MPa. At a trigger pressure of 0.6 MPa, one out of ten drops exploded, while at a trigger pressure of 1.3 MPa, 19 out of 27 drops exploded. The difference in composition was negligible. Furthermore, no particular effect of water depth (i.e. cooling time) could be established. These last two observations are applicable for both the 9 and 11-mm diameter drops.

Drops of molten silicon:
This alloy required higher trigger pressures in order to explode, compared to the ferrosilicon drops. We were able to establish a trigger threshold at about 2 MPa. Above this value, 80 % of the triggered drops exploded. No explosions occurred if the trigger pressure was below this value. Furthermore, we found that we could not trigger silicon drops below a water depth of 400 mm, as the drops were beginning to solidify. Indeed, we found that in several cases, the drops had already started to solidify at the instant of triggering. Large pieces of metal were found along with the powder, indicating that a solid shell had formed on (parts of) the surface of the molten drop.

The effect of alloying the silicon with Al and/or Ca was astonishing; only 0.04 % Ca was enough to prevent steam explosions, even at trigger pressures up to 10 MPa. The effect of aluminum-addition was similar, but in a few cases explosions were achieved, at elevated trigger pressures. One interaction was very mild (trigger pressure 5 MPa), while the other one was one of the most powerful explosions during the course of this program. The applied trigger pressure was 11.3 MPa, considerably more than normal values (1.5-5 MPa). Thus, it seems like the actual levels of Ca-additions prevents steam explosions of molten silicon when the applied trigger pressure is in the 1-10 MPa ranger. Additions of Al to the silicon reduce the likelihood of steam explosions considerably, but under strong trigger pressures, this alloy may still fragment explosively in water.

9.15.2 Fall velocities

A surprising effect of impurities was found regarding the fall velocity in the water as measured with the video system. For silicon drops the velocity increased by a factor two when the drops were alloyed, whether it was 0.04 % Ca, 0.4 % Al or both. A similar effect was found for the ferrosilicon drops, however, the increase in fall velocity was less dramatic (see tables 9.5-9.7).

9.15.3 Generation of hydrogen

As the melt reacts chemically with the vapor-film, hydrogen forms and is detached regularly from the vapor film as the drop descends. Upon fragmentation of the melt, the rate of hydrogen generation increases due to the larger surface area. With a suitable collector system, we have measured the amount of hydrogen generated for various drop releases and interactions in water, see table 9.15 for a summary. Typical amounts of hydrogen collected are in the 1-7 ml range, depending on the characteristics of the fragmentation event, if any. This amount of hydrogen indicates that between 0.5% and 1.0% of the melt has been oxidized through a gas-phase reaction involving SiO. This may not sound like a problem, but in large-scale granulation industry, this is 2 liters per kg granulated material, indeed an amount that has to be considered in terms of safety.

The effect of alloying elements (Al and Ca) is the formation of the stable oxides Al_2O_3 and CaO on the surface of the granule, thus increasing the rate of hydrogen generation.

9.15.4 The formation of colloidal material

A violent steam explosion causes the formation of very small particles, presumably with a diameter less than 50 μm. These particles are not recovered from the water through settling over time, but they stay floating in the water. Depending on the severity of the interaction, losses up to 55 % (Si) and 35 % (FeSi75) have been registered.

The colloidal material appears to be a mixture of combustion-formed particles (i.e. silica) and solid metal, based on both the X-ray diffraction pattern of recovered colloidal material and the lack of hydrogen to account for a complete combustion of the material not recovered from the water chamber after an experiment.

9.15.5 PV-energy

The pressure-volume energy of a steam bubble has been calculated for a number of steam explosion experiments. This is a quantitative measurement of the explosion efficiency. Typical PV-energies measured are between 5 and 40 J/g, for both Si and FeSi75. In terms of fraction of total enthalpy of the drops, the energy transferred is up to 1.0 % for Si, and 2.5 % for FeSi75.

9.15.6 Time-pressure traces

In the process of assessing the probability for large-scale explosions, we have to define what triggers a steam explosion and what kind of action that follows. For the latter we have made several pressure measurements, and the results clearly show that the a typical steam explosion generates higher pressure peaks (or larger impulses) than the trigger transient, relative to a point 100 mm from the molten drop. Furthermore, by the use of high-speed video techniques, we have been able to explain the time-pressure history of a typical steam explosion. It was found that as the steam bubble has grown to its maximum size, it would collapse and cause water jets to rush inwards and impact in the center of the former bubble. This will induce a shock wave, travelling out to be registered by the pressure transducer. This pressure transient is able to trigger a new steam explosion, if a drop is located nearby.

10. OXIDATION OF LIQUID SILICON - RESULTS

This chapter will summarize the results concerning oxidation of molten silicon. Some of the results have been published earlier (Hildal and Tuset, 2000, Hildal and Tuset, 2001).

10.1 Introduction

The composition of the silicon is the same as that shown in table 8.2, that is, four different compositions. These are either “low” in both Al and Ca, “high” in Al or Ca, or “high” in both Al and Ca.

The silicon samples have been oxidized using the apparatus described in chapter 5. The samples have been melted in an inert atmosphere and oxidized at elevated temperatures; 1450 and 1550 °C. Identical alloys have been granulated using the apparatus described in chapter 6. We will describe the characteristics of the various oxidized samples and compare the oxidized samples with those granulated in water.

The microprobe images shown later in this chapter normally show the active elements; Si, Al, Ca, O and sometimes Fe. The colors represent a composition interval (in weight percent), with a definition given to the right of each image.

10.2 Oxidation of pure silicon (alloy A)

10.2.1 Oxidized samples – general observations

The surfaces of the specimens are dominated by a white, patchy SiO_2-layer. The thickness of this oxide layer varies from a few micrometer up to 100-120 μm. The oxide layer is rather porous, which can easily be seen from microprobe analysis of the specimen (figure 10.2). The intensity of the back-scattered electrons is lower than the corresponding intensity for a massive sample, for which the sum of the weight percent contributions from all the elements would equal 100. A sum less than 100 imply porosity.

Several spherical particles are located inside the silica, forming a band 50 μm from the silicon matrix. These particles are rich on Si, around 80-90 weight percent. Porosity in the sampling area may account for the failure to reach 100 % on a weigh percent basis. The Si-spheres form a band along the silicon matrix, approximately 50 μm from the matrix. It is highly unlikely, least to say

impossible, that these particles are drops of molten Si that have mixed with molten silica just after the water injection. Silica is not liquid at the low temperatures in question (1450-1550 °C), and the oxidation products are bound to be either solid silica or gaseous phases according to the reactions 10.1 and 10.2:

$$Si_{(l)} + H_2O_{(g)} = SiO_{(g)} + H_{2(g)} \qquad \Delta H>0 \qquad (10.1)$$

$$Si_{(l)} + 2H_2O_{(g)} = SiO_{2(s)} + 2H_{2(g)} \qquad \Delta H<<0 \qquad (10.2)$$

The experimental evidence clearly indicates that reaction 10.1 is the dominant. If, on the other hand, reaction 10.2 took place to a certain extent, the formation of solid silica would block any transfer of particles from the silicon-phase. Thus, we cannot explain the occurrence of Si-particles if reaction 10.2 takes place. However, if the oxidation of liquid silicon results in the formation of gaseous SiO, we can indeed offer an explanation of the Si-particles inside the surface silica, details to follow in section 10.2.2.

The assumption that reaction 10.1 is dominant is also supported by the fact that a layer of SiO_2 was found on the interior walls of the little carbon crucible. Again, reaction paths not including gaseous SiO cannot explain how silicon was transported from the melt several (2-8) millimeters up along the crucible walls. Particles of Si inside this oxide layer, similar to those found in the surface silica layer, also indicate that a reaction/condensation that involves SiO-gas took place. The silica layer along the walls has a thickness of about 20-40 μm.

10.2.2 The formation of silica – reaction path

The suggested reaction path for the oxidation of liquid silicon also applies to silicon alloyed with small amounts of Al and Ca, excepth for some small modifications. We will discuss alloyed silicon in section 10.3-10.5.

Silicon, being the by far dominant element (in pure silicon samples more or less the only element), will be the first element to participate in the reaction with vapor subsequent to the water injection toward the melt. We have established that reaction 10.1 takes place, causing the partial pressure of SiO to increase close to the surface of the melt. Thus, there will be a concentration gradient of SiO pointing away from the surface. The fate of the SiO-gas now depends on whether there is sufficient oxygen available to form SiO_2. If not, the SiO will eventually condense and form SiO_2 and solid Si as the temperature of the gas decreases. In other words, both of the two reactions

$$2SiO_{(g)} = Si_{(s,l)} + SiO_{2(g)} \quad (10.1)$$

and

$$SiO_{(g)} + H_2O_{(g)} = SiO_{2(s)} + H_{2(g)} \quad (10.2)$$

are responsible for the silica layer observed. Figure 10.1 illustrates how these reactions occur at different distances from the surface. Close to the surface, where the partial pressure of vapor is lower than at distances further out, reaction 10.1 dominates, and the result is a mixture of silica and silicon as the SiO-gas condenses. Further out, the SiO-gas reacts more or less completely with vapor and form solid SiO_2.

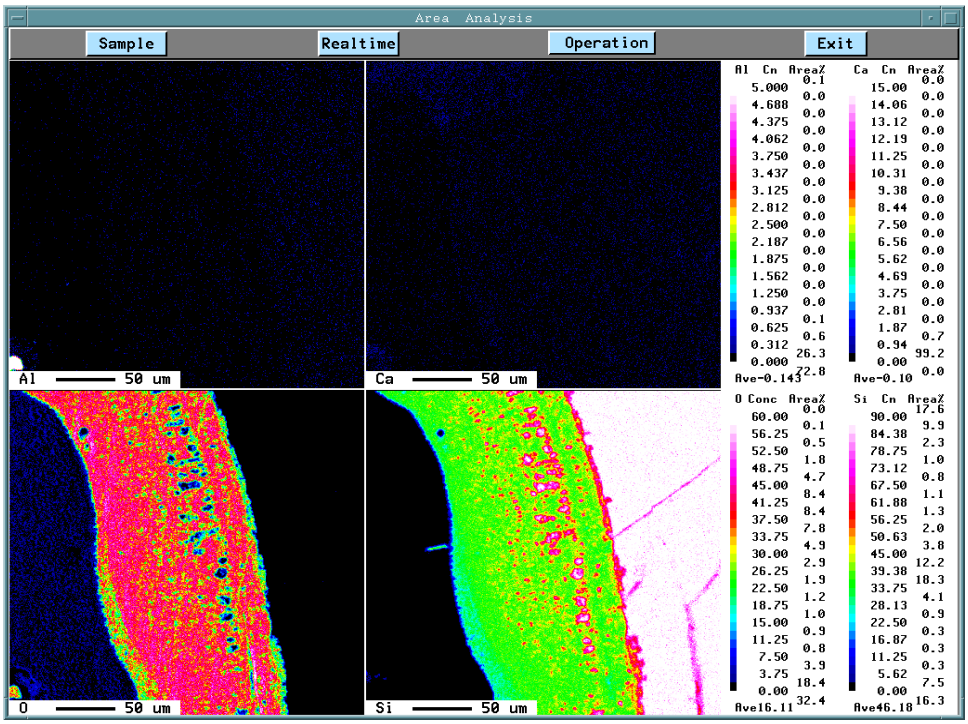

Figure 10.1 – Microprobe element mapping of the surface oxide on silicon (alloy A) oxidized in molten state (1450 °C) with a 0.2-ml water-jet.

In both cases the resulting silica will be porous, quite consistent with the observations we made.

10.2.3 Oxidized samples – effect of melt temperature

On the effect of increased melt temperature prior to oxidation, the most striking difference is the change in color of the oxide layer, from white to

brown. Besides from that, the SiO_2-layer does not appear to be any different from the lower melt temperature.

Silica is also observed on the crucible walls, just as it was for the lower temperature melt. Clusters of Si-rich particles have formed close to the wall. No carbon analysis was made, but we expect these particles to be SiC, which is consistent with the amount of Si detected within. The origin of such particles could be a combination of SiO reacting directly with the crucible, or a reaction involving carbon in the saturated silicon melt.

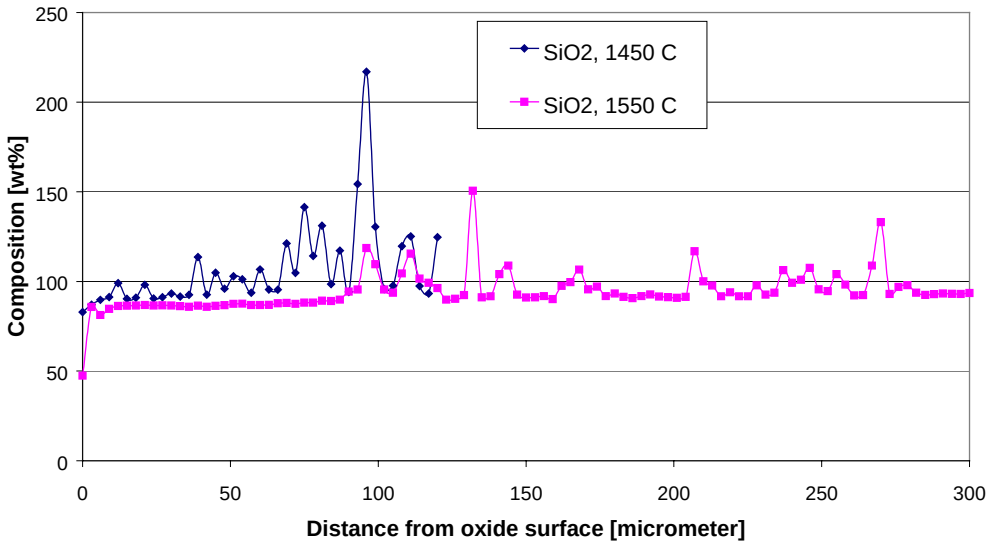

Figure 10.2 – Concentration profiles of the surface oxide from two silicon melts (alloy A, 1450 °C and 1550 °C), oxidized with a 0.2-ml water-jet.

The thickness of the SiO_2-layer is larger for the sample oxidized at the highest melt temperature. The oxide layer of pure silicon oxidized at 1550 °C reaches a thickness of 300 μm, while a sample oxidized at 1450 °C has a maximum thickness of 130 μm (figure 10.2). The density of the oxide layers does not change noticeably when the melt temperature is increased. In figure 10.2, the composition of the oxide layers is plotted against the distance from the oxide surface. The concentration of SiO_2 is less than 100% for both of the samples, indicating that there is some porosity in the oxide. We also note that the concentration increases well above 100 % some places. This is an effect of small spheres of Si inside the layer of SiO_2. The microprobe uses SiO_2 as standard, and if the probe detects an area of pure silicon, it will give us values that are too high. Figure 10.1 shows the element analysis of the surface of silicon oxidized at 1450 °C. As we can see from the picture, there exist several

spheres of pure silicon in the oxide layer, and these will give us wrong estimates on the concentration of SiO_2.

The partial pressure of SiO in equilibrium with molten Si and vapor increases with temperature. Thus, we could expect that the silica were denser for samples oxidized at 1550 °C compared to those oxidized at 1450 °C. However, for pure silicon no consistent change of porosity was detected with respect to different melt temperatures.

The interface between the oxide layer and the metal is somewhat rougher (see figure 10.3) for silicon melt oxidized at 1550 °C, however, the difference is not large. The effect becomes more apparent for alloyed melts, and will be discussed in sections 10.2-10.4.

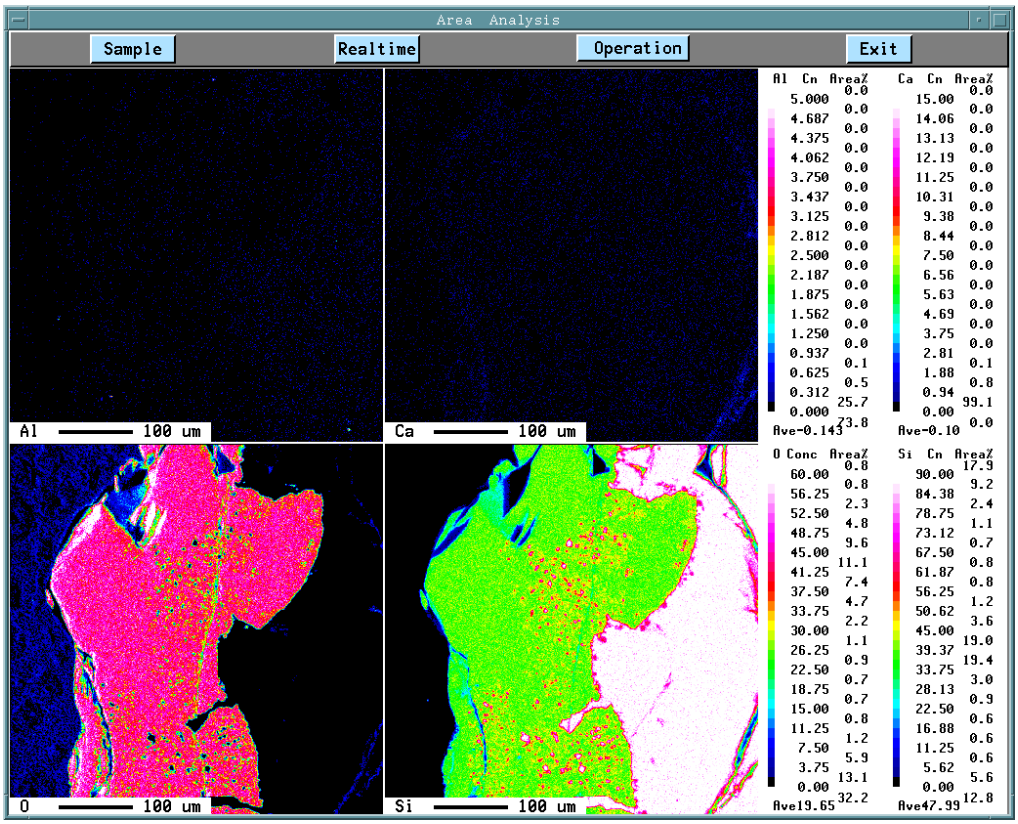

Figure 10.3 - Microprobe element mapping of the surface oxide on silicon (alloy A) oxidized in molten state (1550 °C) with a 0.2-ml water-jet.

URN:NBN:no-2125

10.2.4 Water-granulated samples

Figure 10.4 is an element mapping of the same alloy, granulated in water. Due to the experimental layout, all of the drops released into water have a temperature equal to the liquidus temperature, approximately 1412 °C. The most striking difference between figure 10.1 and 10.4 is the absence of the porous layer of SiO_2 on the drop of melt granulated in water. The surface is clean, with no traces of any oxide. However, there is evidence in the form of collected hydrogen that there has been a chemical reaction between silicon and water. As discussed in section 8.8, approximately 1 ml of hydrogen is recovered from the water when a 1-g drop of pure silicon quenches in the watertank. Based on the lack of oxygen-containing compounds on the surface of the granule, we conclude that the oxidation products formed in the reaction between water vapour and silicon have been gaseous, presumably SiO. The gaseous products have been efficiently washed away from the surface of the drop. The exact mechanisms are not established, but we realize that the gas film is by no means steady; transient conditions apply as the chemical reactions take place. Video-recordings reveal that gas bubbles are released from the wake behind the drop at quite regular intervals, thus, we assume that these bubbles carry SiO-gas away from the vapor film surrounding the molten drop.

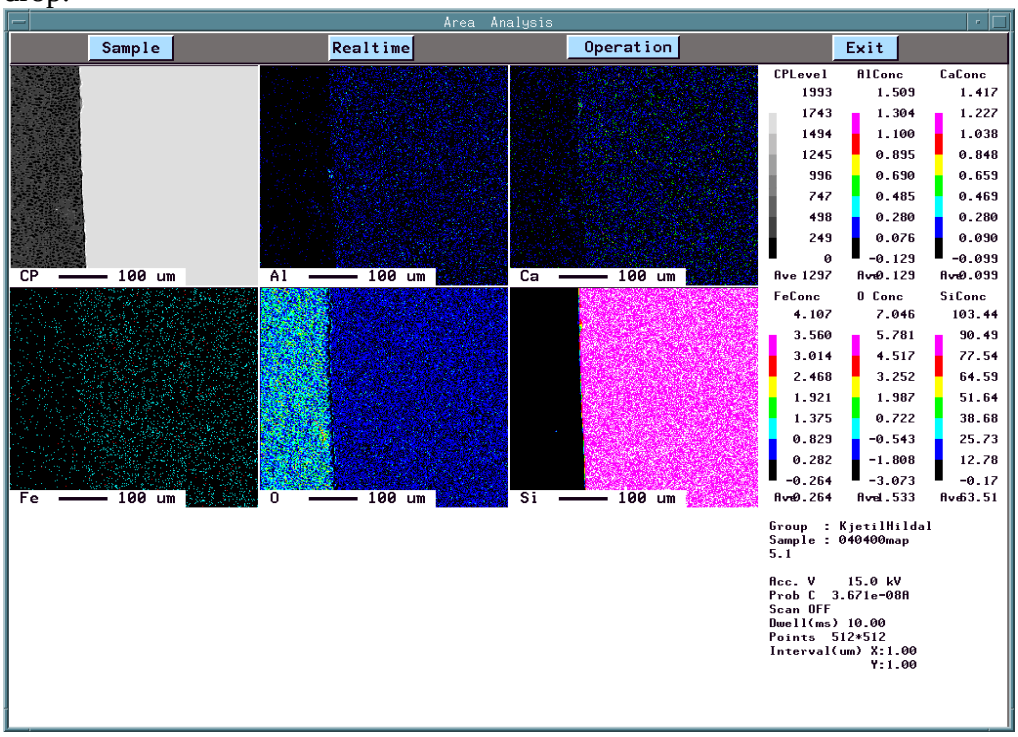

Figure 10.4 – Microprobe element mapping of the surface of a drop of liquid silicon (alloy A, liquidus temperature) quenched in water.

Several drops of pure silicon quenched in water were examined the same way. In general, no oxide was detected on the surface of the drop. The only location silica could be detected with the microprobe, was on the bottom of the drop (the side leaning against the impactor surface). We believe that SiO-gas is trapped beneath the drop, thus, some of the gas eventually condenses on the surface of the drop. The bottom of the drop is also quite irregular compared to the smooth, spherical top, confirming the observations from video recordings. The generation of vapor and other gases makes the drop to shake after arriving at the impactor.

10.2.5 FeSi-drops quenched in water

A few granules of FeSi75 quenched in the water-tank were also examined with the microprobe. Since iron oxides are reduced at the temperatures in question (around 1400 °C), the oxide layer on the surface will only constitute of the three oxides SiO_2, Al_2O_3 and CaO, depending on the composition of the melt. The granules that were examined were FeSi75 with no alloying elements, see table 8.1 (alloy F1/F2). Except for the different microstructure of the granules, no differences were found relative to pure Si-drops. No oxide layer could be detected, except from a few sporadic spots of SiO_2 at the bottomside of the drop (the area resting against the impactor surface).

10.3 Oxidation of silicon with 0.4 % Al (alloy B)

10.3.1 Samples oxidized with a small water-jet

The specimens containing Al appear similar to the pure silicon-samples. A white, patchy oxide layer is covering the entire metal surface and most of the interior of the crucible. At the lower melt temperature, the thickness of the oxide is typically 35-55 μm. A layer of mixed oxide of Al_2O_3 and SiO_2 is deposited as a thin film along the interface between the matrix of silicon and a porous layer containing only SiO_2, see figure 10.5.

The oxide extends up the crucible walls, but here only very small amounts of Al are present. Instead, the concentration of Si is very high, and microprobe results indicate that some SiC is deposited along the walls, together with pure Si. Away from the wall/oxide interface, the oxygen concentration increases and we find the usual, porous SiO_2-layer. Traces of Al can be found along the interface between pure Si and the oxide layer.

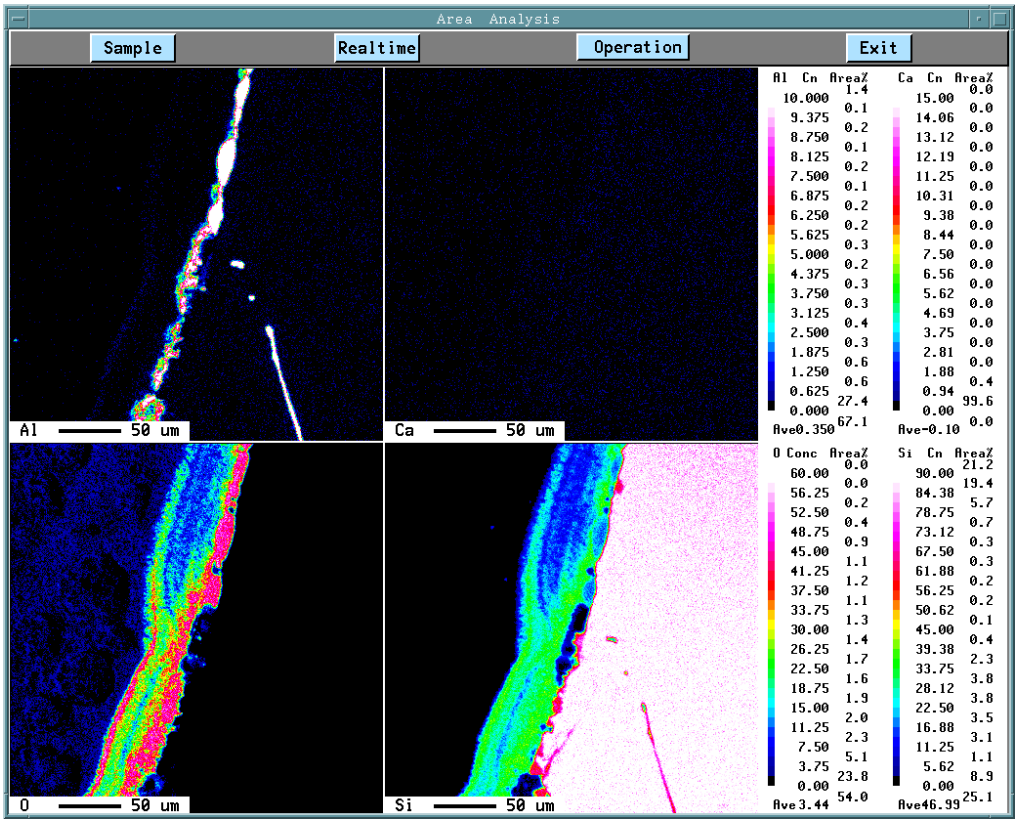

Figure 10.5 – Microprobe element mapping of the surface oxide on silicon (alloy B) oxidized in molten state (1450 °C) with a 0.2-ml water-jet.

The effect of increased melt temperature prior to oxidation is an increase in the thickness of the porous silica layer. The thickness of the slag-film (mixture of SiO_2 and Al_2O_3) is more or less the same. The oxide layer is also here rather patchy, with a maximum thickness of approximately 150 μm. Some Si-particles can be found inside the oxide layer. This was also found, but to a somewhat higher extent, in the pure specimen. The difference in melt temperature has not changed the appearance or the composition of the oxide deposited on the crucible walls.

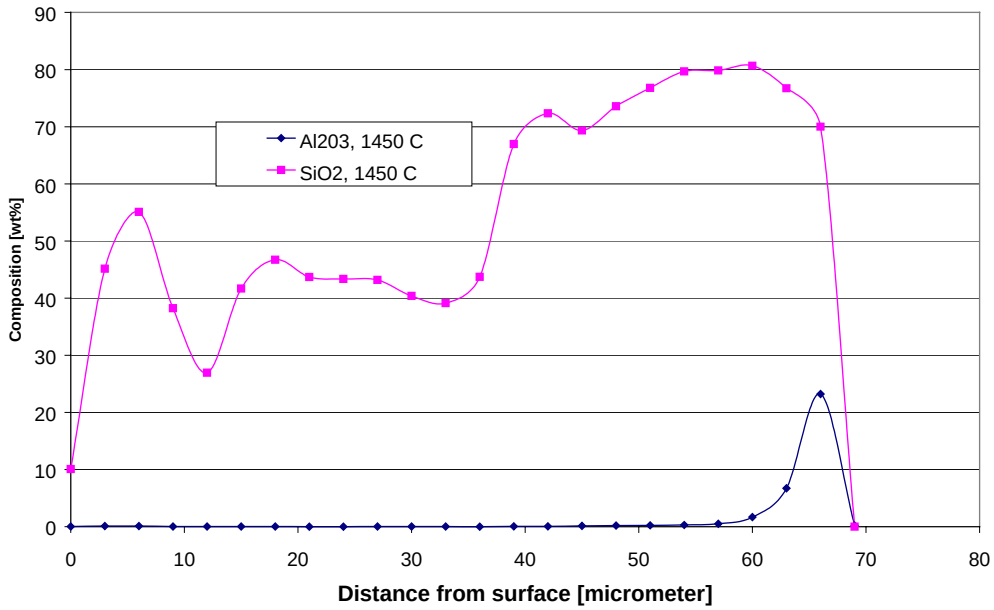

Figure 10.6 – A concentration profile of the surface oxide on silicon (alloy B, 1450 °C) oxidized with a 0.2-ml water jet.

Figure 10.6 shows the concentration profile of the surface oxide layer. The Al-content is zero through most of the oxide, but close to the silicon matrix it raises up to about 20 % (in terms of weight percent Al_2O_3). If we now compare with figure 10.7, where the melt was oxidized at 1550 °C, we note that the overall thickness of the oxide layer has increased by a factor two. Both figure 10.6 and 10.7 is based on analysis from regions containing thick oxide layers, relatively to the rest of each sample.

URN:NBN:no-2125

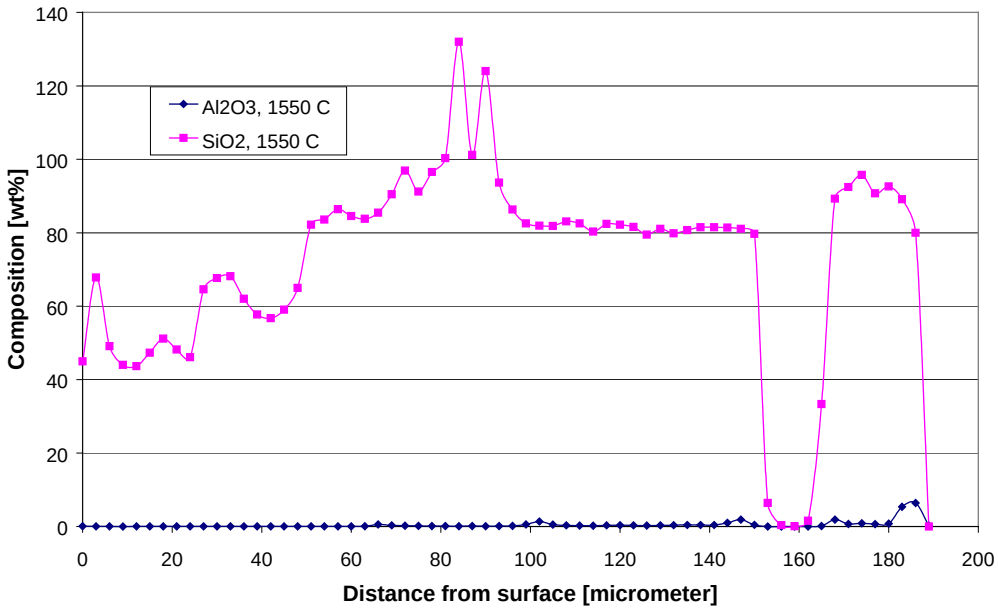

Figure 10.7 – A concentration profile of the surface oxide on silicon (alloy B, 1550 °C) oxidized with a 0.2-ml water jet.

10.3.2 Water-granulated samples

For the granulated samples, a very thin film (~ 5-10 μm) of slag was found on some parts of the surface of the solidified drop. The composition of this slag was typically 60% SiO_2 and 40% Al_2O_3. We were not able to detect any porosity of the slag film. Similar as for the pure silicon drops granulated in water, no porous SiO_2 was found on the outside of the slag. Approximately 80 % of the surface contained no oxide at all. Again, we believe the reason for the lack of SiO_2 relates to the oxidation mechanism. Gaseous SiO, which forms initially, is carried away from the surface due to the flow field around the drop. This may also influence on the oxidation of Al, as the results clearly indicate much thinner, and mostly absent films of slag on the granulated samples. For the samples oxidized with the apparatus described earlier, the oxide film contains a thicker mixture of Al_2O_3/SiO_2 as well as the porous layer of SiO_2 outside this mixture.

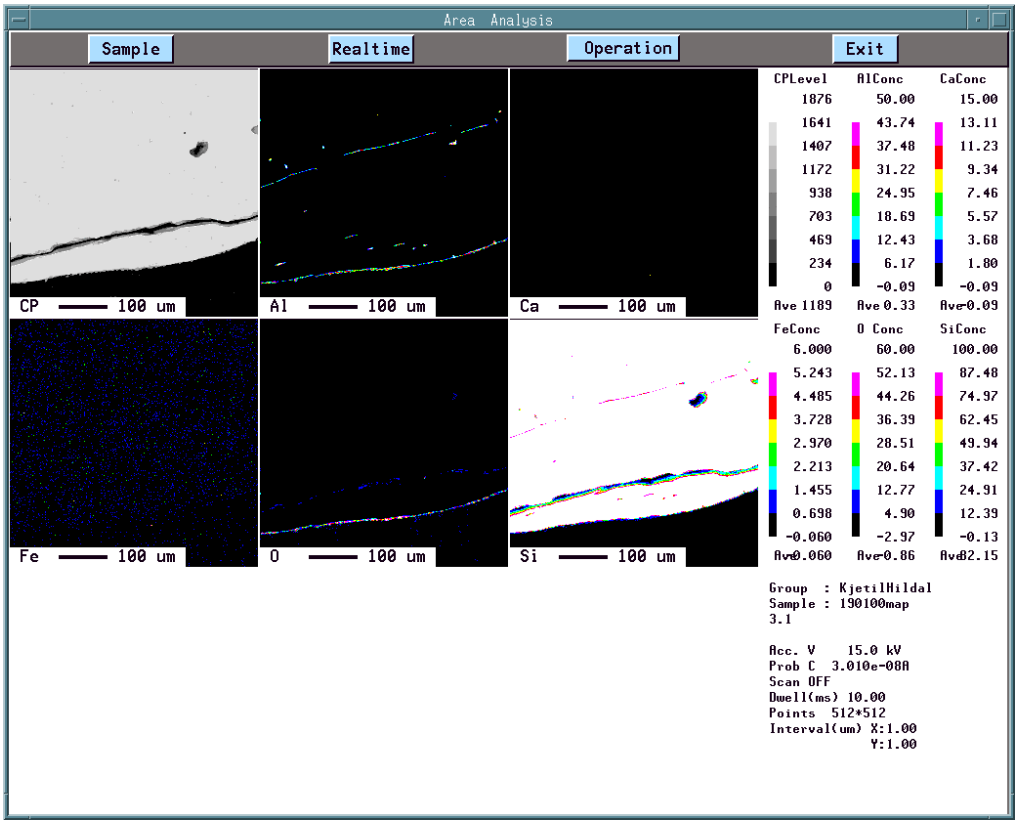

Figure 10.8 – Microprobe element mapping of the surface of a drop of liquid silicon (alloy B, liquidus temperature) quenched in water.

Similar to figures 10.5 and 10.6, a concentration profile of the surface oxide layer was obtained, shown in figure 10.9. The thickness of this slag film is about 5-10 μm, similar to those observed for the oxidized samples (see figure 10.6 and 10.7. However, we found that the slag film contained more Al_2O_3 than silica.

URN:NBN:no-2125

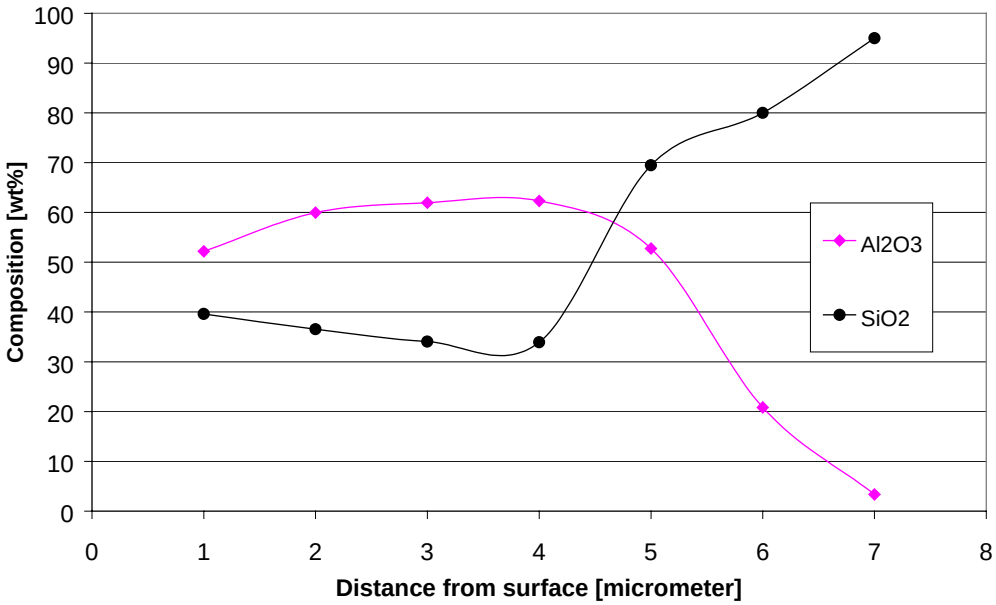

Figure 10.9 – A concentration profile of the surface oxide on a drop of liquid silicon (alloy B, liquidus temperature) quenched in water.

10.4 Oxidation of silicon with 0.04 % Ca (alloy C)

Even small additions of calcium will have a strong influence upon the probability for steam explosions during granulation of Si and FeSi. Thus, it is necessary to investigate how Ca change the surface properties of melts that otherwise would be likely to explode if a suitable trigger was applied.

10.4.1 Silicon oxidized with a small water-jet

The oxide appears similar to those previously described; a patchy, white oxide covers the surface of the metal and the crucible walls. The oxide has a square-wave form, with a high degree of regularity. The thickness is about 80 μm, but there are areas between the "squares" with no detectable oxide at all. The lengths of such "squares" of oxide are between 150 and 400 μm. Separation distances are of the order 100 μm.

The slag-forming element Ca behaved similar to Al with respect to the formation of a dense slag film on the surface of the silicon matrix. Further away from the slag/metal interface, a silica layer is dominating. The silica is as usual rather porous, depending on melt-temperature prior to oxidation. Thus, gaseous SiO is also here a key element in the oxidation reaction.

URN:NBN:no-2125

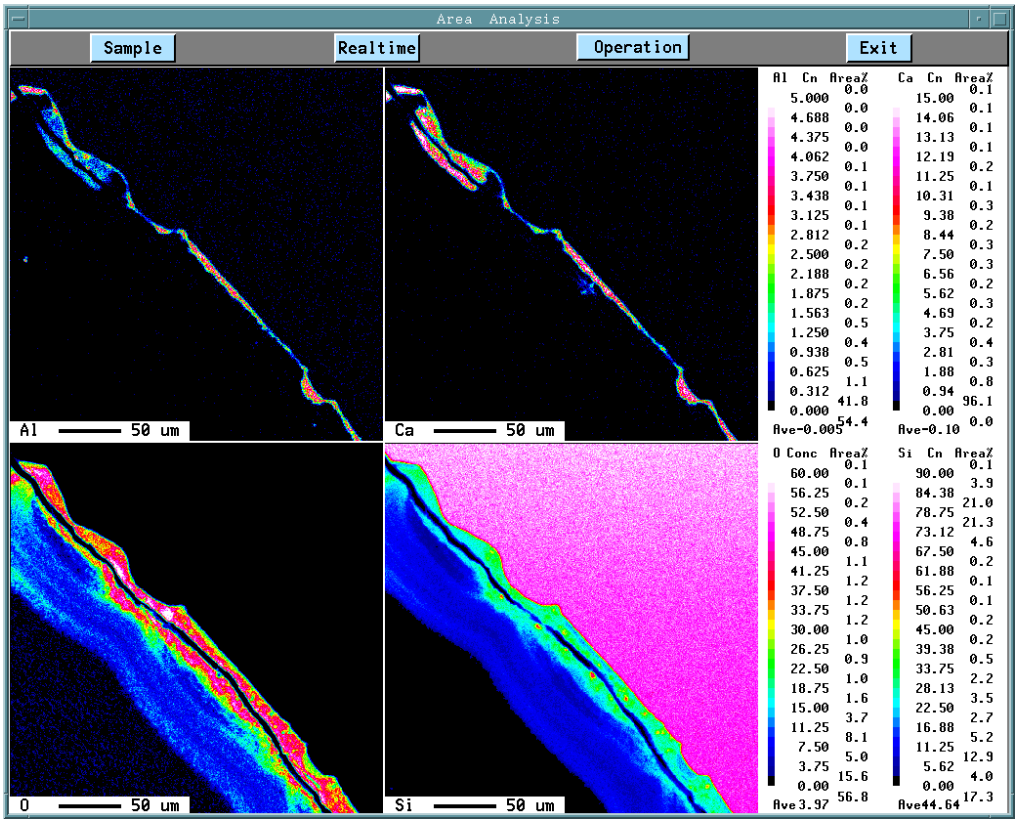

Figure 10.10 – Microprobe element mapping of the surface oxide on silicon (alloy C) oxidized in molten state (1450 °C) with a 0.2-ml water-jet.

Close to the silicon-matrix, the oxide consists of a mixture of SiO_2, Al_2O_3 and CaO. A concentration profile is shown in figure 10.11, showing the amounts of silica and CaO as we move inward toward the silicon matrix. Al_2O_3 is not shown in the figure, as typical levels were of the order 2 wt%. Aluminum is only present as a contamination element in these samples (about 0.06 %, see table 8.2). It will influence on the formation of a slag, but in a negligible way compared to that of calcium.

The slag film, appearing between 80 and 90 μm in figure 10.11, is thin compared to the total oxide. The concentration of silica away from this slag film is relatively low relative to the observations in figure 10.2 (pure silicon), but quite similar to the observations for Al-addition only (figures 10.5 and 10.6). The content of SiO_2 is around 30%, the rest being voids in the silica. Closer to the slag film the concentration of silica increases markedly to values around 90%. The large drop in SiO_2-concentration around 70 μm is due to cracks in the sample.

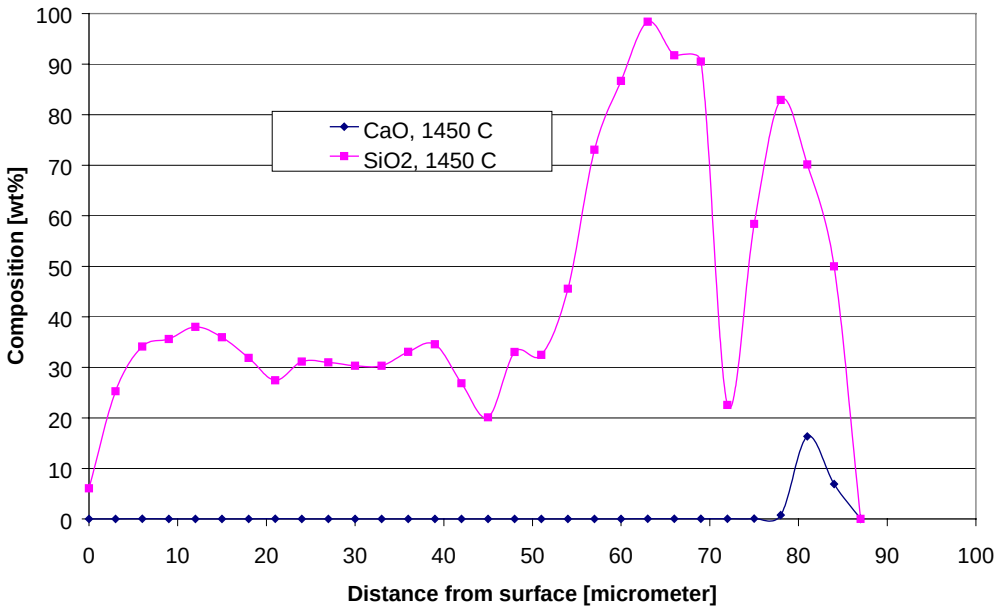

Figure 10.11 – A concentration profile of the surface oxide on silicon (alloy C, 1450 °C) oxidized with a 0.2-ml water jet.

Some oxide has been deposited on the crucible walls. No signs of either Al or Ca can be found, but high concentrations of Si and O. It appears that some melt has climbed up along the wall, giving pure Si along the graphite wall, with an outer layer of SiO_2. However, further up on the wall, only SiO_2 can be found, indicating that a condensation of SiO-gas has taken place. From the microprobe pictures available, no spheres of silicon can be detected.

Figure 10.12 shows the concentration profile for the same alloy, but this time the melt was heated to 1550 °C prior to water injection. The observations are very much the same as those described in section 10.1 and 10.2. The final silica layer at the surface is denser than for the melt oxidized at 1450 °C.

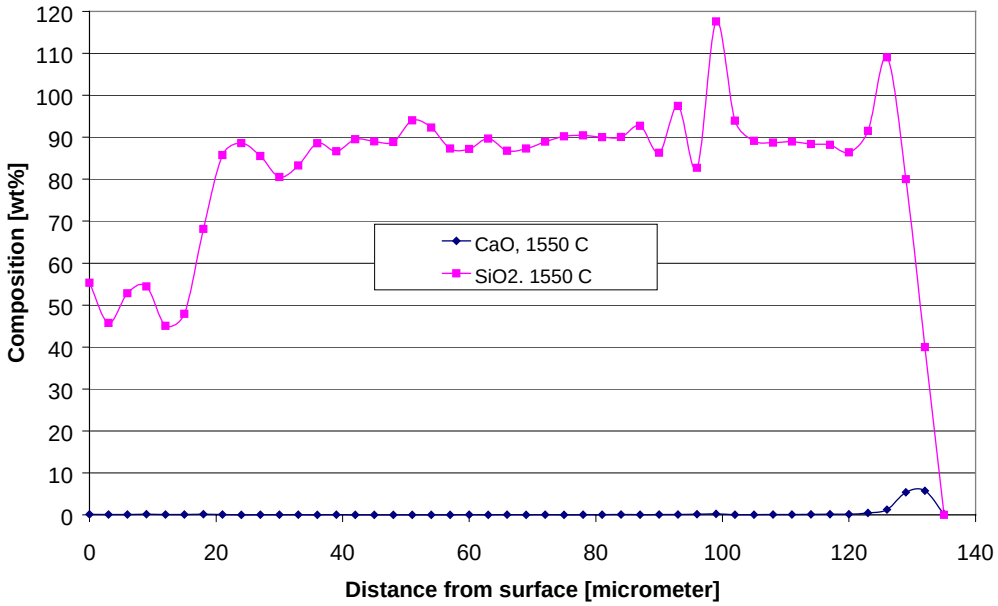

Figure 10.12 – A concentration profile of the surface oxide on silicon (alloy C, 1550 °C) oxidized with a 0.2-ml water-jet.

10.4.2 Water-granulated samples

In figure 10.14, a microprobe scan of the surface of a granulated drop of silicon (alloy C) is shown. This image is representative for areas of the drop containing some oxide. However, most of the surface (about 80-90 %) of the drop is clean. In that sense the surface appears very similar to that of alloy B described in the section 10.3.2. The thickness of the oxide is so thin that a step-analysis similar to that of figure 10.9 was not performed due to microprobe accuracy limitations on such small length scales.

When we compared these results to microprobe investigations of similar alloys granulated in water, we found that there were differences of the same kind as for the other compositions. In general, the surface of the granules did not contain any oxides. On a very limited (~10 %) part of the surface, we found a thin film of slag. The thickness of this slag film was of the order 1 μm. This made it difficult to obtain good quantitative analysis of the oxide. However, the oxide was very low on CaO, an upper estimate is 5 %. Traces (max 3 %) of Al_2O_3 were also found in this slag film, together with SiO_2. Apparently, the lack of SiO_2-formation on the surface of the drop affects the formation of CaO.

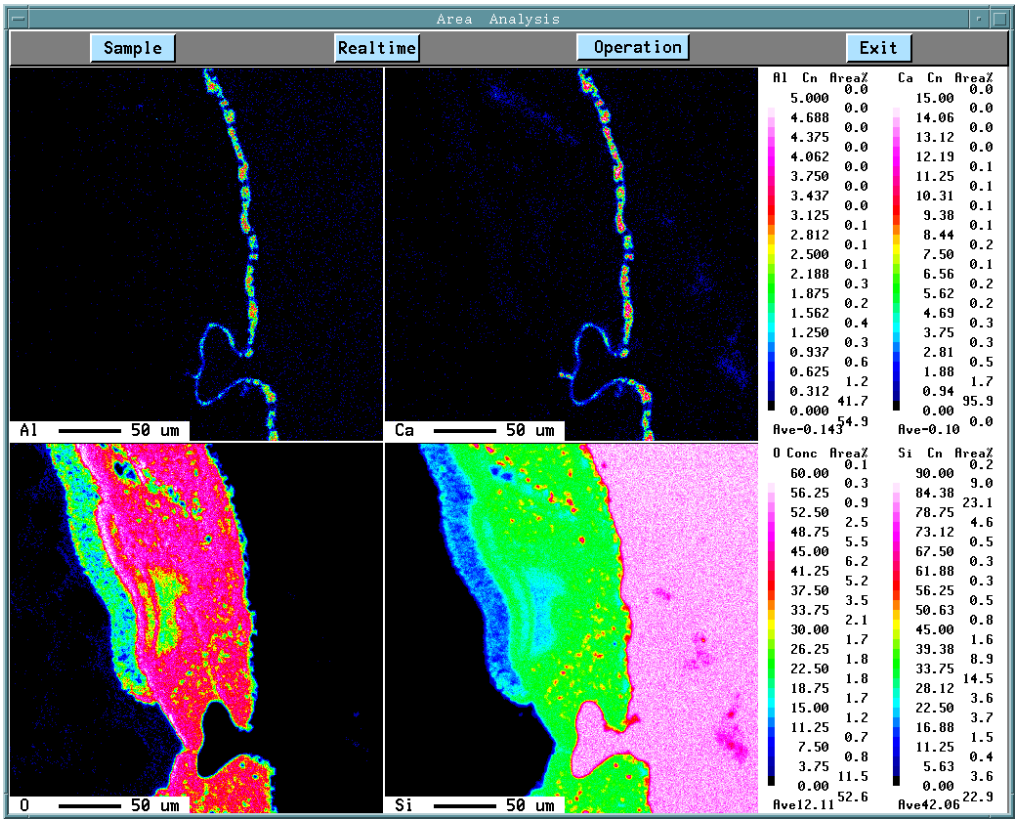

Figure 10.13 – Microprobe element mapping of the surface oxide on silicon (alloy C) oxidized in molten state (1550 °C) with a 0.2-ml water-jet.

The results from the microprobe investigation of this sample is not quite consistent to other findings (see chapter 8), where it was established that alloying the silicon with 0.04 % Ca prevented steam explosions completely. However, there is no drastic change of the appearance of the surface. There has been some slag formation, limited to a minor part of the surface.

It is quite clear that the conditions for the oxidation process have been different when we compare the microprobe scans for granulated drops and oxidized melts.

URN:NBN:no-2125

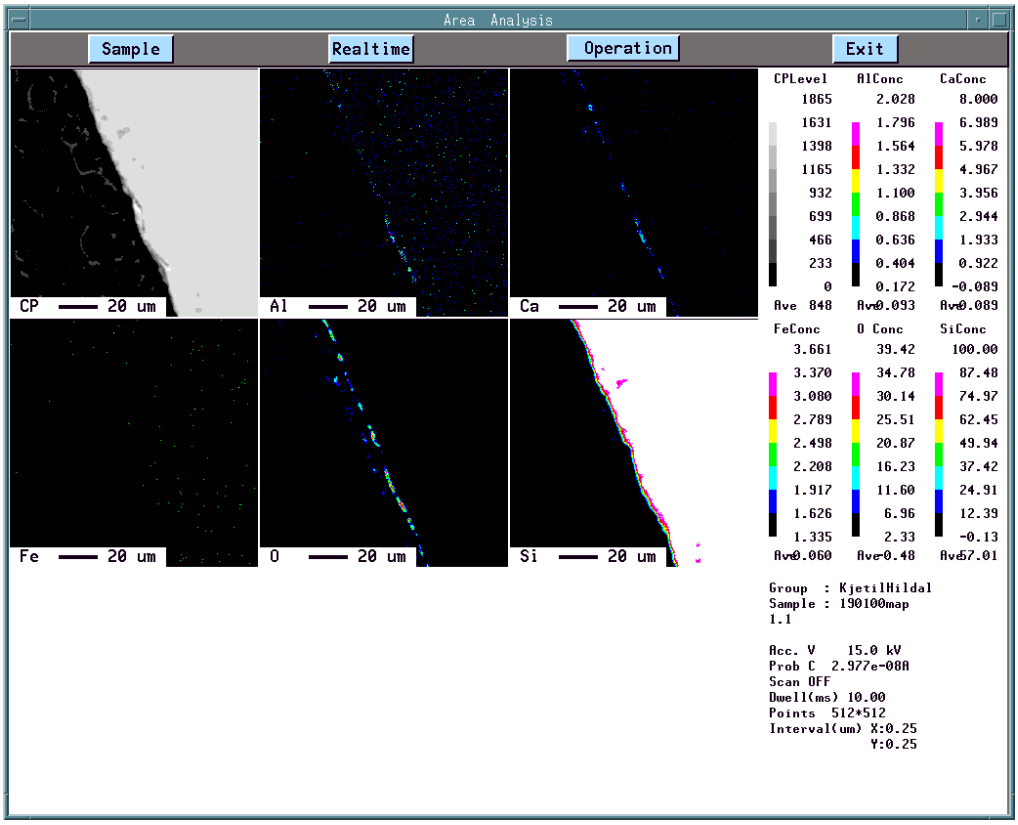

Figure 10.14 – Microprobe element mapping of the surface of a drop of liquid silicon (alloy C, liquidus temperature) quenched in water.

10.5 Oxidation of silicon with 0.4 % Al and 0.04 % Ca (alloy D)

10.5.1 General observations/effect of melt temperature

The effect of alloying the melt with both Al and Ca results in the formation of a firm layer of mixed oxides between the metal matrix and the outer layer of porous silica. The characteristics of the surface oxide are shown in figures 10.15-16 (element mapping) and figures 10.17-18 (concentration profiles) for the two different melt temperatures in question. As observed for other alloyed samples (previous sections), the silica layer, which varies in thickness, is most porous for the samples at the lowest temperature. Pure silica is also in this case deposited on the crucible walls, but there are no silicon spots seen in any of these layers, indicating that the deposited SiO has been fully oxidized.

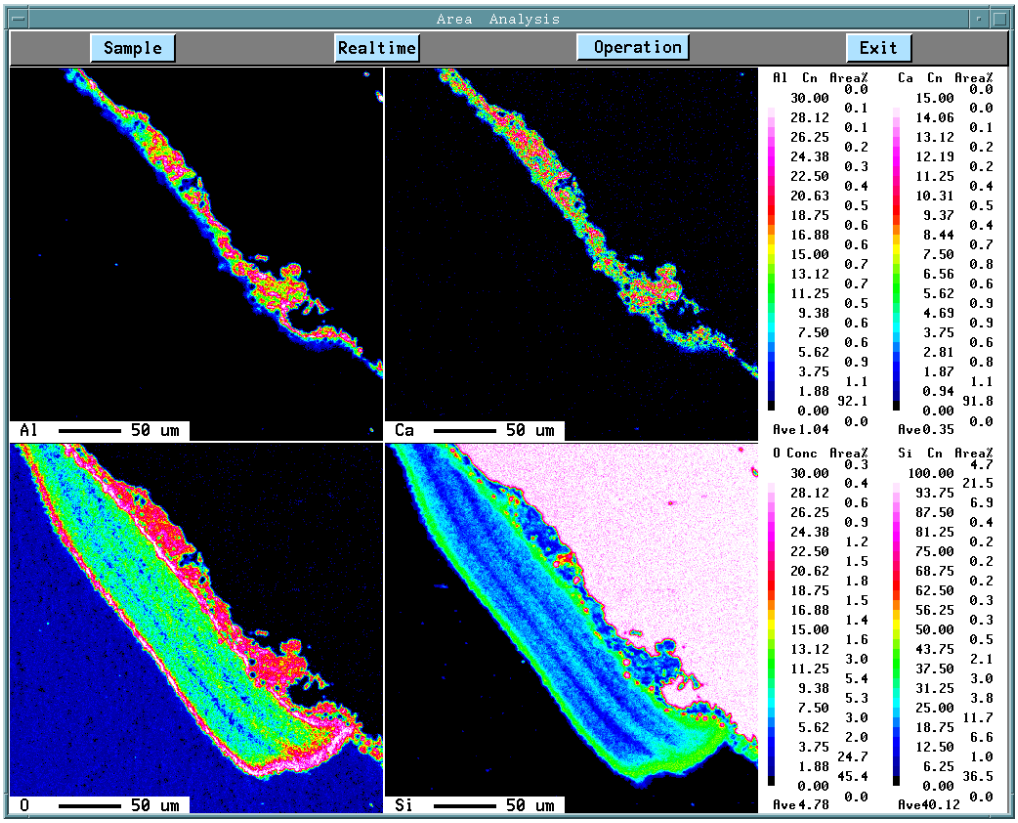

Figure 10.15 – Microprobe element mapping of the surface oxide on silicon (alloy D) oxidized in molten state (1450 °C) with a 0.2-ml water-jet.

The mixed oxide layer, which covers the entire surface of the metal, has the appearance of a mineralized substance consisting of small grains that differs in composition, but the shape of the interface towards the metal matrix reveals that this layer must have been in a molten state when formed. According to the chemical analysis given in figure 10.17, the mixed oxide layer consists in average of 15 % CaO, 35 % Al_2O_3 and 50 % SiO_2, and this gives a liquidus temperature of about 1500 °C. It is therefore not unrealistic that a liquid slag has formed at the interface in this case, even with an initial metal temperature of 1450 °C. The direct oxidation to a slag is a highly exothermic reaction, which may lead to an instant increase in the surface temperature. The irregularity of the slag/metal interface and the presence of silicon droplets in the slag phase as seen from figure 10.15 is typical for a situation where reactants, due to chemical reactions between two liquids, are transferred across the interface at high rates. The interfacial tension may then drop to zero, interfacial turbulence and instabilities are created which may lead to spontaneous emulsification (Turkdogan, 1983) as pictured in figure 10.15.

Similar tendencies was also noticed for the Ca-alloyed sample that unintentionally contained 0.06 % Al.

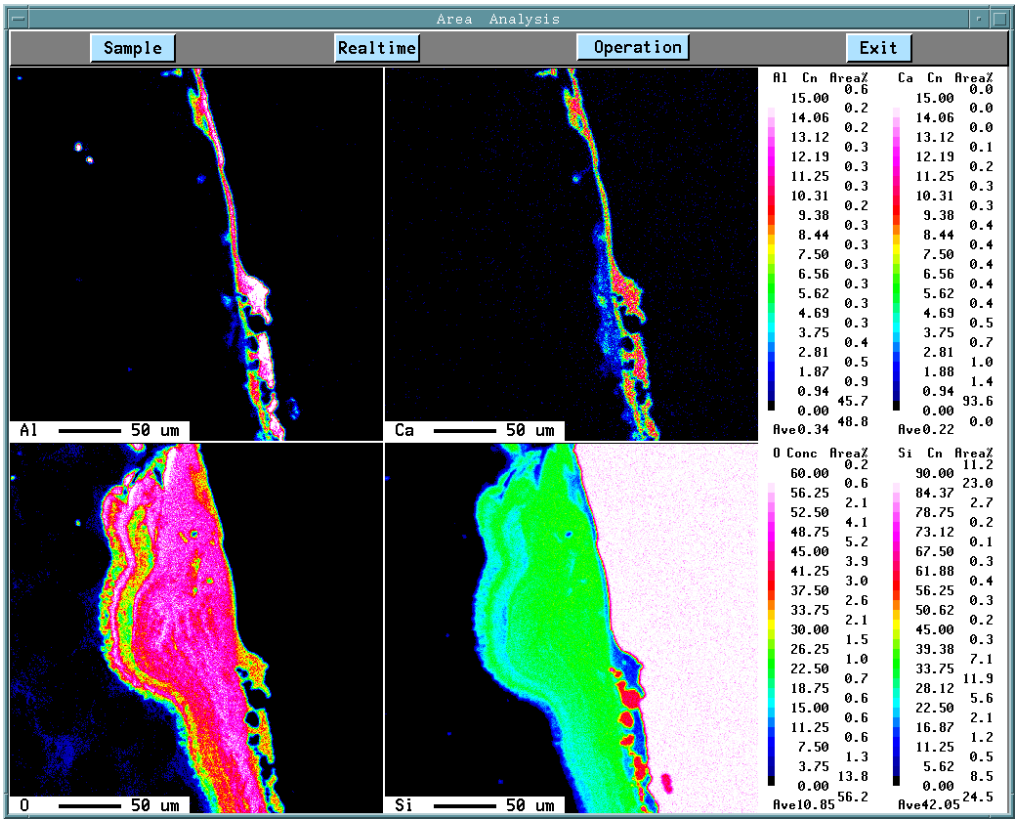

Figure 10.16 – Microprobe element mapping of the surface oxide on silicon (alloy D) oxidized in molten state (1550 °C) with a 0.2-ml water-jet.

From figures 10.17 and 10.18, we clearly see the density-difference of the porous silica layer between samples oxidized at different melt-temperatures. There is no change in the composition of the mixed oxide layer. It appears that the thickness of the mixed oxide layer is larger for the melt oxidized at 1450 °C, however, this merely reflects that the surface oxide is patchy on both melts. Thus, the choice of location for the microprobe analysis will play a role when we compare two arbitrary element mappings. The overall impression based on the microprobe examination is that the mixed oxide did not change noticeable with respect to composition and thickness when the temperature of the melt was raised from 1450 °C to 1550 °C.

URN:NBN:no-2125

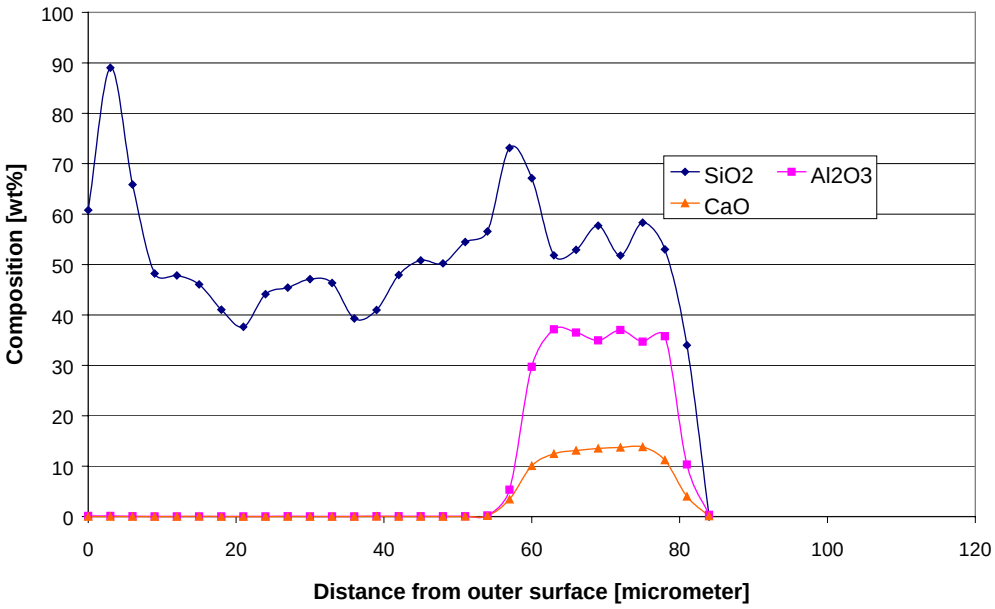

Figure 10.17 – A concentration profile of the surface oxide on silicon (alloy D, 1450 °C) oxidized with a 0.2-ml water jet.

The silica-concentration is about 50% for the melt oxidized at 1450 °C (figure 10.17). There are some fluctuations in the SiO_2-concentration; most of these are related to the porosity of the silica layer. The thickness of the mixed oxide (slag) is about 20 μm, a quite representative value for these specimens.

When the melt temperature was raised to 1550 °C prior to water-injection, the concentration of SiO_2 in the outer, porous layer was found to increase noticeable. Figure 10.18 shows the concentration as we move in from the outer surface. The porosity of the silica is much less, and the silica-concentration is around 80-90 %. The same explanation is given here as for the pure silicon; the elevated temperature accounts for a higher partial pressure of SiO. Thus, upon condensation, the corresponding silica becomes denser than for the lower temperature melt.

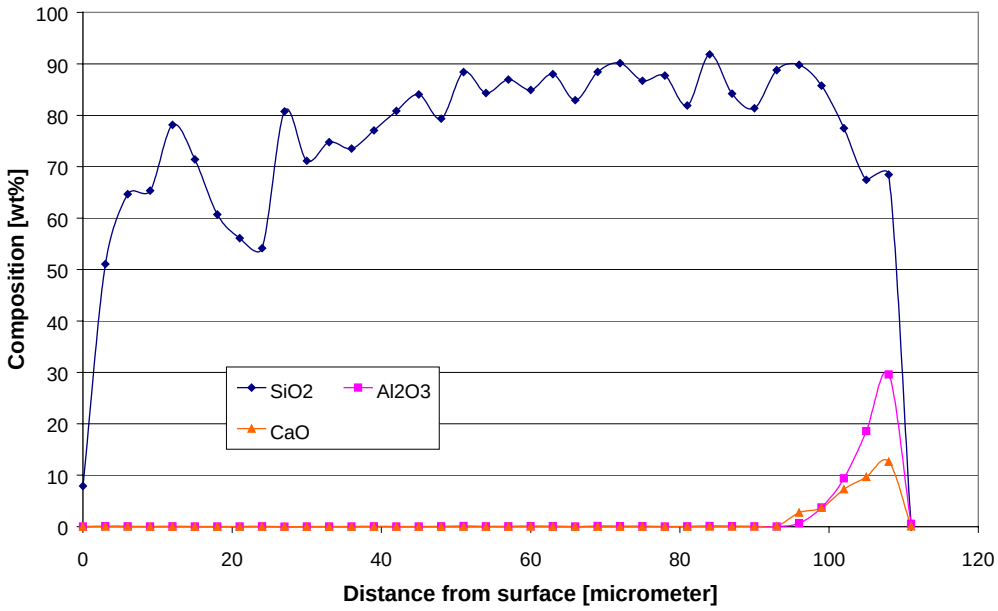

Figure 10.18 – A concentration profile of the surface oxide on silicon (alloy D, 1550 °C) oxidized with a 0.2-ml water jet.

10.5.2 Water-granulated samples

The composition profile of the surface of a granulated drop of alloyed silicon (alloy D) is shown in figure 10.19. Note that the melt was only at liquidus temperature upon water contact. The composition appears to be roughly the same as those of the water-oxidized melts shown previously in figures 10.17-18. The thickness of the slag is about 20 μm, which is roughly the same as observed in figure 10.17. The composition is somewhat different than for the oxidized melts. The microprobe element analysis shows that there is more Al_2O_3 than silica in the slag. Close to the interface, the composition of the slag is found to be approximately 35% SiO_2, 45% Al_2O_3 and 20% CaO, which is very close to the equilibrium composition of a slag being formed on silicon with 0.5% Al and 0.06% Ca at 1550 °C (see figure 3.7). Figure 10.20 shows the elemental mapping of the surface oxide layer on a granulated drop of alloy D. However, there is no porous silica outside this oxide, which by now is conclusively the main difference between the melt oxidized with water and the molten drops quenched in water.

The granulated drop has a rather smooth, well-defined interface. On the other hand, the water-sprayed sample has a non-uniform interface between matrix

and oxide mixture. One explanation for this may be the interfacial turbulence, as described earlier.

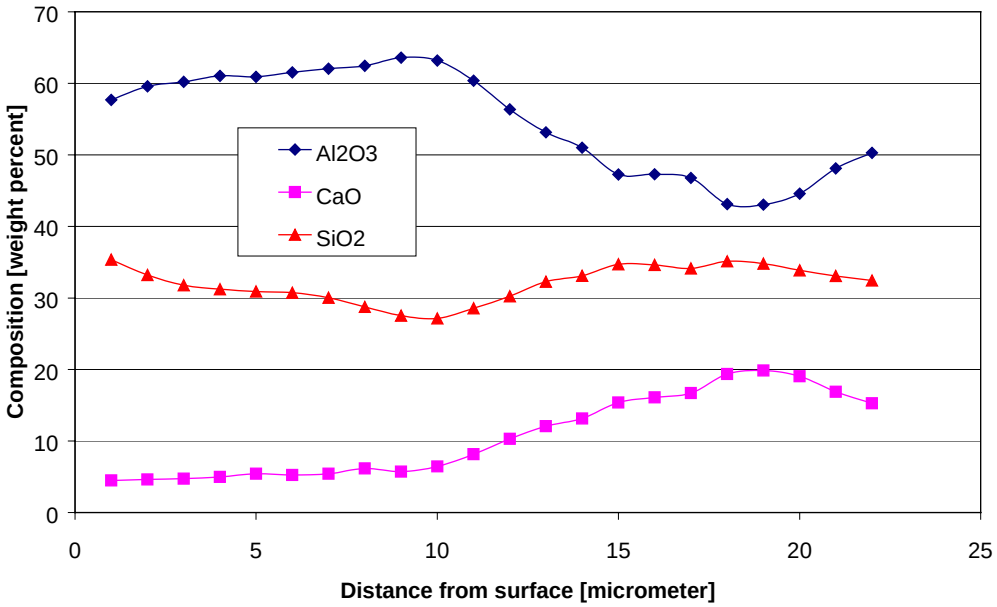

Figure 10.19 – The concentration profile of the surface slagfilm from a water-granulated drop of alloyed Si (alloy D).

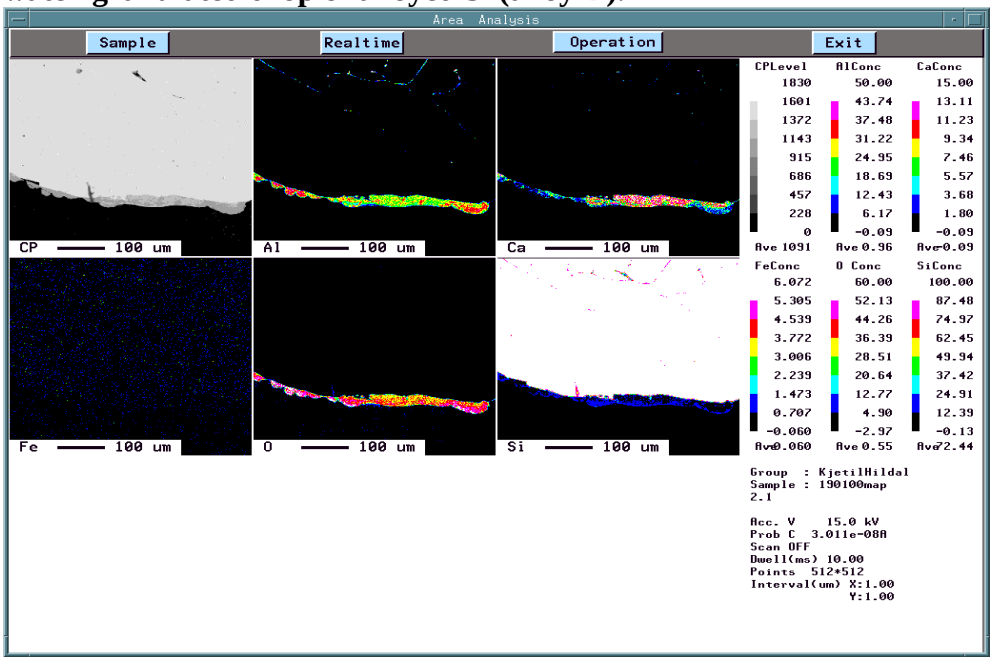

Figure 10.20 – Microprobe element mapping of the surface of a drop of liquid silicon (alloy D, liquidus temperature) quenched in water.

10.6 Microprobe investigations of debris from a steam explosion

The last couple of sections have shown that the mechanism for oxidation of silicon quenching in water is dominated by formation of SiO-gas. With this in mind, we sought to explain the formation of colloidal material, previously discussed in section 9.9 by investigating the debris recovered from the water chamber following various melt-water interactions. The debris was sieved before the microprobe investigation, thus, we were able to see whether any variations concerning oxide formation on different sized particles existed.

10.6.1 Debris from a violent explosion

The debris from experiment D-107-1 (pure silicon, see table 9.2 for an element analysis) was recovered from the tank and sieved. The smallest sized debris (45-104 μm) showed no signs of having originated from a condensation or reaction involving SiO-gas. Hardly any oxygen-containing particles were found in the analysed samples. The particles did not have a regular shape, in fact, they appeared as needles, spheres, or more rectangular geometry. Figure 10.21 shows a typical microprobe scan of such particles (particles in the 45-104 μm range).

The occurrence of elements except Si is neglectable, as evident from figure 10.21. The Si-particles should in theory be all white (corresponding to 100% Si), but this sort of mapping is not all that accurate when it comes to quantifying the element concentrations. According to the operator, the above mapping shows only pure silicon particles, the complete lack of oxygen in these particles is the most important evidence.

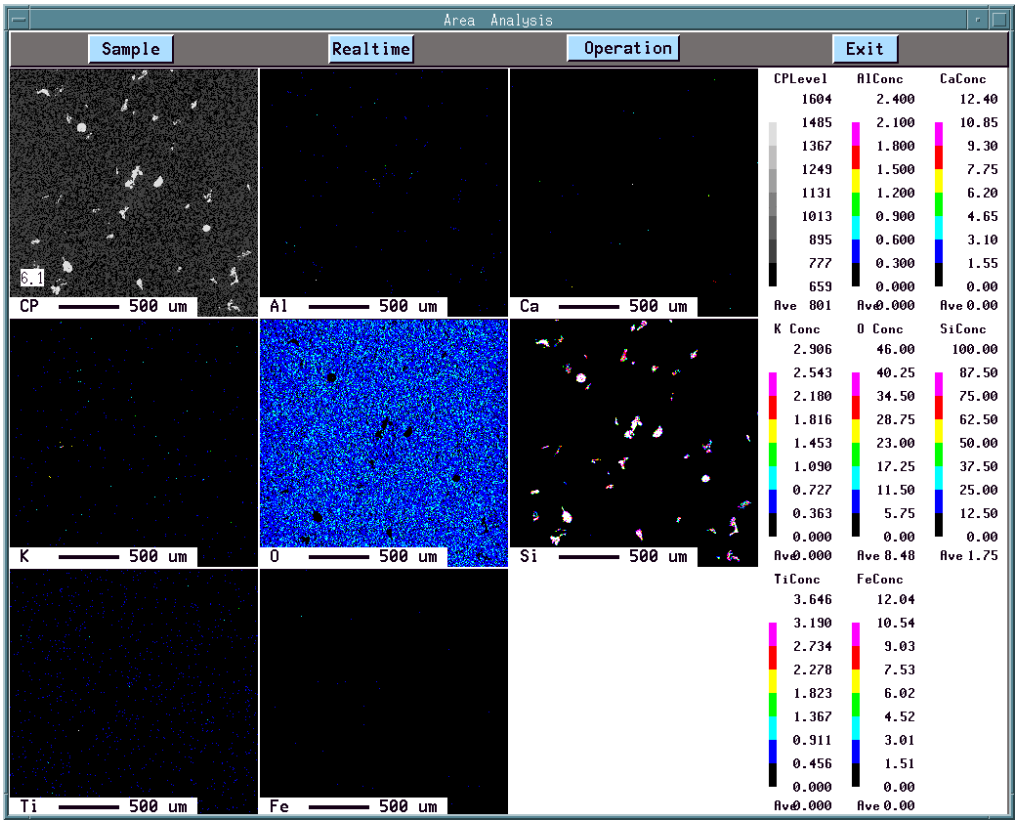

Figure 10.21 – Microprobe mapping of a fraction of the debris (< 104 μm) recovered from the water chamber following a violent steam explosion of a molten drop of pure silicon (alloy A).

A few particles were found that had a composition consistent with SiO_2. However, the general impression is that the large majority of the investigated debris of the smallest size originated from the fragmentation of the melt during the explosion, not as a result of condensation of SiO-gas. The larger debris from this explosion was all silicon-particles, with some occurrences of a very thin (1-3 μm) oxide at the surface. It is fair to say they appeared identical to the drops that only quenched in water (except for the scale factor) discussed in the previous sections. However, as discussed in section 8.9, we did not recover particles less than 50 μm, thus, we are not in a position to conclude about their origin.

A similar analysis was conducted on debris recovered after a coarse fragmentation of pure silicon (experiment D-120-1). The results were in complete accordance with those previously described. The particles had in

general no oxide surface layer, but occasionally a thin deposit of oxygen, about 1-3 μm could be detected.

10.6.2 Debris from a coarse fragmentation – alloyed silicon

The surface of particles originating from a coarse fragmentation of alloy D (Si + 0.4% Al + 0.04% Ca) differed from those of pure silicon. The slag-forming elements Al and Ca ensured that a slag film was visible on particles in all size ranges. One can imagine that if the slag-formation on such fragmented particles is rapid enough, these particles may experience a similar protection as those of the larger drop, i.e. the fragmented drop has a protective slag-film, which may cause larger stability for late pressure transients. However, it is not obvious that such a chemical reaction could compete with the time-scale of the explosion (of the order 20 ms). The slag-formation on the debris may be irrelevant relative to safety issues.

Figure 10.22 and 10.23 shows microprobe element mappings of the debris from the D-139-1 experiment, where a drop of alloy D was triggered and fragmented coarsely. The particles appeared equal independent of the size (the debris was sieved prior to the microprobe analysis). The oxide imaged in figure 10.22 represents the maximum thickness discovered. The oxide shown in figure 10.23 is more representative for the whole population of particles; a thin slag-film covering the surface. Occasionally, the slag-film vanishes completely.

Microprobe analyses of sieved debris were conducted on other alloyed samples as well. Silicon drops alloyed with Al (alloy B) had similar surface characteristics compared to those previously described. The surface oxide was quite thin, 1-5 μm, and usually quite low in Al_2O_3 (below 15%). However, the existence of oxygen on the surface of most particles, regardless of the size, is consistent with the increase of hydrogen in the water, as discussed in section 8.8. Obviously, this relates directly to the larger surface area of the melt after the fragmentation has been initiated. No effort has been made to quantitatively relate the amount of oxide detected on debris to the amount of hydrogen collected by our experimental apparatus, a task that would be very complicated and inaccurate.

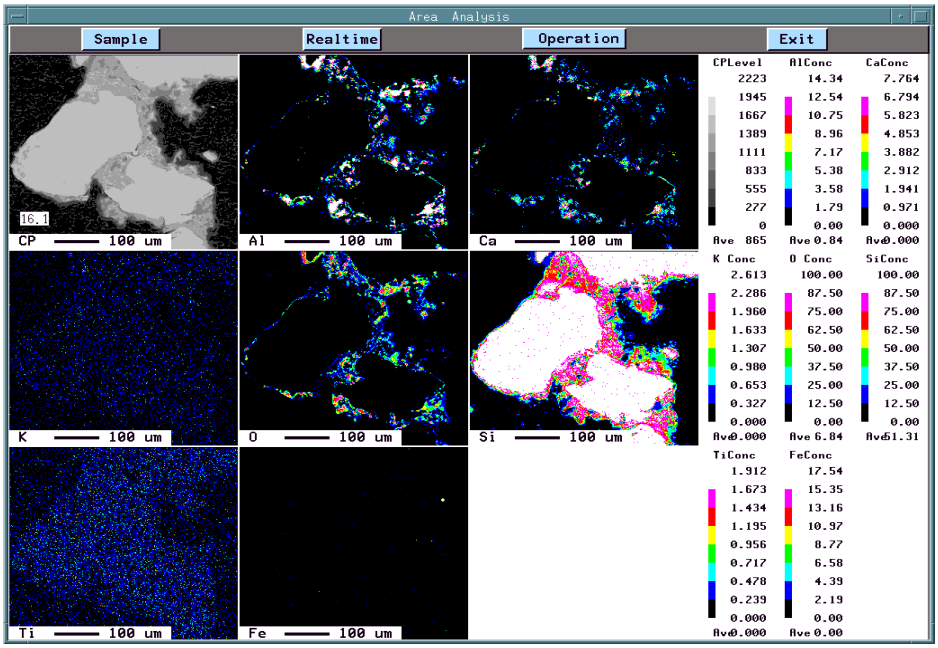

Figure 10.22 – Microprobe element mapping of debris (1.6-3.3 mm) recovered from the water-chamber following a coarse fragmentation of alloy D, experiment D-139-1.

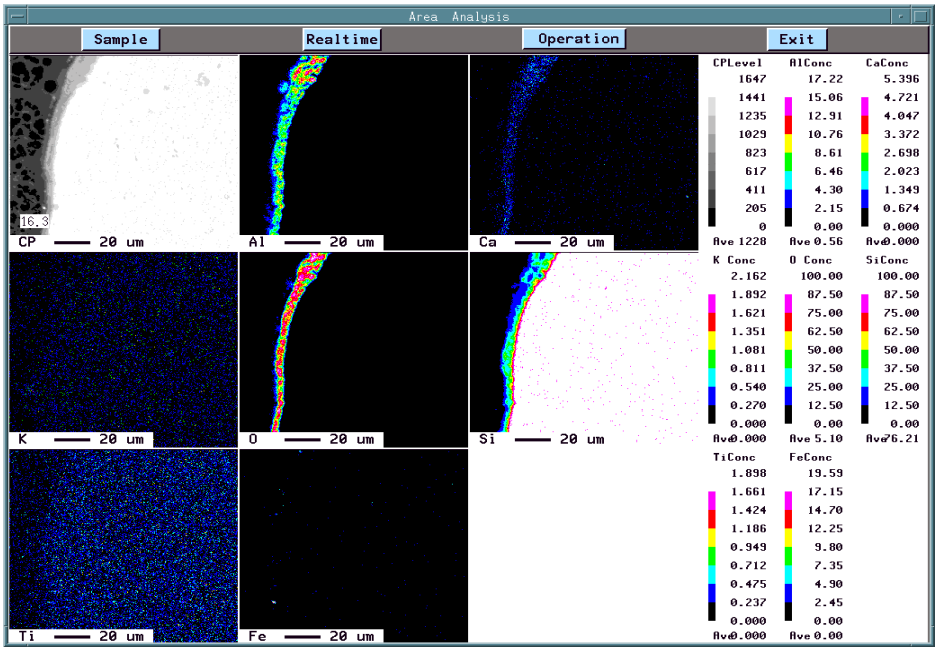

Figure 10.23 – Microprobe element mapping of the surface of the same debris (same size interval) as shown in figure 10.22. A thin slag-film containing the main oxides is covering the silicon matrix.

URN:NBN:no-2125

10.7 Summary

The comparison between silicon-melts exposed to a small water-jet and molten drops of silicon quenched in water has revealed information concerning the course of events during the oxidation process of the molten silicon. The evidence presented in chapter 10 strongly indicates that the first oxidation product to form is SiO-gas, a thermodynamically stable gas in the actual temperature range, which forms by an endothermic reaction with water. The oxidation process will then proceed in two different directions, depending on the available oxygen in the proximity of the gas-metal interface. If there is sufficient oxygen, i.e. as vapor, the SiO-gas may react completely and form SiO_2. This process is more likely to occur at a certain distance away from the interface. On the other hand, if there is not sufficient oxygen nearby, i.e. close to the gas-metal interface, the gas will eventually condense as it cools down, forming solid SiO_2 and silicon, as observed from microprobe investigations of the surface oxide layer on water-oxidized silicon melts. Furthermore, the lack of porous silica on the quenched drops also supports our view that the initial oxidation product is SiO. However, in the case of a descending drop of metal, the flow conditions are apparently of such a nature that SiO-gas is not allowed to react close to the surface and be deposited there. Instead, it is washed away together with vapor and hydrogen. As mentioned in an earlier section, hydrogen bubbles are observed in the water tank as they climb toward the water surface from the falling drop.

The addition of small amounts of Al and Ca to the silicon strongly influences the composition of the surface oxide. When both Al (0.4%) and Ca (0.04%) were added to pure silicon, a slag film forms on the surface of the silicon melt. This slag film may be liquid (depending on the composition) down to temperatures as low as the liquidus temperature of silicon. Also, the surface temperature may rise due to the exothermic heat liberated, thus allowing the slag to be liquid. If a liquid slag forms, the evaporation of SiO will virtually be blocked. Our results show that the slag forms relatively late (compared to the time-scale for generation of SiO-gas), as we would expect since the melt is almost pure silicon. The very existence of a slag film also implies a higher rate of hydrogen generation, which is important for stabilizing the vapor film surrounding the descending metal-drop in water.

The reaction rates are affected by the temperature of the melt upon oxidation. This is demonstrated by the increased density of the silica as the melt temperature is increased from 1450 °C to 1550 °C. Furthermore, the metal-oxide interface appears more irregular for silicon melts oxidized at 1550 °C, especially those high in both Al and Ca. The irregularity of the interface implies that the interfacial turbulence has been high, due to an overall faster

chemical reaction rate. As the reaction rate increases, the mass transfer across the interface also goes up, thus lowering interfacial tension.

11. SUMMARY AND CONCLUSIONS

11.1 Molten drops of pure (Fe)Si released into water – a qualitative description

Based on the experimental evidence presented in the last two chapters, we can now describe in detail the important physical events taking place during the quenching of a drop of molten metal (Si or FeSi75) in water, as well as the steam explosion that may be initiated using an external trigger source.

11.1.1 Entrance in water and onset of film boiling

The molten drop reaches a vertical velocity of about 2.8 m/s, assuming free fall from the furnace 40 cm above the water surface. The drop falls in an inert atmosphere and no chemical reactions take place at the surface, opposite to normal industrial granulation. As the drop breaks the water surface, it will be immersed in a bag of air. Our results show that we were not able to trigger a steam explosion during these early stages of the metal-water contact. The air bag effectively blocks direct liquid-liquid contact, regardless of any pressure waves passing through the system. Eventually the air bag is replaced by a vapor film, apparently when the drop is about 100 mm below the water surface. The heat transfer from the drop is limited to that of film boiling (including radiation) from a molten sphere. Film boiling heat transfer is not rapid enough to generate vapor at such rates that violent fragmentation of the drop occurs.

11.1.2 Quenching of Si in water – generation of SiO

As the drop descends in the water, the molten silicon is continuously oxidized by the vapor film surrounding the drop, and gaseous SiO is formed in a heat-consuming reaction at the vapor-metal interface. This is supported by mostly indirect evidence, such as the presence of hydrogen in the water, the absence of silica on quenched drops and the presence of a porous silica with silicon-inclusions at the surface of melts oxidized with the apparatus described in chapter 5. Our results quite clearly show that the formation of SiO is the dominant oxidation mechanism under the current conditions.

11.1.3 Explosion probability – trigger strength dependence

We found that spontaneous explosions cannot occur for this system of liquids (Si-water or FeSi75-water). But by applying an external pressure source, we

were able to trigger steam explosions for both Si and FeSi75. Acoustic waves in the MPa range were generated in order to collapse the vapor film that prevents direct liquid-liquid contact. As the pressure wave passes through the vapor film the local saturation temperature of the water changes accordingly allowing liquid water to form.

For 9-mm drops of FeSi75, our experiments indicated that the probability for a violent interaction between the melt and the water was 0.1 for a trigger pressure of 0.6 MPa. When the trigger pressure was increased to 1.3 MPa, the probability increased to 0.7, reflecting the stochastic nature of the process. However, it seems fair to say that the trigger threshold must be around 0.5 MPa.

Larger drops (11-mm) of the same alloy have a lower trigger threshold. The experiments showed an explosion probability of 0.5 when the trigger pressure was 0.3 MPa. Thus, the threshold must be less than this value. The fact that larger drops are more easily triggered than smaller drops of the same alloy has been reported earlier (Gunnerson, 1979).

Molten drops of silicon require a much larger trigger pressure in order to collapse the vapor film. We did not record any explosions when the trigger pressure was below 2.0 MPa. With increasing trigger pressure above this value, the probability went up. Our data indicate an 80% probability for a steam explosion if the trigger pressure exceeds 2.0 MPa.

11.1.4 Explosion probability – water depth dependence

Molten drops of FeSi75 could be triggered at any depth down to 785 mm, which is the maximum depth for our experiments. Silicon drops, however, could only be triggered down to water depths of 400 mm. Based on the debris analysis from several explosions obtained at 400 mm, we could establish that the molten drops had started to form a solid shell, which would prevent liquid-liquid contact upon vapor film collapse, a necessary condition for a steam explosion. At deeper water levels, we believe that this shell is thick enough to prevent direct contact between water and melt. Note that if the temperature of the melt is above liquidus temperature, as would be the case in typical granulation processes, the drops would be in a molten state for a longer time (thus deeper water) than these experiments suggest, thus extend the vertical distance that allows triggering of the molten drops.

11.1.5 Steam explosion – fragmentation and generation of pressure waves

The sequence of events that take place after the vapor film has been collapsed is described in detail in section 9.12.2. The fragmentation of the drop causes vapor-bubble growth in a cyclic manner, similar to the results reported by Nelson and Duda (1982) on molten drops of iron-oxide. The collapse of a vapor-bubble causes water to flow inward to fill up the previously steam-occupied space. Upon impact in the center, the local pressure rises and a pressure wave is formed. This pressure transient will then act as a new trigger pulse, and can trigger other drops nearby and fragment the exploding drop further.

The results reported in this work show that for Si and FeSi75, the two first bubble-growths are responsible for most of the fragmentation of the drop. The second bubble is virtually always larger than the first. For “normal” explosions of pure silicon-drops, the first steam bubble has a diameter about 25 mm, while the second bubble normally has a diameter two-three times larger. However, the pressure peaks generated by the bubble-collapses do not reflect the difference in size; they tend to take on values both higher and lower than measured from the first pressure pulse. Without having any experimental evidence, we suspect that hydrogen gas present in the steam/melt mixture prevents (in some cases) a direct impact of water at the center, as explained in section 9.12.2.

The pressure peaks generated by the collapse of the first and second steam bubble are *of the same magnitude or larger than the initial trigger transient.* Thus, an explosion can in theory trigger a neighbor drop if the separation between them is not too large, i.e. ≅ 400 mm or less, depending on the peak pressure of the initial explosion. Indeed, this shows quantitatively that large-scale steam explosions are possible (at least the initial trigger stage) in silicon-rich alloys - water systems, consistent with the qualitative observations during industrial granulation of such alloys.

11.2 The effect of alloying the melt with small amounts of Al/Ca

11.2.1 Fall velocity

The fall velocity is surprisingly found to strongly depend on the content of surface-active elements (Al and Ca), both for molten drops of Si and FeSi75. When a small amount of Al or Ca was added to the otherwise pure silicon, the average fall velocity increased from 0.23 to 0.48 m/s when 0.4% Al or 0.04% Ca or both were added to the otherwise pure silicon. For FeSi75, the average

fall velocity increased from 0.33 to 0.44 m/s when 0.4% Al was added to the alloy. We have not been able to determine why such small additions of other elements can cause a two-fold increase in the fall velocity. The presence of Al and Ca increases the generation of hydrogen gas, which may change the properties of the gas-film surrounding the drop. About twice as much hydrogen is generated for alloyed drops, but it is still hard to see how the properties of the vapor-hydrogen mixture could be affected in a way that doubles the fall velocity. The formation of a thin slag film will indeed change the surface properties of the drop, and it could be that the shape of the drop is slightly altered by the existence of such a slag film.

11.2.2 Increased stability of the vapor film

In terms of granulation safety, the most important effect of Al/Ca-additions is to increase the rate of hydrogen-generation, thus making the gas-film around the molten drop more resistant to collapse upon external pressure transients. The addition of Ca has a larger positive effect on the vapor-film stability than that of Al. We have never been able to register steam explosions when Si has been alloyed with 0.04% Ca, but there has been a couple of explosion-like interactions when the silicon-metal was alloyed with 0.4% Al. Needless to say, when both elements were added, no explosions occurred. The generation of hydrogen is directly linked to enhanced oxidation at the vapor-metal interface in the presence of aluminum and calcium.

Increased stability due to non-condensable gas is reported by several investigators, i.e. Akiyoshi *et.al.* (1990) and Corradini (1981). Thus, our results are consistent with previous investigations.

We have no evidence that there are additional effects on the *explosion-probability* caused by the addition of Al and/or Ca. The existence of a thin slag film at the surface of the molten drop inevitable changes the physical properties of that surface. For instance, the viscosity of typical Al_2O_3-CaO-SiO_2-slags is factor 10000 larger than that of pure liquid silicon. However, the consequences of such a change cannot be established based on the present work. An attractive approach seems to be to model the vapor-metal interface as the vapor is exposed to a pressure transient. If the composition of the slag film is known (or somehow can be estimated from thermodynamic equilibrium considerations), so are its physical properties. Thus, it would be possible to calculate whether the fragmentation of the surface (for example using a Rayleigh-Taylor approach) is altered by the presence of a 5-10 μm liquid slag film.

REFERENCES

Akiyoshi, R., Hishio, S., and Tanasawa, I., *Production of rapidly solidified particles by thermal interaction between molten metal and water*, Heat Transfer Manufacturing and Materials Processing, Am. Soc. Mech. Eng., HTD-V113, 71-76, 1989.

Akiyoshi, R., Hishio, S., and Tanasawa, I., *A study of the effect of non-condensable gas in the vapor film on vapor explosion,* Int. J. Heat Mass Transfer, vol.33, 603-609, 1990.

Anderson, R.P., and Armstrong, D.P., Fuel-Coolant Interactions, ASME HTD, vol.19, 31-40, 1981.

Angelini, S., Takara, E., Yuen, W.W., and Theofanous, T.G., *Multiphase transients in the premixing of steam explosions,* Nuc.Eng.Des., vol.146, 83-95, 1994.

Angelini, S., Theofanous, T.G., Yuen, and W.W., *The mixing of particle clouds plunging into water,* Nuc. Eng. Des., vol.177, 285-301, 1997.

Arakeri, V.H., Catton, I., and Kastenberg, W.E., *An experimental study of the molten glass/water thermal interaction under free and forced convection,* Nucl. Sci. Eng., vol.66, 153-166, 1978.

Baines, M., Board, S.J., Buttery, N.E., and Hall, R.W., *The hydrodynamics of large-scale fuel-coolant interactions,* Nucl. Tech., vol.49, 27-39, 1980.

Becker, K.M., and Lindland, K.P., *The effect of surfactants on hydrodynamic fragmentation and steam explosions,* Dep. Nuc. Eng., RIT, Stockholm, Sweden, Report KTH-NEL-50, 1991.

Berenson, P.J., *Film boiling heat transfer from a horizontal surface,* J. Heat Transfer, Trans. ASME, vol.83, 351-358, 1961.

Bergstrøm, T., *A review of molten metal-water interactions,* Proc. 52nd El. Furnace Conf., Nashville, 303-308, 1994.

Berthoud, G., *Vapor explosions,* Ann. Rev. Fluid. Mech., vol.32, 573-611, 2000.

URN:NBN:no-2125

Bjerknes, T.M., *Oksidasjon av silisium* (*Oxidation of silicon*), Project work (in Norwegian), NTNU, Trondheim,1997.

Board, S.J., and Hall, R.W., *Propagation of Thermal Explosions, Part 1: Tin-Water Experiments,* Central Electricity Generation Board Report RD/B/N2850, 1974b.

Board, S.J., and Hall, R.W., *Propagation of Thermal Explosions, Part 2: Theoretical Model,* Central Electricity Generation Board Report RD/B/N3249, 1974a.

Board, S.J., and Hall, R.W., *Recent advances in understanding large-scale vapor explosions,* Proc. Comm. Saf. Nuc. Install. Meet. Sodium-Fuel Interact., Fast Reactor, Tokyo, 249-293, 1976.

Board, S.J., Hall, R.W., and Hall, R.S., *Detonation of fuel coolant explosions,* Nature, vol.254, 319-321, 1975.

Brandes, E., *Smithells metals reference book,* 1983.

Breen, B.P. and Westwater, J.W., *Effect of diameter of horizontal tubes on film boiling heat transfer,* Chem. Eng. Prog., vol.58 (7), July, 1962.

Bromley, L.A., *Heat transfer in stable film boiling,* Chem.Eng.Prog., vol.46 (5), 221-227, 1950.

Bromley, L.A., LeRoy, N.R. and Rollers, J.A., *Heat transfer in forced convection film boiling,* Ind.Eng.Chem., vol.45, 2639-2646, 1953.

Carslaw, H.S., and Jaeger, J.C., *Conduction of heat in solids,* Clarendon Press, Oxford, 1959.

Cess, R.D. and Sparrow, E.M., *Subcooled forced-convection film boiling on a flat plate,* J. of heat transfer, Transactions of the ASME, 377-379, 1961.

Cho, D.H., Fauske, H.K., and Grolmes, M., *Some aspects of mixing in large-mass, energetic fuel-coolant interactions,* Proc. Int. Meeting on Fast Reactor Safety and Related Physics, 5-8 October, Chicago, 4, 1852-1861, 1976.

Ciccarelli, G., and Frost, D.L., Nucl. Eng. Des., vol.146, 109-132, 1994.

Colgate, S.A., and Sigurgeirsson, T., *Dynamic mixing of water and lava,*

Nature, vol.244, 552-555, 1973.

Corradini, M.L., *Phenomenological modeling of the triggering phase of small-scale steam explosion experiments,* Nucl. Sci. Eng., vol.78, 154-170, 1981.

Corradini, M.L., *Modeling film boiling destabilization due to a pressure shock arrival,* Nuc.Sci.Eng., vol.78, 154-170, 1983.

Corradini, M.L., Kim, B.J.,Oh, M.D., *Vapor explosions in light water reactors: A review of theory and modeling,* Prog.Nuc.Eng., vol.22 (1), 1-117, 1988.

Corradini, M.L., *Multiphase flow: Gas/Liquid,* In The Handbook of Fluid Dynamics, Chapter 17, CRC Press, 1998.

Coughlin, J.P., Bulletin of the Bureau of Mines, U.S. Government Printing Office, Washington, 1954.

Dhir, V.K. and Purohit, G.P., *Subcooled film boiling heat transfer from spheres,* Nuc.Eng.Des., vol.47, 49-66, 1978.

Dowling, M.F., Ip, B.M., and Abdel-Khalik, S.I., *Suppression of vapor explosions by dilute aqueous polymer solutions,* Nucl. Sci. Eng., vol.113, 300-313, 1993.

Drumheller, D.S., *The initiation of melt fragmentation in fuel-coolant interactions,* Nucl.Sci.Eng., vol.72, 347-356, 1979.

Dufresne, J., *Presentation of the ESCADRE system together with a practical application,* Int. Sympos. Severe accidents in nuclear power plants, Sorrento, Italy, March 1988.

Epstein, M. and Hauser, G.M., *Subcooled forced-convection film boiling in the forward stagnation region of a sphere or a cylinder,* Int. J. of heat and mass transfer, vol.23, 177-189, 1980.

Epstein, S.G., *Molten aluminum-water explosions: An update,* Light Metals 1993, 845-853, Metallurgical Society of AIME, 1992.

Epstein, S.G., and Miller, R.E., Light Metals 1987, TMS-AIME, Warrendale, PA, USA, 693-698, 1987.

Farber, F.A. and Scorah, R.L, *Heat transfer to water boiling under pressure,* Trans. ASME J. Heat Transfer, vol.84, 1955.

Fauske, H.K., *Some aspects of liquid-liquid heat transfer and explosive boiling,* Proc.First Conf. on Fast Reactor Safety, 2-4 April, Beverly Hills, CA, 992-1005, ANS, 1974.

Fletcher, D.F., *A review of the available information on the triggering stage of a steam explosion,* Nuc.Saf., vol.35 (1), 1994.

Fletcher, D.F. and Theofanous, T.G., *Explosive melt-water interactions,* Adv. Heat Transfer, vol.29, 129-212, 1997.

Fletcher, D.F., and Thyagaraja, A., *The CHYMES coarse mixing model,* Prog. Nuc. Energy, vol.26, 31-61, 1991.

Flory, K., Paoli, R., and Mesler, R., *Molten metal-water explosions,* Chem. Engr. Prog., vol.65, 50-54, 1969.

Fodemski, T.R. and Hall, W.B., *Forced convection film boiling on a sphere immersed in (a) sub-cooled or (b) superheated liquid,* Proc. 7th Int. Heat Transfer Conf., München, vol.4, 375-439, 1982.

Francis, P., and Self, S., *The eruption of Krakatau,* Sci. Am., vol.249, 146-159, 1983.

Frederking, T.H.K. and Clark, J.A., *Natural convection film boiling on a sphere,* Adv. Cryog. Eng., vol.8, 501-506, 1963.

Gunnerson, F.S., *Film boiling destabilization from hydrodynamic and thermodynamic considerations with application to the understanding of vapor explosion phenomena,* Technical report no. NE-66 (79) NRC-318-1, U.S. Nuclear Regulatory Commission, Washington DC, April 1979.

Henricks, R.C. and Baumeister, K.J., NASA Technical Note TND-5124, June, 1969.

Henry, R.E., and Fauske, H.K., *Nucleation processes in large scale vapor explosions,* ASME J. Heat Transfer, vol.101, 280-287, 1979.

Henry, R.E., and Fauske, H.K., *Required initial conditions for energetic steam explosions,* ASME.HTD.V19, Am.Soc.Mech.Eng., Nov.15-20, 99-108, 1981.

Henry, R.E., Hohmann, H., and Kottowski, H., *The effect of pressure on NaCl-H_2O explosions,* Proc. of the 4th CSNI Spec. Meet. On FCI in Nuc. Reac. Saf., CSNI Report no. 37, vol.1, 308-323, Bournemouth, UK, 1979.

Henry, R.E., and Miyazaki, K., *Effects of system pressure on the bubble growth from highly superheated water,* Topics in Two-Phase Heat Transfer and Flow, ed. S.G. Bankoff, 1-10, ASME, New York, 1978.

Hinze, J.W., and Graham, H.C., *The active oxidation of Si and SiC in the viscous gas-flow regime,* J. Electrochemical Soc., vol.123, no.7, 1066-1073, July 1976.

Hohmann, H., *Experimental investigations of spontaneous and triggered vapor explosions in the molten salt/water system,* Proc. Int. Meet. Therm. Nuc. Reac. Saf., Chicago, 1982.

Inoue, A., and Bankoff, S.G., *Destabilization of film boiling due to arrival of a pressure shock: Part I Experimental,* J. Heat Transfer, vol.103, 459-464, 1981.

Inoue, A., Ganguli, A., and Bankoff, S.G., *Destabilization of film boiling due to arrival of a pressure shock: Part II analytical,* J. Heat Transfer, vol.103, 465-471, 1981b.

Inoue, A., *Study on transient heat transfer of film boiling due to arrival of pressure shock,* Paper FB39, Proc. 4th Int. Heat Transfer Conf., Munich, Germany, 1982.

Ito, T., Nishikawa, K. and Shigechi, T., *Forced convection film boiling heat transfer from a horizontal cylinder to liquid cross-flow upward (1st report, Saturated liquid),* Bulletin of the JSME, vol.24 (198), 2107-2114, 1981.

Ivey, H.J. and Morris, D.J., *On the relevance of the vapor liquid exchange mechanism for subcooled boiling heat transfer at high pressure,* AEEW-R Report 137, 1962.

Kalinin, E.K., Berlin, I.I. and Kostyuk, V.V., *Film boiling heat transfer,* Adv. Heat Transfer, vol.11, 51-198, 1975.

Katz, D.L., and Sliepcevich, C.M., *Liquefied natural gas/water explosions; Cause and effect,* Hydrocarbon Process, 50, 240-244, 1971.

URN:NBN:no-2125

Kim, B., and Corradini, M.L., Proc. 5th Int. Meeting Therm. Nucl. Reac. Saf., vol.2, 1098-1107, 1984.

Kim, H., Krueger, J., and Corradini, M.L., *Single droplet vapor explosions: Effect of coolant viscosity,* Proc. 4th Int. Meet. On Nuc. Reac. Therm.-Hydr., 10-13 October, Karlsruhe, Germany, vol.1, 261-267, 1989.

Knowles, J.B., *A mathematical model of vapor film destabilization,* Report AEEW-R-1933, 1985.

Kobayasi, K., *Counter-comment to Hesson & Witte's comment on "Film boiling heat transfer around a sphere in forced convection",* J. of Nuclear Science and Technology, vol.3, (10), 449-450, 1966.

Kondo, S., Togo, Y., and Iwamura, T., PNC, vol.251, 76-112 and 285-305, 1976.

Kowal, M.G., Dowling, M.F., and Abdel-Khalik, S.I., *An experimental investigation of the effects of surfactants on the severity of vapor explosions,* Nucl. Sci. Engr., vol.115, 185-192, 1993.

Kutateladze, S.S., *A hydrodynamic theory of changes in the boiling process under free convection,* Akod. Nauk SSSR Tech Nauk, vol.4, 1951.

Kutateladze, S.S., *Heat transfer in condesation and boiling,* AEC-tr.3770, 1959.

Liu, C. and Theofanous, T.G., *Film boiling on spheres in single- and twophase flows, Part 1: Experimental studies; Part 2: A theoretical study,* Nat. Heat Transfer Conf., Portland, USA, August 1995.

Long, G., *Explosions of molten metal in water - causes and prevention,* Met. Prog., vol.71, 107-112, 1957.

Lundstrøm, P.Å., and West, Å., *Granulation of ferroalloys and Si-metal,* Electric Furnace Conf. Proc., 309-315, 1994.

Michiyoshi, I., Takahashi, O. and Kikuchi, Y., *Heat transfer and the low limit of film boiling,* Proc. of the 1st world conference on experimental heat transfer, fluid mechanics and thermodynamics, Dubrovnik, Yugoslavia, 1404-1415, 1988.

Morsund, S., *Oksidasjon av flytende Si-metall (Oxidation of liquid silicon),* Project work (in Norwegian), NTNU, Trondheim, 1998.

Naylor, P., *Film boiling destabilization,* Ph.D. Thesis, University of Exeter, 1985.

Nelson, L.S., *Steam explosions of single drops of pure and alloyed molten aluminum,* Nuc.Eng.Des., vol.155, 413-425, 1995.

Nelson, L.S., Bonazza, R., Brooks, P.W., and Corradini, M., *Triggering Steam Explosions of Single Drops of a Molten Ferrosilicon Alloy with a Simple Encapsulated Mechanical Impactor,* Metallurgical and Materials Transactions B, vol.30B, 1083-1088, December 1999b.

Nelson, L.S., Bonazza, R., Brooks, P.W., and Corradini, M.L, *Quenching 10-20 mm-Diameter Drops of Molten Ferrosilicon in Water and on Solids,* Draft report, Department of engineering and engineering physics, University of Wisconsin-Madison, March 1997.

Nelson, L.S., Bonazza, R., Brooks, P.W., and Corradini, M.L, *Steam Explosions of Molten Ferrosilicon Drops Released into Water: Effects of Triggering, Alloying and Water Temperature,* Final Report, Department of engineering physics, University of Wisconsin-Madison, March 1998.

Nelson, L.S., Bonazza, R., Brooks, P.W., Corradini, M.L., and Hildal, K., *Triggered Steam Explosions of Molten Ferrosilicon Drops: Behavior of Solenoid-Driven and Pneumatic Impactors; Ability to Trigger the Explosions at Various Water Depths; Energetics of the Explosions; Fall Histories; Colloidal Material Deposited During the Explosions,* Final Report, Department of engineering physics, University of Wisconsin-Madison, March 1999a.

Nelson, L.S., Brooks, P.W., Bonazza, R., Corradini, M.L., and Hildal, K., *The quenching and steam explosions of drops of molten silicon released into water,* Final report, Department of Engineering Physics, University of Wisconsin-Madison, March 2000.

Nelson, L.S. and Duda, P.M., Report No. NUREG/CR-2295, SAND81-1346, Sandia National Lab., Albuquerque, New Mexico, USA, September 1981.

Nelson, L.S. and Duda, P.M., *Steam explosions with single drops of iron oxide melted with a CO2 - laser,* High Temperatures-High Pressures, vol.14, 259-281, 1982.

URN:NBN:no-2125

Nelson, L.S. and Duda, P.M., Report No. NUREG/CP0027, U.S. Nuclear Regulatory Commision, Washington D.C., vol.2, 981-986, 1983.

Nelson, L.S., Duda, P.M., Report No. NUREG/CR-2718, SAND82-1105, Sandia National Lab., Albuquerque, New Mexico, April 1985.

Nelson, L.S., Eatough, M.J., and Guay, K.P., *Initiation of explosive molten aluminum-water interactions at wet or underwater surfaces,* ANS Proc. Nat. Heat Transfer Conf., 24-27 July, Houston, US, vol.3, 219-227, 1988.

Nelson, L.S., and Guay, K.P., *Suppression of steam explosions in tin and Fe-Al_2O_3 melts by increasing the viscosity of the coolant,* High Temp.-High Press., vol.18, 107-111, 1986.

Nelson, L.S., Hogeland, S.R., and Roth, T.C., Report No. SAND99-0976, Sandia National Lab., Albuqerque, New Mexico, July 1999.

Nishikawa, K. and Ito, T., *Two-phase boundary layer treatment of free convection film boiling,* Int.J. Heat Mass Transfer, vol.9, 103-115, 1966.

Nishikawa, K., Ito, T. and Matsumoto, K., *Investigation of variable thermophysical property problem concerning pool film boiling from vertical plate with prescribed uniform temperature,* Int.J. Heat Mass Transfer, vol.19, 1173-1182, 1976.

Nukiyama, S., *The maximum and minimum values of the heat Q transmitted from metal to boiling under atmospheric pressure,* Int. J. Heat Mass Transfer, vol. 9, 1934.

Nusselt, W.Z., Z.Ver. deut. Ing., vol.60, 541-569, 1916.

Nygaard, L., Brekken, H., Lie, H.U., Magnussen, Th.E., and Sveine, A., *Water granulation of ferrosilicon and silicon metal,* Proc. Infacon 7, eds. Tuset, Tveit and Page, Trondheim, Norway, June 1995.

Pachaly, B., *Process development in the MCS-production: For example water granulated silicon,* Proc. Silicon for the chemical industry, Loen, Norway, June 8-10, 1994.

Page, F.M., Chamberlain, A.T., and Grimes, R., *The safety of molten aluminium-lithium alloys in the presence of coolants,* J. de. Phys. Colloq. C3, vol.48, 63-73, 1987.

Peppler, W., and Till, W., Proc. Int. Conf. Sci. Technol. Fast Reactor Safety, vol.2, 497-502, 1986.

Ranz, W., and Marshall, W., Chem. Engr. Prog., vol. 48, 141, 1952.

Ratto, M., Ricci, E., and Costa, P., *Oxidation of metals with highly reactive vapors: Extension of Wagner theory,* Met. Mat. Trans. B, vol.32B, 903-911, October 2001.

Reid, R.C., *Rapid phase transitions from liquid to vapor,* Adv. Chem. Engr., vol.12, 105-208, 1983.

Rhim, W-K., and Ohsaka, K., *Thermophysical properties measurement of molten silicon by high-temperature electrostatic levitator: density, volume expansion, specific heat capacity, emissivity, surface tension and viscosity,* J. Crystal Growth, vol.208, 313-321, January, 2000.

Rosenqvist, T., *Thermodynamical data for metallurgists,* Tapir Forlag, Trondheim, Norway, 1983.

Sakurai, A., *Film boiling heat transfer,* Proc. of 9th Int. Heat Transfer Conf., Jerusalem, Israel, vol.1, 157-187, 1990a.

Sakurai, A., Shiotsu, M. and Hata, K., *A general correlation for pool film boiling heat transfer from a horizontal cylinder to subcooled liquid: Part 2 - Experimental data for various liquids and its correlation,* J. of heat transfer, Transactions of the ASME, vol.112, 554-561, May, 1990b.

Sallach, R.A., Elrick, R.M., Douglas, S.C., and Oullette, A.L., *Reactions between some cesium-iodine compounds and the reactor materials 304 Stainless steel, Inconel 600 and silver, Volume I. Cesium hydroxide reactions,* Report NUREG/CR-2921 (SAND 83-0395), US Nuclear Regulatory Comission, June, 1984.

Schei, A., Tuset, J.Kr., and Tveit, H., *Production of high silicon alloys,* Tapir Forlag, Trondheim, Norway, 1998.

Schigechi, T., Ito, T. and Nishikawa, K., *Forced convection film boiling heat transfer from a horizontal cylinder to liquid cross-flow upward (2nd report, Subcooled liquid),* Bulletin of the JSME, vol.26 (214), 554-561, April, 1983.

Schins, H., Nuc. Eng. Des., vol.94, 983-998, 1986.

URN:NBN:no-2125

Serway, R.A., *Physics for scientists and engineers with modern physics,* 3rd ed., International edition, Saunders College Publishing, 1992.

Sharon, A., and Bankoff, S.G., PCH, PhysicoChem. Hydrodyn., vol.2, 177-202, 1981.

Shioutsi, M., Hata, K. and Sakurai, A., *Heterogeneous spontaneous nucleation temperature on solid surface in liquid nitrogen,* Proc. of Cryogenic Eng. Conf., Los Angeles, FF-18, 1989.

Skelton, W.T.W., Kowal, M.G., and Abdel-Khalik, S.I., *Effect of borid acid on the severity of vapor explosions in pure water and surfactant solutions,* Nucl. Eng. Des., vol.155, 359-368, 1995.

Sparrow, E.M., *The effect of radiation on film boiling heat transfer,* Int.J. Heat Mass Transfer, vol.7, 229-238, 1964.

Theofanous, T.G., *The study of steam explosions in nuclear systems,* Nucl. Eng. Des., vol.155, 1-26, 1995.

Theofanous, T.G., Yuen, W.W., and Angelini, S., *Premixing of steam explosions: PM-ALPHA verification studies,* DOE/ID-10504, June, 1998.

Turkdogan, E.T., Grieveson, P. and Darken, L.S., *Enhancement of diffusion-limited rates of vaporization of metals,* J. Phys. Chem., vol. 67, 1647-1654, August 1963.

Wagner, C., *Passivity during the oxidation of silicon at elevated temperatures,* J. App. Phys., vol. 29 (9), 1295-1297, 1958.

Yao, Shi-Chune and Henry, R.E., *An investigation of the minimum film boiling temperature on horizontal surfaces,* J. Heat Transfer, Trans. ASME, vol.100, 260-267, 1978.

Yaws, C.L., Ky-Yen, L., Hopper, J.R., Fang, C.S. and Hansen, K.C., *Semiconductor silicon: Physical and thermodynamic properties,* Solid State Technology, 87-92, January, 1981.

Yuen, W.W., and Theofanous, T.G., *On the existence of multiphase thermal detonations,* Int.J.Mul.Flow, vol.25, 1505-1519, 1999.

Zuber, N., *Hydrodynamic aspects of boiling heat transfer,* AEC Report AECU 4439, 1959.

NOMENCLATURE

C_{pl}, C_{pv}, C_{pw}	=	Specific heats of cooling liquid, vapor and heater material, respectively
D, d	=	Diameter of sphere, [m]
D'	=	Non-dimensional cylinder diameter, $(g(\rho_l-\rho_v)/\sigma)^{1/2}$
Fr	=	Froude number, U^2/gD
G	=	Gravitational acceleration, [m/s^2]
H	=	Heat transfer coefficient, q/T, [W/m^2°K]
h_{fg}	=	Latent heat of vaporization, [J/kg]
K	=	Thermal conductivity, [W/m^2°K]
Nu	=	Nusselt number, hD/k_v
Pr	=	Prandtl number, $C_p\mu/k$
q	=	Heat flux, [W/m^2]
R	=	Radius of sphere, [m]
Re	=	Liquid flow Reynolds number, $UD\rho_l/\mu_l$
Sc	=	Liquid subcooling parameter, $C_{pl}T_{sub}/h_{fg}$
Sh	=	Vapor superheat parameter, $C_{pv}T_w/h_{fg}$
T	=	Temperature, [°K]
T_H	=	Spontaneous nucleation temperature, [°K]
T_{min}	=	Minimum film boiling temperature, [°K]
T_{sat}	=	Saturation temperature of the liquid, [°K]
T_w	=	Sphere surface temperature, [°K]
T_∞	=	Liquid pool or free stream temperature, [°K]
U	=	Free stream velocity, [m/s]
u	=	Velocity in the tangential direction (x-component), [m/s]
v	=	Velocity in the normal direction (y-component), [m/s]
w	=	Mass flux density, [kg/m^{2}s]

Greek

α	=	Thermal diffusivity, $k/\rho C_p$; or void fraction
β	=	Coefficient of thermal expansion of the liquid
ΔT_{min}	=	Minimum difference between surface temperature and the saturation temperature of the liquid to sustain film boiling
ΔT_{sub}	=	Difference between the saturation temperature of the liquid and the pool or free stream temperature, T_{sat}-T_∞

ΔT_w	=	Difference between the surface temperature and the saturation temperature of the liquid, T_w-T_{sat}
δ	=	Boundary layer thickness [m]; or ratio of vapor and liquid boundary layers
μ	=	Dynamic viscosity, [kg/msec]; or viscosity ratio μ_v/μ_l
ν	=	Kinematic viscosity, [m^2sec]
ρ	=	Density [kg/m^3]; or density ratio ρ_v/ρ_l
σ	=	Surface tension, [N/m]

APPENDIX A – Preparation of test rods

The test rods that are used to make drops of molten ferroalloys are made at locations of NTNU, Trondheim, Norway. The procedure on how these drops are made is given here as an appendix.

The starting material is silicon of high purity obtained from Scanwafer, Glomfjord, Norway. This material comes in bulk-size and has to be crushed to smaller pieces. Alloying element such as iron and aluminum are cut from scrap material. Calcium is added as $CaSi_2$-powder, with a composition given in table A1.

Table A1. Nominal composition of the $CaSi_2$-powder used for the addition of Ca to the Si-alloys used for single-drop release experiments.

Element	Composition [wt%]
Ca	30-33
Si	60-62
Fe	4-6

We want to minimize the use of powder, to reduce the risk of loss to the surroundings during preparation. However, we have accounted for a loss of 25 % of the fine powder, thus adding more initially than the final composition would suggest. SINTEF found during the beginning of this program that the final levels of Ca in the Si-alloys did not correspond to the theoretical levels, and this was attributed to the loss of powder during preparation, thus, some additional powder had to be used to achieve the desired compositions. The loss of 25 % is a “guesstimate”.

The amount of each element is weighed on a digital weight, with an accuracy of 10^{-5} grams. The total amount of material to be melted is typically 430 gram when making 10-mm diameter rods, and 500 grams when making 15-mm diameter rods. The solid material is placed in a graphite crucible (ID 8 cm, OD 10 cm, height 25 cm). The crucible is put in a Balzer induction-heated closed furnace (model VSG 10, nr. 336), which is evacuated prior to the heating and filled with argon-gas. The melting is then carried out at an argon pressure of 0.7 bars. The current through the coil is gradually increased to avoid thermal stresses in the crucible. Initially, the current is around 40 A (500 V), and as the crucible is getting red, the current through the coil is increased to about 53 A (720 V). This procedure was established due to the detection of cracks in the crucible, and certain times complete failure and a loss of melt into the furnace. This largely depended on the quality of the crucibles. We found that cheaper,

more porous crucibles were in fact less likely to break than denser, more expensive crucibles. An explanation for this could be that as silicon penetrates the crucible and solidifies, more pores are favorable to avoid stresses in the crucible due to the expansion of silicon as it solidifies. In the case of less pores, the solidifying silicon has no way to go, and may cause cracks and breakage of the crucible.

The temperature of the melt is measured with a pyrometer, and we can also observe the melt directly through a glass-covered opening on top of the furnace. When the silicon melt has reached 1500 °C, the power is switched off, and then the melt is poured into a casting form when crystals are beginning to grow from the crucible walls. The casting form is also located inside the furnace. After the pouring, the furnace is opened, the casting form removed and water chilled. Finally, the silicon alloy is removed from the form as 10 or 15-mm diameter rods. Samples of the broken rods are usually used for chemical analysis of the batch.

APPENDIX B – Time-pressure traces for steam explosions of molten Si or FeSi75

During the year of 2000, we improved our analyzing techniques for the granulation experiments to include a pressure transducer submerged in the water chamber. The transducer was connected to an oscilloscope for an online-reading of the pressure. The oscilloscope was programmed to start recording the time-pressure coordinates when a sudden increase in pressure was detected. After some trial and error in the beginning, we eventually settled for a sampling rate of 10^6 samples/second, with a memory of 32 K. That gave us a total sampling time of 32 ms, which was sufficient to record all pressure activity.

The time-pressure traces reproduced here are in general using the same scales to simplify comparison between the individual traces. A few exceptions will occur due to extreme pressure values. Note that the first strong peak in each figure is the trigger pulse from the impactor. Drops are triggered at a certain distance from the water surface, given in the figure text.

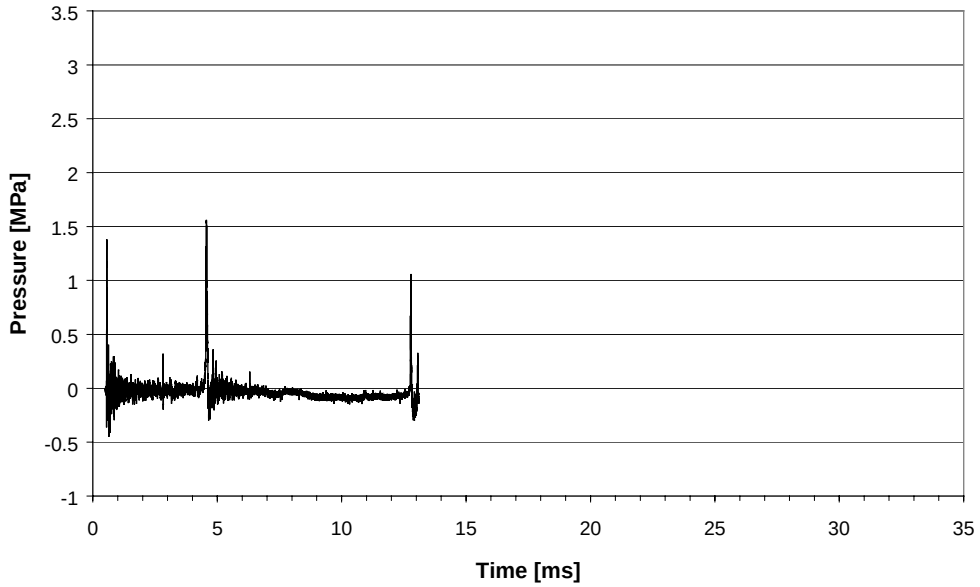

Figure A.1 – Time-pressure trace (D-168-1-5) for an exploding drop of FeSi75, triggered at 340 mm.

URN:NBN:no-2125

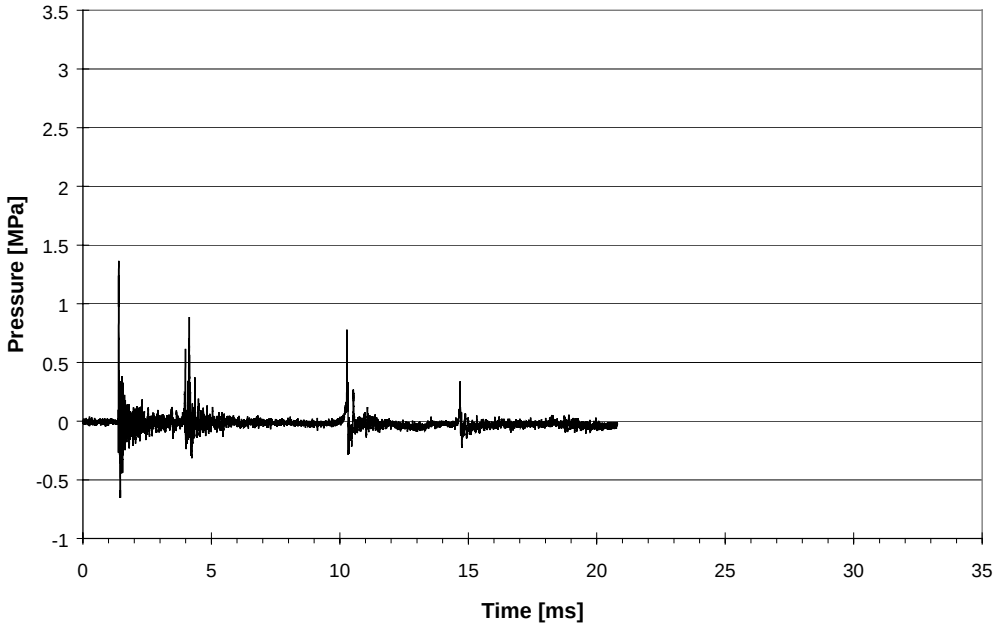

Figure A.2 – Time-pressure trace (D-170-1-4) for an exploding drop of molten FeSi75, triggered at 530 mm.

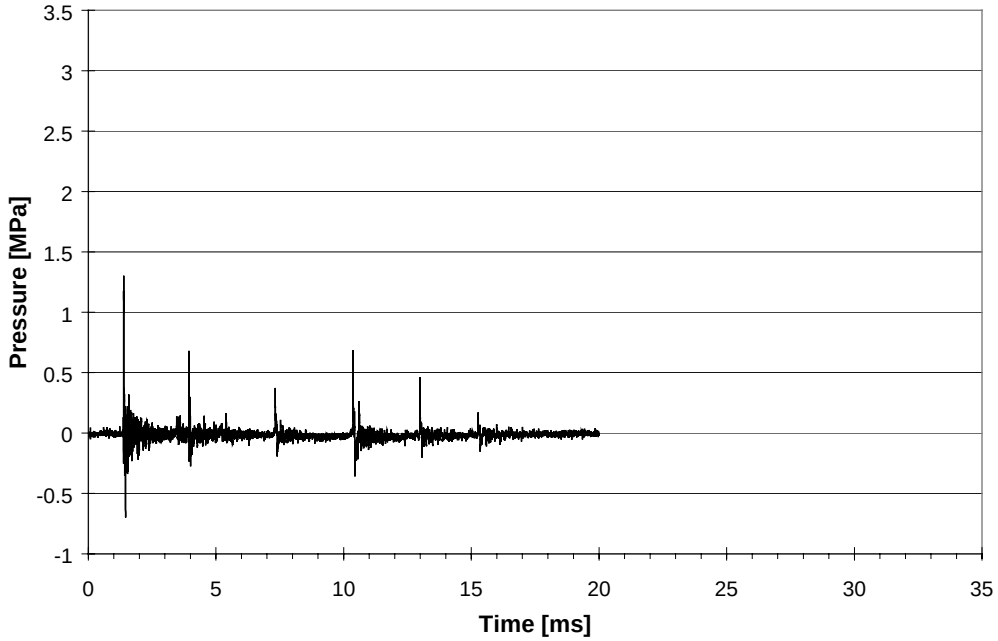

Figure A.3 – Time-pressure trace (D-178-1-4) for an exploding drop of molten FeSi75, triggered at 425 mm.

URN:NBN:no-2125

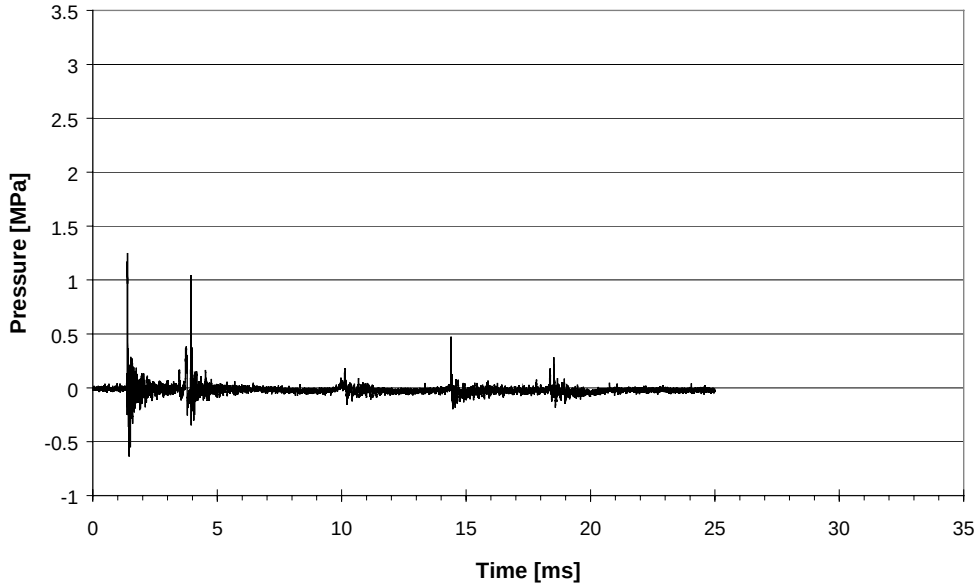

Figure A.4 – Time-pressure trace (D-180-1-4) for an exploding drop of molten FeSi75, triggered at 440 mm.

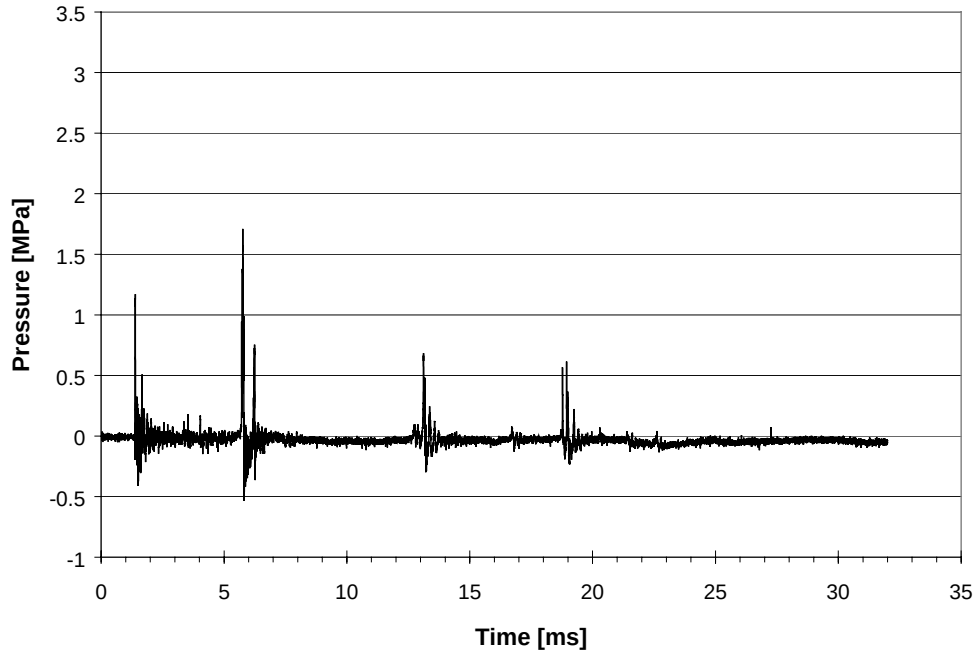

Figure A.5 – Time-pressure trace (D-182-1-4) for an exploding drop of molten FeSi75, triggered at 285 mm.

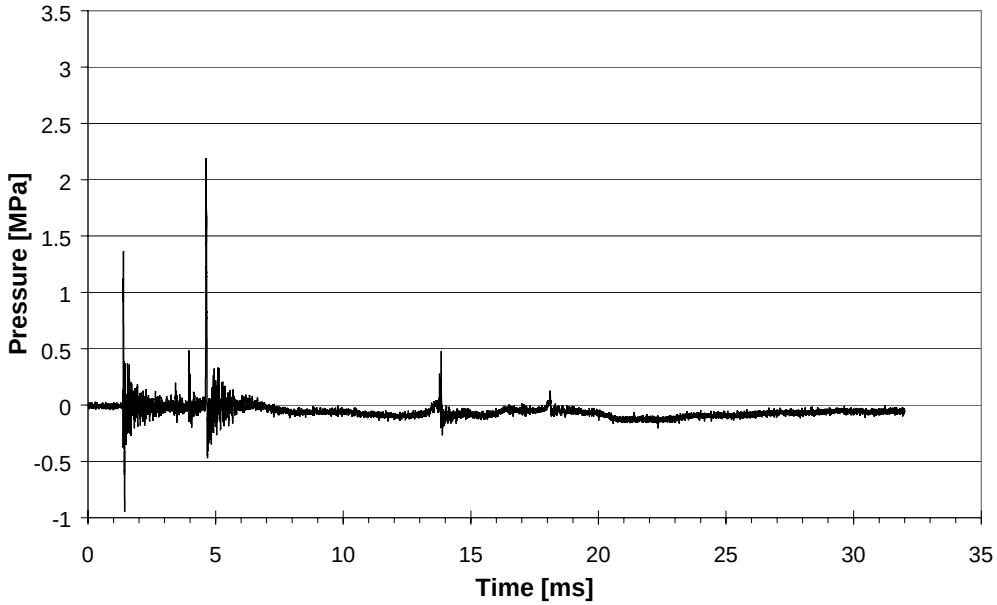

Figure A.6 – Time-pressure trace (D-187-1-4) for an exploding drop of molten FeSi75, triggered at 335 mm.

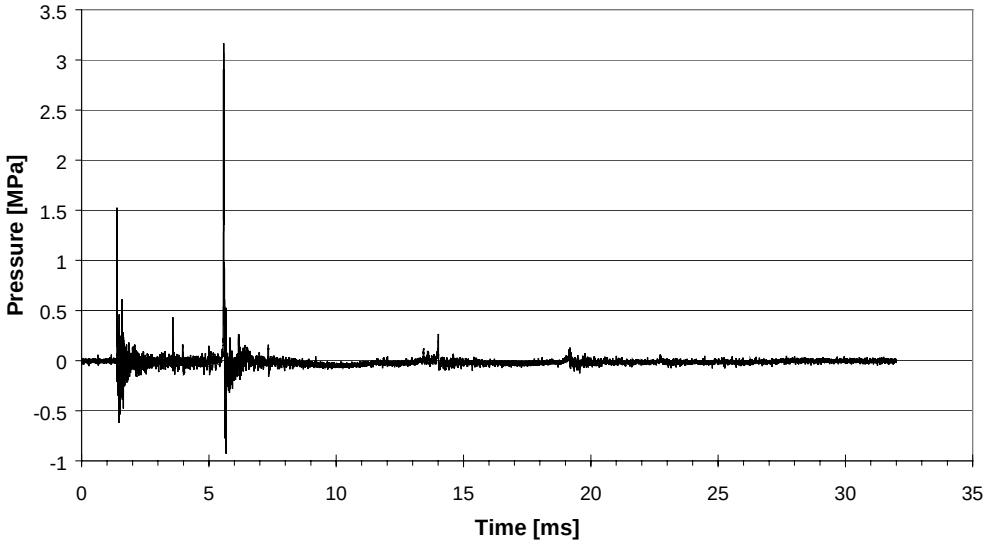

Figure A.7 – Time-pressure trace (D-188-1-4) for an exploding drop of molten FeSi75, triggered at 220 mm.

URN:NBN:no-2125

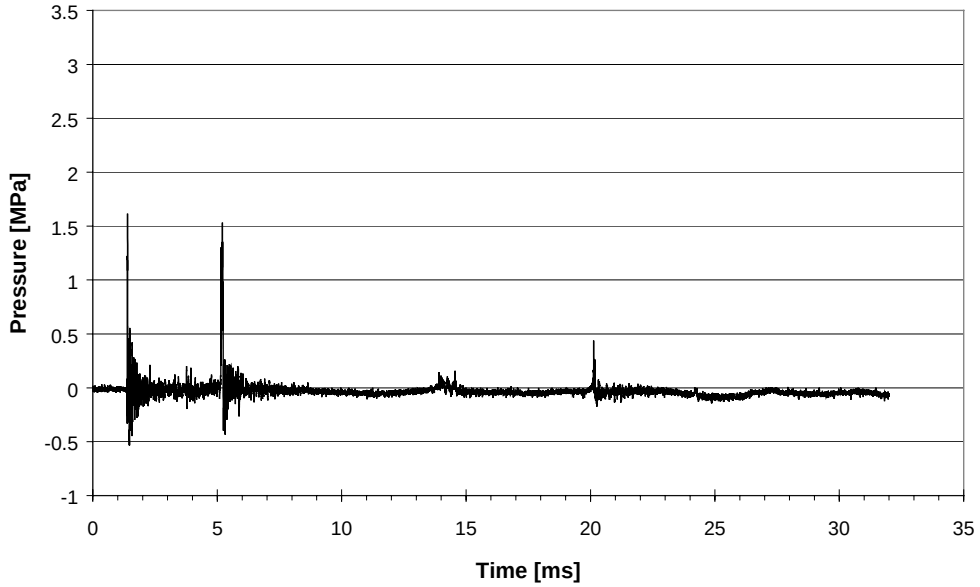

Figure A.8 – Time-pressure trace (D-199-1-4) for an exploding drop of molten FeSi75, triggered at 275 mm.

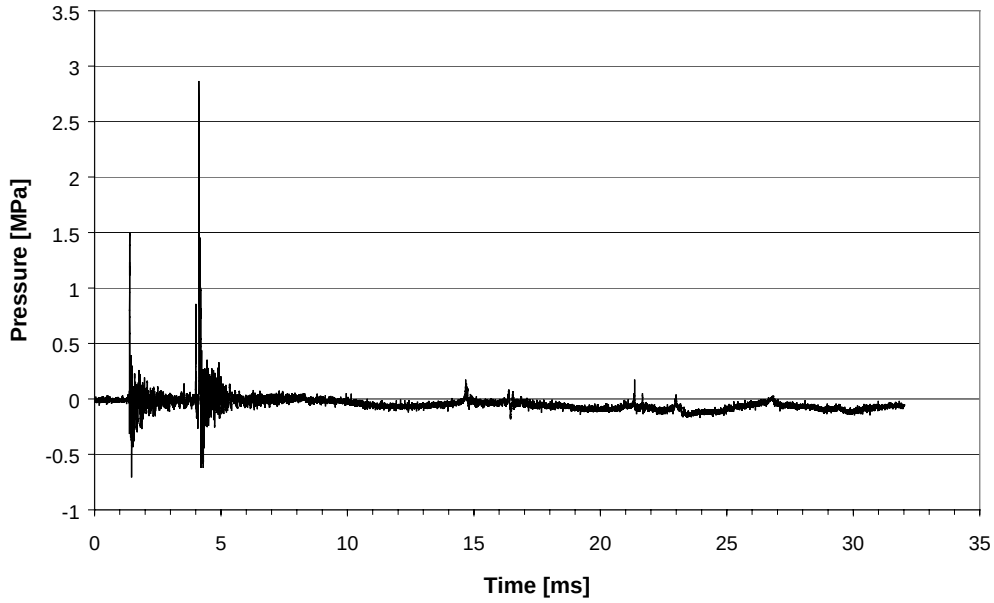

Figure A.9 – Time-pressure trace (D-202-1-4) for an exploding drop of molten Si, triggered at 305 mm.

URN:NBN:no-2125

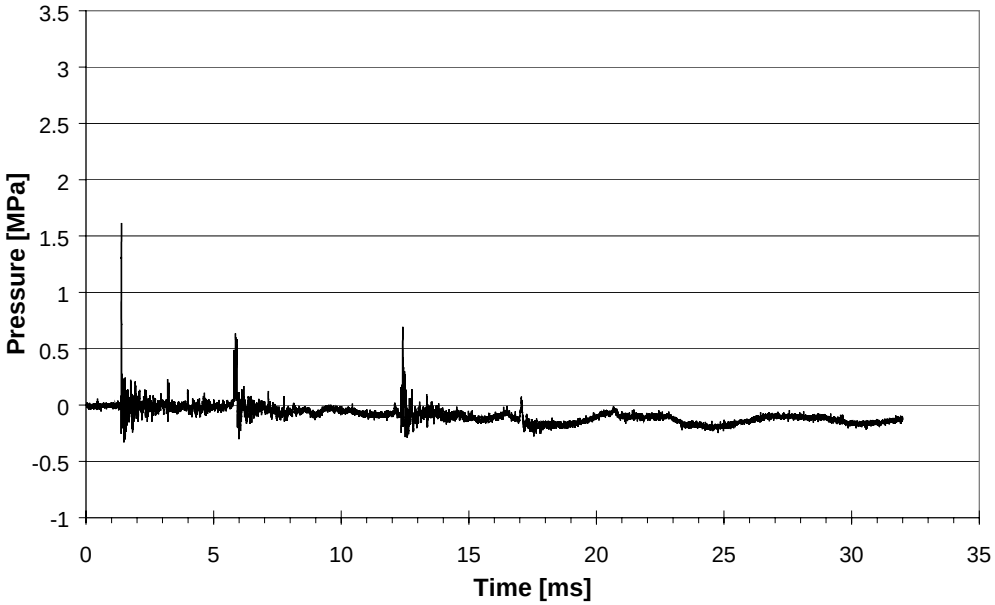

Figure A.10 – Time-pressure trace (D-209-1-4) for an exploding drop of molten Si, triggered at 310 mm.

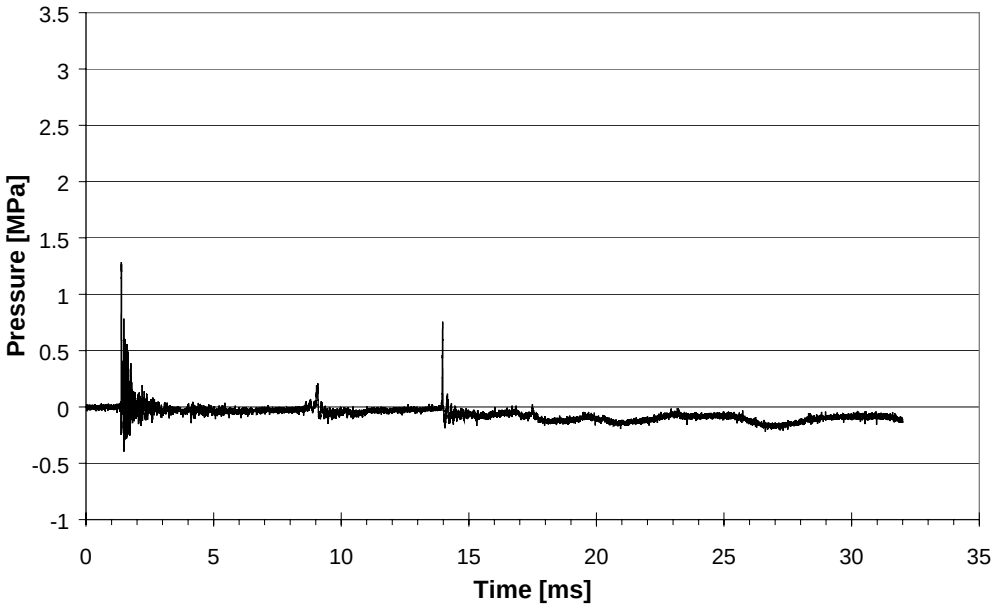

Figure A.11 – Time-pressure trace (D-214-1-4) for an exploding drop of molten Si, triggered at 150 mm.

URN:NBN:no-2125

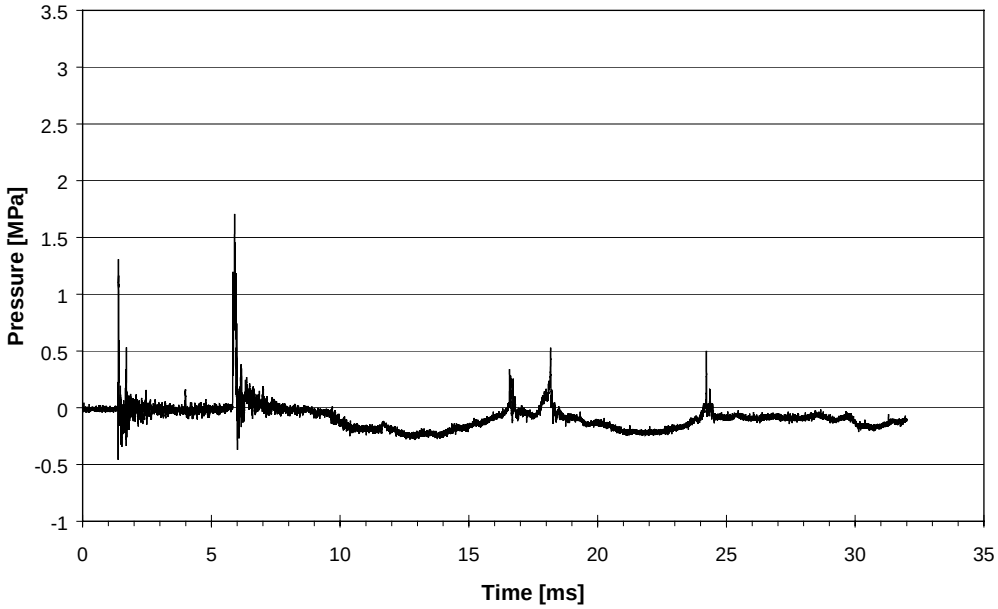

Figure A.12 – Time-pressure trace (D-217-1-4) for an exploding drop of alloyed Si (0.4 % Al), triggered at 150 mm.

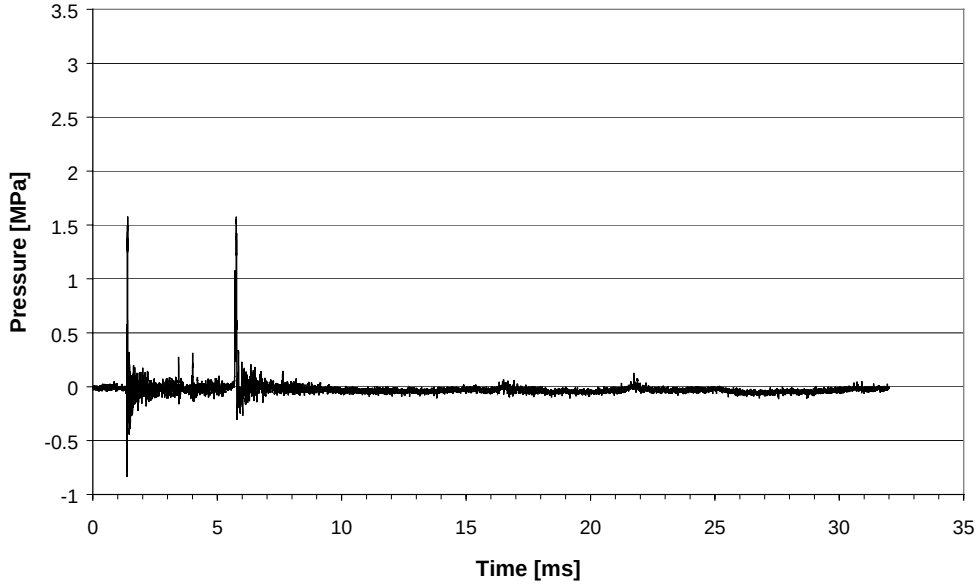

Figure A.13 – Time-pressure trace (D-223-1-4) for an exploding drop of molten Si, triggered at 260 mm.

URN:NBN:no-2125

APPENDIX C – Thermodynamical calculations using EES

The energy history of a molten drop released from the experimental furnace into the water chamber was analyzed using the equation solver EES, designed for thermodynamical application. EES contains an internal database with a wide range of properties for various fluids.

C.1 – Heat transfer during fall from furnace to water

The heat transfer regime is a combination of convection and radiation. The equations used by EES for the convection heat transfer are as follows:

```
h=k*Nusselt/D                          {Heat transfer coefficient}
Q=A*integral(h*(T_drop-T_gas),t,0,sqrt(2*H_air/g))      {Heat flux from drop}
Nusselt=2+0.6*sqrt(Re)*Pr^(1/3){Nusselt number given by Ranz and Marshall for
freely falling liquid drops}
Pr=C_p*mu/k                            {Prandlt number}
A=pi*D^2                               {Area of the molten drop}
Re=D*V_rel/Nu_argon                    {Reynolds number}
V_rel=abs(V_drop-V_argon)              {Relative velocity}
V_argon=0.274                          {Gas velocity}
T_drop=1685                            {Temperature of drop}
T_gas=300                              {Estimated temperature of gas}
V_drop=g*t                             {Free fall velocity of drop}
g=9.81                                 {Acceleration of gravity}
C_p=1000*SPECHEAT(Argon,T=T_gas,P=1)   {Spesific heat of argon, 1 atm,
400 K, compensated for unit difference in EES archive}
k=CONDUCTIVITY(Argon,T=T_gas,P=1){Thermal conductivity of argon, 1 atm,
400 K}
mu=VISCOSITY(Argon,T=T_gas,P=1)  {Dynamic viscosity of argon, 1 atm, 400
K}
Nu_argon=mu/rho                        {Kinematic viscosity of argon, 1 atm,
400 K}
rho=DENSITY(Argon,T=T_gas,P=1)         {Density of argon, 1 atm, 400 K}
D=9*10^(-3)                            {Diameter of molten Si-drop}
H_air=0.4                              {Fall distance from furnace to water
surface}
dT=Q/(m*C_si)                          {Temperature drop due to convection}
C_si=0.2476/0.2388                     {Spesific heat of Si, 1690 K}
m=1                                    {Mass of the falling drop}
```

This set of equations gives the following solution:

URN:NBN:no-2125

$A = 0.0002545$ [m^2]
$C_{si} = 1.037$ [J/g-K]
$dT = 2.899$ [K]
$h = 45.54$ [W/m^2-K]
$k = 0.01787$ [W/m-K]
$\mu = 0.00002285$ [kg/m-s]
$\nu_{argon} = 0.00001426$ [m^2/s]
$Q = 3.006$ [J]
$\rho = 1.603$ [kg/m^3]
$T_{drop} = 1685$ [K]
$V_{argon} = 0.274$ [m/s]
$V_{rel} = 2.527$ [m/s]
$C_p = 521.5$ [J/kg-K]
$D = 0.009$ [m]
$g = 9.81$ [m/s^2]
$H_{air} = 0.4$ [m]
$m = 1$ [g]
Nusselt = 22.94
Pr = 0.667
Re = 1595
$t = 0.2856$ [s]
$T_{gas} = 300$ [K]
$V_{drop} = 2.801$ [m/s]

The equation system is checked for unit consistency.

For the radiation part, the set of equations is given by the following set:

```
Q=E_drop*A*t                          {Heat loss from the drop during the fall}
E_drop=sigma*(T_drop^4-T_gas^4)       {Heat flux from drop}
sigma=5.67*10^(-8)                    {Stefan-Bolzmann`s constant}
T_gas=300                             {Temperature of the gas}
A=4*pi*(9*10^(-3)/2)^2                {Area of the drop}
t=sqrt(2*H_air/g)                     {Time for drop to reach the water
surface}
H_air=0.4                             {Distance from furnace to water surface}
g=9.81                                {The acceleration of gravity}
T_drop=273+1410                       {Temperature of the drop}
m=1                                   {Mass of the drop}
dT=Q/(m*C_p)                          {Temperature drop due to radiation}
C_p=2.476*0.1/0.2388                  {Spesific heat of Si, 1690 K}
```

The numerically obtained solution is given by:

$A = 0.0002545$ [m^2]
$dT = 31.85$ [K]
$g = 9.81$ [m/s^2]
$m = 1$ [g]
$\sigma = 5.670E-08$ [$J/s-m^2-K^4$]
$T_{drop} = 1683$ [K]
$C_p = 1.037$ [J/g-K]
$E_{drop} = 454444$ [$J/s-m^2$]
$H_{air} = 0.4$ [m]
$Q = 33.02$ [J]
$t = 0.2856$ [s]
$T_{gas} = 300$ [K]

URN:NBN:no-2125

We note that the dominant heat transfer regime during the fall through the gas mixture is by far the radiation part, about a factor 10 larger than the convection part.

C.2 – Heat transfer during melt-water contact

The heat loss calculated in the previous section is accounted for by allowing the melt to cool without freezing below the liquidus temperature. The vapor temperature is at least larger than the minimum film boiling temperature, which can be obtained from equation (2.38) and (2.39). Performing the calculation with EES, the following solutions are obtained for the interface temperature for the thermal boundary layer:

C_ψ = 1.037 [J/g-K]
C_{pv} = 1.976 [kJ/kg-K]
k_{si} = 57 [W/m-K]
k_v = 0.03146 [W/m-K]
P = 101.5 [kPa]
P_{cr} = 22064 [kPa]
ρ_{Si} = 2547 [kg/m^3]
ρ_v = 0.4883 [kg/m^3]
R_α = 0.000449
T_{cr} = 647.1 [K]
T_l = 453.2 [K]
T_m = 1412 [K]
T_{min} = 453.3 [K]
T_{sat} = 373 [K]
T_{Si} = 1380 [K]

The interface temperature is found to be T_I=453 K, and this value will be used for the vapor temperature when calculating the heat transfer from the drop. Note that in this particular system, T_I and T_{min} as predicted from equation (2.34) and (2.35) is roughly equal due to the low value of R_α.

```
{The Nusselt number correlation is that of Dhir and Purohit, 1978}

Nus=Nus_0+0.8*Re^(0.5)*(1+Sc*Pr_v/(Sh*Pr_l*mu))
Nus_0=0.8*(g_0*rho_v*(rho_l-
rho_v)*h_fg*1000*D^(3)/(mu_v*k_v*deltaT_w))^(1/4)      {Nusselt number based
on the saturated film boiling heat transfer coefficient averaged over the sphere}

{The parameters in the above equation are defined as:}

Sc=c_pl*deltaT_sub/h_fg          {liquid subcooling parameter}
Sh=c_pv*deltaT_w/h_fg            {vapor superheat parameter}
Re=U*D*rho_l/mu_l                {liquid flow Reynolds number}
Pr_l=PRANDTL(Water,T=T_infinity,P=P_amb)   {Prandlt number for the liquid}
```


URN:NBN:no-2125

```
Pr_v=PRANDTL(Steam_NBS,T=T_f,P=P_amb) {Prandtl number for the vapor}
mu=mu_v/mu_l                {Viscosity ratio}

{Defining the thermophysical parameters:}

c_pl=SPECHEAT(Water,T=T_infinity,P=P_amb) {Spesific heat of the liquid}
c_pv=SPECHEAT(Steam_NBS,T=T_f,P=P_amb)    {Spesific heat of the
vapor}
mu_l=VISCOSITY(Water,T=T_infinity,P=P_amb)
mu_v=VISCOSITY(Steam_NBS,T=T_f,P=P_amb)
deltaT_sub=T_sat-T_infinity                          {Subcooling of
the liquid}
deltaT_w=T_w-T_sat          {Difference between wall temperature and
saturation temperature}
rho_l=DENSITY(Water,T=T_infinity,P=P_amb)  {Density of the liquid}
rho_v=DENSITY(Steam_NBS,T=T_f,P=P_amb)
k_v=CONDUCTIVITY(Steam_NBS,T=T_f,P=P_amb)

{Thermodynamical values, best estimates}

U=0.3                       {Constant fall velocity of the drop}
D=9*10^(-3)                 {Estimated drop size}
T_infinity=20+273           {Free stream water temperature}
T_w=1380+273                {Surface temperature of the drop, compensated
for heat losses during the initial fall from the furnace to the water surface}
T_sat=373                   {Saturation temperature at 1 atm}
T_f=400+273                 {Estimated film temperature}
P_amb=1                     {Ambient pressure}
h_fg=2258                   {Latent heat of vaporization}
g_0=9.81                    {Acceleration of gravity}

{Calculating the heat transfer coefficient from the Nusselt number:}

Nus=h*D/k_v

L=0.4                       {Fall distance in water}

{Finding the energy loss during free fall}

dQ=h*pi*D^2*(T_w-T_infinity)*L/U
m=1                                  {Mass of the drop}
dT=dQ/(m*C_p)               {Temperature drop due to radiation}
C_p=2.476*0.1/0.2388        {Spesific heat of Si, 1690 K}
```

The solution of the above system is given by:

C_p = 1.037 [J/g-K]
c_{pl} = 4.183 [kJ/kg-K]
c_{pv} = 1.974 [kJ/kg-K]
D = 0.009 [m]
δT_{sub} = 80 [K]
δT_w = 1280 [K]
dQ = 222.8 [J]
dT = 214.9 [K]
g_0 = 9.81 [m/s^2]
h = 482.9 [W/m^2-K]
h_{fg} = 2258 [kJ/kg]
k_v = 0.03143 [W/m-K]
L = 0.4 [m]
m = 1 [g]
μ = 0.01528
μ_l = 0.001006 [kg/m-s]
μ_v = 0.00001537 [kg/m-s]
Nus = 138.3
Nus_0 = 47.61
Pr_l = 7.033
Pr_v = 0.9648
P_{amb} = 1 [bar]
Re = 2680
ρ_l = 998.3 [kg/m^3]
ρ_v = 0.4813 [kg/m^3]
Sc = 0.1482
Sh = 1.119
T_f = 453 [K]
T_∞ = 293 [K]
T_{sat} = 373 [K]
T_w = 1653 [K]
U = 0.3 [m/s]

The importance of the interface temperature (the controlling temperature for film-boiling heat transfer) is illustrated in figure C-1, where the total heat transfer *Q* is plotted vs. the interface temperature T_I.

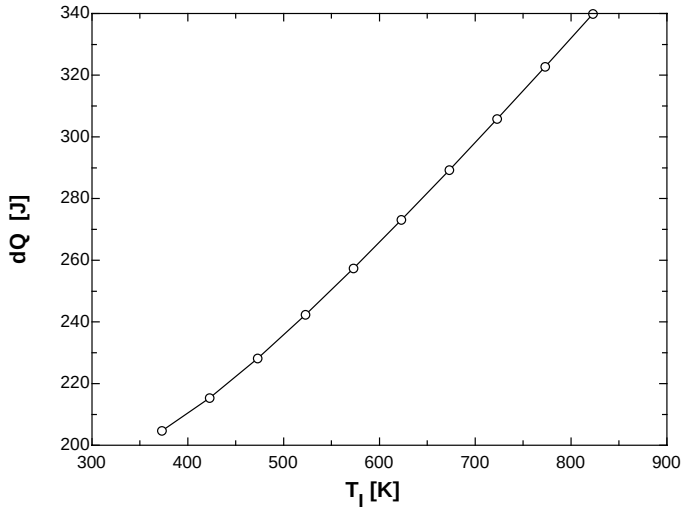

Figure C.1 – The heat transfer as a function of the vapor-drop interface temperature in the thermal boundary layer.